INVESTIGATIONS ON CATHODE MATERIALS FOR LITHIUM ION BATTERY

A THESIS

Submitted in partial fulfilment of the
requirements for the award of the degree
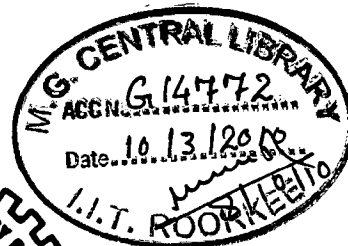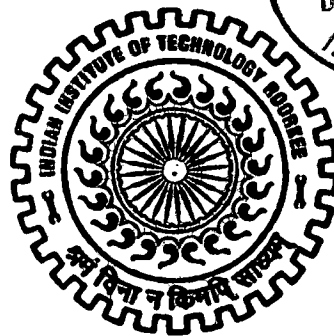*of*

DOCTOR OF PHILOSOPHY

in

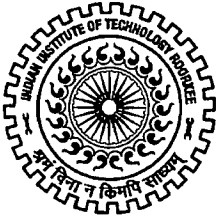METALLURGICAL AND MATERIALS ENGINEERING

by

GURPREET SINGH

DEPARTMENT OF METALLURGICAL AND MATERIALS ENGINEERING
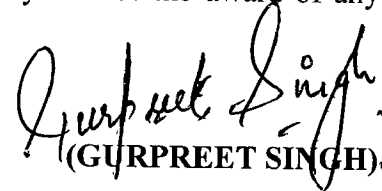INDIAN INSTITUTE OF TECHNOLOGY ROORKEE
ROORKEE - 247 667 (INDIA)
JULY, 2009

INDIAN INSTITUTE OF TECHNOLOGY ROORKEE
ROORKEE

CANDIDATE'S DECLARATION

I hereby certify that the work which is being presented in the thesis entitled **INVESTIGATIONS ON CATHODE MATERIALS FOR LITHIUM ION BATTERY** in partial fulfilment of the requirements for the award of the degree of Doctor of Philosophy and submitted in the Department of Metallurgical and Materials Engineering of the Indian Institute of Technology Roorkee, Roorkee is an authentic record of my own work carried out during a period from July, 2005 to July, 2009 under the supervision of Dr. Anjan Sil, Associate Professor, Department of Metallurgical and Materials Engineering, Indian Institute of Technology Roorkee, Roorkee and Dr. Sudipto Ghosh, Associate Professor, Department of Metallurgical and Materials Engineering, Indian Institute of Technology Kharagpur, Kharagpur.

The matter presented in the thesis has not been submitted by me for the award of any other degree of this or any other Institute.

(GURPREET SINGH)

This is to certify that the above statement made by the candidate is correct to the best of our knowledge.

(Sudipto Ghosh)
Supervisor

(Anjan Sil)
Supervisor

Date: 22/7/09

The Ph.D. Viva-Voice Examination of Mr. **GURPREET SINGH**, Research Scholar, has been held on _____

Signature of Supervisors

Signature of External Examiner

Abstract

Environmental friendly and cheaper cathode material for lithium ion battery has been chosen as a material to work upon. Various experimental and computational investigations have been carried out on pristine and doped $LiMn_2O_4$. Chromium (Cr) and Magnesium (Mg) have been chosen as the dopants. Change in morphology from truncated octahedron to perfect octahedron has been observed with the increase in Cr content in $LiMn_2O_4$. Decrease in the particle size from ~ 250 nm to ~ 80 nm has been observed with increasing dopant concentration. Apart from the decrease in lattice parameter of the cubic spinel structure with the increase in Cr content, no major change has been observed in the crystal structure. No change in the space group symmetry is observed for the entire doping range of Cr, i.e., $LiCr_xMn_{2-x}O_4$; $0.0 \leq x \leq 0.5$. From the electrochemical performance of the materials it has been observed that Cr suppresses the fall in capacity in the 4 V range, and the voltage step which occur in the 4 V regions also gets disappear with the increase in Cr content. Decrease in capacity has been observed with the increase in Cr content. Impedance spectroscopy results show that the bulk impedance increases and hence electrical conductivity of the material reduces with the increase in dopant concentration. The electrical conductivity of the material has been observed to be of the order of 10^{-5} S/cm.

Coexistence of two phases having space groups of Fd3m and $P4_332$ in the Mg doped $LiMn_2O_4$ spinel has been observed. X-ray powder diffraction (XRD) studies show that the crystal structure of $LiMg_xMn_{2-x}O_4$ for x < 0.25 is a single phase cubic spinel which has space group of Fd3m. The cubic spinel structures having space group of Fd3m and $P4_332$ are found to coexist in the compound for x = 0.25. The structure becomes single phase cubic spinel with space group $P4_332$ for x > 0.25. Microscopic observations have shown the particle size ranging from 100 to 350 nm. It has been observed that the particle size decreases with the increase in Mg content. Thermal studies show an exponential decay relationship between the Mg doping content and the decomposition temperature to form nonstoichiometry ($LiMg_xMn_{2-x}O_{4-\delta}$) in the air atmosphere. Fourier transform infrared spectroscopy shows the increase in number of vibrational bands with the increase in Mg content, which indicates ordering of the ions in case of ordered spinel structure and consequent reduction of the space group symmetry from O_h^7 to O^7. Effect of citric

acid content on the various structural and electrochemical properties of layered $LiNi_{1/3}Mn_{1/3}Co_{1/3}O_2$ has been studied. Average particle size of ~ 200 nm has been observed with higher citric acid content. First cycle coulombic efficiency of ~93% has been observed for R'=3 (where R'= ratio of citric acid to metal ions) in the voltage range of 4.6 V to 2.5 V.

First principles calculations have been performed for the doped lithium manganese oxide spinels. Effect of doping spinel $LiMn_2O_4$ with Cr and Mg has been studied using the first-principles spin density functional theory within GGA (generalized gradient approximation) and GGA+U. GGA and GGA+U based calculations predict different ground states for pristine $LiMn_2O_4$ and same ground state for doped systems. Body centered tetragonal phase was found to be the ground state structure using GGA and face centered orthorhombic using GGA+U for $LiMn_2O_4$. Both GGA and GGA+U based calculations for $LiM_{0.5}Mn_{1.5}O_4$ (M= Cr or Mg) show base centered monoclinic as ground state and for LiMMnO4 (M= Cr or Mg) body centered orthorhombic as ground state. We find that GGA based calculations show the pristine $LiMn_2O_4$ as metallic while GGA+U based calculations predict it to be insulating. For doped spinels, GGA based calculation predicts the ground state to be half metallic while GGA+U predicts it to be insulating or metallic depending on the doping concentration. Calculation based on GGA+U predicts insulator-metal-insulator transition as a function of doping in case of Cr and in case of Mg the ground state is found to go from insulating to a half metallic state as a function of doping. Analysis of the charge density and the density of states suggest a charge transfer from the dopants to the neighboring oxygen atoms and manganese atoms. We have calculated the Jahn-Teller active mode displacement Q_3 for doped compounds using GGA and GGA+U. The bond lengths calculated from the calculations using GGA+U are found to be in better agreement with the experimental bond lengths. Based on the bond lengths of metal and oxygen, we have also estimated the average oxidation states of the dopants.

Acknowledgement

"Thanks to Invisible Supreme Power"

The journey was not that easy as I was thinking before joining the Ph.D. at Indian Institute of Technology, Roorkee (I.I.T., Roorkee). Without the cooperation of my near and dear ones it was not possible for me to reach the stage of writing my Ph.D. thesis. During this time period I have experienced some sweet as well as bitter things. Washing away the bitter moments and having some sweet memories in mind, here I am in the position to acknowledge persons who made it little easy for me.

I would foremost like to thank my supervisors, Dr. Anjan Sil and Dr. Sudipto Ghosh, who not only guided me in the darkness of the journey but also encouraged me at every moment of the last four years. Useful subject discussions with them really helped me in understanding the various problems and finding their solutions. Moral support provided by them at Indian Institute of Technology, Kharagpur (I.I.T. Kharagpur) is a thing which can not be washed away from the mind. While working with them you can not get off the track of scientific and spiritual world.

I would like to give my special thanks to two senior professors at Indian Institute of Technology, Kanpur (I.I.T. Kanpur), Prof. Rajendra Prasad and Prof. Sushil Auluck. Their passion for computation and physics of materials always kept me enthusiastic about the subject. Learning the computational code from the scratch and ending up with the interpretation of the results was never going to be easy without their kind help. I would like to thank some of the faculty members at Manipal with whom I have shared my time to time memories. I would like to thank Prof. Ashok Rao, Dr. Utpal Deka, Dr. (Late.) Rajesh Kumar, Prof. Raman Jha, Dr. M.Pandey, Dr. S. Dahal, Dr. N. Bhattacharya and many more.

Friends play a special role at different stages of life. I would like to thank some of my friends who helped me in reaching the writing stage of Ph.D. thesis. I would like to thank Dr. Amrish Panwar, Dr. Shampa Mondal, Shyam lal, Pankaj Sharma. Boys like Vinod Sharma, S umit, Pawan Sapra, Vishal Sahore, Rajveer Singh, Ashutosh Prashar, Vikas Sharma, Vikram Rathore, Sravan and Sushant always encouraged me to achieve the required work.

Contents

List of Figures

XIII

List of Tables

List of Publications

1. Gurpreet Singh, Amrish Panwar, Anjan Sil and Sudipto Ghosh, "Synthesis and characterization of $LiMn_2O_4$ nanoparticles using citric acid as chelating agent", Advanced Materials Research, Vol. 67 (2009) pp 227-232.

2. Gurpreet Singh; Anjan Sil; Sudipto Ghosh, "Structural, Thermal and Morphological Studies of Magnesium Substituted Lithium Manganese Oxide Spinels", Physica B (In Press),doi:10.1016/j.physb.2009.06.148.

3. Gurpreet Singh, S. L Gupta, Rajendra Prasad, S. Auluck, Rajeev Gupta, Anjan Sil, "Supression of Jahn-Teller distortion by chromium and magnesium doping in spinel $LiMn_2O_4$: A first-principles study using GGA and GGA+U", Journal of Physics and Chemistry of Solids (In press.), doi:10.1016/j.jpcs.2009.07.001.

4. Gurpreet Singh, Amrish Panwar, Anjan Sil and Sudipto Ghosh, "Morphological changes in the citric acid assisted $LiCr_xMn_{2-x}O_4$ (0.0 $\leq x \leq 0.5$) materials", Ceramic Silikaty, (Under Revision).

5. Gurpreet Singh, Anjan Sil, Sudipto Ghosh and Amrish Panwar, "Effect of citric acid content on synthesis of $LiNi_{1/3}Mn_{1/3}Co_{1/3}O_2$ and its electrochemical characteristics", Ceramics International, (Under Revision).

6. Amrish Panwar, Gurpreet Singh, Sampa Mondal and Sudipto Ghosh, "Investigation of Manganese Based Cathode Materials for Lithium Ion Battery Technology", PSSARA, 2006, RCI, Hyderabad.

Chapter 1

Introduction

The standard of living, growing population and technological advancement pose increasingly high global demand for the various energy resources available. Energy resources available to us can be divided into two categories viz. conventional and non-conventional. Conventional energy resources are non-renewable sources of energy, which can not be replenished in a short time. These can be classified mainly into fossil fuels, hydraulic and nuclear energy. Fossil fuels such as coal, petroleum and natural gas are the major sources of energy. These are formed by the decomposition of remains of dead plants and animals buried under the soil for a long time. Various products such as petrol, kerosene, diesel, and residual oil can be obtained by processing the crude petroleum at different temperatures. Nuclear fuels such as U^{235} is also a crucial source of energy.

The sources of energy, which are produced continuously in nature and inexhaustible, are usually called renewable sources of energy or non-conventional energy. Non-conventional energy resources such as wind (Hayman et al., 2008), solar energy (Ginley, et al., 2008), tidal energy (Sims, 2008) and biomass (Farrell and Gopal, 2008) provide pollution free environment. For example bio-fuel is any fuel that derives from biomass - living organism or their metabolic byproducts, such as manure from cows. Agriculturally produced biomass fuels, such as biodiesel and ethanol can be burnt in internal combustion engines or boilers. Low grade solar thermal devices are used in solar water heaters, solar cookers and solar driers for domestic and industrial applications. Since the conventional energy resources such as petroleum and coal, which are able to fulfill present day demand for modern society, are becoming expensive due to their limited reserves and non-renewable nature, the need for the non-conventional resources are increasing day by day.

With the growth of electronic industries the demand for suitable energy resources is also increasing. It is a fact that energy resources are not keeping pace with the progress in the computer industry, telecommunication sector and transport sector etc. Therefore search for

energy resources suitable for these industries is gaining a global thrust among the researchers. Vehicles which use conventional resources such as petrol and diesel are slowly being replaced by the electric vehicles for which the sources of energy are fuel cells (Whittingham and Zawodzinski, 2004), (Crabtree and Dresselhaus, 2008), (Anis et al., 2008), supercapacitors (Winter and Brodd, 2004), (Simon and Gogotsi, 2008) and batteries (Thackeray, 2002). Fuel cell is composed of mainly an oxidant, fuel and electrolyte. It carves up the fuel into electrons and protons and forces the electrons to travel through the outer part of the circuit. Another catalytic process takes the electron back in, combining them with the protons and oxidants to form waste products. Various types of fuels such as hydrogen, hydrocarbons and alcohol can be used in the fuel cells. Fuel cells with solid oxide electrolyte are known as Solid Oxide Fuel Cells (SOFC) and are most common in this category.
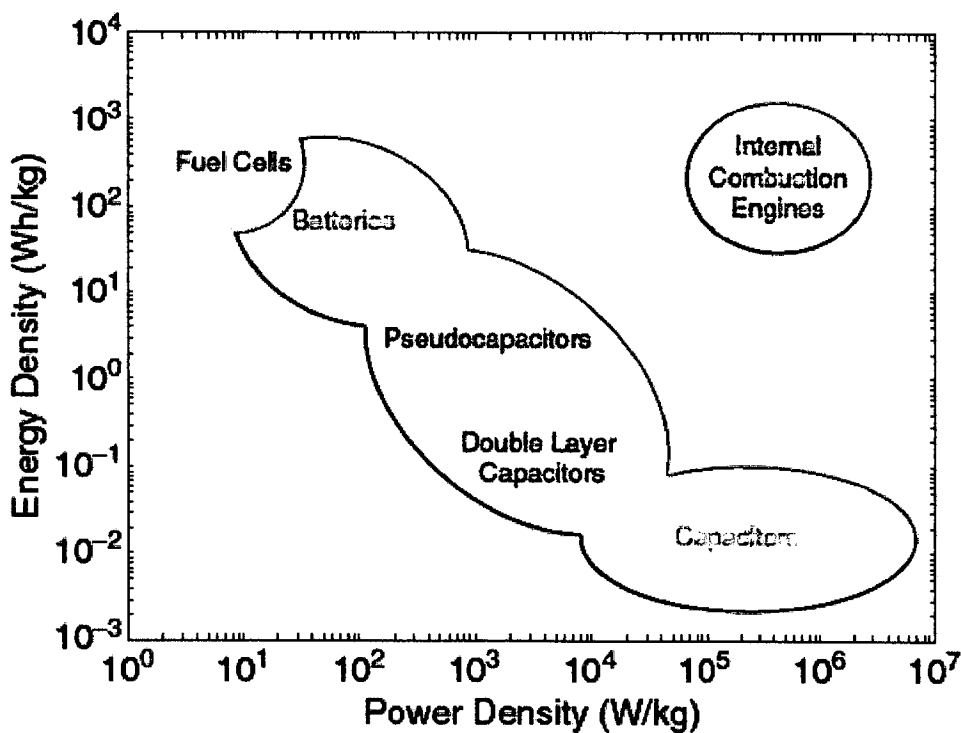
Fig. 1.1: Mapping between power density and energy density for different energy resources (Whittingham, 2008)

It operates at high temperature (600°C to 1000°C), which results in longer start up times and issues related to chemical compatibility. Research for developing the high performance

materials at lower operating temperature is on its way to the new generation fuel cell technology. Fuel cells are very useful as power sources in remote locations, such as spacecraft, remote weather stations, large parks, rural locations, and in certain military applications. Other source of energy such as supercapacitor usually has very high energy density. In contrast to the traditional capacitors available, these capacitors do not have conventional dielectric material. In order to get higher storage capacity, use of activated charcoal is one of the options available. It is a kind of a sponge and is made up of very rough and small particles. Nanotubes have replaced charcoal, because it can provide similar charge storage capability, but these are mechanically arranged in such a manner that they provide a high surface area. Internal resistance of these capacitors is very less, which makes them very efficient. Supercapacitors are used in MP3 players, cell phones, flashlights etc. In some countries these capacitors have been used in commercial buses.

Electronic devices such as laptops, personal digital assistants (PDAs), video cameras and mobile phones need small portable power devices such as batteries. Batteries are at high demand in the market because of their capability to fulfil all the required needs for portable electronic devices as well as electric vehicles (Daniel et al., 2008). This is because batteries can provide higher energies than capacitors, where as capacitors are high power devices with limited energy storage capability. A comparison of power density and energy density for batteries, capacitors and fuel cells is shown in Fig. 1.1. In addition, voltage delivered by capacitors varies strongly with the state of discharge whereas batteries provide constant output voltage. Fuel cells, operating on liquid fuels such as methanol, can have high-energy storage, but their power output is limited.

Advancement in the technology from lead acid battery to present day's Li-ion battery is not sufficient in keeping pace with the technological progress in computers and other portable electronic devices. Among the various batteries available, Li-ion batteries are in highest demand because they are amenable to variable discharge rates and high energy density compared to lead acid, nickel-cadmium (Ni-Cd) and nickel metal hydride (Ni-MeH). A comparison of different battery technologies in terms of volumetric and gravimetric energy densities is shown in Fig. 1.2. Li-ion batteries have captured almost the total battery market as far as portable electronic devices are concerned. Today, Ni-MeH is the principle battery

5

used in majority of the hybrid electric vehicles, but these are likely to be replaced by the low cost Li-ion batteries which have higher energy density. Specific capacity, long cycle life and better safety of these batteries are the issues which are always at thrust among the researchers across the world and need immediate attention for next generation Li-ion batteries (Whittingham, 2004).
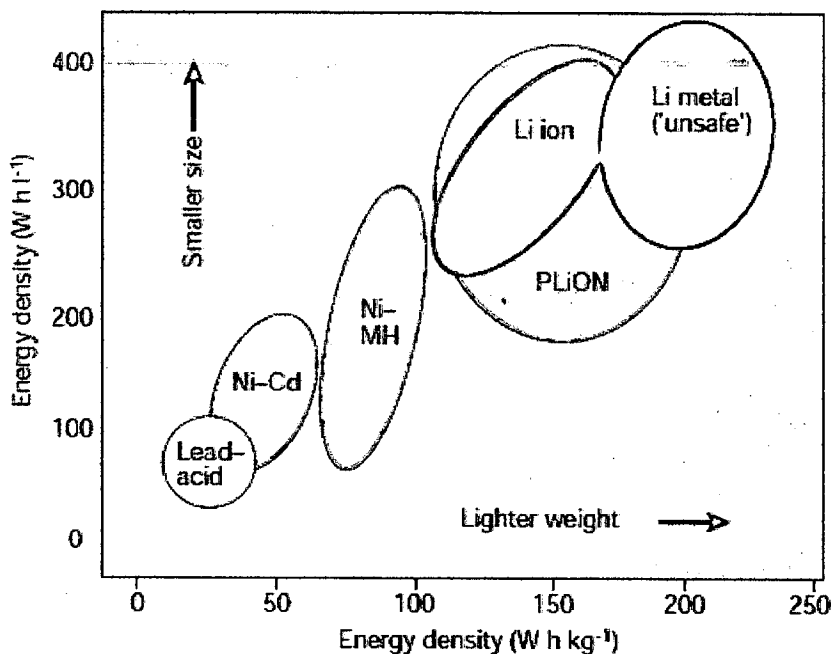
Fig. 1.2: Comparison of different battery technology in terms of volumetric and gravimetric energy densities (Tarascon and Armand, 2001)

Li-ion batteries have three major components namely cathode, anode and electrolyte. Performance of the battery is dependent on the characteristics of these components. Lithium is known to be the most electropositive material having a potential of -3.04 V with respect to standard hydrogen electrode. It is also the lightest material with an equivalent weight of 6.94 gm mol^{-1} and specific gravity of 0.53 gm cm^{-3}. These batteries provide a high operating potential ~ 3.06 V depending on the electrode materials used. By 1972, electrochemical intercalation was already defined. In the same year Exxon embarked on a large project using TiS_2 as positive electrode and metallic lithium as negative electrode. Lithium perchlorate in

dioxolane was used as electrolyte. Earlier, lithium metal was used as anode material. But it encountered some serious drawbacks such as dendrite formation due to the reaction of lithium metal with the electrolyte, leading to explosion hazards. Li-Al alloys solved the problem of dendrite formation in these cells but still had the problem of short cycle life due to the large volume changes during charging/discharging. New concept of using lithium in its ionic form rather than metallic form opened the doors for the commercialization of these batteries. The researchers at Bell labs in United States demonstrated successful intercalation of graphite with lithium (Basu, 1981, Murphy et al., 1977). A working model of a Li-ion battery is shown in Fig 1.3. During the charging of battery lithium ion moves from cathode host to the anode through electrolyte. An electron flows through the outer circuit in order to maintain the charge balance. The reverse process occurs during the discharging stage of the battery. Another approach to solve the dendrite problem was improvement in electrolyte. Bellcore researchers introduced polymeric electrolytes in liquid Li-ion systems. They developed the first reliable and practical rechargeable Li-ion HPE (hexa-fluropropylene) battery known as plastic Li-ion (PLiON) (Goztz, et al., 1995, Tarascon, et al., 1996). Such batteries have been commercialized in 1999. Next generation Li-ion cells confusingly called Li-ion polymer use a gel-coated microporus poly-olefin separator bonded to the electrodes, rather than P(VDF-HFP) based membrane (copolymer vinylidene difluoride with hexa-fluoropropylene) used in plastic Li-ion cells. Goodenough proposed Li_xMO_2 (M= Co, Ni, Mn), as new cathode materials, which can provide high capacities and good cycle life.

In Japan, June 1991, Sony Corporation used C and $LiCoO_2$ as anode and cathode materials to commercialize these batteries, known as Lithium Ion Batteries. China has emerged as a new hub for these batteries. Cylindrical cells (18650 standard) was used in early stages. However, presently prismatic shaped cells with Al-laminated versions and square shaped cells have mostly filled the market together with the rapid spread of cellular phones. Some of the basic requirements, which an ideal cathode material should satisfy, are as follows:

1. Structural changes should be minimum during insertion/extraction of lithium ions.

2. An ion such as transition metal ion, with a variable oxidation state, which can easily reduce/oxidize must be present.

3. Electronic conductivity of the materials should be high, so as to minimize the requirements of additional additives such as acetylene black.

4. It should be thermally stable in a wider range of temperature.

5. It should be environmental friendly and cheap.
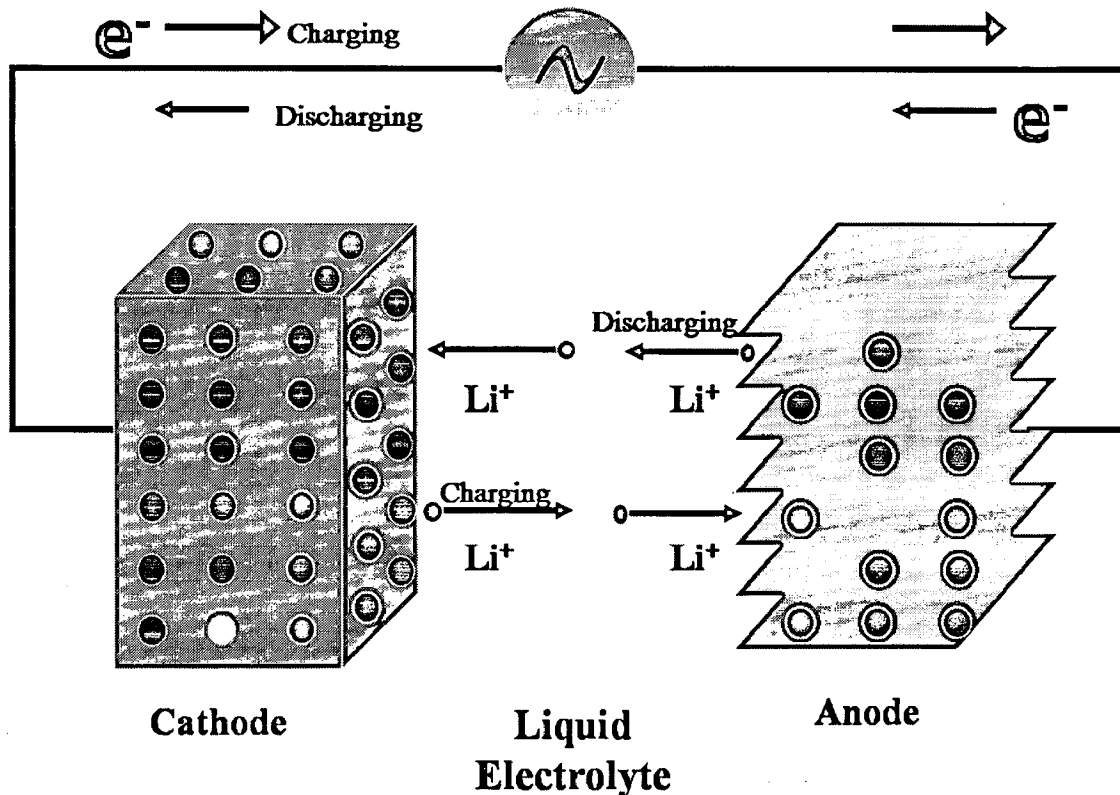
Fig. 1.3: Working of Lithium Ion Battery

Within the last two decades, much attention has been paid to understand the properties of $LiCoO_2$ (Mizushima et al., 1980), $LiNiO_2$, $LiMnO_2$, $LiMn_2O_4$ (Armstrong and Bruce, 1996, Tian et al., 2004, Kubo et al., 1997) and $LiFePO_4$ (Padhi et al., 1997), which are currently among the most important cathode materials. Advantages such as lower price, lack of toxicity and better thermal stability of manganese based spinel cathode material over $LiCoO_2$ are well known. On the other hand, the spinel has a lower specific capacity compared to $LiCoO_2$ and it faces serious problems in storage and cycle life at higher temperatures. Researchers in this area are steadily working to better understand the complexity of this

material and to overcome the above said problems. Vast literature on this material presents several discrepancies with regard to different aspects like: phase transition of the as prepared material below room temperature; phase transition in the 4V range; origin of capacity fading during storage and cycling; Mn dissolution as a function of the state of charge and products formed during dissolution.

Since electronic properties also play a very crucial role in the electrochemical performance of these materials, therefore, properties such as electronic structure, conductivity and stability of the material have also been discussed using first principles study. The state of art in the first principles electronic structure methods for solids is based on density functional theory (DFT) (Payne et al., 1992).

Among the various possible cathode materials for lithium ion battery, manganese oxide based spinel is an attractive cathode material due to the cheaper and non toxic nature of manganese present in the structure. For this reason $LiMn_2O_4$ has been chosen for the present study. Mn is present in +3 and +4 oxidation states in the crystal structure in equal amount. Mn^{+3} can be categorized in two possible states namely low spin and high spin. The high spin Mn^{+3} is a Jahn-Teller active ion and gives rise to a distorted octahedron when it is octahedrally coordinated by the oxygen ligand. During this process the degeneracy of the various d-orbitals gets destroyed and two of the five d-orbitals get shifted up to the higher energy states and the rest three orbitals acquire lower energy states, and hence lead to the distortion in the local octahedron. Mn^{+3} low spin and Mn^{+4} are Jahn-Teller inactive ions. Jahn-Teller distortion present in the structure is the main cause of the capacity loss after a number of cycles of charging and discharging. In order to get rid of Jahn-Teller distortion and improve the capacity retention the dopants such as Cr and Mg have been doped. Cr, when present in +3 oxidation state and Mg^{+2} are Jahn-Teller inactive ions. We have doped Cr and Mg in order to replace Mn^{+3} present in the structure. Among the best possible dopants Cr and Mg are cheap and easily available and therefore the present study focuses on Cr and Mg as dopants in $LiMn_2O_4$.

In connection with Cr and Mg doped $LiMn_2O_4$, extensive literature survey was carried out. The literature survey suggests few important gaps. Morphological changes associated with

the doping have not been studied schematically, not only for the Cr and Mg doped $LiMn_2O_4$ but also with all other doped $LiMn_2O_4$. Therefore studies on morphological changes were taken up. In addition to this, controversy exists on the space group symmetry of the Mg doped $LiMn_2O_4$. Therefore in-depth X-ray diffraction study of Mg doped $LiMn_2O_4$ was taken up. Further very few ab-initio studies have been carried out for doped spinel. Therefore an attempt has been made to study the structural and electronic properties of the doped materials using First principles by considering spin polarization in to account. Jahn-Teller distortion has also been studied for the doped $LiMn_2O_4$ systems. An effort has also been made to calculate the oxidation states of various ions present in the structure.

$LiNi_{1/3}Mn_{1/3}Co_{1/3}O_2$ has been found to be best alternate to $LiCoO_2$ in the sense of electrochemical performance. In fact according to many its performance is at par with $LiCoO_2$. Exhaustive literature survey suggested that this system is well characterized. However the effect of processing parameters on the performance of $LiNi_{1/3}Mn_{1/3}Co_{1/3}O_2$ has not been thoroughly studied and thus was taken up in the present study.

Chapter 2

Literature Review

Rechargeable lithium batteries involve reversible insertion of lithium ions (guest species) into a host matrix (electrode material) named as lithium insertion compound. The lithium insertion/extraction process occurring with a flow of ions through the electrolyte is accompanied by respectively a reduction/oxidation reaction of host matrix assisted by the flow of electrons through the outer circuit. Open circuit voltage is defined as the ratio of the chemical potential difference between the cathode and the anode to Faraday constant. Redox energies of cathode and anode should lie within the band gap of the electrolyte (E_g) to obtain the proper thermodynamic stability. Hence the electrochemical stability requires the following condition (Fig. 2.1):

$$eV_{oc} = \mu_{Li\,(c)} - \mu_{Li(a)} < E_g$$
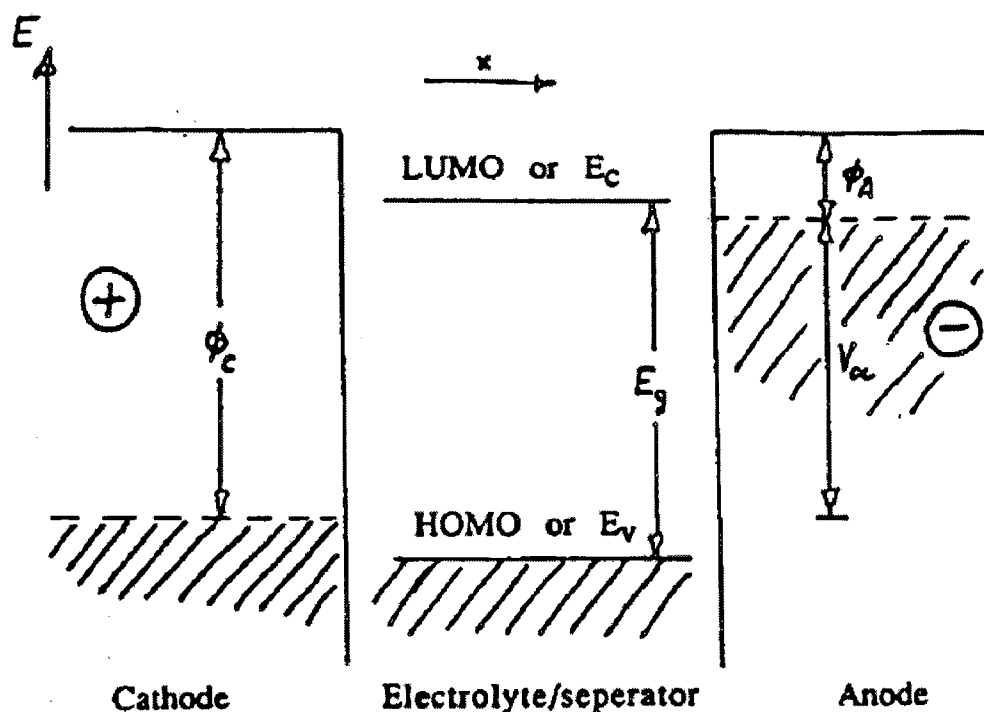
Fig. 2.1 Cell at open circuit (Goodenough et al., 1993)

2.1 Overview of Various Components of Lithium Ion Batteries

2.1.1 Anode:

Although lithium in its metallic form is the most favorable choice for anode material but due to safety issues on the use of lithium metal electrode, alternate insertion materials such as lithium alloys and carbon have been proposed (Tarascon and Armand, 2001). The rocking chair battery pioneered in the mid 80's, solved the safety problem by replacing metallic lithium with lithium insertion compound. The choice of the anode material is based on properties that include fast insertion kinetics, and a redox potential with respect to Li which is less than that of cathode to provide a sufficiently large cell voltage. In the early stages, oxide such as Li_xWO_2 was employed as anode material. Some alloys of lithium metal such as Li_9Al_4 (Hamon et al., 2001), (Wen et al., 1979), $Li_{21}Si_5$ (Weydanz et al., 1999), $Li_{17}Sn_4$ (Wen

14

et al., 1981) and Li₃Bi (Zhou et al., 2003) also solved the safety issues but their shorter cycle life due to the large volume changes during insertion/extraction of lithium made them less favorable for the use as anode material. Amorphous hydrogenated silicon (Feng et al., 1992) thin films have also been used as an electrode (Kulova et al., 2006) for the lithium ion battery. The intercalation capacities of films grown at 250° C are ~1750 and ~500 mAh/g in the first cycle and 100th cycle respectively. Most of the improvements in anodes actually implemented over the last decade have involved carbonaceous materials. Amorphous carbon has already been in use for the various applications and its various properties such as electrical conduction has been improved in the recent past (Silva and Carey, 2003) in order to get the desired performance. The mechanism of lithium intercalation that gives rise to a maximum uptake corresponding to LiC_6 (Fig. 2.2) is well understood.
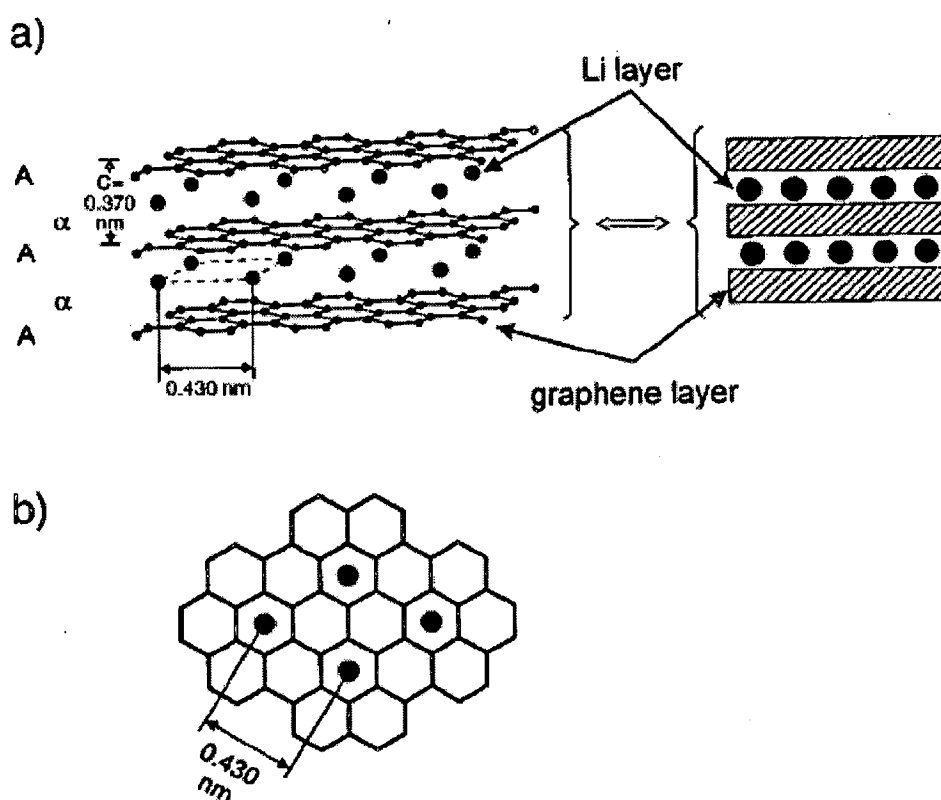
Fig. 2.2: Structure of LiC_6. (a) Left: schematic of AA layer stacking sequence and the α α interlayers ordering of the intercalated lithium. Right: simplified representation. b) View perpendicular to the basal plane of LiC_6. (Winter et al., 1998)

15

When graphite electrode is polarized to negative potentials during initial intercalation in an ethylene carbonate based solution (electrolyte), the organic solvent reductively decomposes on graphite surface to form a stable surface film. This is often known as solid electrolyte interface (SEI) (Winter and Brodd, 2004). Due to the self discharge of Li_xC_6 the growth of solid electrolyte interface increases and hence leads to the increased internal resistance. This leads to the decrease in the power density with the number of cycles.

Lithium cannot be readily accommodated in the interlamellar graphene galleries of soft carbon such as petroleum coke and hence low capacities are observed. For graphitized soft carbons, the level of disorder has a direct effect on the mechanism of the reaction with lithium. Capacities well above the theoretical limit of 372 mAh/g are observed, but are inevitably associated with a large hysteresis. Specific new forms of carbon which have replaced petroleum coke and give rise to high capacity/rate capability of anodes, include MCMB (mesocarbon microbeads or spherical graphite) (Winter et al., 1998, Dahn et al., 1993, Flandrois and Simon, 1999, Endo et al., 2000, Noel and Suryanarayanan, 2002), MCF (microcarbon fiber) (Tokumitsu et al., 1996, Kasuh et al., 1997) and natural and synthetic graphite flakes. MCMBs in particular, are very useful. They exhibit large capacity on heat treatment at low temperatures and on graphitization at higher temperature. MCMB materials are derived from petroleum industry byproducts or coal products, but are expensive owing to low yields.

2.1.2 Electrolytes:

The basic requirements for an electrolyte in Li-ion battery are as follows:

1. High ionic conductivity to minimize the cell resistance and thereby its resistive heating.
2. High chemical stability to prevent decomposition of electrolyte on the surface of highly reducing anode materials as well as highly oxidizing cathode material.
3. Electrochemical stability to tolerate the high voltage difference between anode and cathode (> 4 V) without being reduced or oxidized.
4. It should be ideally electronic insulator to avoid the short circuiting of the electrodes and ionic conductor.

5. Electrolyte potential should have limited variations as a function of Li^+ content.

6. Low melting point to provide sufficient conductivity at sub-ambient temperatures and prevent solidification and phase separation.

7. High boiling point to provide safety and prevent explosions that may result from high pressure buildup in the cell.

8. It should be non toxic.

9. It should have low cost.

$LiPF_6$ was proposed as an electrolyte solute for lithium-based batteries in the late 1960s, and soon its chemical and thermal instabilities were known. Even at room temperature, equilibrium exists:

$$LiPF_6 \rightleftharpoons LiF + PF_5$$
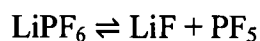
The generation of the gaseous product, PF_5, drives the equilibrium to the right, and this process is favored at higher temperatures. In the presence of nonaqueous solvents, the strong Lewis acid PF_5 tends to initiate a series of reactions, such as ring-opening polymerization or cleavage of ether linkages (Robert et al., 1992, George et al., 1968). Apart from the selection of the solute in the electrolyte, solvent has to be proper. Various organic solvents of the electrolyte solution such as EC (ethylene carbonate) (Pistoia et al., 1970, Xu et al., 2001), DEC (diethyle carbonate) (Peled et al., 1998, Aurbach et al., 1995), PC (propylene carbonate) (Fong et al., 1990, Nishi et al., 1990, Yamaura et al., 1993, Zhang et al., 1993) and THF (Tetra hydro furan) (Subbarao et al., 1990, Surampudi et al., 1993) etc. have been used successfully in the batteries. It is common practice to mix two or more solvents so as to obtain a desired set of properties which is suitable for high performance batteries. Since the electrolytes based on PC are reported to decompose in contact with graphitized carbon anode a suitable solvent mixture (EC/DEC) has been recommended (Wang et al., 2005).

In order to get rid of the above problems associated with the $LiPF_6$ and solvents polymeric electrolytes were introduced. Polymeric membrane has been used as both separator and electrolyte (Xu et al., 2004). Rechargeable lithium batteries having the solid polymer electrolytes have been studied. There are two kinds of polymer gel system. One is where the polymer gel is sandwiched between lithium ion battery electrodes where a different polymer (PVDF) from the separator is used as binder in electrode. Second system refers to as porous

polymer gel system prepared from copolymers of vinylidene fluoride with hexa flouoropropylene, PVDF-HFP, and typical lithium ion battery electrolytes, LiPF$_6$/EC-DMC (Kono et al., 1999, Gozdz et al., 1994).

2.1.3 Cathode:

Sony corporation successfully introduced commercial Li-ion batteries into the market in 1991, in which LiCoO$_2$ (Mizushima et al., 1980, Goodenough, 2007) was used as cathode material. Even after decades it is the most promising cathode material. The choice of cathode material is dictated by the applications. In portable devices, material which is expensive and performs moderately at high rates can be tolerated. But for high power application, such as in electric vehicles, low cost and higher rate capabilities are mandatory. NEC in 1996 (Numata et al., 2000, Tsunoda et al., 2000, Amemiya et al., 2001) and Sanyo in 2001 (Narukawa et al., 2002), in the market, have introduced some inexpensive materials such as LiMn$_2$O$_4$.

An ideal cathode material for Li-ion battery should satisfy the following conditions:

1. Li$^+$ intercalation in the case of layered structure or insertion for one or three dimensional structures should take place.

2. To show a high open circuit voltage, it has to have low Fermi level and low site energy for Li$^+$.

3. Number of sites for Li$^+$ has to be high and hosting structure has to feature low weight and high Li$^+$ density (number of lithium ions per unit weight or per unit volume).

4. The Li$^+$ intercalation/insertion has to be reversible, i.e., with no or reversible structural changes, to allow cyclability.

5. Low cost

6. Lack of toxicity

7. Ease of synthesis

2.2 Layered Oxide Cathodes

Various oxide materials such as $LiMO_2$ (M = Co, Mn, V, Ni,) (Armstrong and Bruce, 1996, Tian et al., 2004, Kubo et al., 1997) are found to have layered structure in which the Li^+ and M^{3+} ions occupy the alternate (111) planes of the rock salt structure to give a sequence of O-Li-O-M-O layers along the c-axis of the unit cell. Crystal structure of these layered compounds consist of closed packed array of oxygen with ABCABC.......stacking sequence (Fig. 2.3) with the presence of M and Li ions in the octahedral sites in between the alternating layers of oxygen planes (Orman et al., 1980). The structure is known as O3 layer structure since Li^+ ions occupy octahedral sites and there are three MO_2 sheets per unit cell. Insertion and extraction of the Li-ions from the lithium planes allowed by the MO_2 layers which are strongly (covalent) bonded.
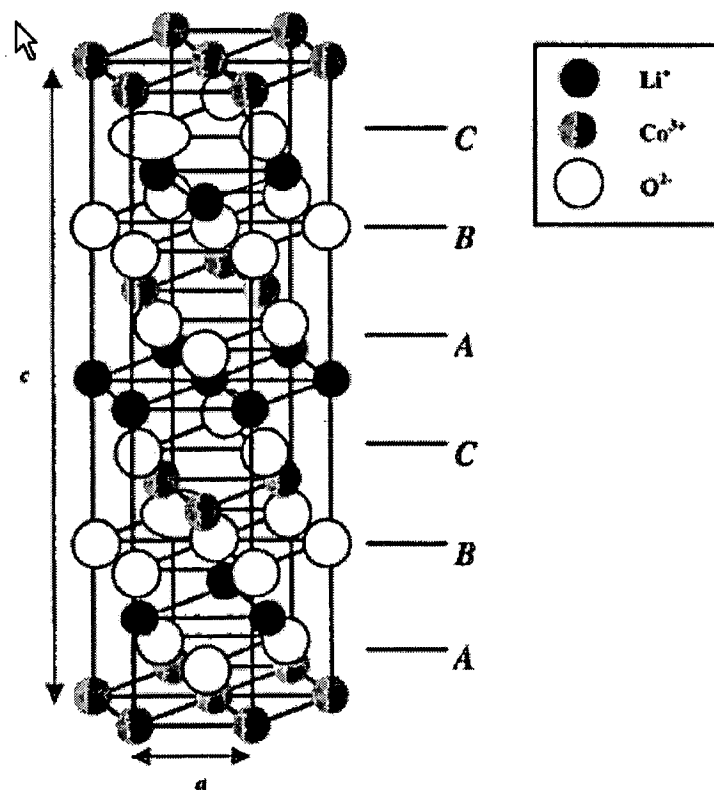
Fig. 2.3: Layered structure of $LiCoO_2$

19

The layered form of $LiCoO_2$, which has a rhombohedral symmetry, belongs to the space group R-3m. Li_xCoO_2 can be completely and reversibly deintercalated to form CoO_2. In case of CoO_2 phase the different O-Co-O slabs, held together by weak Vander Waals forces, slide with respect to each other, so that the closed packed oxygen layers have an ABAB......stacking sequence as opposed to the ABCABC....sequence of $LiCoO_2$ (Amatucci et al., 1996). A high lithium chemical potential associated with highly oxidized Co^{3+}/Co^{4+} couple provides a high cell voltage around 4 V and discharge voltage does not change significantly with the degree of lithium extraction/insertion x in $Li_{1-x}CoO_2$ (Wang et al., 1999, Tukamoto et al., 1997). Direct Co-Co interaction with a partially filled t_{2g}^{6-x} band associated with the $Co^{3+/4+}$ couple leads to high electronic conductivity for $Li_{1-x}CoO_2$. A strong preference of Co^{3+} ($t_{2g}^6 e_g^0$) and Co^{4+} ($t_{2g}^5 e_g^0$) ions for octahedral sites provides good structural stability for $Li_{1-x}CoO_2$ without encountering a migration of $Co^{3+/4+}$ ions from octahedral sites of Co planes to the octahedral sites of the lithium plane via the neighboring tetrahedral sites. It has been experimentally found that $LiCoO_2$ has a capacity of ~ 140 mAh/g, which is 50% of its theoretical value. The limitation in capacity can be attributed to an ordering of Li-ions and consequent structural distortions (hexagonal to monoclinic) of around x = 0.5 in $Li_{1-x}CoO_2$ and side reactions when potential (with respect to Li) is greater than 4.2 V.

Due to the presence of less toxic and less expansive Ni in place of Co, $LiNiO_2$ has an advantage over $LiCoO_2$. But this material encounters some of the problems such as (i) difficulty to synthesize (Dutta et al., 1992), (ii) Jahn-Teller distortion associated with low spin Ni^{3+} (Nakai et al., 1998), (iii) Irreversible phase transition occurring during the charge-discharge process (Ohzuku et al., 1993) and (iv) exothermic release of oxygen at elevated temperature and safety concerns in charged state (Dahn et al., 1994). However, some of the difficulties have been overcome by partial substitution of Co for Ni. For example Jahn-Teller distortion has been suppressed using this substitution. $LiNi_{0.85}Co_{0.15}O_2$ has a practical capacity around 180 mAh/g, which is 30 % higher than $LiCoO_2$ (Li et al., 1997).

Spinel oxide cathodes: Spinel compounds, such as Fe_3O_4 (Chakravorty et al., 2002), Mn_3O_4 (Boucher et al., 1971), having general formula of $A[B_2]X_4$ have received attention as possible solid-solution electrode for room temperature lithium batteries. Their electrochemical

performance at higher temperatures has also been investigated. In a cubic spinel with space group of Fd3m form a cubic closed packed array; A-cations occupy one-eighth of available tetrahedral sites (8a) and the B cations one-half of the octahedral sites (16d). The remaining tetrahedral (8b, 48f) and octahedral (16c) form the interstitial space of the structure (Thackeray et al., 1987). In the lithiated spinels $Li_xFe_3O_4$ (Thackeray et al., 1981), $Li_xCo_3O_4$ (Thackeray et al., 1983) and $Li_xMn_3O_4$ (Thackeray et al., 1985), the A-site cations restrict Li^+-ion diffusion through the interstitial space of the $[B_2]X_4$ spinel framework. Cyclic voltammetry studies have shown that the lithium insertion reactions for $x \leq 1$ are irreversible. Attention has therefore been primarily on lithium spinels $Li[Mn_2]O_4$ (M = Mn, Ti, V) (Thackeray et al., 1987) in which the Li^+ ions reside in the interstitial space of $[B_2]X_4$ framework. These materials are particularly attractive, as lithium can not only be inserted into, but also extracted from, their structure, which offers the possibility of significantly increasing their usefulness as working cathodes for Li-ion batteries. Manganese oxide based cathode materials can be used in the wide voltage range. (Leroux et al., 1997) has reported the use of manganese oxide as a 3 V cathode material for lithium ion batteries. $LiTi_2O_4$ (Murphy et al., 1983) inserts an additional lithium into the empty 16c octahedral sites to give the lithiated spinel ${Li_2}_{16c}[Ti_2]_{16d}O_4$, which occurs with a flat discharge profile at a much lower voltage around 1.5 V (Picciotto et al., 1984). An additional lithium can be inserted into the 16c sites of LiV_2O_4. The lithium ions could also be extracted form the 8a tetrahedral sites of LiV_2O_4. However, LiV_2O_4 suffers from a migration of the vanadium ions during these processes, which leads to poor capacity retention. Lithium extraction from LiV_2O_4 to a composition $Li_{0.27}V_2O_4$ is accompanied by migration of some vanadium ions from the B-sites of the interstitial octahedral sites of spinel structure. This process reduces the crystal symmetry from cubic to trigonal (Picciotto et al., 1985). Attempts to stabilize $[V_2]O_4$ spinel framework during delithiation by doping the tetrahedral sites of LiV_2O_4 with a small concentration of zinc had met with partial success. The various phase transitions occurring in the structure and other critical issues have also been studied in the recent past (Narayan et al., 2006). In case of $LiCo_2O_4$ (Choi and Manthiram, 2002) spinel, the extraction of lithium from 8a sites occur at a potential of ~ 3.9 V, the insertion of additional lithium into the 16c sites occurs around 3.5 V. However, the system suffers from huge polarization loss as indicated by large separation between the discharge and charge profiles, which could possibly be related

to low temperature synthesis. Electrochemical studies on $CuCo_2S_4$, $CuNi_2S_4$, $CuFe_2S_4$ and Co_3S_4 have shown $CuCo_2S_4$ to be the most promising cathode (Eisenberg, 1981). Reactions of lithium with $CuCo_2S_4$ are topochemical and are reversible up to three Li^+ ions per mole; this corresponds to an electrode capacity of 262 mAh/g as compared to 240 mAh/g for layered TiS_2 (Sinha et al., 1986), which can incorporate one Li^+ ion, reversibly, per formula unit. Like TiS_2, $CuCo_2S_4$ is capable of extended cycling, but it operates at lower cell voltage. Particularly good electrochemical behaviour has been reported for Fe_3O_4 and LiF_5O_8 (Thackeray et al., 1981). Electrode capacities in excess of 600 mAh/g have been obtained from these materials. But unfortunately, these cells tend to loose capacity with continuous cycling, particularly if discharged too deeply, because of slow dispersion of Li_2O into the electrolyte.

$LiFePO_4$ (Padhi et al., 1997) with olivine type structure has emerged as a new cathode material with a good theoretical capacity of ~170 mAh/g and a flat voltage profile at ~3.4 V. Low cost and safety make this material as an attractive cathode for the coming generation of Li-ion battery.

2.3 Spinel Oxide Cathode

2.3.1 LiMn$_2$O$_4$ as a Cathode Material for Lithium Ion Battery

2.3.1.1 Crystal structure of LiMn$_2$O$_4$
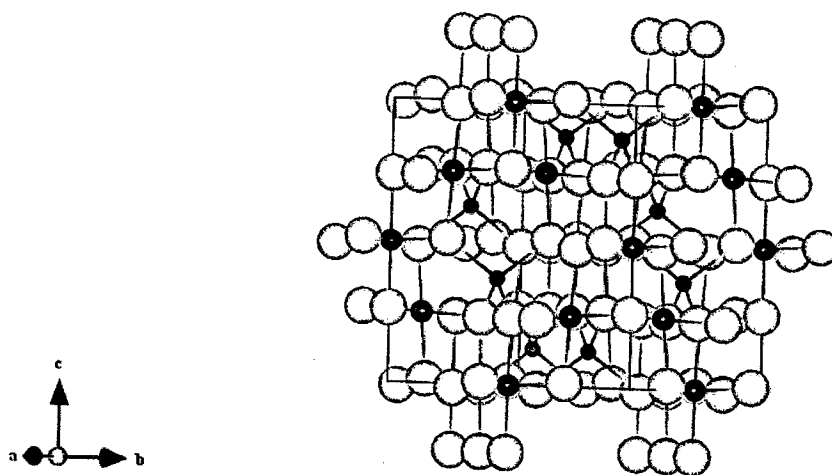
Fig. 2.4: Cubic spinel structure of LiMn$_2$O$_4$, Li: Red spheres, Mn: Green spheres, O: White spheres

The ideal spinel structure consists of a cubic closed packed array of anions in which one-eight of the tetrahedral and one half of the octahedral interstices are occupied by cations (Bragg, 1915; Nishikawa, 1915). In a binary spinel AB$_2$X$_4$, where X represents an anion, and A and B are cations, two extreme distributions of the cations among the available sites are possible. The normal distribution A[B$_2$]X$_4$, and the inverse distribution B[AB]X$_4$, where the ions indicated by parentheses occupy octahedral sites. Intermediate cation distributions may be represented as (A$_{1-x}$B$_x$)-[A$_x$B$_{2-x}$]X$_4$, where x is the so called degree of inversion, equal to zero and unity for normal and inverse arrangement respectively. Unit cell of a spinel structure consists of eight formula units of AB$_2$X$_4$ having 32 anions 24 cations, for a total of 56 atoms. Anions located at 32e sites are arranged in cubic closed packed arrangement and construct an FCC structure. A total of 96 interstices are formed between the anions in the cubic unit cell, but only 24 are occupied by cations in AB$_2$X$_4$ compounds.

In a normal cubic spinel structure of $LiMn_2O_4$, lithium (Li^+) occupies 8a tetrahedral sites; manganese ($Mn^{3+/4+}$) occupies 16d octahedral sites; oxygen (O^{2-}) form a cubic closed packed arrangement and are located at 32e sites. The 8a and 16d sites form a three dimensional pathway for lithium diffusion. Thackeray et al., 1996 have observed the XRD pattern of $Li_{0.6}Mn_{2.4}O_4$, which was obtained by heating $LiMn_2O_4$ above 1200 °C and then cooling it down to room temperature. It was concluded that the structure can be attributed to the occupation of Mn^{2+} ions in the tetrahedral sites along with Li^+ ions, where a fraction of Li^+ ions are substituted for Mn^{2+} and can be written as $(Li^+_{1-x}Mn^{2+}_x)_{8a}[Mn^{4+}_{1-x}Mn^{3+}_{1+x}]_{16d}O_4$. This phenomenon has been correlated to the loss of oxygen from the structure. Such kind of spinel might be assigned to inverse spinel structure.

Average oxidation state of manganese in $LiMn_2O_4$ is +3.5, which is at critical point. The ratio of Mn^{3+}/Mn^{4+} in $LiMn_2O_4$ is one. Mn^{3+} ($t_{2g}^3e_g^1$) is known as Jahn-Teller active ion that causes a local distortion in the structure, however Mn^{4+} and Mn^{2+} are Jahn-Teller inactive ions. Average oxidation state of manganese ions in $LiMn_2O_4$ is +3.5, which is critical oxidation state. Below this oxidation state the structure becomes distorted structure because of the increment in Mn^{3+} ions. Therefore, even a slight disturbance (increment of Mn^{3+} concentration) induces the Jahn-Teller distortion as a result of the average Mn valence decreasing to keep the charge neutrality. Hence the local structure of cubic spinel transforms to tetragonal spinel structure.

Tetragonal spinel structure can be obtained via electrochemical or chemical insertion of lithium into $LiMn_2O_4$. This causes the displacement of the lithium ions in the 8a sites to neighboring vacant 16c sites. Another way to obtain tetragonal spinel $LiMn_2O_4$ is heating the sample to a higher temperature. Such spinel is represented by general formula such as $LiMn_2O_{4-\delta}$. Tetragonal spinel can also be obtained by cooling down the cubic $LiMn_2O_4$ spinel structure below the room temperature.

Transition from cubic to tetragonal phase has been a controversial issue during the past few years. Yamada and Tanaka, 1995, found that stoichiometric $LiMn_2O_4$ undergoes a first order structural phase transition from a cubic to a tetragonal structure on cooling the material below 280 K and attributed such transition to a Jahn-Teller distortion (Fig. 2.5). They concluded that mass fraction of tetragonal phase increases with decreasing temperature and

become nearly constant to a level of 65% below 260 K. Oikawa et al., 1998, proposed a low-temperature phase with orthorhombic symmetry (*Fddd*), based on temperature dependent spectra of X-ray diffraction, neutron diffraction, and electron diffraction studies. Carvajal et al., 1998, proposed a partial charge ordering of Mn^{3+} and Mn^{4+} to account for this phase transition. They also claimed that at 230 K, the entire sample converts to a single orthorhombic phase. There remains a controversy between single-phase orthorhombic vs two-phase coexistence of tetragonal / cubic models. Yang et al., 2001, have shown that oxygen non stoichiometery is the sole and necessary condition for this phase transition. In other words, if this phase transition occurs, the sample is not oxygen stoichiometric, and contains oxygen vacancies. Equivalently, this phase transition should not occur in a strictly stoichiometric sample. Therefore, the issue such as phase transitions is closely related to the structural properties of these spinels.
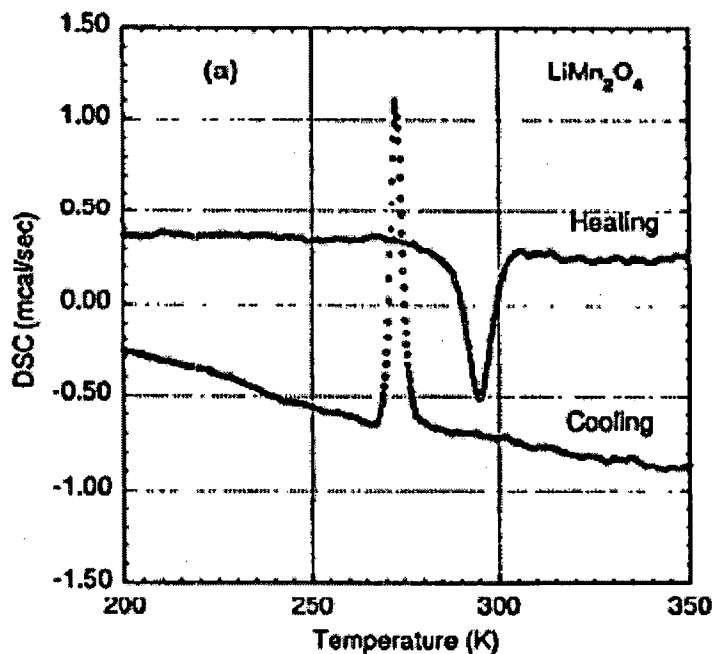
Fig. 2.5: Differential Scanning Calorimetry (DSC) traces of $LiMn_2O_4$ (Yamada and Tanaka, 1995)

Jahn and Teller (Goodenough, 1998) have shown that if the electronic state of a non-linear molecule is orbitally degenerated then there is always at least one vibrational coordinate along which the molecule may distort so as to reduce its energy. In other words, the ground

state of a non-linear molecule cannot be orbitally degenerated in its static equilibrium position. They have also shown that the degree of distortion increases with the bonding or antibonding power of the degenerate electrons. In both the layered and spinel crystal structures, the transition metal is octahedrally coordinated by oxygen. Although the five d-levels when each occupied by a single electron outside of a closed shell core are degenerate in a free transition metal ion, in an octahedral environment, the degeneracy is broken. Crystal field theory (CFT) shows that the interaction of the d-orbitals with the electrostatic potential due to the negatively charged oxygen ions of the octahedron produces an increase in the energy of the $d_{3z^2-r^2}$ and $d_{x^2-y^2}$ orbitals with respect to the energy of the d_{xy}, d_{yz} and d_{xz} orbitals. This occurs because the $d_{3z^2-r^2}$ and $d_{x^2-y^2}$ orbitals have lobes pointing toward the negatively charged oxygen ions while the lobes of the d_{xy}, d_{yz} and d_{xz} orbitals point between oxygen ions. The schematic diagram showing the interaction between the ligands and d-orbitals is given in Fig. 2.6. The $d_{3z^2-r^2}$ and $d_{x^2-y^2}$ orbitals directly overlap with the p_x, p_y and p_z orbitals of oxygen forming bonding and antibonding σ levels referred as e_g^b and e_g^*. Since the energy of the p-orbitals are below the energy of the d-orbitals, the bonding e_g^b levels are predominantly of oxygen p character while the antibonding e_g^* levels (frequently referred to as e_g) consist mainly of the metal d-orbitals. The d_{xy}, d_{yz} and d_{zx} orbitals which do not directly overlap with p orbitals to form σ bonds are frequently said to form a set of non bonding levels denoted by t_{2g} (Fig. 2.7 and 2.8). In an octahedral environment, the t_{2g} levels are below the e_g levels. The structural phase transitions are believed to be caused by the cooperative Jahn-Teller distortions, associated with Mn^{3+} ions. In particular, the $LiMn_2O_4$ compound, with the average manganese valence +3.5, is regarded as having an equal number of randomly distributed Mn^{4+} and Mn^{3+} ions above room temperature. Though in the cubic spinel phase all manganese sites are equivalent, the high spin Mn^{3+} ions favor dynamic Jahn-Teller distortions, which are presumably responsible for the structural phase transition at temperature $\sim$ 285 K accompanied by a corresponding charge ordering. It is still not clear that whether the low temperature phase of $LiMn_2O_4$ is orthorhombic or tetragonal. Also, according to the recent studies, the phase transition does not lead to a total transformation of the spinel structure until a temperature of ~70K is reached and only partial segregation of Mn^{4+} and Mn^{3+} ion was found.
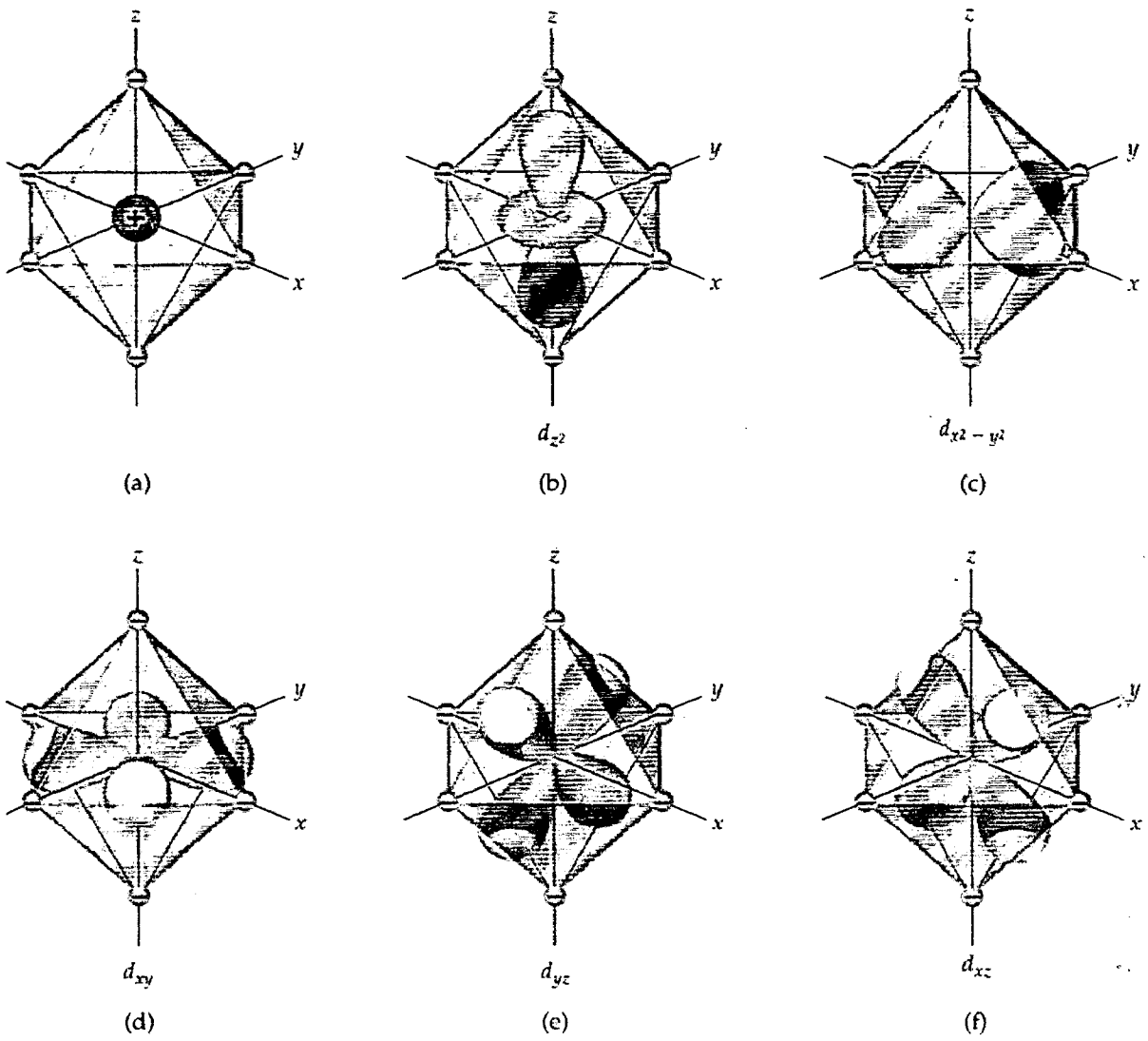
Fig. 2.6: Ligand /d-orbital interactions
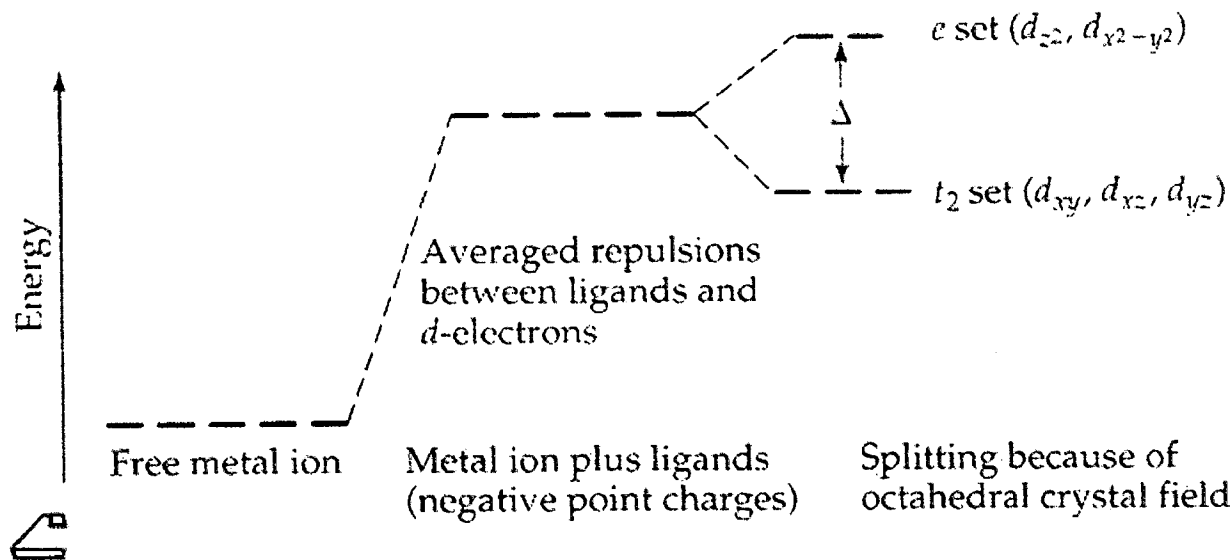
Fig. 2.7: Two effects of crystal field
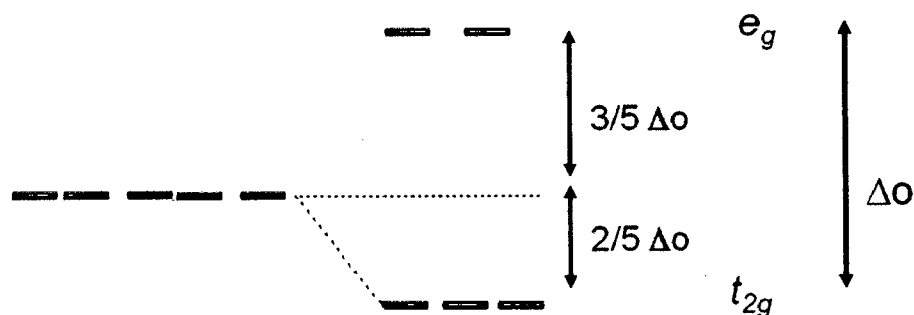
Δo is the crystal field splitting

$E(t_{2g}) = -0.4\Delta o \times 3 = -1.2\Delta o$

$E(e_g) = +0.6\Delta o \times 2 = +1.2\Delta o$

Fig. 2.8: Splitting of d-orbitals in an octahedral field

A detailed study on the thermal stability of $LiMn_2O_4$ above room temperature was carried out by Thackeray et al., 1996. It was shown that the cubic $LiMn_2O_4$ changes to tetragonal spinel structure above 880 °C. The value of c/a was found to be 1.02. Li_2MnO_3 with monoclinic symmetry and tetravalent manganese oxidation state was found to exist up to a temperature of ~1000 °C. $LiMnO_2$ having orthorhombic symmetry and trivalent manganese oxidation

state exists up to 1120 °C. As the temperature was raised the presence of manganese on the tetrahedral sites as Mn^{2+} was confirmed by the XRD pattern. At 1000 °C, this spinel phase had a tetragonal symmetry, whereas at 1200 °C it had a cubic symmetry. Hence the stoichiometric spinel phase was found to be stable up to a temperature of 780 °C. Fig. 2.9 shows the TGA plot of the $LiMn_2O_4$ heated up to 1180 °C.
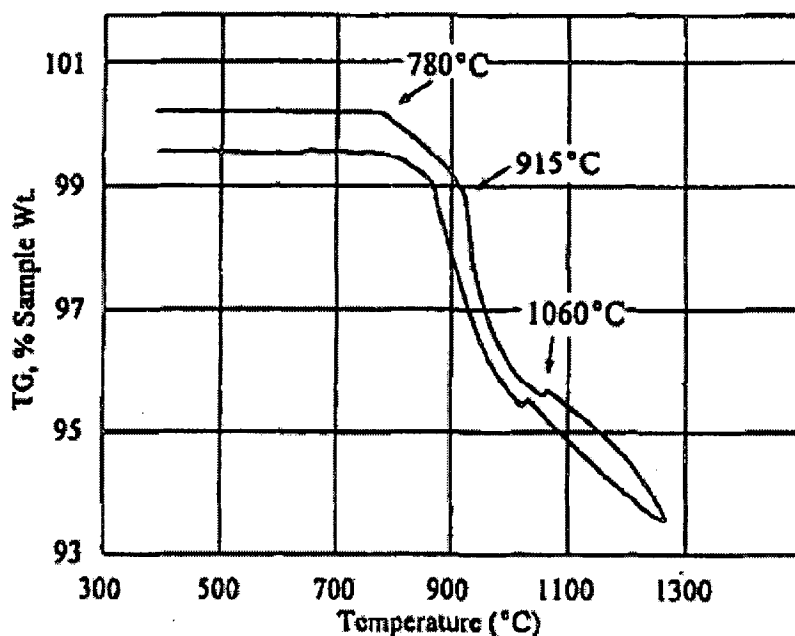
Fig. 2.9: A TGA plot of $LiMn_2O_4$ (Thackeray et al., 1996)

Lithium insertion in manganese spinels was first demonstrated by Thackeray et al., 1983. Lithium was inserted electrochemically in $Mn^{2+}[Mn_2^{3+}]O_4$ and $LiMn_2O_4$ was formed at room temperature. Insertion of lithium in spinel $LiMn_2O_4$ was preferred because it offers the possibility of having only Li^+ ions in the interstitial space of Mn_2O_4 network. The c/a ratio of Mn_3O_4 and $Li_2Mn_2O_4$ was found to be same, which shows that the electrons compensating Li^+-ion insertion reduce Mn^{4+} to Mn^{3+} and magnitude of the cooperative Jahn-Teller distortion is a function of concentration of Mn^{3+} in the octahedral sites. Structure of $LiMn_2O_4$ was determined by refinement of the integrated Bragg intensities obtained from the XRD. The 16d sites were found to be fully occupied by Mn to give the $[Mn_2]O_4$ framework. The

29

remaining manganese was displaced from the tetrahedral 8a sites to occupy randomly with the Li^+ ions the remaining octahedral 16c positions. The observation of fully occupied 8a sites in $Li_2Mn_2O_4$ indicates that lithiation of $LiMn_2O_4$ proceeds by a simple insertion of Li^+ ions into the 16c sites without displacement of the 8a Li^+ ions into 16c positions. In $LiMn_2O_4$, the 8a sites are occupied by Li^+ ions, and the Li^+-Li^+ electrostatic forces are apparently not strong enough to displace a Li^+ ion from an 8a to a 16c site.

FTIR spectroscopy techniques are capable of probing directly the near neighbor environment of oxygen coordination around the Li and Mn ions. The number of active bands in the vibrational spectra of lithium transition metal oxide based compounds depends on the symmetry and increases significantly for tetragonal ordered spinel structure. The normal cubic spinel structure consists of Li^+ ions located at tetrahedral sites of O_h^7 space group and have a point symmetry T_d. The transition metal ions occupy octahedral sites and have point symmetry D_{3d}. The oxygens occupy the 32e sites with site symmetry of C_{3v}. Haas, 1955, has summarized the various structural transformations of spinel structure. The lattice modes of normal spinel $LiMn_2O_4$ are discussed in the O_h^7 spectroscopic group. The ordering of the ions in case of ordered spinel reduces the space group symmetry from O_h^7 to O_7. The number of atoms in the unit cell remains same however the enlargement of the smallest Bravais cell by a factor of 4 results in great increase in the number of allowed modes (White et al., 1967). The symmetry reduction leads to the increase in cell volume which results in increase in the number of allowed modes. The spinel structure of $LiMn_2O_4$ consist of MnO_6 octahedra connected to one another in three dimensions by edge sharing, LiO_4 tetrahedra sharing each of their four corners with a different MnO_6 unit cell essentially isolated from one another, a three dimensional network of octahedral 16c and tetrahedral sites through which lithium ions can move through the lattice (Julien et al., 2003, Julien et al., 2004). Considering the spinel structure constituted by MnO_6 octahedra and LiO_4 tetrahedra, the molecular approach assumes that elemental units are weakly connected (Tarte et al., 1970). The free MnO_6 octahedron belongs to the O_h group and displays six fundamental vibrational modes. The free LiO_4 tetrahedron belongs to the T_d group and displays four fundamental vibational modes. However out of ten only four are IR active modes.

In the FTIR spectrum of $LiMn_2O_4$ the high frequency bands located at 615 and 513 cm^{-1} are attributed to asymmetric stretching modes of MnO_6 group, whereas the low frequency bands at approximately 225, 262, 355 and 420 cm^{-1} have a mixed character due to the presence of the binding modes of O-Mn-O bonds and modes of LiO_4 group (Julien et al., 2003). The infrared species are very sensitive to oxidation state of cations, therefore the band at 615 cm^{-1} exist for λ-MnO_2 spinel, where Mn ions are in the 4+ oxidation state. Upon lithium substitution for Mn ($Li_{1+x}Mn_{2-x}O_4$) in the spinel lattice part of the Li^+ ions are located in the 16d octahedral sites. Therefore a small tetragonal distortion is expected. As the lithium content increases from 0.01 to 0.33 blue shift occurs for the high wave number and band splitting for the high degree of substitution i.e $x>0.25$ appears. This blue shift occurs from 615 to 644 cm^{-1} in the range $0.01 \leq x \leq 0.33$. The emergence of additional bands in the FTIR spectrum of $Li_{1.33}Mn_{1.67}O_4$ is attributed to the presence of Li ions in the 16d octahedral sites. Taking into account that the 16d octahedral sites are occupied by two cations with different charge and mass, the factor group also gives additional bands. This is observed in the high wave number region by the presence of two bands at 610 and 644 cm^{-1} for $Li_{1.33}Mn_{1.67}O_4$.

2.3.1.2 Electrochemical Performance of $LiMn_2O_4$

The electrochemical data demonstrate that lithium is extracted from the tetrahedral sites of the spinel structure at approximately 4 V in a two-stage process, separated by only 150 mV for a composition of $Li_{0.5}[Mn_2]O_4$. The two-step process is due to ordering of the lithium ions on one half of the tetrahedral 8a sites. The high voltage associated with these two reactions can be attributed to the deep energy well in which the tetrahedral lithium ions reside, and the high activation energy, that is required for the lithium ions to move from one 8a tetrahedron into another 8a site via an energetically unfavorable neighboring 16c octahedron. Lithium insertion into $Li[Mn_2]O_4$, occurs at approximately 3 V. In case of $Li_2Mn_2O_4$, the inserted lithium ions occupy the 16c octahedral sites and that the electrostatic $[Mn^{3+}]_{16d}$-Li^+ interactions are still sufficiently strong enough to keep a fraction of the lithium ions on the 8a sites. Structure refined by neutron diffraction necessitates the coexistence of lithium ions in face shared tetrahedra and octahedra despite a very short Li^+_{8a}-Li^+_{16c} interatomic distance of only 1.83 Å. These findings demonstrated the near equivalence in the potential energy of the

31

8a and 16c sites at this composition, which is not surprising as the lithium ions in $Li_{1+x}[Mn_2]O_4$ (0≤x≤1) move through the 8a-16c network.

Ohzuku et al., 1990, studied the reduction mechanism of spinel related manganese dioxide in lithium non-aqueous cells. The experimental results indicate that a spinel related manganese dioxide ($MnO_{1.93}$), which is a cubic spinel, could be reduced up to a capacity of 230 mAh/g with three reduction steps, which are characterized by voltage levels at 2.86, 3.95 and 4.10 V. In their study, the XRD and electrochemical data indicated that the electrochemical reduction of the spinel related manganese oxide proceeds in the following three steps (Fig. 2.10) :

1. At an average composition range of 0.27(2) < x < 0.60(3) in $Li_xMn_2O_4$, the reduction proceeded in two cubic phases, i.e. a_c = 8.045(6) Å and a_c = 8.142(2)Å, which is characterized by a constant open-circuit voltage of 4.110(5) V.

2. At a composition range of 0.60(3) < x < 1.00 in $Li_xMn_2O_4$, the reduction proceeded in a homogeneous phase, which was characterized by an S-shaped open-circuit voltage curve [mid-point: 3.94(1) V] together with a continuous lattice expansion from 8.142(2)   to 8.239(3) .

3. At an average composition range of 1.00 < x < 2.00 in $Li_xMn_2O_4$, the reduction proceeded in two phases, which are characterized by an L-shaped open-circuit voltage curve at 2.957(5) V and the coexistence of a cubic $LiMn_2O_4$ phase [a_c = 8.239(3)Å]   and a tetragonal $Li_2Mn_2O_4$ phase [a_T = 5.649(2)Å, c_T = 9.253(5)Å].
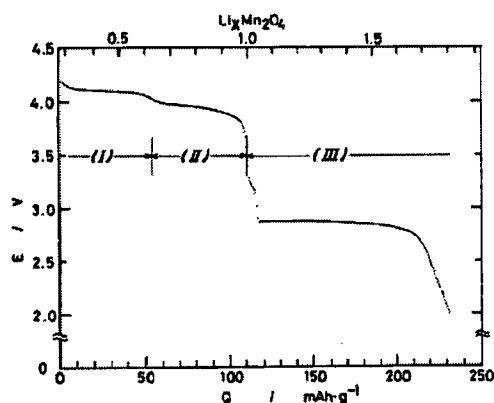
Fig. 2.10 Discharge curve of $LiMn_2O_4$ (Ohzuku et al., 1990)

32

2.4 Approach for the Enhanced Electrochemical Performance of Manganese Based Spinels

Manev et al., 1993, have shown that the synthesis of $LiMn_2O_4$ for secondary lithium cells should be performed at a temperature lower than 750 °C, since a thermal treatment above this temperature can cause significant chemical reduction and thus decrease its specific capacity. Moreover, the increase of the synthesis temperature above 750 °C leads to a considerable reduction of the specific surface area of the samples and correspondingly to deterioration of their utilization at high discharge rates. It has been shown that the increase of the specific surface area leads to remarkable increase of capacity. Specific surface area was found to decrease with the increase in temperature upto 650 °C, while between 650 and 750 °C a well-defined plateau appears, and above 750 °C the specific surface area reduces again. Between 600 and 800 °C the stoichiometric product ($LiMn_2O_{4-y}$; y=0) is synthesized, and subsequently in the range 800 to 900 °C, a considerable decrease of the stoichiometric coefficient y is observed reflecting the partial chemical reduction of the $LiMn_2O_4$ spinel. Oxygen loss above 800 °C has been observed by DTA/TG curve. The effect of the disturbed stoichiometry can be explained by the fact that the reduction most probably leads to a decrease of the +4 manganese on account of the increase of the +3 one. In the stoichiometric spinel half of the manganese has +3 valency and the other half is of +4 valency.

$$Li[Mn^{3+}Mn^{4+}]O_4 \hspace{3cm} (1)$$

Considering that oxygen is of -2 valency, it follows that the change in the reduced spinel $LiMn_2O_{4-y}$ can be presented analogously to eqn (1):

$$Li[Mn^{4+}_{4y} \, Mn^{3+}_{1-2y} \, Mn^{4+}_{1-2y} \,]O_{4-y} \hspace{2cm} (2)$$

where Mn^{3+}_{4y} is the amount of +3 manganese on account of the oxygen vacancies, which cannot be transformed to +4 during the extraction of Li-ions. Furthermore, using Thackeray's expression of the intercalation process for the stoichiometric spinel:

$$Li_{1-x}[Mn^{3+}_{1-x}Mn^{4+}_{1+x}]O_4 \hspace{2.5cm} (3)$$

for the partially-reduced spinel becomes:

$$Li_{1-x}[Mn^{3+}_{4y}Mn^{3+}_{1-2y-x}Mn^{4+}_{1-2y+x}]O_{4-y}$$
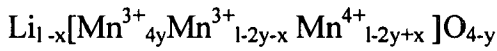
The latter expression can be defined only at $0<x<1-2y$. Taking into account the condition $x <$ $1-2y$, one can easily estimate that at $y = 0.1$, the theoretical specific capacity is reduced from 154 to 123 mAh/g. This can explain the reduction of the specific capacity with the rise of the temperature above 800 °C.

Gummow et al., 1994, have shown that the rechargeable capacity of 4 V $Li_xMn_2O_4$ spinel cathodes $(0\leq x\leq 1)$ can be improved by modifying the composition of the spinel structure. Stoichiometric spinel cathodes (having general formula $Li[Mn_{2-\delta}Li_\delta]O_4$) such as $Li[Mn_{1.66}Li_{1.33}]O_4$ $(Li_4Mn_5O_{12})$ is reached when all the manganese ions are tetravalent. $LiMn_2O_4$ $(\delta=0)$ offers the highest 4V capacity (154 mAh/g) based on the mass of fully oxidized composition Mn_2O_4, whereas an ideal $Li_4Mn_5O_{12}$ electrode $(\delta=0.33)$ offers no capacity at all at 4 V because the manganese ions are tetravalent (it is not possible to oxidize these cations further by electrochemical extraction of lithium, at least at practical voltages). Other stoichiometric spinels having $\delta=0.03$ and 0.10, are found to deliver capacity of 101 and 77 mAh/g respectively when cycled between the voltage limits between 4.45 V and 3.50 V. The cycling stability of these spinels compared to $LiMn_2O_4$ was attributed predominantly to the suppression of Jahn-Teller distortion in the spinel electrode at the end of the discharge. When the cells were cycled between the wider voltage limits of 2.70 V and 4.45 V, a clear superior cycling ability of lithium doped spinels was achieved. This is because $Li/LiMn_2O_4$ cell loses capacity rapidly because it enters the tetragonal region of the phase diagram at the end of discharge at 4V, whereas $Li/Li_{1.05}Mn_{1.95}O_4$ cell remains within the cubic region of the phase diagram. Higher content of δ such as 0.22 and 0.29 show very little capacity at 4 V, but these electrodes show good reversibility when cycled over both the 3 V and 4 V regions. When voltage range for these compositions extended between 2.5 V and 4.45 V, these electrodes yielded total capacities of 160 mAh/g and 140 mAh/g for $\delta=0.22$ and $\delta=0.29$ respectively.

Defect spinels having general formula $Li_{1-\delta}Mn_{2-2\delta}O_4$ with $0\leq\delta\leq0.11$ can be formed by reaction of lithium and manganese salts at temperature between 400 and 600 °C. The initial capacity obtained from a $Li/Li_{0.975}Mn_{1.95}O_4$ cell was 117 mAh/g. However their cycling stability is inferior compared to lithium doped spinels. It has been found that oxygen

deficiency also plays a crucial role on electrochemical performance of the material. The lithium as well as oxygen rich compounds ($Li_{1+x}Mn_2O_{4+\delta}$) show higher capacity and higher cycle life compared to $LiMn_2O_4$, but the oxygen deficient spinel ($LiMn_2O_{4-\delta}$) shows very poor cyclability in the 4 V region. Oxygen deficient spinels also show a very small discharge plateau at about 3.2 V. It has been shown that there is a linear relationship between the capacity at 3.2 V and oxygen deficiency.

A fundamental problem prohibiting a wider use of the Mn spinel as a 4 V cathode for lithium ion batteries is a remarkable capacity fading at elevated temperatures. Doping with different metal ions including Li^+, Mg^{2+}, Ga^{3+}, Zn^{2+}, Al^{3+}, Ni^{2+}, Cu^{2+}, Co^{3+}, Cr^{3+} and Fe^{3+} has been suggested to stabilize its structure, thus improving the elevated temperature performance (Thirunakaran et al., 2004). The doping ions substitute Mn^{3+} and so, reduce the capacity that is delivered at 4 V. Heavy doping results in a manganese oxidation state approaching to +4. These heavily doped compounds deliver no capacity at 4 V, but show a capacity at 3 V or 5 V (Robertson et al., 1997). Doping ions also have other benefits such as reduced solubility of manganese in electrolyte. Doubly doped materials such as $LiMn_{1.5}Ni_{0.5-\delta}Mg_\delta O_4$ show a promising high voltage cathode material for lithium ion battery (Ooms et al., 2002). Monovalent dopant such as Li^+, as explained earlier, helped in attaining better cyclability, but it showed problems on storage at high temperature. Divalent metals such as Zn and Ni or trivalent metals Cr, Ga and Al show the best performance. Ni and Cr are particularly effective in reducing the Mn dissolution and, so, the spinel instability. Reports indicate that Al, Zn and Ga may reside in 8a tetrahedral sites. In principle, they could create diffusion problems for Li^+ along the 8a-16c-8a paths, but atleast for limited substitutions considered, this does not occur and, instead, show a well stabilized capacity. Excellent data have often been reported for double doping (Thirunakaran et al., 2009). Not only may different cations be used to replace Mn, e.g., Ga-Cr, but S or F also may be used to partially replace O (Molenda et al., 2005, Son et al., 2005).

2.5 Effect of Cr Doping on $LiMn_2O_4$ Performance

Neutron diffraction carried by Oikawa et al., 1999, shows that Cr can successfully be doped in the octahedral sites which are otherwise occupied by Mn. The oxidation state of Cr remains unchanged in the 4 V region of the $Li/LiMn_{2-y}Cr_yO_4$ cell, the ideal reversible reaction during the charge/discharge process can be represented as

$$Li(Mn_{2-y}Cr_y)O_4 \rightleftharpoons Li_x(Mn_{2-y}Cr_y)O_4 \qquad\qquad (x \geq y)$$
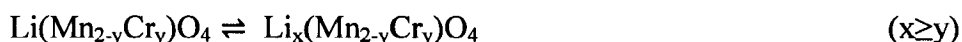
Yamada (Yamada, 1996) reported that the fading of capacity for the $Li/LiMn_2O_4$ cell in the 4 V region increases not on cycling in the deep-discharge region but by cycling in a deep-charge region where most Li^+ ions were deintercalated from the cathode material. The introduction of Cr^{3+} ions into the 16d positions stabilizes a network composed of $[Mn_{2-y}Cr_y]O_6$ octahedra over many cycles in the 4 V region because parts of Li^+ ions remain in the cathode. Similarly, the $Li/Li[Mn_{2-y}Li_y]O_4$ cell in which the reaction

$$Li(Mn_{2-y}Li_y)O_4 \rightleftharpoons Li_x(Mn_{2-y}Li_y)O_4 \qquad\qquad (x \geq 3y)$$
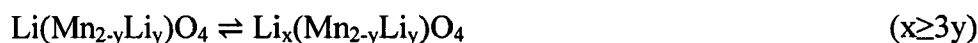
proceeds also exhibits good cycle performance for the same reason. In the fully charged state, the amount of remaining Li^+ ions in the reaction is three times large as that in above said reaction when y is same. Therefore, substitution of Li with a y value greater than 0.05, which is required for capacity retention at high temperature, leads to a reduction in the initial capacity. Robertson et al., 1997, have done a detailed study on the effect of various dopants on electrochemical performance of $LiMn_2O_4$. While several M^{3+} species such as Ti, Ga, Fe and Al were incorporated into the $LiMn_2O_4$ spinel lattice, only Cr^{3+} stabilized the cathode material and resulted in acceptable electrochemical performance with 1 m/o concentration. This was attributed to a combination of ionic size coordination site and crystal structure preferences, and oxidation state stability. Cr meets all the criteria. While most of the other metals show the formation of inverse spinel structure and reasonably large difference in the ionic radii. The low doping concentration level did not alter the particle morphology, but it was sufficient to stabilize the $LiMn_2O_4$ structure and prevent cathode degradation in a working cell. The fade rate was significantly reduced with the addition of Cr, but the initial capacity dropped with increase in dopant content, as expected. It was found that even 0.1 m/o

Mn replacement with Cr caused a decrease in the fade rate, but stability with cycle number was not attained until > 0.5 mole percent. Results show that modest Cr doping in $LiMn_2O_4$ provided higher capacities after 50 to 100 cycles compared to the unmodified spinel and the gap continued to expand. In the range of Cr doping concentration of 0.6 to 1 m/o, capacities of ~110 mAh/g were observed after 100 cycles. The compositions $LiMn_2O_4$ and $LiCr_{0.02}Mn_{1.98}O_4$ were chosen to study the effect of varying (i) lithium salt in the electrolyte, (ii) test temperature, and (iii) current density. Cells containing Li methide-based electrolyte and Cr modified $LiMn_2O_4$ spinel were less moisture sensitive and maintained >110 mAh/g after more than 80 cycles, with the electrolyte remaining colorless. Chromium-doped cathodes had a 10% higher initial discharge capacity (122 mAh/g) with $LiPF_6$-containing electrolytes (vs. Li methide at room temperature) but showed a steady capacity fade with cycle number. This is attributed to trace amounts of moisture in the solvent. Effect of current density was also studied. As the current density increased, initial discharge capacity decreased and fade rate increased. As charge/discharge rates were raised, there was progressively less time for Li^+ ion to diffuse through the $LiMn_2O_4$ crystallites. At higher rates, only lithium ions located in the outer regions of grains were accessible for reaction, causing a reduction in capacity. Higher rates also promoted lithium dendrite growth through the Li-solution interface into the electrolyte, accelerating degradation of the organic solvents and reducing cell performance. The relatively rapid fade at low current densities was attributed to electrolyte oxidation during the extended period at high charge voltage, resulting in a corrupted solid electrolyte interface and poorer Li transport. Conversely high current densities produced cathode surface polarization and voltages outside the cycling range, which caused premature degradation of spinel structure and an early performance decline. Same results were observed for unmodified spinels.

Sigala et al., 1997, have carried out Rietveld analysis of the structure modifications induced by electrochemical lithium deintercalation in the wider voltage range. It has been shown that Cr substitution ($LiCr_yMn_{2-y}O_4$) is beneficial to the overall performances (capacity, specific energy and cyclability) for $y \leq 0.62$, and that $y=0.25$ gives the best result. For $y > 0.62$, the cyclability is inferior to that for $LiMn_2O_4$, and the capacity fading becomes very fast for $y \geq 0.75$. It was observed that upon substitution of Mn^{3+} by Cr^{3+} a capacity decrease occurs in the voltage range of 3.5 V to 4.3 V, however, the capacity loss due to such substitution was

recovered at higher voltages. The electron energy loss spectroscopy (EELS) study confirmed that the deintercalation occurring in the voltage range 3.5-4.3 V corresponds to a Mn^{3+}-Mn^{4+} oxidation. Further deintercalation between 4.3 and 5.1 V mainly corresponds to a Cr^{3+}-Cr^{4+} oxidation with the formation of a significant amount of Cr^{6+} for the highest chromium content of y = 0.75. Cr^{6+} is carcinogenic, toxic, extremely mobile, and difficult to remove from aqueous systems. Therefore its presence is not beneficial from environmental as well as battery point of view. In the starting compounds LiM_2O_4, M = Cr, Mn, Rietveld refinements show that the 8a and 16d sites of the spinel structure are occupied by Li and M, respectively. The Li deintercalation occurring at voltages up to 5.1 V induces structural defects which do not disappear completely upon the subsequent intercalation down to 3.5 V; their concentration increases upon cycling. Such defects consist of M cations occupying an 8a site (T_d defect) or a 16c site (16c defect), instead of 16d. Both defects imply a lowering of the tetrahedral Li concentration which accounts for the experimentally observed capacity loss upon cycling. In another detailed study carried by Sigala et al., 2001, on the influence of Cr content on the electrochemical performance of $LiMn_2O_4$, it has been shown that an overcharge up to 5.7 V indicates that the material with y = 0.25 is stable against oxidation and that the electrolyte oxidation remains rather low within a large voltage range (~0.6 V) above the end of deintercalation voltage. The Cr substitution is also beneficial to the specific energy (specific energy = specific capacity × average voltage) that is higher by 16% as compared to $LiMn_2O_4$ for 0.25 ≤ y ≤ 0.62.

Ikuta et al., 2004, have studied the effect of Cr substitution on phase transitions of $LiMn_2O_4$ using differential scanning calorimetry (DSC) and low temperature XRD. It was found that the phase transition temperature depends not only on the Cr composition but also on the preparation temperature of the sample. It was found that in the case of $LiMn_2O_4$, calcination temperature does not have any effect on the transition temperature. On the contrary, two exothermic peaks during the cooling process were observed for $LiCr_{0.02}Mn_{1.98}O_4$ prepared between 760 and 810 °C. From the DSC and low temperature XRD results the distribution of Cr was schematically illustrated. It was proposed that the Cr distribution in the sample prepared at relatively high-temperature would be homogeneous. On the contrary, the Cr distribution in the sample prepared at relatively low-temperature would be inhomogeneous. The phase transition was suppressed in the region of high Cr concentration. It was observed

that the phase transition was much clearer in the low Cr concentration region in which the composition is nearly $LiMn_2O_4$. The phase transition for the Cr substituted spinels prepared at intermediate temperature appears at around 280 K in the low Cr concentration region at first. After that the second phase transition occurs at around 245 K in the high Cr concentration region. The lattice parameter decreases with the increase in Cr concentration on isothermal condition. The lattice parameter increases with increasing preparation temperature up to 790 °C. This tendency caused by the reduction of manganese ions in the homogeneous region. Contrary to this tendency, the lattice parameter decreases with increasing preparation temperature above 790 °C. The distribution of transition metal ions prepared at high-temperature should become more homogeneous than the sample at low-temperature. This change in ionic distribution would affect the decrease of the lattice parameter.

Yamaguchi et al., 1999, have shown that in case of Cr doped $LiMn_2O_4$ the standard enthalpy of formation decreases with the increase in Cr content. Rojas et al., 2007, have carried out the thermal analysis of the Cr doped $LiMn_2O_4$. It has been shown that the Cr doped spinels are stable upto a higher temperature compared to $LiMn_2O_4$. The oxygen loss from the structure starts at higher temperature compared to pristine $LiMn_2O_4$. The increase in the transition temperature is found to be linear with the increase in Cr content. The enhancement of the thermal stability of Cr doped $LiMn_2O_4$ can be explained on the basis of the crystal field stabilization energy (Dunitz and Orgel, 1957). For Cr^{3+} the estimated the octahedral stabilization energy is 224.83 KJ mol^{-1}, and for Mn^{3+} it is 135.65 KJ mol^{-1}. Hence it is likely to assume that the progressive substitution of Mn^{3+} by Cr^{3+} in the octahedral sites, results in stabilization of spinel structure.

Wang and Lu, 2003, have discussed the dissolution behavior of chromium doped spinel lithium manganate in $LiPF_6$ at elevated temperatures. It has been shown that the particle size decreases with the increase in doping amount of chromium. It was found that more Mn ions were dissolved from undoped $LiMn_2O_4$ powders than from chromium doped $LiMn_2O_4$, demonstrating that doping chromium ions into the spinel lithium manganese oxide could suppress the dissolution of manganese ions. Dissolution of Cr ions was also observed in the electrolyte in the earlier period of immersing process. This shows that the surface of the

particles have less stable structure than the interior of the particles. Concentration of the dissolved manganese and chromium ions greatly increased with the rise in temperatures. It is indicted that doping chromium ions in $LiMn_2O_4$ can suppress the dissolution reaction of manganese ions at elevated temperatures, thereby leading to lowered degree of capacity fading. Yoshio et al., 2001, have shown that either Li^+ or Cr^{3+} significantly improved the storage and cycling performance of spinel $LiMn_2O_4$ at elevated temperature, especially both doped spinel. $Li_{1.02}Cr_{0.1}Mn_{1.9}O_4$ shows very low rate of capacity retention, 0.1% per cycle, and maintained a steady discharge capacity of 114 mAh/g, 95 % of the initial discharge capacity over 50 cycles at $50^{\circ}C$. The chemical analysis and XRD measurements indicate that the capacity loses of $LiMn_2O_4$ are mainly due to the dissolution of the manganese ions in to the electrolyte solution, this leads to further transformation to a little oxygen deficient lithium rich spinels such as $Li_{1+x}Mn_{2-y}O_{4-z}$. The improvements in their electrochemical profiles for the Cr^{3+} and Li^+ modified spinel is attributed to that the partial substitution of Mn by Cr stabilize its structure, thus minimizing the dissolution of Mn into electrolyte, as well as maintaining its original morphologies.

Sun and Oh, 2001, have reported the synthesis of the oxysulfide spinels. Minute substitution of oxygen with sulphur has been reported along with manganese substitution with Cr. The $LiCr_{0.19}Mn_{1.81}O_{3.98}S_{0.02}$ electrode shows no capacity loss in the 3 V and 4 V regions. Although the electrode delivers a capacity of 120 mAh/g, it shows excellent cycleability and retains 99% of the initial capacity after 50 cycles at the C/4 rate. The electrochemical cycleability of the $LiCr_{0.19}Mn_{1.81}O_{3.98}S_{0.02}$ electrode was examined in the 3-V region since the stoichiometric spinel $LiMn_2O_4$ experience a major loss of capacity in this voltage region due to Jahn-Teller distortion. This cell was first discharged to the 2.4 V and then cycled between 3.5 and 2.4 V. Interestingly, the $Li/LiCr_{0.19}Mn_{1.81}O_{3.98}S_{0.02}$ cell initially delivers a discharge capacity of 88 mAh/g, which rapidly increases to 119 mAh/g after 50 cycles. By contrast, it is well known that spinel suffers severe capacity loss in the 3-V region. The $Li/LiCr_{0.19}Mn_{1.81}O_{3.98}S_{0.02}$ cell displayed excellent capacity retention at all C-rates, 115 mAh/ g at the 0.2 and 0.5 C rates. The discharge capacity falls to 110 mAh/g at the 1 C-rate and 100 mAh/g at the 2 C-rate.

FTIR analysis of $LiMn_2O_4$ doped with Cr has been performed by Wu et al., 2001. It has been observed that upto a doping level of $x<0.4$ in $LiCr_xMn_{2-x}O_4$, there is no change in the spectra. There is no change in the stretching bands at 514 cm^{-1} and 634 cm^{-1}. This is due to the resemblance in the mass and ionic radii values. For the higher doping content $0.4<x<0.8$ there is a change in the position of the band present at 514 cm^{-1} towards the higher wavenumber. This is due to the conversion of Cr^{3+} to Cr^{6+}. In order to maintain the charge neutrality the content of Mn^{3+} increases and hence leads to an obvious change in the spectra. Since the spinel structure remained for all the Cr-doped samples, the characteristic Cr-O vibration modes similar to those of chromium oxides are not observed in IR spectra.

2.6 Effect of Mg Doping on $LiMn_2O_4$ Performance

Mg doped $LiMn_2O_4$ spinels have been proposed as the potential candidate for lithium ion battery cathode material. Hayashi et al., 1999, have shown that the cycle performance of $LiMg_yMn_{2-y}O_4$ is better compared to $LiMn_2O_4$. A metal excess model was proposed in the study, to explain the various effects. In this model some of the metal ions were located at 16c octahedral sites and can be written as $(Li)_{8a}[Li_{\delta/(4-\delta)}Mg_{8/6(4-\delta)}Mn_{118/6(4-\delta)}]_{16c}[Mg_{1/6}Mn_{11/6}]_{16d}O_4$. The presence of excess metal ions located at the 16c sites were supposed to contribute to the stabilization of the spinel structure. In order to compensate the theoretical capacity reduction in $LiMg_{1/6}Mn_{11/6}O_4$, nonstoichiometric spinel oxide such as $LiMg_{1/6}Mn_{11/6}O_{4-\delta}$ was prepared under the controlled oxygen partial pressure. The single-phase regions of $LiMg_{1/6}Mn_{11/6}O_{4-\delta}$ ($\delta < 0.04$) were wider than that of $LiMn_2O_4$ ($0 \leq \delta \leq 0.018$). The initial discharge capacity of $\delta = 0.032$ (104 mAh/g) was 5 mAh/g higher than that of $\delta = 0$ (99 mAh/g). The increase in capacity was responsible for the reduction of some Mn^{4+} to Mn^{3+}. The diffusion coefficient of lithium ion in the nonstoichiometric ($\delta = 0.032$) sample was smaller than that of stoichiometric spinel $LiMn_2O_4$. In the nonstoichiometric composition, the migration of lithium ions passing 8a-16c-8a would be slightly restricted, because the excess metal ions at the 16c sites prevent easier diffusion of the lithium ions.

Carvajal et al., 1998, have shown that the structural transition present in $LiMn_2O_4$ at 290 K is a first order transition. It has been shown that charge ordering is accompanied by simultaneous orbital ordering due to the Jahn-Teller effect in Mn^{3+} ions. Basu and Seshadri,

2000, have also discussed the charge-ordering phenomenon in $LiMn_2O_4$. They have shown that charge-ordering transition and Jahn-Teller distortions of the $Mn^{3+}O_6$ octahedra are distinct phenomena. Since the tendency to charge ordering is suppressed when charges on ions are not simple fractions, Mg has been substituted for Li to take Mn away from an average valence of 3.5. It has been shown that the transition is suppressed with as little as 4 atom% of Mg substitution for Li. Increase in Mg content causes the strain in the crystal structure which is reflected by peak broadening in the XRD patterns. Broadening was observed for even very small content of Mg (less than 5 atomic %), which shows that octahedra are locally distorted and form structures that are cubic in nature. DSC study has also confirmed the charge-ordering phenomenon in the structure.

Jeong et al., 2001, have also discussed the behavior of Mg doped $LiMn_2O_4$ compound as a cathode material for Li-ion battery. It has been shown that the cycle performance of Mg-substituted spinel phases is better than that of the pure spinel $LiMn_2O_4$. The discharge capacity of the Mg substituted spinel $LiMg_{0.1}Mn_{1.9}O_4$ at the 70th cycle is more than 88% of that at the first cycle. These results are in consistent with the results which were earlier obtained by Hayashi et al., 1999. It has also been reported that the charge transfer resistance and capacitance of the $LiMg_{0.1}Mn_{1.9}O_4/Li$ cell are smaller and the diffusion coefficient is higher than that of $LiMn_2O_4/Li$ cell. Park et al., 2001, have synthesized Mg doped oxysulfide spinel such as $Li_{1.02}Mg_{0.1}Mn_{1.9}O_{3.99}S_{0.01}$. Electrochemical characterization of the material was performed in order to check the effect of Mg and S on material's performance as cathode for Li-ion battery. Electrochemical performance was measured in the voltage range of 4.4 - 3.0 V. It was concluded that the single phase could be obtained only in the lightly doped spinel compound. The initial capacity of the doped powders was found to decrease because of the decrease in the amount of extractable lithium. The removal of lithium from the spinel manganese oxides is accompanied by an oxidation of Mn^{3+} to Mn^{4+}. Given that Mg^{2+} ions cannot be oxidized in this potential range, the Mn^{3+} content determines the amount of removable lithium. Thus, only (1.02-x)Li can be extracted from $Li_{1.02}Mg_xMn_{2-x}O_4$. For $Li_{1.02}Mg_{0.1}Mn_{1.9}O_4$ and $Li_{1.02}Mn_2O_{3.99}S_{0.01}$ cells, however, the initial capacity is 99 mAh/g and is retained after 28 cycles. $Li_{1.02}Mg_{0.1}Mn_{1.9}O_{3.99}S_{0.01}$ only delivers 85 mAh/g although

capacity fading is not detected after 28 cycles. This is because the oxidation state of Mn is increased not only by the substitution of Mg^{2+} for Mn, but also by that of S for O.

Capsoni et al., 2003, have discussed structural transitions occurring in Mg doped $LiMn_2O_4$. It has been shown that the inhibition of the Jahn-Teller transition is related to the ratio $r= [Mn^{4+}/Mn^{3+}]$ as deduced from the charge distribution model $[Li_{1-xt}{}^{+}Mg_{xt}{}^{2+}]_{tetr}[Li_{y+xt}{}^{+}Mg_{xo}{}^{2+}Mn_{1-3y-2x}{}^{3+} Mn_{1+2y+x}{}^{4+}]_{octa}$ where $x=x_o+x_t$. The occupancy factors indicate that tetrahedral sites are preferred by Mg ions for $x \leq 0.06$ and the octahedral one for higher Mg content. The presence of Mg on the tetrahedral site was confirmed from the XRD patterns. The (440) reflection (at $2\theta \sim 64°$) is a suitable indicator of the transition onset. A clear splitting of this peak for the x=0.02 was observed at 213 K. The low temperature XRD experiments on x=0.06 do not give any splitting evidence down to 100 K. For y=0.02 and x=0.02, r=1.177 was found. This value is very close to r_{lim}=1.18, beyond which the Jahn-Teller transition is inhibited. For x=0.06, a value r=1.34 was obtained for which the Jahn-Teller transition was no longer observed. Hence it was concluded that for x=0.02 the Mg substitution allows to obtain an undistorted cubic spinel phase: the Jahn-Teller transition temperature is remarkably lowered from room temperature down to 213 K and this material may receive applications in a very large temperature range. Deng et al., 2004, have discussed a new method of preparation to obtain oxygen stoichiometric spinel. A new type of Mg-doped $LiMn_2O_4$ spinel with controlled oxygen stoichiometry was synthesized by annealing with extra LiOH at low temperatures after calcinations at ultra high temperatures. The new materials were found to be oxygen-rich spinels based on chemical analysis and they were oxygen stoichiometric with metal cation vacancies. In contrast to spinel materials prepared by conventional method, the new materials exhibited greatly improved cycling performance and reduced Mn dissolution at elevated temperature because of their oxygen stoichiometry, improved crystallinity, and small surface area.

Structural properties of $LiMn_2O_4$ doped with high content of Mg ($LiMg_{0.5}Mn_{1.5}O_4$) have been determined by many authors. $LiMg_{0.5}Mn_{1.5}O_4$ has been synthesized by many techniques such as sol-gel, solid state etc. In one of the study conducted by Suryakala et al., 2006, it has been shown that $LiMg_{0.5}Mn_{1.5}O_4$ synthesized via sol-gel technique has cubic spinel structure with space group Fd3m. However another study carried by Nakamura et al., 2008, has shown that $LiMg_{0.5}Mn_{1.5}O_4$ has a cubic spinel structure with $P4_332$ as space group. Cubic spinel

structure with space group $P4_332$ is an ordered spinel structure with different atomic arrangement from that of cubic spinel structure obeying Fd3m space group. It has been shown that for the doping content of Mg up to x=0.3 in $LiMg_xMn_{2-x}O_4$, the structure is single phase cubic spinel with Fd3m as space group, and for x>0.3 structure changes to ordered spinel structure with space group $P4_332$. In some studies the coexistence of different phases have been observed by many authors in various oxide materials (Bhattacharya et al., 1990) Group theory predicts four infrared active modes for the cubic spinel $LiMn_2O_4$. With the change in symmetry from Fd3m to $P4_332$, i.e when the structure becomes ordered spinel structure, the numbers of allowed infrared modes are expected to increase from 4 to 21. The infrared spectrum of $LiMn_{1.5}Mg_{0.5}O_4$ is known to be fully consistent with cation ordering and cubic P symmetry (Preudhomme, 1974).

2.7 Layered $LiNi_{1/3}Mn_{1/3}Co_{1/3}O_2$ Cathode Material

In 2001, Ohzuku and Makimura, proposed a new layered Lithium insertion material "$LiCo_{1/3}Ni_{1/3}Mn_{1/3}O_2$" for Li-ion batteries. Layered $LiCo_{1/3}Ni_{1/3}Mn_{1/3}O_2$ was prepared by a solid state reaction at 1000 °C in air and examined in nonaqueous lithium cells. $LiCo_{1/3}Ni_{1/3}Mn_{1/3}O_2$ showed a rechargeable capacity of 150 mAh/g in 3.5–4.2 V or 200 mAh/g in 3.5–5.0 V. $Li/LiCo_{1/3}Ni_{1/3}Mn_{1/3}O_2$ operate at 0.2–0.25 V lower than that of a cell having $LiCoO_2$ or $LiMn_2O_4$ as cathode and at 0.15–0.3 V higher than that of a cell having $LiNiO_2$ as a cathode material. Since then this material has attracted many researchers and an enormous work on this material has been done in the recent past. Yabuuchi and Ohzuku, 2003, in another research work carried out the cyclic behavior and rate capability of lithium cells with $LiCo_{1/3}Ni_{1/3}Mn_{1/3}O_2$. This material showed a rechargeable capacity more than 200 mAh/g with excellent capacity retention. The charge and discharge coulombic efficiencies are approximately 99% in this case after 30 cycles. It has also been shown that the unit cell volume remains almost constant, i.e. zero-volume change until x=0.67 in $Li_{1-x}Co_{1/3}Ni_{1/3}Mn_{1/3}O_2$. It has been shown that if we define the C-rate with respect to 200 mAh/g, observed at low rate discharge of 0.17 $mAcm^{-2}$ or 18.3 mAg^{-1}, 8C (1600 mAh/g) discharge is

possible in this compound. It has been emphasized that this material is equivalent or even better than $LiCoO_2$ for the use as cathode material for Li-ion battery.

Hwang et al., 2003, have shown that the valence state of Ni, Co and Mn in $LiCo_{1/3}Ni_{1/3}Mn_{1/3}O_2$ are +2, +3 and +4 respectively. The first charge and discharge capacities of the material synthesized at 900 °C were 212 and 188 mAh/g, respectively. The first charge and discharge capacities for the material synthesized at 800 °C were 209 and 173 mAh/g, respectively. The irreversible capacities of the $LiNi_{1/3}Co_{1/3}Mn_{1/3}O_2$ material synthesized at 800 and 900 °C can be determined to be 36 and 24 mAh/g, respectively. From the in situ X-ray absorption spectroscopy (XAS) observation of $LiNi_{1/3}Co_{1/3}Mn_{1/3}O_2$ during charging/discharging processes it has been observed that the irreversible capacity is due to the part of Ni that cannot be reduced during the discharging process. Results indicate that $LiNi_{1/3}Co_{1/3}Mn_{1/3}O_2$ material is a high-capacity electrode and has excellent capacity retention. The major problem with the material has shown to be its irreversible capacity, which needs to be improved before its commercialization.

Todorov and Numata, 2004, have prepared $Li_{1+x}(Mn_{1/3}Co_{1/3}Ni_{1/3})_{1-x}O_2$ ($x \geq 0$) mixed oxides with different Li/M molar ratios (M = $Mn_{1/3}Co_{1/3}Ni_{1/3}$). It was observed that the discharge capacity decreases with increasing Li/M ratio. However the capacity fade on cycling was much smaller when Li content was high. Result indicated that the optimum Li/M molar ratio is 1.10 for high first cycle coulombic efficiency. However, the first cycle coulombic efficiency was not high compared to Li–Mn spinel or $LiCoO_2$. The highest coulombic efficiency of 89.7% was obtained for the Li/M ratio of 1.10. Structural information was reported using neutron diffraction data by Kobayashi et al., 2005, $Li_{1-y}Ni_{1/3}Mn_{1/3}Co_{1/3}O_2$ (y=0.1-0.7) was synthesized electrochemically. Discharge capacity of 160 mAh/g in the voltage range of 4.6-2.5V was observed. Change in the oxidation state of Ni from +2 to +3 and then to +4 was observed by X-ray absorption near edge structure (XAFS) spectra during de-lithiation. The Co K-edge extended X-ray absorption fine structure (EXAFS) results indicated that the change in valence state from Co^{3+} to Co^{4+} as y increased was clearly detected by a decrease of the Co-O distances. The Mn K-edge EXAFS results indicated that the Mn-O bond lengths showed essentially no change over the whole composition range. Liu et al., 2006, have carried out the Fe and Al doping in $LiNi_{1/3}Mn_{1/3}Co_{1/3}O_2$. Doping was made in place of Co, which is costly and highly toxic in nature. Not much encouraging results were

obtained in their study. Fe doping lowered the delithiation potential plateau of $LiNi_{1/3}Co_{1/3}Mn_{1/3}O_2$ but hinder the diffusion of its Li^+ ion due to disordered occupation of the doped Fe ions at the 3a sites. In contrast, low-content Al doping improved the capacity retention of $LiNi_{1/3}Co_{1/3}Mn_{1/3}O_2$. However, the capacity retention became poor for the higher content of Al. Metal oxides (ZrO_2, TiO_2, and Al_2O_3) coated $LiNi_{1/3}Mn_{1/3}Co_{1/3}O_2$ has also been reported by Li et al., 2006. It was observed that $LiNi_{1/3}Mn_{1/3}Co_{1/3}O_2$ prepared by a spray drying method exhibited poor cyclic performance when it was operated at rates of 0.5C and 2C in 3-4.6V. Coating of the material with the metal oxides helped in obtaining the good cyclic performance of the material at 0.5C and 2C rates. It was observed that such poor behavior of $LiNi_{1/3}Mn_{1/3}Co_{1/3}O_2$ is due to the increase in surface resistance and charge transfer resistance. The presence of a thin metal oxide layer could remarkably suppress the increase in the total resistance (sum of the surface resistance and the charge transfer resistance), which was attributed to the improvement in good cyclic performances. Similarly coating of carbon has also been reported by Kim et al., 2007. It has been shown that carbon-coated material has improved thermal stability and electrochemical performance compared with bare material. From DSC analysis, the carbon coated layer on the surface of $LiNi_{1/3}Mn_{1/3}Co_{1/3}O_2$ active material is found to suppress the oxygen generation. The rate capability of the material is improved by carbon coating; the capacity retention of a 1 wt. % carbon-coated sample at the 5C rate is 87.4% with respect to that at the 0.2C rate. After 50 charge-discharge cycles, the discharge capacity retention of the 1 wt. % carbon-coated material is 98%, i.e., similar to that of bare material.

2.8 First Principles' Studies (Density Functional Theory)

Some first principles studies on lithium manganese oxides have been carried by the researchers. The manganese cation is typically high spin with a very large magnetic moment. Mn^{3+} is a prototypical Jahn-Teller ion, giving rise to a tetragonal deformation of the oxygen environment around it. Since lithium is fully ionized to Li^+ in these oxides, charge neutrality requires that insertion or removal of Li from the structure is accompanied by electron transfer to and from the manganese-oxide host, changing the effective valence state of the Mn ion. While the Mn ion in MnO_2 is believed to have the electronic configuration $t_{2g}^3 e_g^0$, lithiation

up to $LiMnO_2$ leads to occupation of the doubly degenerate e_g level. In octahedral symmetry the two e_g orbitals consist of an antibonding combination of the $3d_z^2/3d_{x^2-y^2}$ and oxygen p orbitals, so that their occupation leads to an increase in the oxygen-metal bond length. In one type of Jahn-Teller distortion, the symmetry between the occupied and empty level is spontaneously broken by an increase in two of the metal-oxygen bonds along the $3d_z^2$ orbital. Although Mn^{3+} is almost always a Jahn-Teller ion and Mn^{4+} never is, disagreement exists what average valence is required to cause a Jahn-Teller distortion in structures with mixtures of Mn^{3+} and Mn^{4+}. In $LiMn_2O_4$ where the average valence of Mn is 3.5, a tetragonal unit cell distortion has been found below room temperature, with the cubic-tetragonal transition temperature being very dependent on Li and oxygen stoichiometry.

Mishra and Ceder, 1999, have carried out detailed structural study on manganese based oxides. A series of LDA and GGA calculations with ferromagnetic and antiferromagnetic spin ordering for lithiated manganese oxides have been carried out. Spin polarization has been shown to have a significant effect on energies. Therefore spin polarization effect should be included in the calculations in order to determine the correct information regarding the structure. In the compositions $LiMn_2O_4$ and $LiMnO_2$ stable antiferromagnetic ordering of the Mn ions was found. It was observed that GGA can produce stable Jahn-Teller distortion in this system, in contrast to the LDA. A detailed work on layered $LiMnO_2$ has also been carried out by Prasad et al., 2005. Effect of various dopants on structural stability of lithium manganese oxides have been observed using first principles studies. Divalent dopants which oxidize a neighboring Mn to the Jahn-Teller inactive 4+ oxidation state promoted the rhombohedral structure stabilization to a greater extent than trivalent dopants. Within the class of divalent dopants, the filled shell systems Mg and Zn were found to be more effective than those with partially filled e_g shells. Within the class of trivalent dopants, those with partially filled t_{2g} shells were more effective than those with filled or empty shells. Not many studies have been performed on the doped $LiMn_2O_4$. To the best of our knowledge no first principles study has been carried out on Mg doped $LiMn_2O_4$. However study on the Cr doped $LiMn_2O_4$ has been carried out by Shi et al., 2003. They have performed the Cr doping in supercell of $LiMn_2O_4$, which consist of 8 formula units of $LiMn_2O_4$. So the calculation was performed on 56 atoms in the framework of local density approximation (LDA). Spin polarization effect was not taken into account in all the structures, which Mishra and Ceder,

47

1999, have shown to be very crucial in explaining the correct ground state energy and other structural property. Electronic properties were also checked in the Cr doped $LiMn_2O_4$. It was found that the structure of material is more favorable in total energy when the doping chromium atoms are dispersed in $LiMn_2O_4$. With increasing Cr dopant, more electrons are transferred to the oxygen while the positive valence states of Mn atoms are less affected. Consequently, the doping of Cr ions possess a higher valence than Mn in $LiMn_2O_4$, agreeing qualitatively with previous experimental results. Average intercalation voltage was also calculated in various doped structure. It was found to be in agreement with the experimental studies. Owing to the restriction in the computational resources, authors have not relaxed all the structures.

Ouyang et al., 2008, have recently discussed the Jahn-Teller distortion and electronic properties of $LiMn_2O_4$. Jahn-Teller distortion has been discussed in the cubic spinel structures. It has been shown that the crucial properties such as distortion of $Mn^{3+}O_6$ octahedra instead of Mn^{4+} can be explained using GGA+U (U = Hubbard parameter) method. GGA+U calculations have shown that Mn exist in mixed valence state of Mn^{3+} and Mn^{4+}, while GGA predict Mn to be in $Mn^{+3.5}$ oxidation state. The local atomic position of Mn^{3+} and Mn^{4+} ions present in $LiMn_2O_4$ are shown in Fig. 2.11.
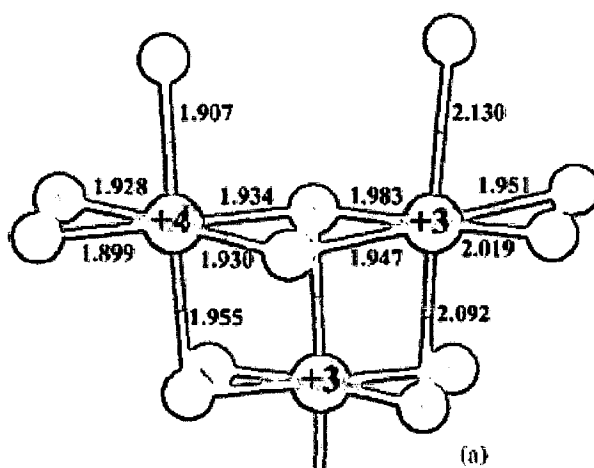
Fig. 2.11: Local atomic positions around Mn^{3+} and Mn^{4+} in $LiMn_2O_4$ obtained from GGA+U based calculations (purple: transition metal ions and red: oxygen, Ouyang et al., 2008)

48

This is in good agreement with the experimental studies. GGA+U method is shown to be able to localize electrons to Mn $3d_z^2$ orbits in the majority spin channel, and open a gap of about 0.5 eV between the Mn $3d_z^2$ and Mn $3d_{x^2-y^2}$. Therefore GGA+U shown to have better results compared to GGA. All the results were obtained by considering Mn to possess antiferromagnetic (AFM) nature.

It can be seen from the above reported literature that although the effect of final composition and atomic positions on the properties of cathode have been extensively studied, the in depth study of the morphological changes occurring in the various systems as a result of doping have not been reported by the authors. Thus in the present study the effect of doping on the morphological changes has been studied. It was also noted that further studies are required in the Cr doped $LiMn_2O_4$ cathode material, which is a potential cathode material for lithium ion battery.

Contradictory results for the Mg doped $LiMn_2O_4$ have been reported in the literature. Suryakala et al., 2006 have reported Fd3m as the space group for the $LiMg_{0.5}Mn_{1.5}O_5$, however Nakamura et al., 2008 have reported that the cubic spinel structure changes its space group symmetry from Fd3m to $P4_332$ for x>0.3 in $LiMg_xMn_{2-x}O_4$. It has been noticed that the synthesis route followed by the researchers is same in both the cases. Therefore in the present study attempt has been made to resolve this controversy by carrying out in-depth X-ray diffraction study of $LiMg_xMn_{2-x}O_4$ (0.0≤x≤0.5), produced by method (Sol-gel) which is identical to both the above mentioned studies. It has also been observed that the thermal analysis has not been carried out for the Mg doped $LiMn_2O_4$ for a wide range of doping concentration ($LiMg_xMn_{2-x}O_4$; 0.0≤x≤0.5), which has been attempted in the present study.

First principles' calculations have been performed by many authors on pristine $LiMn_2O_4$ and layered $LiMnO_2$. It has been mentioned by Mishra and Ceder, 1999 that spin polarization calculation are necessary to get the true ground state of the system. Apart from the work carried by Shi et al., 2003 no calculations have been performed on the doped $LiMn_2O_4$. Even in the study by Shi et al., the structures have not been relaxed, and the calculations were not spin polarized. Therefore in-depth ab-initio computation was carried out on the Cr and Mg doped systems, by taking into account the spin polarization effect.

Chapter 3
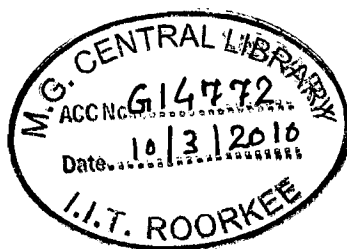
Experimental and Computational

Procedure

3.1.1 Sol-Gel Synthesis

Sol-Gel synthesis is a promising materials preparation technique which is widely used for the synthesis of glasses and ceramics. It is also a well established technique for the synthesis of the cathode materials for lithium ion battery. This technique allows better control over many properties. Some advantages and disadvantages of this processing technique are given below.

This process can be carried out at lower temperature. In the case of glasses the process is essentially attractive for the production of those compositions which require high melting temperatures. For example, silica glass may be obtained in the vicinity of 1000 °C rather than 2000 °C. High homogeneity and purity of the resulting materials can be obtained by using this technique. Wet gel can be prepared in stoichiometric conditions and a degree of purity which depends only on the starting ingredients can be easily achieved. The composition of the final glass mainly depends on the sintering process which is performed at lower temperature and thus reduces the risk of loss of more volatile solute.

The energy saving which might be obtained in case of sol-gel due to the low processing temperature is, however, largely offset by the high cost of initial ingredients necessary for making the gel. The treatment of the gel, drying – curing and sintering stages, are also, in practice, more complicated and time-consuming than direct melting in classical glass-practice.

In sol-gel processing, a solution is prepared from a metal alkoxide that incorporates the elements of the oxide. A chelating agent, with large side chains may also be added to control the hydrolysis reaction kinetics. The gel is dried and fired to burn off residual organic compounds and densify the network into a uniform, amorphous oxide. Subsequent heat treatment can cause crystallization.

In present thesis work all the materials syntheses have been done using sol-gel method.

3.1.1.1 Synthesis of LiMn$_2$O$_4$ Spinel

Metal acetates or nitrates were chosen as starting materials. Lithium acetate and Manganese acetate in stoichiometric amount were taken separately in beakers. Distilled water was added as a solvent to dissolve these acetates. Water was added so as to obtain a saturated solution of metal ions. During this process following reaction took place

$$Mn^{2+} + 2OH^- \rightarrow Mn(OH)_2$$
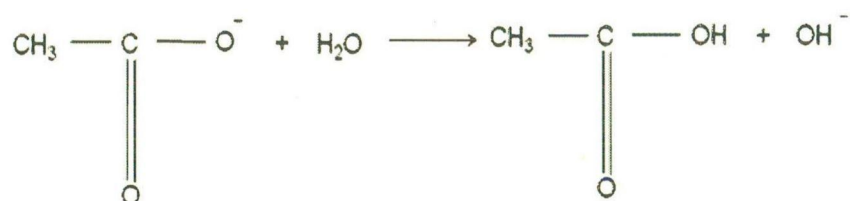
Citric acid was dissolved in distilled water separately. Citric acid was used as a chelating agent in the present study. Ratio of the citric acid to metal ion was maintained at 1:1. All the saturated solutions of lithium acetate, manganese acetate and citric acid were mixed together. pH of the resultant solution was made to be ~7 by using ammonia solution and nitric acid. After mixing all the saturated solutions together, resultant solution was stirred with the help of a magnetic stirrer and temperature of the resultant solution was maintained between 80-90 °C. During this process the chelating agent makes a chelating complex. The possible reaction is given below, where M = Li, Mn. As water gets evaporated, the viscosity of the solution slowly increased with time. Finally a transparent thick gel was obtained.
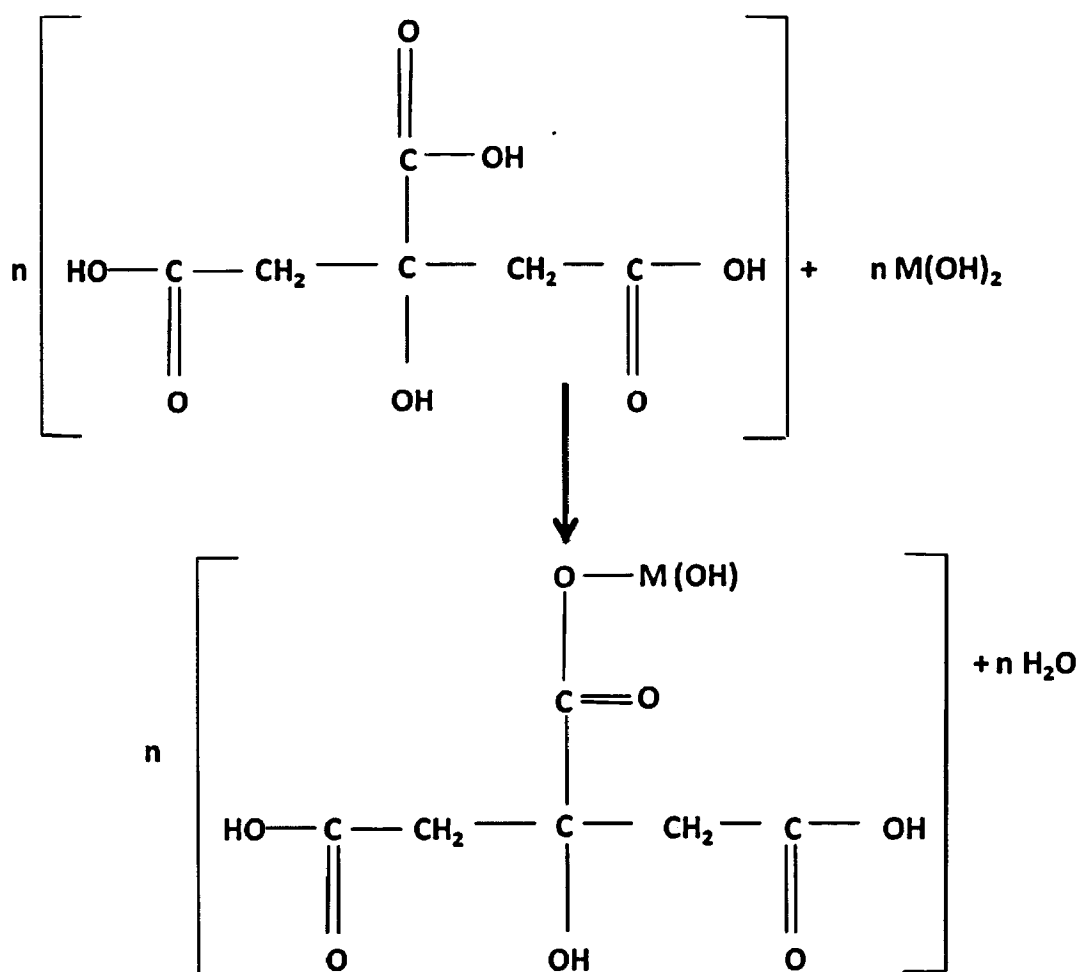
The gel was decomposed at 350 °C in 2 hours and after that the temperature was raised to 750 °C to carry out the calcinations. Calcination was carried out for 12 hours in presence of air. Final precursors were collected and grinded with the help of mortar and pestle.

3.1.1.2 Synthesis of Cr and Mg Doped LiMn$_2$O$_4$ Spinels

The doping of the transition metal was performed using this technique. Procedure for the preparation of Cr or Mg doped LiMn$_2$O$_4$ is similar to that of the synthesis of LiMn$_2$O$_4$. In this case an additional saturated solution of chromium nitrate or magnesium nitrate in distilled water was added along with the saturated solutions of other metal acetates to get the final sol. Various precursors having compositions of LiCr$_x$Mn$_{2-x}$O$_4$ (x = 0.0, 0.1, 0.2, 0.3 and 0.5) and LiMg$_x$Mn$_{2-x}$O$_4$ (x = 0.05, 0.10, 0.15, 0.25, 0.35, 0.5) were made in order to check the effect of Cr or Mg on the various properties of LiMn$_2$O$_4$. Rest all other parameters such as pH of

the solution, citric acid to metal ion ratio, decomposition and calcination temperature were kept same. However in case of Mg doped $LiMn_2O_4$ samples powders were repeatedly calcined for four times to attained the phase purity in the synthesized material. However the decomposition, calcination time and temperatures for the processing of the doped materials are same as that used in $LiMn_2O_4$.

A flowchart showing the procedure for the sol-gel synthesis of various cathode materials for lithium ion batteries is shown in the Fig. 3.1.

| Lithium Acetate | Manganese Acetate | Acetate or Nitrate of Doped Metal | Citric acid |

Saturated Solution in Water

Continuous Stirring at 80-90 °C with the help of magnetic stirrer

Gel Formation

Calcination at Different Temperatures

Various Characterizations
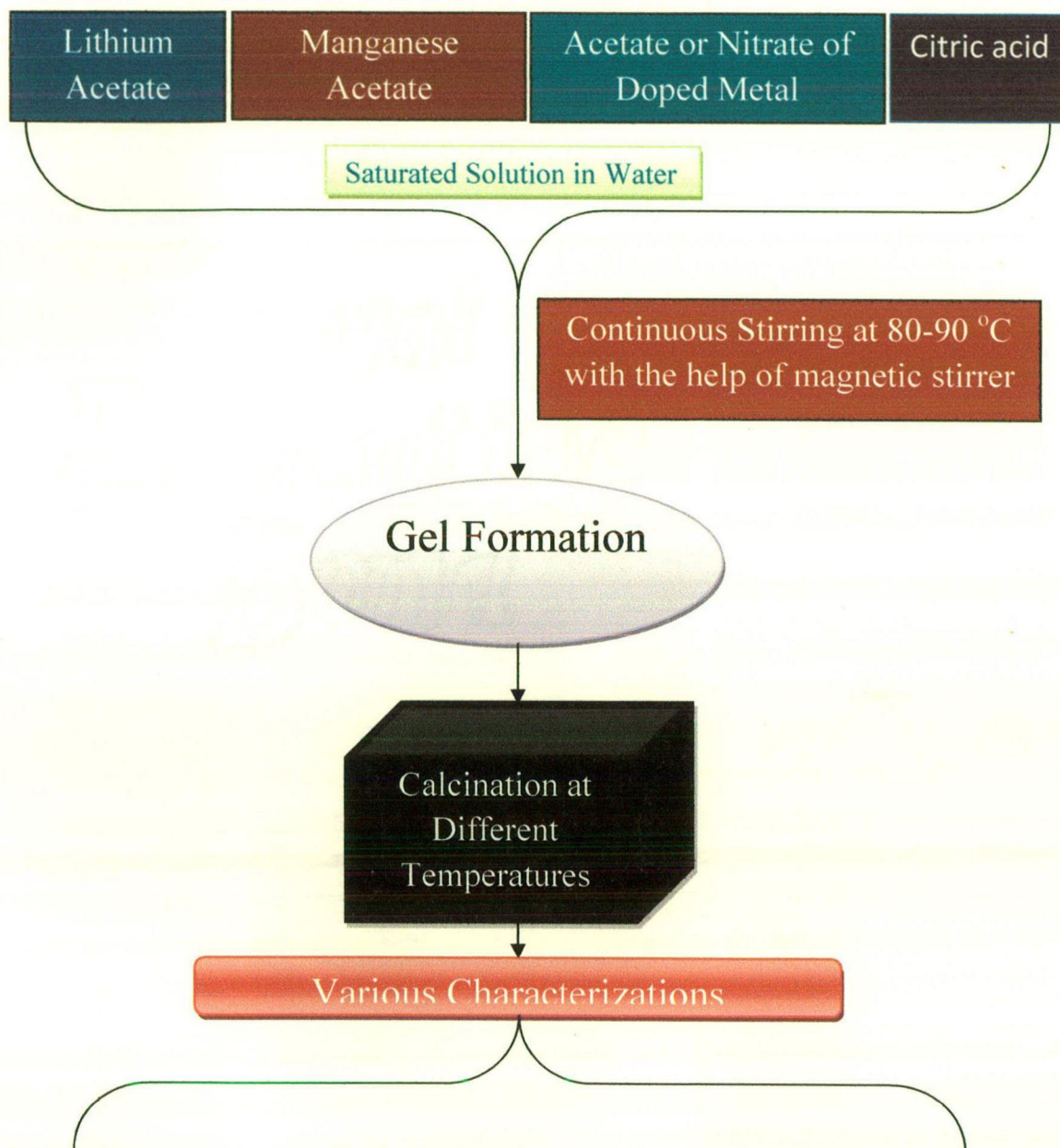
XRD, FESEM, DTA/TG, IMPEDANCE SPECTROSCOPY, ELECTROCHEMICAL PERFORMANCE

Fig. 3.1: Flow chart for the synthesis route via sol-gel process

3.1.1.3 Synthesis of Layered LiNi$_{1/3}$Mn$_{1/3}$Co$_{1/3}$O$_2$

For the synthesis of layered LiNi$_{1/3}$Mn$_{1/3}$Co$_{1/3}$O$_2$, lithium acetate, manganese acetate, nickel acetate, cobalt nitrate and citric acid were used as starting materials. All the metal acetates or nitrates and citric acid were dissolved separately in distilled water. Citric acid to metal ion ratio was varied in order to check the effect of citric acid content on the various properties of the material. pH of the resulting solution was maintained at ~ 9 with the help of ammonia solution and nitric acid. Solution was thoroughly mixed with the help of magnetic stirrer and a temperature of 80 to 90 ^{o}C was maintained during this process. After the removal of water to a limited extent a thick gel was obtained. Decomposition of the gel was performed at 450 ^{o}C for 5 hours. After that the precursors were taken out at room temperature, and were grounded thoroughly using mortar and pestle. Calcination of the grounded precursor was performed at 850 ^{o}C for 18 hours.

3.1.2 Various Characterization Techniques Used

3.1.2.1 X-Ray Diffraction (XRD)

A diffraction beam may be defined as a beam composed of a large number of scattered rays mutually reinforcing each other. Diffraction is therefore, essentially a scattering phenomenon and not one involving any "new" kind of interaction between the X-rays and atoms. Atoms scatter incident X-rays in all directions, and we shall see presently that in some of these directions the scattered beam will be completely in phase and so reinforce each other to form diffracted beams.

The essential condition which must be met if diffraction is to occur is given as

$n\lambda = 2d \sin \theta$

where n is called the order of reflection; it may take on any integral value consistent with *sin* θ not exceeding unity and is equal to the number of wavelengths in the path difference

between the rays scattered by adjacent planes. Therefore for a fixed value of λ and d, there may be several angles of incidence at which diffraction may occur.
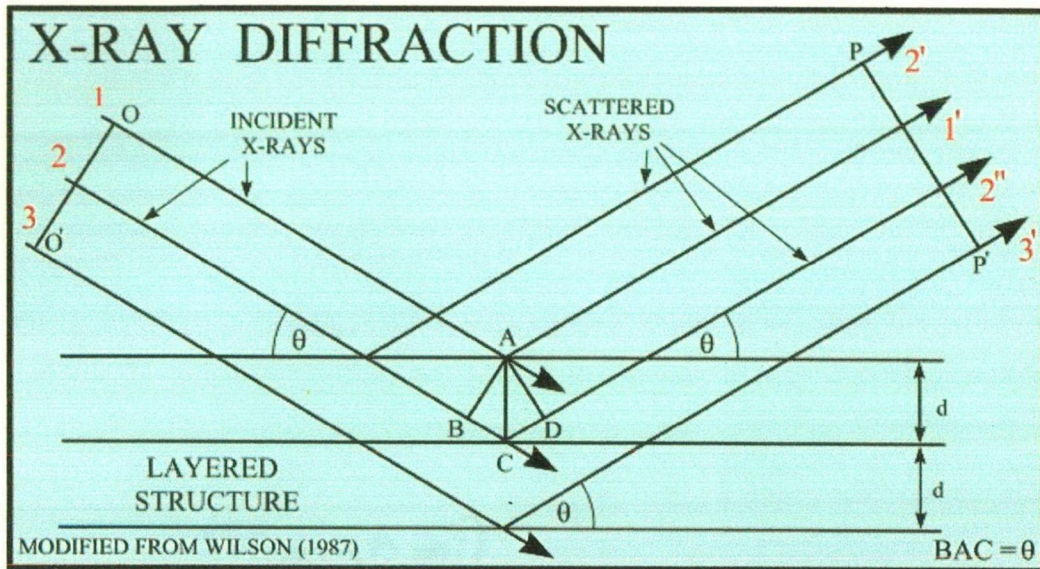
Fig. 3.2: Scattering of X-rays from the lattice planes

The diffracted beam is rather strong compared to the sum of all the rays scattered in the same direction, simply because of the reinforcement which occurs, but extremely weak compared to the incident beam since the atom of the crystal scatter only a small fraction of energy incident on them. If the atoms are arranged randomly in space, scattering occurs in all directions and is weak and hence intensities add. But if the atoms are periodically arrange as in perfect crystals, then scattering occur in very few directions, those satisfying the Bragg's Law, the intensity is strong and is called diffraction and hence amplitudes add. If scattering occurs in the directions, which do not satisfy the Bragg's law (Fig. 3.2), there will be no intensity as the scattered rays cancel one another.

In order to find the positions of the number of atoms in a unit cell of known shape and size, one makes use of observed relative intensities of the diffracted beams, since the intensities are determined by atom positions. The atom positions are found by trial and error method, because there is no known general method for directly calculating atom positions from the observed intensity data. The following are the basic two equations

58

$$I = |F|^2 M \left(\frac{1 + \cos^2 \theta}{\sin^2 \theta \cos \theta} \right)$$

$$F = \sum_1^N f_n e^{2\pi i (hu_n + kv_n + lw_n)}$$

which give the value of the structure factor F for the *hkl* reflection in terms of the atom positions *u, v,* and *w*. Since the relative intensity I, the multiplicity factor M, and the Bragg angle are known for each line on the pattern, one can find the value of $|F|$ for each reflection from the former equation. But $|F|$ measures only the amplitude of each reflection relative to another (Cullity, 1977)

Atom positions, therefore, can be determined only by trial and error. A set of atom positions is assumed, the intensities corresponding to those positions are calculated, and the calculated intensities are compared with observed ones, the process being repeated until satisfactory agreement reached. A Fourier series is a type of infinite trigonometric series by which any kind of periodic function may be expressed. Now the one essential property of the crystal is that its atoms are arranged in a periodic fashion. But this means that electron density is also a periodic function of position in the crystal, rising to a maximum at the point where an atom is located and dropping to a low value in the region between the atoms. To regard a crystal structure in this manner, as a positional variation of electron density rather than an arrangement of atoms, is particularly appropriate where diffraction is involved, in that X-rays are scattered by electrons and not by atoms as such. Since the electron density is a periodic function of the position, a crystal may be described analytically by means of Fourier series. This method is very useful in the determination of structure because it can be shown that coefficient of the various terms in the series are related to the F values of the various X-ray reflections. But this is of no use until structure factor is known in both magnitude and phase. A function called "Patterson function", whose coefficients are related to the experimentally observable $|F|$ values and which gives, not electron density, but information regarding the

59

various interatomic vectors in the unit cell. The information is frequently enough to determine the phase of the various structure factors; then another kind of a series can be mapped out the actual electron density throughout the cell and thus disclose the atomic positions.

The powder diffraction method is the only method that can be employed when a single-crystal specimen is not available. The method is especially suited for determining lattice parameters with high precision and for identification of phases, whether they occur alone or in mixtures such as poly phase alloys, corrosion products, refractories and rocks.

X-ray diffraction (XRD) patterns of the powdered samples in the present work were recorded from X-ray diffractometers (Philips PW3040/60 as well as D8 Advance Bruker AXS embedded with fast detector) using CuK_α radiation (Fig. 3.3). The step size and dwell time were suitably adjusted in order to obtain the good signal to noise ratio. Phase analysis of the various samples was done using X'pert High Score plus software. Rietveld refinement was performed for the XRD patterns of each composition to obtain the accurate values of lattice parameters and atomic positions in the crystal structure.
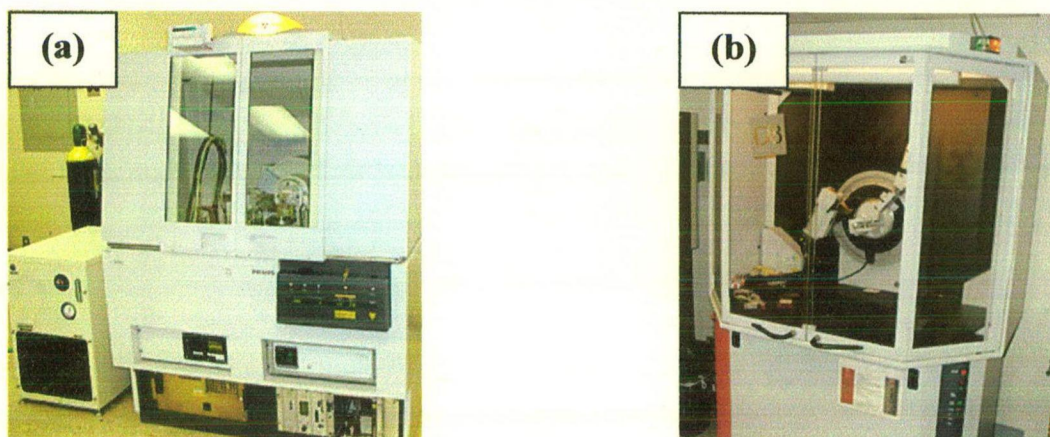
Fig. 3.3: (a) X-ray diffractometer (Philips PW3040/60) and (b) D8 Advance Bruker AXS embedded with fast detector

Basic principle for the Rietveld refinement is described as follows:

$$y_{ic} = y_{ib} + \sum_p \sum_{k=k_1^P}^{k=k_2^P} G_{ik}^p I_K$$

where y_{ic} is the net intensity calculated at point i in the pattern, y_{ib} is the background intensity, G_{ik} is a normalized peak profile function, I_k is the intensity of the kth Bragg reflection, k_1, k_2,... are the reflections contributing intensity to the point i, and the superscript p corresponds to the possible phases present in the sample.

The intensity I_k is given by the expression:

$$I_k = SM_k L_k |F_k|^2 P_k A_k E_k$$

where S is the scale factor, M_k is the multiplicity, L_k is the Lorentz polarization factor, and F_k is the structure factor expressed as,

$$F_k = \sum_{j=1}^n f_j \exp\left[2\pi i (h_r^t r_j - h_k^t B_j h_k)\right]$$

where f_j is the scattering factor of the atom j, and h_r, r_j and B_j are matrices representing the Miller indices, atomic coordinates and anisotropic thermal vibration parameters, respectively, and the superscript t indicates matrix transposition. The factor P_k is used to describe the effects of preferred orientation: no preferred orientation is indicated with $P_k = 1$. The factor A_k is the absorption correction and factor E_k is an extinction correction. The positions of the Bragg peaks from each phase are determined by their respective set of cell dimensions, in conjunction with a zero parameter and the wavelength (or diffractometer constants) provided. All of these parameters may be refined simultaneously with the profile and crystal structural parameters.

Some of the agreement indices which were refined are given below

Profile value

$$R_p = \frac{\sum |y_{io} - y_{ic}|}{\sum y_{io}}$$

Weighted value

$$R_{wp} = \left[\frac{\sum (y_{io} - y_{ic})^2}{\sum w_i y_{io}^2} \right]$$

Bragg value

$$R_B = \frac{\sum |I_{ko} - I_{kc}|}{\sum I_{ko}}$$

Expected value

$$R_{exp} = \left[\frac{N - P}{\sum w_i y_{io}^2} \right]$$

Goodness of fit value

$$\chi^2 = \frac{\sum w_i (y_{io} - y_{ic})^2}{N - P} = \left[\frac{R_{wp}}{R_{exp}} \right]^2$$

where P = number of least square parameters being estimated, N = number of observations, W = weight fraction

All the patterns were refined so as to obtain the desired value of various profile parameters. In case of dual phase compounds the percentage of various phases were also calculated.

62

3.1.2.2 Microstructural Investigations by Field Emission Scanning Electron Microscope (FESEM)

Morphology, size distribution and other microstructural properties of the particles play a crucial role in determining the physical and chemical properties of the various materials (Sanyal et al., 2002). Therefore microstructural properties of the materials for different compositions have been studied by using FESEM. In FESEM the electrons liberated from a field emission source and are accelerated in a high electrical field gradient. Within the high vacuum column these primary electrons are focused and deflected by electronic lenses to produce a narrow scan beam that bombards the object resulting in emission of secondary electrons from the object. These secondary electrons are registered by a detector which produces electronic signals. These signals are amplified and transformed to an image that can be seen on a monitor.

There are two classes of electron emission source: thermionic emitter and field emitter. Emitter type is the main difference between the Scanning Electron Microscope (SEM) and the Field Emission Scanning Electron Microscope (FESEM). Thermionic Emitters use electrical current to heat up a filament; the two most common materials used for filaments are Tungsten (W) and Lanthanum Hexaboride (LaB$_6$). When the heat is enough to overcome the work function of the filament material, the electrons can escape from the material itself. Thermionic sources have relatively low (i) brightness, (ii) evaporation of cathode material and (iii) thermal drift during operation. Field Emission is one way of generating electrons that avoids these problems. A Field Emission Gun (FEG); also called a cold cathode field emitter, does not heat the filament. The emission is reached by placing the filament in a huge electrical potential gradient. The FEG is usually a wire of Tungsten (W) fashioned into a sharp point. The significance of the small tip radius ($\sim$ 100 nm) is that an electric field can be concentrated to an extreme level, becoming so big that the work function of the material is lowered and electrons can leave the cathode. To see the image of the samples, these are first made conductive for current. This is done by coating them with an extremely thin layer (1.5 - 3.0 nm) of gold. Further on, objects must be able to sustain the high vacuum and should not alter the vacuum, for example by losing water molecules or gasses. After the object has been

covered by a conductive layer it is mounted on a special holder. The object is inserted through an exchange chamber into the high vacuum part of the microscope and anchored on a moveable stage. The "secondary electron emission" detector (scintillator) is located at the rear of the object holder in the chamber. Sketch showing the working of a scanning electron microscope is given in Fig. 3.4.

When the primary probe bombards the object, secondary electrons are emitted from the object surface. The secondary electrons, which are attracted by the Corona, strike the scintillator fluorescing mirror that produces photons. The location and intensity of illumination of the mirror vary depending on the properties of the secondary electrons. The signal produced by the scintillator is amplified and transduced to a video signal that is fed to a cathode ray tube in synchrony with the scan movement of the electron beam. The contrast in the 'real time' image that appears on the screen reflects the structure on the surface of the object. Parallel to the analog image, a digital image is generated which can be further processed.

In the present study the calcined powder samples were analyzed under the microscope. Powdered samples were glued onto the sample holder with the help of carbon tape. The microstructural investigations of the powders were carried out using FEI QUANTA 200 F and Supra 40 Carl ZEISS models of FESEM.
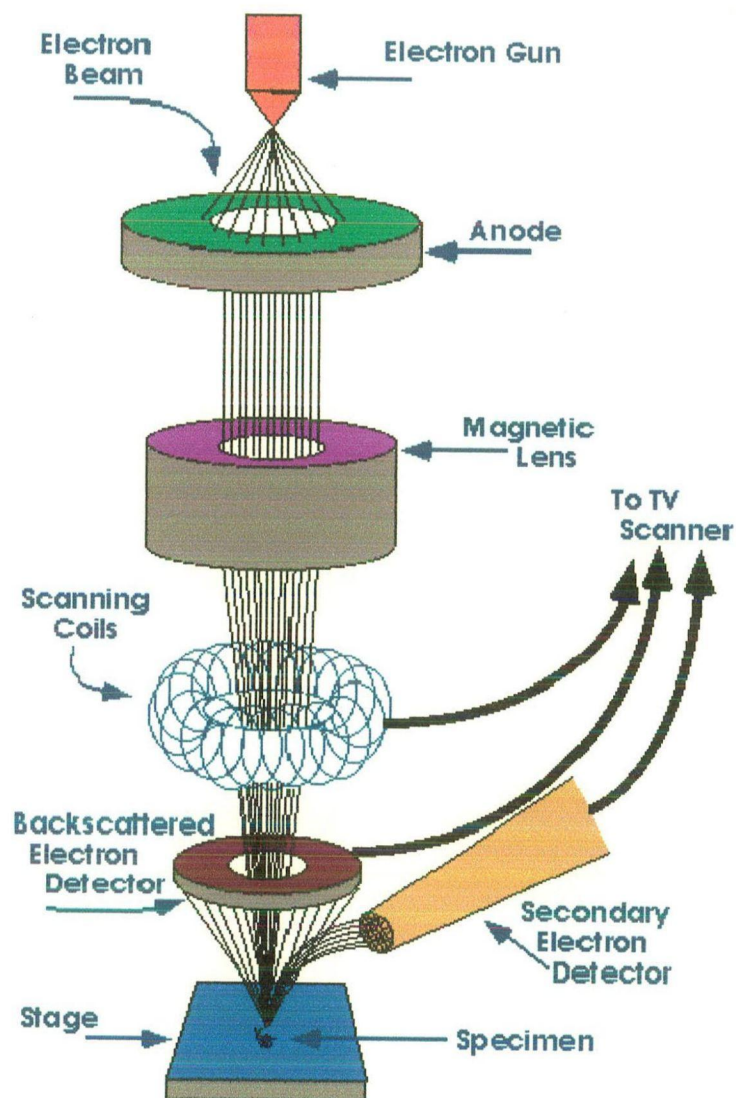
Fig. 3.4: Sketch showing the working of a Scanning Electron Microscope

3.1.2.3 Differential Thermal Analysis (DTA)/Thermogravimetry (TG)

Thermal analysis comprises a group of techniques in which a physical property of a substance is measured as a function of temperature, while the substance is subjected to a controlled temperature program. DTA may be defined formally as a technique for recording the difference in temperature between a substance and a reference material against either time or temperature as the two specimens are subjected to identical temperature regimes in an

65

environment heated or cooled at a controlled rate. The baseline of the DTA curve should then exhibit discontinuities at the transition temperatures and the slope of the curve at any point will depend on the microstructural constitution at that temperature. The essential requirements of the furnace are that it should provide a stable and sufficiently large hot zone and must be able to respond rapidly to commands from the temperature programmer. A temperature programmer is essential in order to obtain constant heating rates. The sample holder assembly consists of a thermocouple each for the sample and reference, surrounded by a block to ensure an even heat distribution. The sample is contained in a small crucible designed with an indentation on the base to ensure a snug fit over the thermocouple bead. The crucible may be made of materials such as Pyrex, silica, nickel or platinum, depending on the temperature and nature of the tests involved.

In the present study the DTA/TG measurements on the various samples were performed from room temperature to 1400 °C in air. Thermal analyses (DTA) of the samples were carried out by a thermal analyzer (Fig. 3.5) (Perkin Elmer, Pyris Diamond) and using alumina as the reference material and heating rate of 10 °C/min in presence of air.
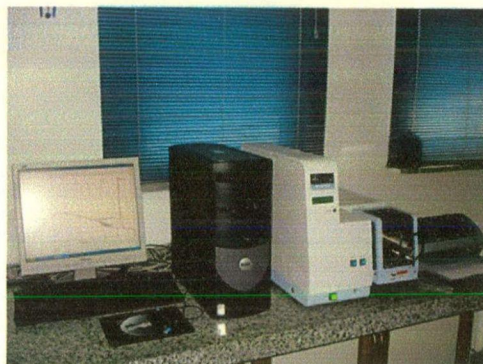
Fig. 3.5: Thermal analyzer (Perkin Elmer)

3.1.2.4 Fourier Transform infrared spectroscopy (FTIR)

In infrared spectroscopy, infrared radiation is passed through a sample. Some of the infrared radiation is absorbed by the sample and some of it passed through (transmitted). The resulting spectrum represents the molecular absorption and transmission, creating a molecular fingerprint of the sample. Like a fingerprint no two unique molecular structures produce the same infrared spectrum. This makes infrared spectroscopy useful for several types of analysis. Each material has an unique combination of atoms, no two compounds produce the exact same infrared spectrum. Infrared spectroscopy can result in a positive identification (qualitative analysis) of every different kind of material. Fourier Transform Infrared (FT-IR) spectrometry was developed in order to overcome the limitations encountered with dispersive instruments. The main difficulty was the slow scanning process. A method for measuring all of the infrared frequencies simultaneously, rather than individually, was needed. A solution was developed which employed a very simple optical device called an interferometer.

Because the analyst requires a frequency spectrum (a plot of the intensity at each individual frequency) in order to make identification, the measured interferogram signal can not be interpreted directly. A means of 'decoding' the individual frequencies is required. This can be accomplished via a well-known mathematical technique called Fourier transformation. This transformation is performed by the computer which then presents the user with the desired spectral information for analysis. Because there needs to be a relative scale for the absorption intensity, a background spectrum must also be measured. This is normally a measurement with no sample in the path of beam. This can be compared to the measurement with the sample in the path of beam to determine the 'percent transmittance'. This technique results in a spectrum which has all of the instrumental characteristics removed. Thus, all spectral features which are present are strictly due to the sample. A single background measurement can be used for many sample measurements because this spectrum is characteristic of the instrument itself.

Samples for FTIR can be prepared in a number of ways. In the present study powder samples were milled with potassium bromide (KBr) to form a very fine powder. Resultant powder

was then compressed into thin pellets, at a load of 10 tons, which were analyzed in a spectrometer. KBr is transparent in the IR. The spectrum was obtained in a range of 400 to 4000 cm^{-1}. Infrared Spectra of the samples were recorded in a Thermonicolet (Anexus) at room temperature on a FTIR 1600 series.

3.1.2.5 Impedance Spectroscopy (IS)

Impedance Spectroscopy (IS) is a very versatile tool to characterize intrinsic electrical properties of any material and its interface. Dynamics of the various mobile ions can be studied satisfactorily using impedance spectroscopic techniques (Dutta and Ghosh, 2005). The basis of IS is the analysis of the impedance of the system under observation when subjected to the applied frequency. IS uses alternating current with low amplitude. The first stage of one impedance investigation includes the performance of the measurement and visualization (graphical presentation) of the results. Every measurement ensures the following three dimensional set of data:

$$D_3 = [\omega, Z', Z''], \tag{1}$$

where ω is the frequency and Z' and Z'' are the real and imaginary parts of the impedance Z:

$$Z(j\omega) = Z' + iZ'' \tag{2}$$

The most commonly applied graphical presentations are the impedance diagram (Nyquist plot), which describes Eqn. (2) in Cartesian coordinates and Bode plot, which uses the following presentation of the impedance in planar coordinates:

$$Z(j\omega) = |Z|\, e^{i\phi}, \tag{3}$$

where $|Z| = (Z'^2 + Z''^2)^{1/2}$ is the modulus and $\phi = \text{Arc cot } Z'/Z''$ is the phase, corresponding to a given frequency. The idealized Nyquist plot of a ceramic oxide specimen consists of three semi-circles. It was found, that the first semicircle corresponds to the bulk properties, the second one to the grain boundaries, while the last one is due to the electrode response. Polycrystalline materials with uniform composition of the grains and grain boundaries show

68

only one bulk and one grain boundary semicircle regardless of the fact whether the grains and grain boundaries are of uniform thickness or not. The semi-circles may overlap and their centers may lie below the horizontal axis. The degree of overlapping depends on the relative time-constants.

In the present study the impedance measurements at room temperature of the samples prepared from calcined powders were made by using impedance analyzer (Agilent 4294A) in the frequency range of 40 Hz to 10 MHz. Each sample was made in the form of cylindrical pellet having 10 mm diameter by taking a known quantity of calcined powder and compacting them with a suitable load. The flat surfaces of these pellets were applied with silver paste followed by baking at ~140°C for electroding.

3.1.2.6 Electrochemical Characterization

In order to check the performance of the material as a battery cathode material, electrochemical measurements were performed. At first the powders were mixed with acetylene black and PVDF in the ratio of 70:15:15 (weight %) respectively.

Fig. 3.6: Glove Box (MBRAUN) maintained at < 0.1 ppm of oxygen and moisture

Preparation of raw cell for testing was done in Argon filled glove box (Fig. 3.6), in which the oxygen and moisture levels were maintained at < 0.1 ppm. A slurry of the powder mixture was made using N-Methylpyrrolidone (NMP) and applied by using a blade onto aluminum foil for coating. The coated foil was dried in a vacuum oven at 120°C for 24 hours. Electrodes of about ~1cm^2 area were cutout from the foil. All these steps were performed in a dry room. A flow chart showing the preparation of the sample electrodes is given in Fig. 3.7. A thin strip of lithium metal was used as reference electrode. Celgard (2400) was used as a separator. 1M $LiPF_6$ dispersed in EC and DEC in 1:1 v/v was used as electrolyte. Electrochemical studies on the materials were performed in a laboratory made cell testing set-up consisting of teflon and stainless steel screw as shown in Fig. 3.8. Electrical contacts were drawn using stainless steel screws. Cells were charged and discharged at a constant current density of 100µA/cm^2 in a voltage range of 4.3 V to 3.0 V. Fig. 3.9 shows the teflon cell and sealed testing jar containing teflon cell placed in a glove box.
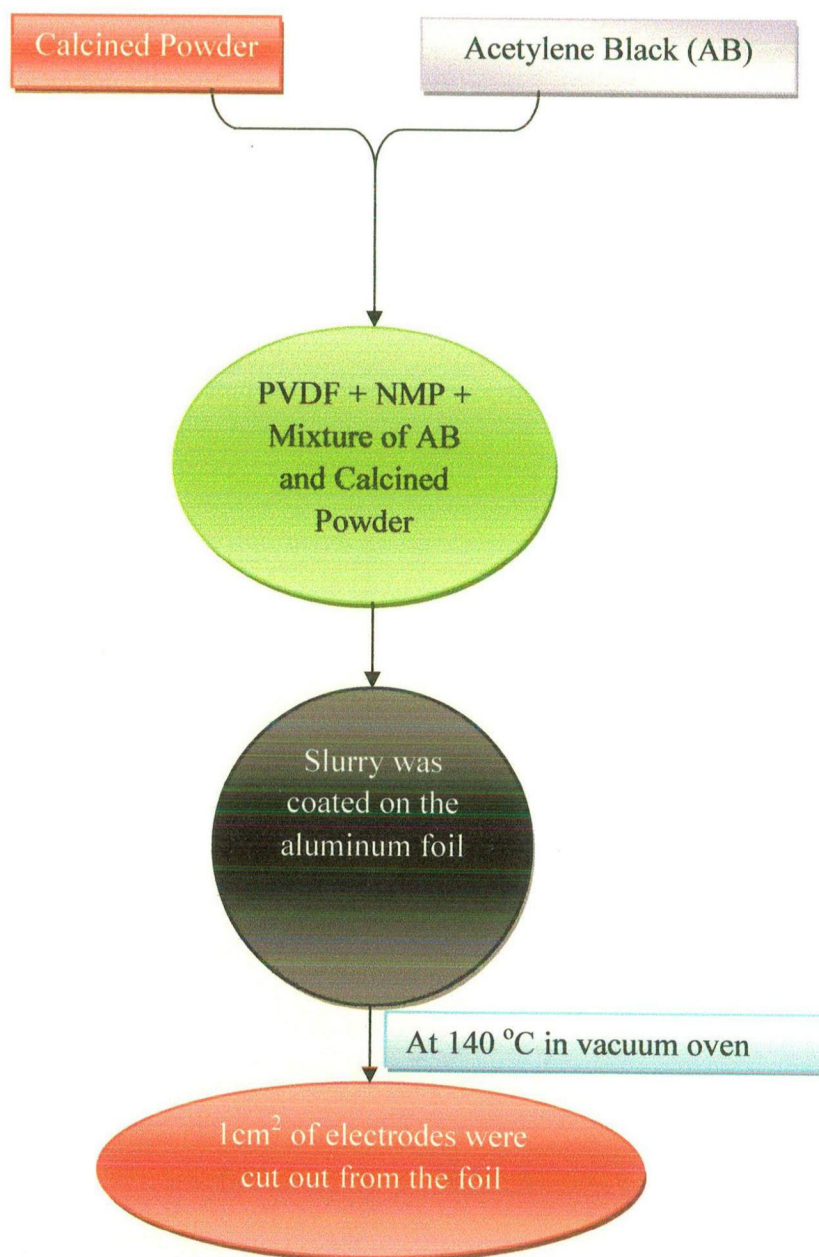
Fig. 3.7: Sample preparation for electrochemical performance measurements
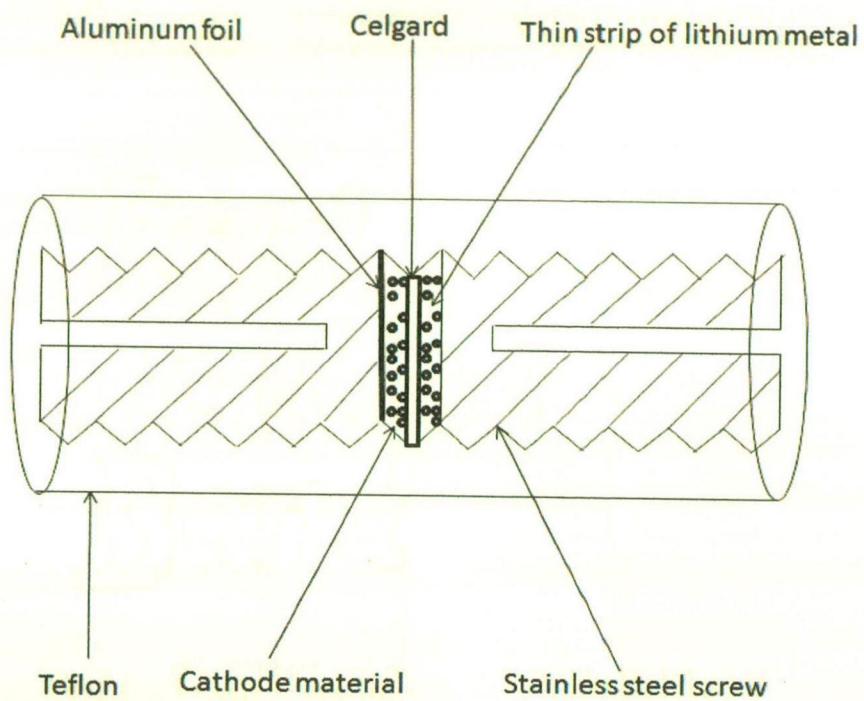
Fig. 3.8: Sketch of raw cell testing arrangement for electrochemical performance
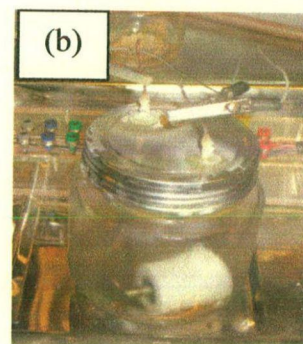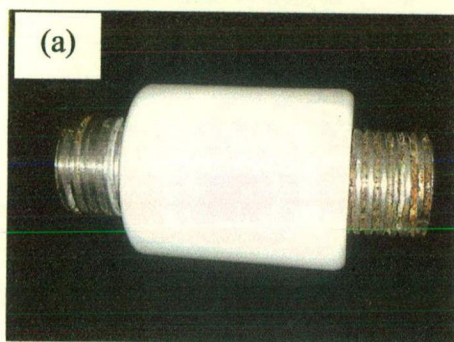
Fig. 3.9: (a) Raw cell (b) Sealed testing jar containing raw cell placed in a Glove Box.

The structure optimization has been done within the DFT (Dreizler and Gross, 1990, Payne et al., 1992) using VASP (*Vienna ab initio simulation package)* (Kresse, 1993, 1996) and the projector augmented wave method (PAW) pseudopotentials (Kresse, 1999). The Kohn-Sham equations (Hohenberg and Kohn, 1964, Kohn and Sham, 1965) were solved using the exchange correlation function of Perdew and Wang (Perdew, 1992) for GGA and GGA+U. A flow chart for calculation of the Kohn-Sham ground state is given in Fig. 3.10.
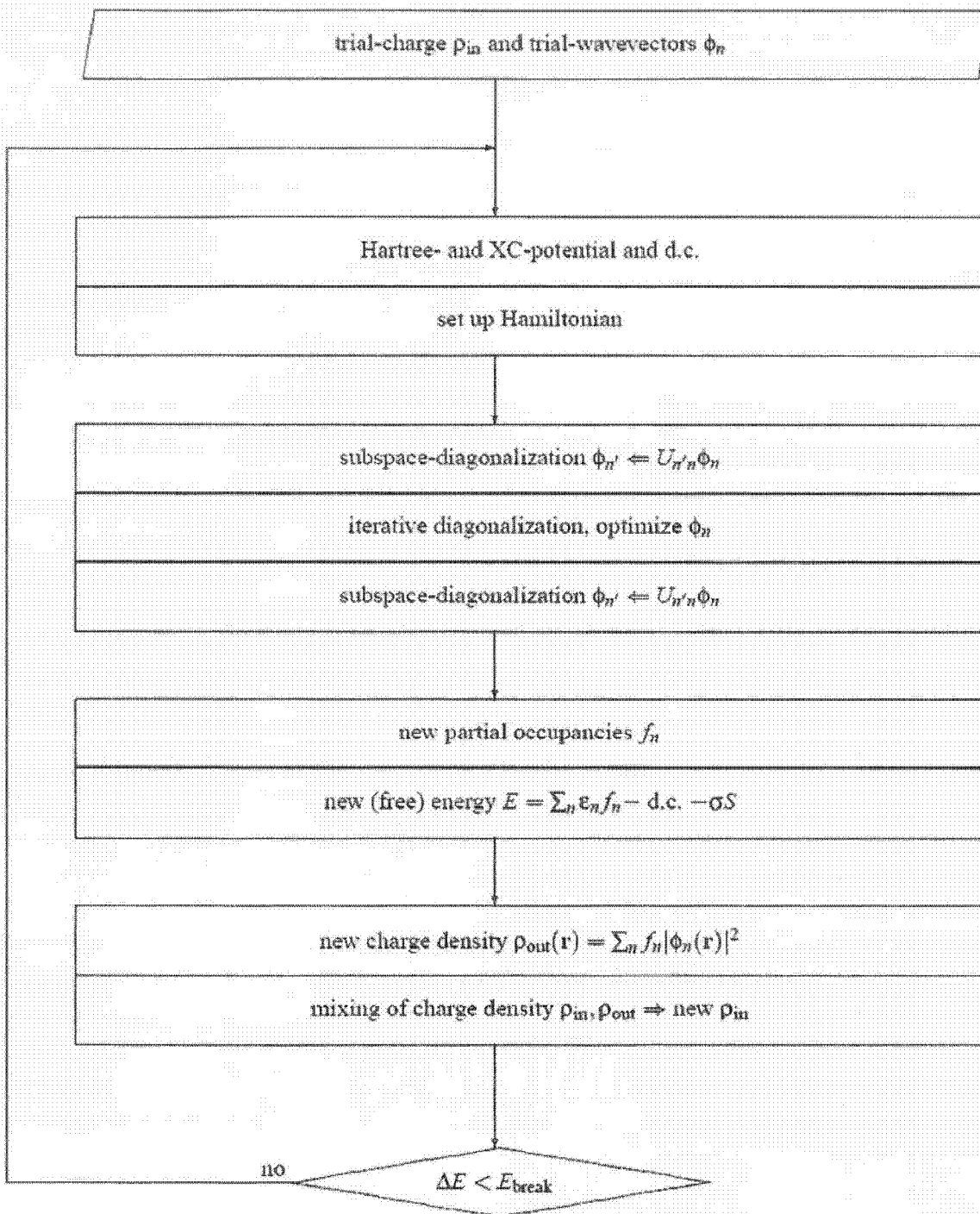
Fig. 3.10: Calculation of Kohn-Sham ground state

3.2.1 Density Functional Theory (DFT)

3.2.1.1 Schrödinger Equation and Early Formulation

Properties of materials such as the index of refraction and its dispersion relation, the bulk modulus and the conductivity are determined by the microscopic behavior of the ions and electrons that constitute the material. The fundamental behavior of atoms, molecules and solids is governed by the laws of quantum mechanics. The use of traditional quantum mechanical methods to understand the rich behavior of many-body systems is, however, rather limited. The Schrödinger Equation describes the quantum state of a physical system. Schrödinger Equation is analytically solvable for a few simple systems and the use of state-of-the-art computers has resulted in numerically exact solutions only for a small number of atoms and molecules. The use of a wavefunction to describe the properties of an N electron system has an intrinsic computational problem. The computational effort to solve the Schrödinger Equation grows exponentially with N. Therefore, the full many-body wavefunction is the correct, though impractical way to describe the behavior of solids and large atoms and molecules.

The first attempt to tackle this problem was made by decoupling the motion of the electrons from each other by describing their interaction within a mean field scheme. This is done in the Hartree-Fock theory. This theory, however, does not include the subtle correlations between particles that are important to understand the behavior of many-body systems. Use of density instead of wavefucntions has been used for the first time by Hohneberg and Kohn. It has been proved that the total energy of a system including that of many body effects of electrons in the presence of static external potential is a unique functional of charge density. Electronic density can be used as the basic variable to describe the ground state properties of the materials. Exact theory has been provided by Kohn and Sham one year later.

The entire formalism given by Hohenberg, Kohn and sham is known as Density Functional Thoery, because electronic density was used as basic variable instead of wavefunctions. Many computational codes are available these days based on the formalism given by them. The calculations are known as ab-initio calculations. First principles calculations or ab-initio

calculations, as implied in its name, are distinguished from empirical methods in requiring only rudimentary information such as nuclear charges, and number of electrons as inputs. For systems with many particles (*i. e.* electrons and nuclei) such as a compound, the Schrodinger equation is intractable. Hence it is necessary to introduce a number of approximations in reaching a solution. Hamiltonian of a molecule is given by

$$H = -\frac{\hbar^2}{2}\sum_i \frac{\nabla_{R_i}^2}{M_i} - \frac{\hbar^2}{2m_e}\sum_j \nabla_{r_j}^2 + \frac{1}{8\pi\varepsilon_0}\sum_{i\neq j}\frac{e^2}{|r_i - r_j|} +$$

$$\frac{1}{8\pi\varepsilon_0}\sum_{i\neq j}\frac{e^2 Z_i Z_j}{|R_i - R_j|} - \frac{1}{4\pi\varepsilon_0}\sum_{i,j}\frac{e^2 Z_i}{|R_i - r_j|} \qquad (3.2.1)$$

where R_i, M_i and Z_i are the ionic positions, masses and atomic numbers. The first two terms represent the kinetic energy of the ions and electrons respectively, the next two terms account for the electron-electron and nucleus-nucleus interactions. The last term represents the interaction between the electrons and the nuclei.

3.2.1.2 Density Functional Theory Approach

The Born-Oppenheimer approximation (Martin, 2004) decouples the electronic motion from the ionic motion. The mass of proton is three orders of magnitude larger than the electron mass. The electrons can be assumed to be always in the ground state of continuously, but relatively slowly varying potential setup by the vibrating nuclei. In this the full wavefunction is the product of ionic and electronic wavefunction. In the Born-Oppenheimer approximation the full wavefunction is a product of electronic and ionic wavefunction.

Mathematically Born-Oppenheimer approximation is given by

$$H_{BO} = -\frac{\hbar^2}{2m_e}\sum_j \nabla_{r_j}^2 + \frac{1}{8\pi\varepsilon_0}\sum_{i\neq j}\frac{e^2}{|r_i - r_j|} + \frac{1}{8\pi\varepsilon_0}\sum_{i\neq j}\frac{e^2 Z_i Z_j}{|R_i - R_j|} - \frac{1}{4\pi\varepsilon_0}\sum_{i,j}\frac{e^2 Z_i}{|R_i - r_j|} \quad (3.2.2)$$

In this Hamiltonian, the ionic positions are parameters instead of variables. Hence the electronic wavefunction depends on the ionic positions parametrically. The dynamics of the

76

ions is treated separately. This is the general way to reduce the full many-body problem to an interacting electron gas, moving in the static external potential V_{ext} setup by the ions.

Hohenberg –Kohn Theorems

These theorems justify the use of electronic density (given as

$$n(r) = N \int dr_2 \ldots\ldots \int dr_N |\psi(r_1 r_2 \ldots\ldots r_N|^2)$$

(3.2.3)

as the basic variable instead of wavefunction to describe the system. It has also been shown that V_{ext} completely determine all the properties of the electronic system.

The Hohenberg-Kohn theorems can be stated as:

1. The external potential and hence the total energy E[n], is a unique functional of the electron density n(r).

2. The ground state energy can be obtained variationally; the density that minimizes the total energy is the exact ground state density.

By using the electron density instead of the electron wavefunctions the number of variables can be reduced from 3N to N.

The ground state energy is represented as

$$E[n] = F[n] + \int n(r)V_{ext}(r)dr$$

(3.2.4)

with

$$F[n] \equiv \underset{\psi \longrightarrow n(r)}{Min} \left\langle \psi | T + V_{ee} | \psi \right\rangle$$

(3.2.5)

where $T = -\dfrac{\hbar^2}{2m_e} \sum_i \nabla_j^2$ and

$F[n]$ is a universal functional and $V_{ext}(r)$ is the Coulomb potential due to the nuclei of the system. According to DFT, if the universal functional $F[n]$ were known, the ground state

energy of the system with external potential $V_{ext}(r)$ is obtained by variationally minimizing the functional $E[n]$ with respect to n using the electron density as the variational quantity. The main issues with the Hohenberg –Kohn theorem is that we can not know the density n(r) without first finding the many body wave functions.

The Kohn-Sham equations provide a procedure for solving the many body problem using the density as basic variable. Exchange and correlation effects play an important role in this formalism. Exchange effects are a consequence of the exchange symmetry between interacting identical fermions. The Coulomb interaction couples the electrons. All the effects arising form this coupling are known as correlation effects. Figure 3.11 shows the schematic representation of Kohn-Sham Theorem
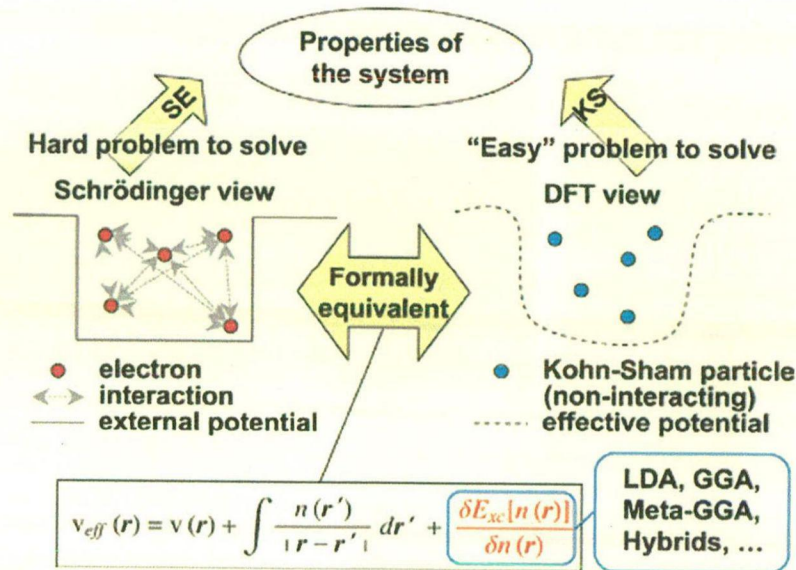
Fig. 3.11: Schematic Representation of Kohn and Sham Theorem

The electron-electron interaction using the mean field scheme is given by

$$E_{ee}^{MFT}[n] = \frac{e^2}{8\pi\varepsilon_0} \iint \frac{n(r)n(r')}{|r-r'|} dr dr'$$

(3.2.6)

This is known as Hartree integral and describes the mean field Coulomb interaction of electron energy density with itself. Instead of calculating the kinetic energy of the interacting

78

system, we calculate the kinetic energy $T_0[n]$ of a non-interacting reference system with a ground state density distribution equal to $n(r)$.

Energy functional

$$E[n] = F[n] + \int n(r)V_{ext}(r)dr \tag{3.2.7}$$

can be written in the form that separates all contributions from exchange and correlation effects from the other terms.

$$E_{KS}[n] = \int dr V_{ext} n(r) + T_0[n] + \frac{e^2}{8\pi\varepsilon_0} \iint \frac{n(r)n(r')}{|r-r'|} dr dr' + E_{xc}[n] \tag{3.2.8}$$

$E_{xc}[n]$ contains the contribution of all exchange and correlation effects. Extremum of the energy functional should be known under the constraint

$$N = \int n(r)dr \tag{3.2.9}$$

We can do it by using Lagrange multiplier μ and it can be given as

$$\delta\left(E_{KS}[n] + \mu(N - \int n(r)dr\right) = 0 \tag{3.2.10}$$

This leads to

$$\frac{\delta T_0[n]}{\delta n} + V_{ext} + \frac{1}{2}\iint \frac{n(r)}{|r-r'|}dr + \frac{\delta E_{xc}[n]}{\delta n} - \mu = 0 \tag{3.2.11}$$

Schrödinger equation for the non-interacting system is given as

$$\left[-\frac{\hbar^2}{2m}\nabla_i^2 + v_i\right]\phi_i = \varepsilon_i\phi_i \tag{3.2.12}$$

where v_i are chosen such that the density equals $n(r)$. The variational form of this equation is given as

$$\frac{\delta T_0[n]}{\delta n} + v_i - \mu = 0 \tag{3.2.13}$$

Problem in eqn. (3.2.11) is mathematically equivalent to this problem provided that

79

$$v_i = V_{ext} + \frac{1}{2} \iint \frac{n(r)}{|r - r'|} dr + \frac{\delta E_{xc}[n]}{\delta n} \qquad (3.2.14)$$

Hence, equation (3.2.11) can be written as

$$\left[\frac{\hbar^2}{2m} \nabla_i^2 + V_{ext} + \frac{1}{2} \iint \frac{n(r)}{|r - r'|} dr + \frac{\delta E_{xc}[n]}{\delta n} \right] \phi_i = \varepsilon_i \phi_i \qquad (3.2.15)$$

This is Kohn-Sham equation.

The Kohn-Sham scheme basically maps the N-interacting electron problem into fictitious particles moving in an effective potential. One of the most common approximations to $E_{xc}[n]$ is the local density approximation (LDA) suggested by Kohn and Sham. Within LDA, $E_{xc}[n]$ is written as

$$E_{xc}[n] = \int n(r) c_{xc}(n) dr \qquad (3.2.16)$$

where c_{xc} is the exchange-correlation energy per electron for a uniform electron gas. LDA, therefore, assumes c_{xc} is local. Purdue and Yue developed the generalized gradient approximation (GGA) to address problem of the LDA by incorporating polynomial terms with the modulus of the electron density gradient. No strict guidelines exist as to when GGA is better than LDA, or vice-versa. In this work GGA is chosen as it typically does better reproducing spin polarization on transition metal ions in oxides. Among many numerical programs for solving the Kohn-Sham equations, VASP (Vienna Ab intio Simulation Package) has been used that solves the Kohn-Sham equations iteratively for valence orbitals using Projector Augmented Wave (PAW) potentials

3.2.1.3 Exchange, Correlation and Local Density Approximation

In Local density approximation (LDA), the exchange-correlation energy of an electronic system is constructed by assuming that the exchange-correlation energy per electron at a

point r in the electron gas $C_{xc}(r)$ is equal to the exchange-correlation energy per electron in a homogeneous electron gas that has the same electron density at the point r. It follows that

$$E_{xc}[n(r)] = \int c_{xc}(n(r))n(r)dr \qquad\qquad 3.2.17$$

So that

$$\mu_{xc}(r) = \frac{\delta[n(r)c_{xc}(n(r))]}{\delta(n(r))} \qquad\qquad 3.2.18$$

with

$$c_{xc}(n(r)) = c_{xc}^{hom}(n(r)) \qquad\qquad 3.2.19$$

This parameterization is based on the quantum Monte Carlo calculations of Ceperley and Alder on homogeneous electron gases at various densities. The parameterization uses interpolation formulas to link these exact results for the exchange and correlation energy at many different densities.

A summary of the contributions of electron-electron interactions in N-electron systems is shown in the figure. It illustrates the conditional electron probability distributions n(r) of N-1 electrons around an electron with given spin situated at r = 0. In the Hartree approximation, Figure 3.12 (a), all electrons are treated as independent; therefore n(r) is structure less. Figure (b) represents the Hartree-Fock approximation where the N-electron wave function reflects the Pauli's Exclusion Principle. Around the electron at r = 0 the exchange hole can be seen where the density of spins equal to that of the central electron is reduced. Electrons with opposite spins are unaffected. In the LDA, where spin states are degenerate, each type of electron sees the same exchange-correlation hole. Figure 3.12 (d) shows electron-electron interaction for non-degenerate spin systems. It can be seen that the spin degenerate LDA is simply the average of the local spin density (LSD).
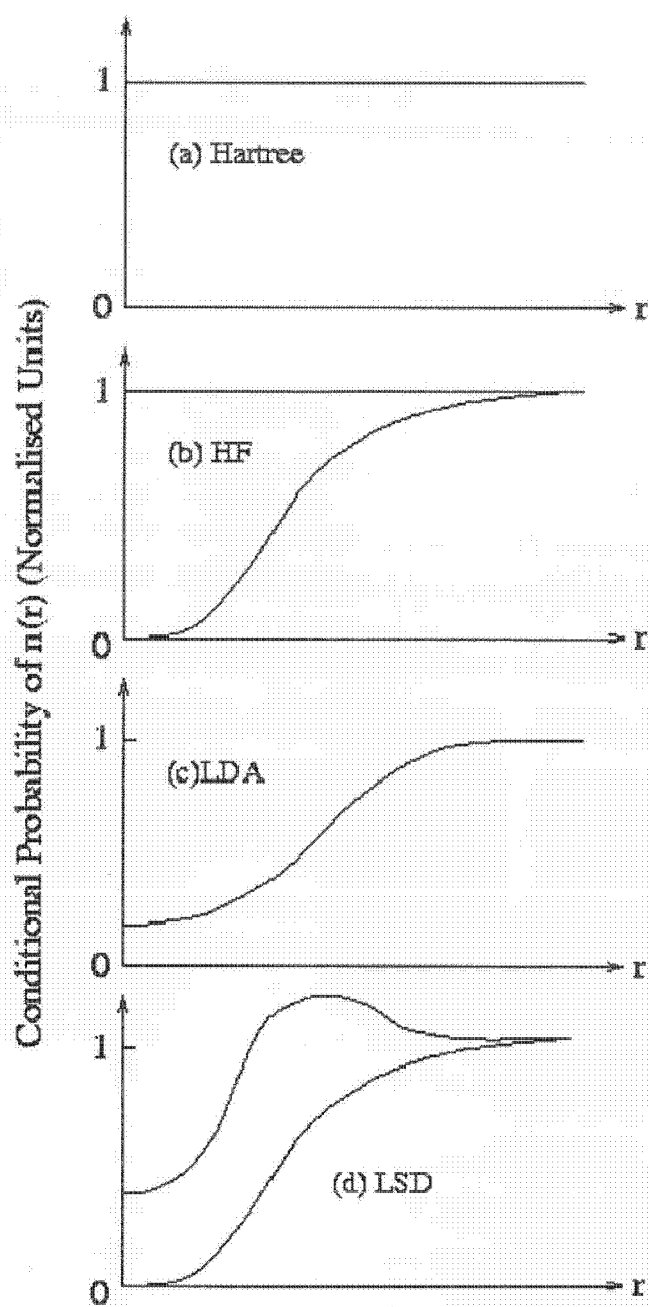
Figure 3.12: Summary of the electron-electron interactions (excluding coulomb effects) in (a) the Hartree approximation, (b) the Hartree-Fock approximation, (c) the local density approximation and (d) the local spin density approximation which allows for different interactions for like-unlike spins.

3.2.1.4 Bloch's Theorem and Plane Wave Basis Sets

This section shows how to handle the infinite number of interacting electron moving in the static field of an infinite number of ions. Essentially, there are two difficulties to overcome: a wave function has to be calculated for each of the infinite number of electrons which will extend over the entire space of the solid and the basis set in which the wave function will be expressed will be infinite.

The ions in a perfect crystal are arranged in a regular periodic way (at 0K). Therefore the external potential felt by the electrons will also be periodic - the period being the same as the length of the unit cell "l". That is, the external potential of an electron at r can be expressed as $V(r) = V(r + 1)$. This is the requirement needed for the use of Bloch's theorem. By the use of this theorem, it is possible to express the wave function of the infinite crystal system in terms of wave functions at reciprocal space vectors of a Bravais lattice.

Bloch's theorem uses the periodicity of a crystal to reduce the infinite number of one-electron wave functions to be calculated to the number of electrons in the unit cell of the crystal. The wave function is written as the product of a cell periodic part and a wavelike part:

$$\varphi_i(r) = \exp(ik.r) f_i(r) \qquad\qquad 3.2.20$$

The first term is the wavelike part; the second term is the cell periodic part of the wave function. This can be expressed by expanding it into a finite number of plane waves whose wave vectors are reciprocal lattice vectors of the crystal

$$f_i(r) = \sum_G c_i G \exp(ik.r) \qquad\qquad 3.2.21$$

Where G are the reciprocal lattice vectors which are defined by G.l=2πm for all l, where l is a lattice vector of the crystal and *m* is an integer. Therefore each electronic wave function is written as a sum of plane waves

$$\varphi_i(r) = \sum_G c_i k + G \exp\{(i(k+G).r)\} \qquad\qquad 3.2.22$$

By the use of Bloch's theorem, the problem of the infinite number of electrons has now been mapped onto the problem of expressing the wave function in terms of an infinite number of reciprocal space vectors within the first Brillion zone of the periodic cell, k. This problem is dealt with by sampling the Brillion zone at special sets of k-points.

The electronic wave functions at each k-point are now expressed in terms of a discrete plane wave basis set. In principle this Fourier series is infinite. However, the coefficients for the plane waves, $c_{i,k+G}$ each have a kinetic energy $(h^2/2m)|k + G|^2$. The plane waves with a smaller kinetic energy typically have a more important role than those with a very high kinetic energy. The introduction of a plane wave energy cutoff reduces the basis set to a finite size.

Another advantage of expanding the electronic wave functions in terms of a basis set of plane waves is that the Kohn-Sham equations take a particularly simple form.

3.2.1.5 Discretisation of k-space and the Brillouin Zone

The Brillouin zone is the region in the reciprocal space where all the eigenstate of the Hamiltonian may be labeled uniquely along k within any $2\pi/a$ range, 'a' is the size of the lattice. The first Brillouin zone is the one closest to the origin i.e. $(-\pi/a \leq k \leq \pi/a)$. We calculate all eigenstates within this region. Fortunately the wave functions and eigenvalues of the Hamiltonian vary smoothly over the brillouin zone so in practice only a limited set of points has to be evaluated. There exist techniques, of how to find which points in the reciprocal space that contribute the most and by that knowledge apply a selective sampling of the k-space. This sampling is done over the first Brillouin zone and when the volume of the super cell V_{SC} is increasing the volume of the Brillouin zone V_{BZ} decreasing according to the formula;

$$V_{BZ} = (2\pi)^3/V_{SC}$$

Thus for larger systems fewer sampling points, so called k-points, are needed to describe the Brillouin zone accurately. The point where $k = 0$ is known as the gamma point, at this point the wave functions can be chosen to be real, thus selecting this point as a sampling point

simplify and speed up calculations. Of course there are other points where the expansion becomes real since e^{ikr} is a periodic function. These points are called high symmetry points, where the gamma point is a special case. Unfortunately the best sampling points are seldom one of these.

Methods have been devised for obtaining very accurate approximations to the electronic potential from a filled electronic band by calculating the electronic wave functions at special sets of k-points. The two most common methods are those of Chadi and Cohen (Chadi and Cohen, 1973) and Monkhorst and Pack (Monkhorst and Pack, 1976).
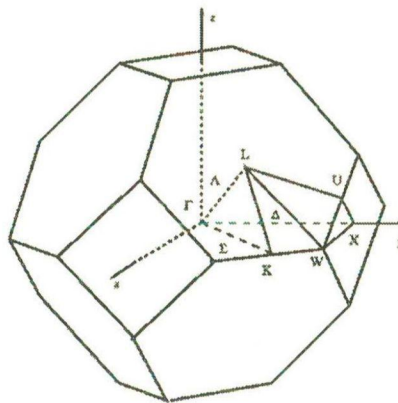
Figure 3.13 First Brillouin zone of FCC lattice showing symmetry labels for high symmetry lines and points

Symbol Description

Γ Center of the Brillouin zone

Simple cube

M Center of an edge

R Corner point

X Center of a face

Face-centered cubic

K Middle of an edge joining two hexagonal faces

L Center of a hexagonal face

U Middle of an edge joining a hexagonal and a square face

W Corner point

X Center of a square face

Body-centered cubic

H Corner point joining four edges

N Center of a face

P Corner point joining three edges

Hexagonal

A Center of a hexagonal face

H Corner point

K Middle of an edge joining two rectangular faces

L Middle of an edge joining a hexagonal and a rectangular face

M Center of a rectangular face

3.2.2 VASP

3.2.2.1 Introduction

VASP (Furthmuller et al., 1994, Kern et al., 1999, VASP the Guide, 2009) is a complex package for performing ab-initio quantum-mechanical molecular dynamics (MD) simulations using pseudopotentials or the projector-augmented wave method and a plane wave basis set. The approach implemented in VASP is based on the (finite temperature) local-density approximation with the free energy as variational quantity and an exact evaluation of the instantaneous electronic ground state at each MD time step. VASP uses effcient matrix digitalization schemes and an efficient Pulay/Broyden charge density mixing. These techniques avoid all problems possibly oc curring in the original Car-Parrinello method, which is based on the simultaneous integration of electronic and ionic equations of motion. The interaction between ions and electrons is described by ultra-soft Vanderbilt pseudopotentials (US-PP) (Vanderbilt, 1985) or by the projector-augmented wave (PAW) method. US-PP (and the PAW method) allow for a considerable reduction of the number of plane-waves per atom for transition metals and first row elements. Forces and the full stress tensor can be calculated with VASP and used to relax atoms into their instantaneous ground-state.

Here is a short summary of some highlights of the VASP code:

• VASP uses the PAW method or ultra-soft pseudopotentials. Therefore the size of the basis-set can be kept very small even for transition metals and first row elements like C and O. Generally not more than 100 plane waves (PW) per atom are required to describe bulk materials, in most cases even 50 PW per atom will be sufficient for a reliable description.

• In any plane wave program, the execution time scales like N^3 for some parts of the code, where N is the number of valence electrons in the system. In the VASP, the pre-factors for the cubic parts are almost negligible leading to an efficient scaling with respect to system size. This is possible by evaluating the non local contributions to the potentials in real space and by keeping the number of orthogonalisations small. For systems with roughly 2000 electronic bands, the N^3 part becomes comparable to other parts. Thus it is expected that VASP is useful for systems with up to 4000 valence electrons.

• VASP includes a full featured symmetry code which determines the symmetry of arbitrary configurations automatically.

• The symmetry code is also used to set up the Monkhorst Pack special points allowing an efficient calculation of bulk materials, symmetric clusters. The integration of the band structure energy over the Brillouin zone is performed with smearing or tetrahedron methods.

3.2.2.2 Algorithm Used in VASP to Calculate the Electronic Ground State

Most of the algorithms implemented in VASP use an iterative matrix-diagonalization scheme: the used algorithms are based on the conjugate gradient scheme (Teter, 1989), block Davidson scheme (Davidson, 1983, Liu, 1978), or a residual minimization scheme - direct inversion in the iterative subspace (RMM-DIIS) (Pulay, 1980). For the mixing of the charge density an efficient Broyden / Pulay mixing scheme (Pulay, 1980, Blugel, 1988, Johnson, 1988) is used. Input charge density and wavefunctions are independent quantities. Within each selfconsistency loop the charge density is used to set up the Hamiltonian, and then the wavefunctions are optimized iteratively so that they get closer to the exact wavefunctions of this Hamiltonian. From the optimized wavefunctions a new charge density is calculated, which is then mixed with the old input-charge density.

3.2.2.3 The Pseudopotential Approximation

A plane wave basis set is usually very poorly suited to expanding the electronic wave functions because a very large number are required to accurately describe the rapidly oscillating wave functions of electrons in the core region. It is well known that most physical properties of solids are dependent on the valence electrons to a much greater degree than that of the tightly bound core electrons. It is for this reason that the pseudo potential approximation is introduced. This approximation uses this fact to remove the core electrons and the strong nuclear potential and replace them with a weaker pseudo potential which acts on a set of pseudo wave functions rather than the true valence wave functions. In fact, the pseudopotential can be optimized so that, in practice, it is even weaker than the frozen core potential (Lin et al., 1993).

The schematic diagram in the Fig. 3.14 below shows these quantities. The valence wave functions oscillate rapidly in the region occupied by the core electrons because of the strong ionic potential. These oscillations maintain the orthogonality between the core and valence electrons. The pseudopotential is constructed in such a way that there are no radial nodes in the pseudo wave function in the core region and that the pseudo wave functions and pseudopotential are identical to the all electron wave function and potential outside a radius cut-off r_c. This condition has to be carefully checked for as it is possible for the pseudo potential to introduce new nonphysical states (so called *ghost states*) into the calculation.

The pseudopotential is also constructed such that the scattering properties of the pseudo wavefunctions are identical to the scattering properties of the ion and core electrons. In general, this will be different for each angular momentum component of the valence wavefunction; therefore the pseudopotential will be angular momentum dependent. Pseudopotentials with angular momentum dependence are called non-local pseudopotentials. The usual methods of pseudopotential generation firstly determine the all electron eigenvalues of an atom using the Schrödinger equation

$$\left\{ -\frac{\hbar^2}{2m} \nabla^2 + V \right\} \psi_{AEl} = c_l \psi_{AEl}$$

where ψ_{AE} is the wave function for the all electron (AE) atomic system with angular momentum component l. The resulting valence eigenvalues are substituted back into the Schrödinger equation but with the parameterized pseudo wavefunction of the form $\psi_{psl} = \sum_{i=1}^{n} \alpha_i j_l$. The pseudopotential is then constructed by directly inverting the Kohn-Sham equation with the p seudo wav e function, ψ_{psl}. I llustration of the full all-electronic (AE) wavefunction and electronic potential (solid lines) plotted against distance, r, from the atomic nucleus is given in Fig. 3.14.
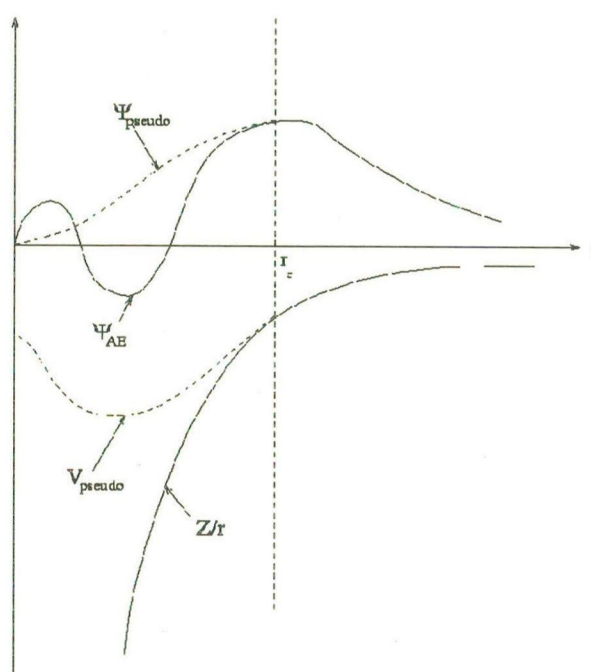
Figure 3.14: An illustration of the full all-electronic (AE) wavefunction and electronic potential (solid lines) plotted against distance, r, from the atomic nucleus. The corresponding pseudo wavefunction and potential is plotted (dashed lines).

The set of plane waves, $\{\exp((k + G).r)\}$, forms a complete basis set (assuming a high enough cutoff) and the additional core states to which they are orthogonal results in a linearly dependent spanning set, that is, an over complete basis set. This linear dependence leads to non-unique pseudo potentials.

A pseudo potential is not unique, therefore several methods of generation also exist. However they must obey several criteria. These are:

1. The core charge produced by the pseudo wave functions must be the same as that produced by the atomic wave functions. This ensures that the pseudo atom produces the same scattering properties as the ionic core.

2. Pseudo-electron eigenvalues must be the same as the valence eigenvalues obtained from the atomic wave functions.

3. Pseudo wave functions must be continuous at the core radius as well as its first and second derivative and also be non-oscillatory.

4. On inversion of the all electron Schrödinger equation for the atom, excited states may also be included in the calculation

Local density approximation fails to describe the systems with d or f electrons. Therefore by introducing a strong intraatomic interaction in a (screened) Hartree-Fock like manner can solve the problem. This approach is known as LDA+U, where U is known as effective onsite Coulomb interaction parameter or Hubbard parameter. In the present study Hubbard parameter (U) was chosen 4.5 eV and 5.0 eV for chromium and manganese respectively as proposed by Wang et al., 2006. The exchange energy is fixed at 1eV. The automatic Monkhorst-Pack scheme (Monkhorst et al., 1976) has been used for the generation of k-points (8x8x8). For optimizing the structure, a conjugate gradient algorithm (CGA) (Press, 1986) has been used. The tetrahedron method with Blöch l corrections (Blochl, 1994) has been used for k integrations to determine the total energy. All the calculations have been done at 0 °K. The plane wave cutoff was set at 550 eV to ensure the good convergence of stress tensor during cell-parameter relaxation. All the structures were fully relaxed.

The conventional unit cell of $LiMn_2O_4$ has 56 atoms. To speed up the calculations a primitive unit cell with 2 formula units having 14 atoms has been used. The primitive unit cell has been chosen using the lattice vectors as

$$\vec{a}' = -\vec{a} + \vec{b} + \vec{c}$$

$$\vec{b}' = \vec{a} - \vec{b} + \vec{c}$$

$$\vec{c}' = \vec{a} + \vec{b} - \vec{c}$$

This transformation modifies the fractional co-ordinates. This transformation results from the fact that the arrangement of ions remains invariant in the Cartesian co-ordinate system as given by,

$$x\vec{a} + y\vec{b} + z\vec{c} = x\vec{a}' + y\vec{b}' + z\vec{c}'$$

The structure on which the calculations were performed is shown in Fig 3.15.
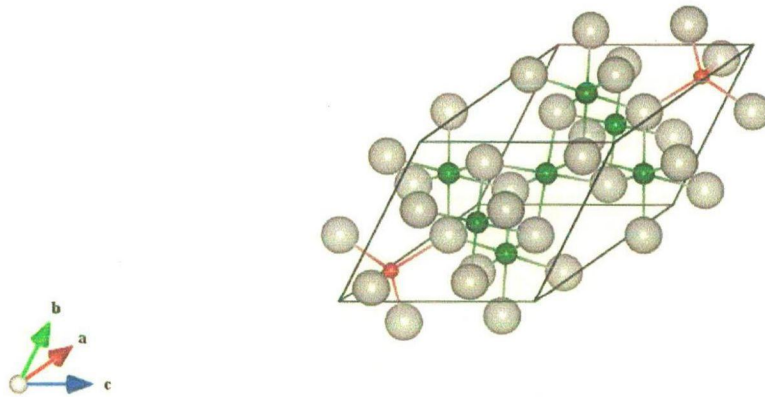
Fig. 3.15: Primitive cell of LiMn$_2$O$_4$ considered for calculations.

The optimized relaxed structures were obtained by repeated sequential relaxing of the volume, the ion positions and the shape of the primitive unit cell. The primitive cell for LiMn$_2$O$_4$ contains two lithium, four manganese and eight oxygen atoms. Lithium atoms occupy the 8a tetrahedral sites (0.125, 0.125, 0.125) and manganese atoms occupy the 16d octahedral sites (0.5, 0.5, 0.5) while the oxygen atoms form a cage and occupy the 32e sites (x, x, x). The four manganese atoms can be distinguished by their positions: Mn(I) (0.5, 0.5, 0.5); Mn(II) (0.5, 0.0, 0.5); Mn(III) (0.0, 0.5, 0.5); Mn(IV) (0.5, 0.5, 0.0). The starting lattice parameters and the oxygen positions have been used as reported in the experimental study (Akimoto et al., 2001). It was found that Mn (I) and Mn(IV) lie in the (110) plane while Mn(II) and Mn(III) lie in the (220) plane. The calculations have been made on the

91

ferromagnetic and anti-ferromagnetic ordering of various manganese atoms to ascertain the ground state. GGA calculations shows ferromagnetic ordering is more stable than anti-ferromagnetic ordering and the energy difference between these orderings is 0.26eV. This is not in agreement with the experimental studies. Further, each manganese atom interacts with its nearest manganese via 90° interactions intermediated by oxygen atoms. The Goodenough – Kanamori rules (Goodenough, 1963) suggest that the interaction should be anti-ferromagnetic (AFM). (Ouyang et al., 2009) have shown that GGA+U is necessary to obtain the AFM ground state. Therefore, spin polarization calculations have been performed for the AFM ordering of the manganese atoms. It was found that the total energy of the system remains almost same (within 1meV) in all the AFM configurations irrespective of the direction of spin assigned to the manganese atoms for pristine $LiMn_2O_4$. So, out of the four manganese atoms one can assign any two manganese atoms as spin-up and the other two as spin-down. In the doped compounds chromium and magnesium were placed at the octahedral sites, which were earlier occupied by manganese atoms. The site preference of the dopants was checked by placing them at various possible sites. It was observed that total energy of the system remains roughly the same (within a tolerance of 40 meV) in the various configurations. The minimum doping concentration for a 14 atoms cell is $x = 0.5$. The compositions were taken as $LiM_xMn_{2-x}O_4$ ($x = 0.5$, 1.0 and M = Cr, Mg). Experimentally, it has been shown that doping is beneficial for lithium ion battery up to a limited extent of dopants (Sigala et al., 2001) and therefore, the calculations have been limited to $x = 1.0$. $LiCr_2O_4$ is a hypothetical oxide, no experimental data is available for this compound even though some theoretical calculations are reported in the literature (Lauer et al., 2004). Calculations have been performed for the following compounds:

(i) $LiMn_2O_4$; (ii) $LiCr_{0.5}Mn_{1.5}O_4$; (iii) $LiCrMnO_4$; (iv) $LiMg_{0.5}Mn_{1.5}O_4$; (v) $LiMgMnO_4$

Results and Discussion: Experimental

4.1.1 Phase Analysis

The material L iMn$_2$O$_4$ after synthesis was characterized using X-ray diffraction (XRD). Phase analysis of the XRD pattern was performed using X'pert High score plus software. XRD pattern of the powdered sample is given in Fig. 4.1.1.
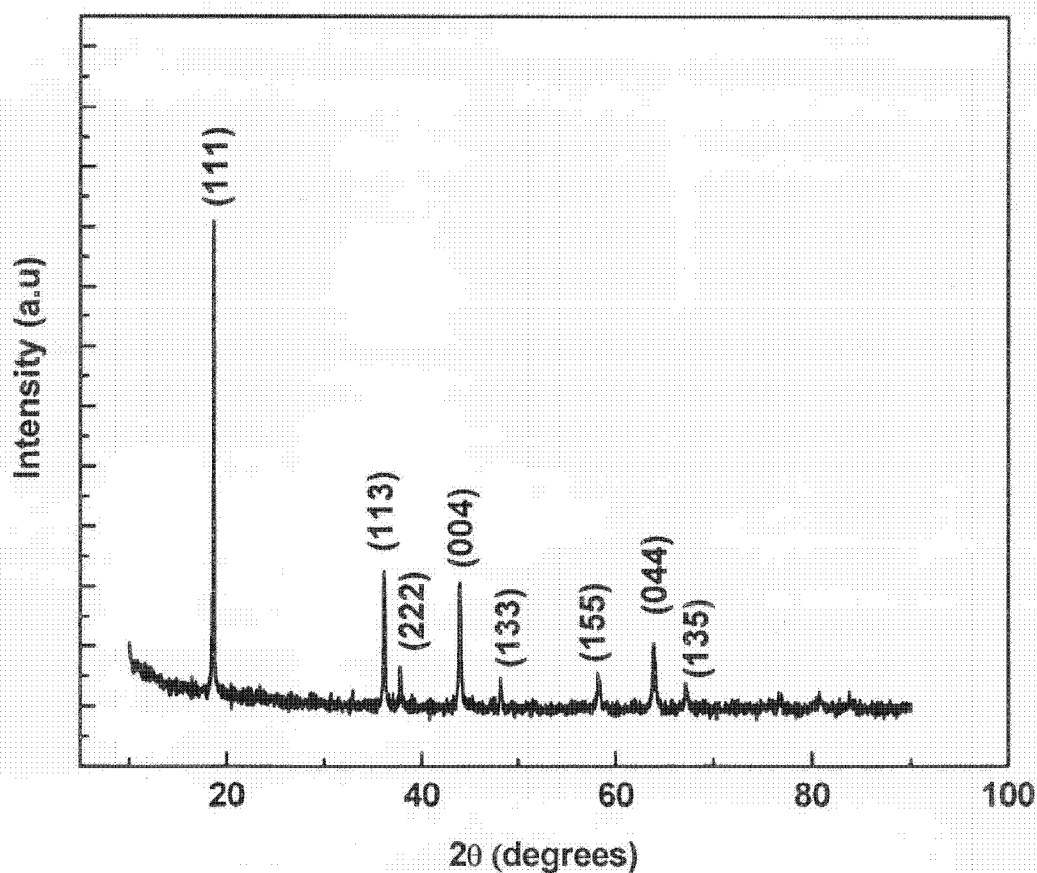
Fig. 4.1.1: X-ray diffraction of the powdered sample of LiMn$_2$O$_4$

95

All the peaks can be indexed to single phase cubic spinel $LiMn_2O_4$ having space group of *Fd3m*. For the determination of the atomic positions in the structure, Rietveld refinement method was used. The refined XRD pattern of $LiMn_2O_4$ is shown in Fig. 4.1.2. The model used for the refinement considers the lithium ions occupying 8a tetrahedral sites, manganese ions on 16d octahedral sites and oxygen ions forming the cage by occupying 32e sites.
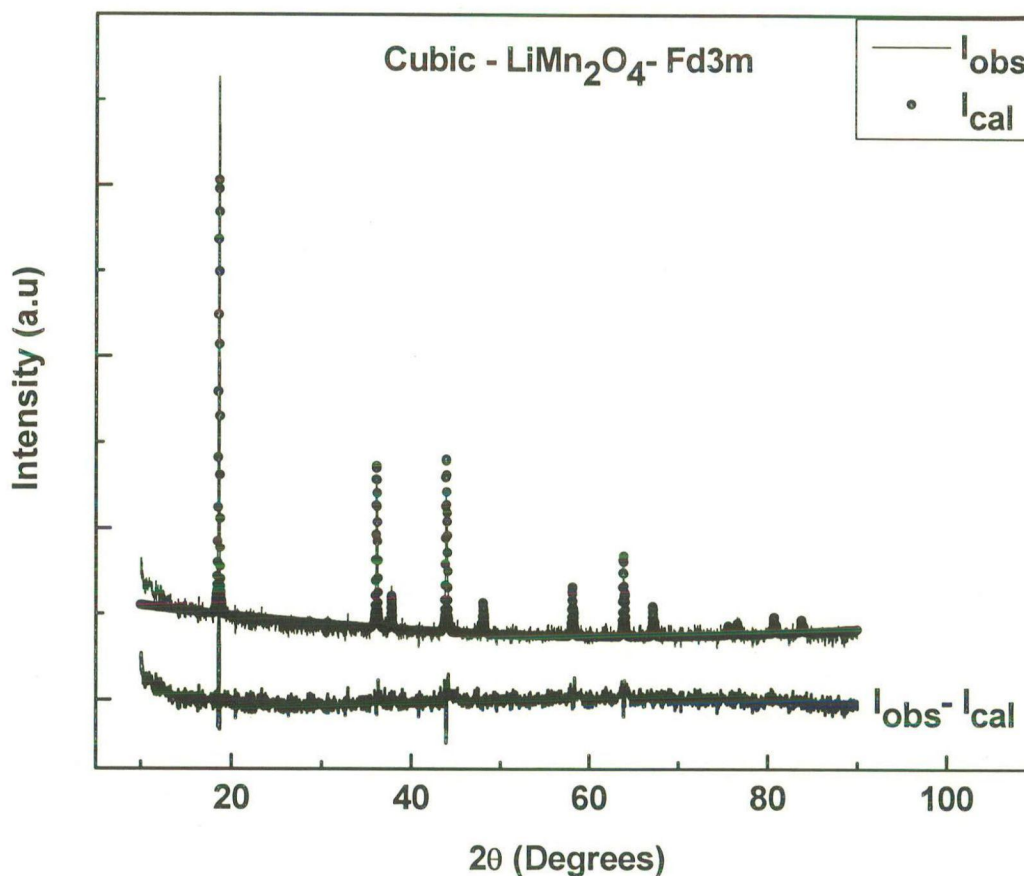
Fig. 4.1.2: Rietveld refined XRD pattern of $LiMn_2O_4$

The atomic positions and the site occupancy values of the different ions were refined to obtain the good refinement parameter values. Results of the various refined values and atomic positions are given in Tables 4.1.1 and 4.1.2 respectively.

Table 4.1.1: Various parameter values after Rietveld refinement

System studied	Lattice parameter (Å)	$R_p(\%)$	$R_{wp}(\%)$	$R_{exp}(\%)$	GOF (Goodness of Fit)
$LiMn_2O_4$	8.2369	6.12	7.83	6.77	1.33

Table 4.1.2: Atomic positions of various elements present in the structure

Atom	Wyckoff Positions	Site Occupancy Factor	x	y	z
Li	8a	1.000	0.125000	0.125000	0.125000
Mn	16d	1.000	0.500000	0.500000	0.500000
O	32e	1.000	0.261000	0.261000	0.261000

4.1.2 Morphological studies

Morphology of the particles obtained after calcination has been observed using field emission scanning electron microscope (FESEM). Micrographs of the powdered sample at lower magnification are shown in Fig. 4.1.3 (a) and (b). From the micrographs it can be observed that particles in the powder are in the state of high agglomeration whose size ranges between 5 and 10 μm. Agglomeration can be explained on the basis of the fact that primary particles tend to agglomerate in order to minimize their surface energy and the reaction after the decomposition proceeds via atomic diffusion.

(a)

| 10 µm | Mag = 4.49 K X | EHT = 5.00 kV | Signal A = InLens | Date :14 Sep 2007 |
| WD = 5 mm | Gun Vacuum = 1.67e-009 mBar | Time :15:18:38 |

(b)

| 1 µm | Mag = 26.00 K X | EHT = 5.00 kV | Signal A = InLens | Date :14 Sep 2007 |
| WD = 5 mm | Gun Vacuum = 1.66e-009 mBar | Time :15:20:12 |

98

200 nm Mag = 118.94 K X EHT = 5.00 kV Signal A = InLens Date :14 Sep 2007
WD = 5 mm Gun Vacuum = 1.63e-009 mBar Time :16:14:17
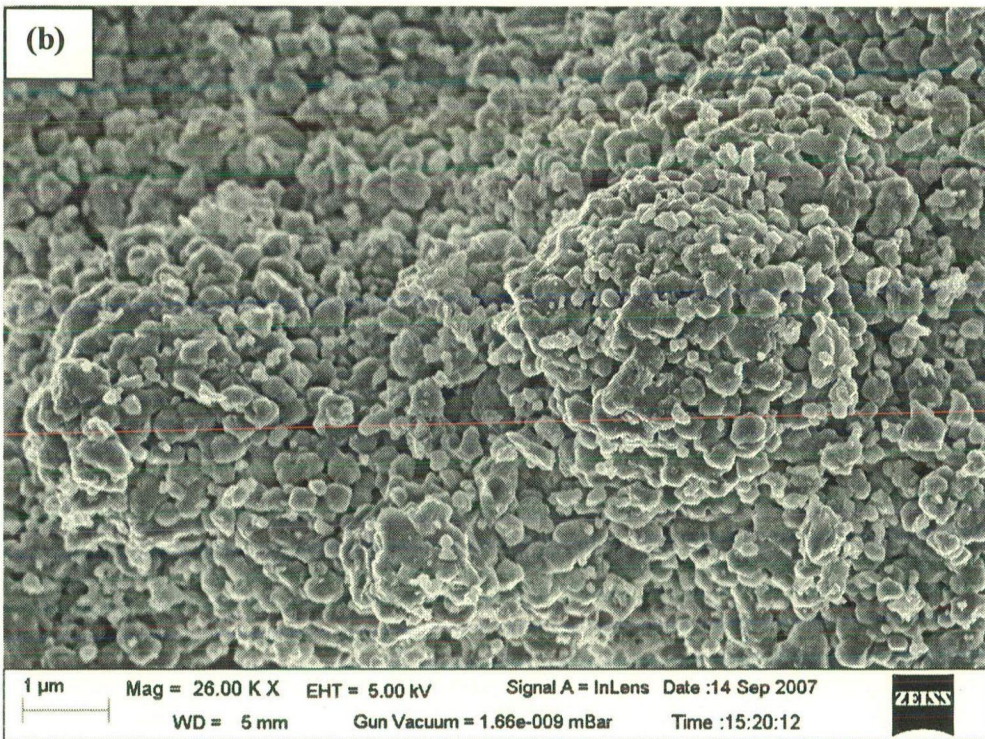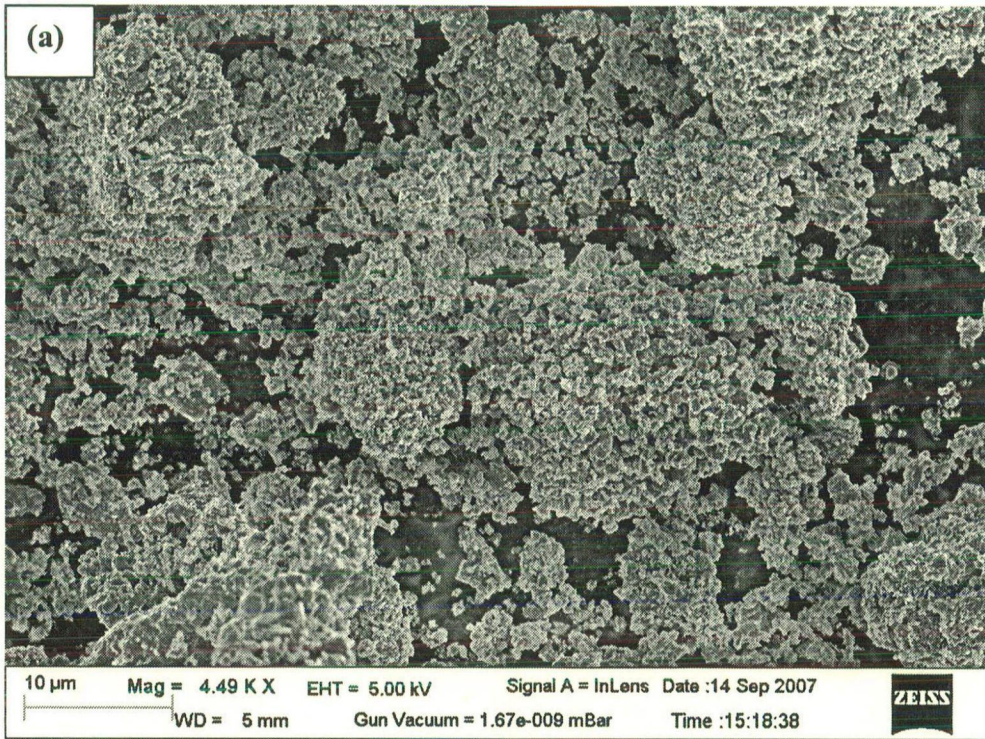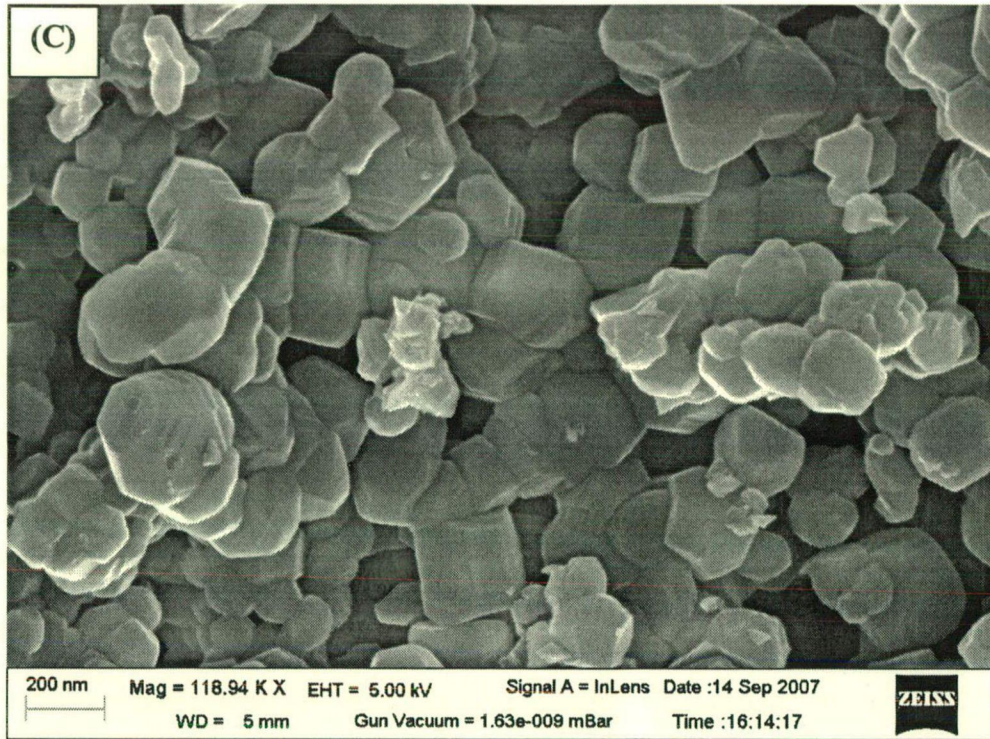
Fig. 4.1.3: Micrographs of $LiMn_2O_4$ taken at various magnifications

1 µm Mag = 40.00 K X EHT = 5.00 kV Signal A = InLens Date :14 Sep 2007
WD = 5 mm Gun Vacuum = 1.67e-009 mBar Time :15:17:31
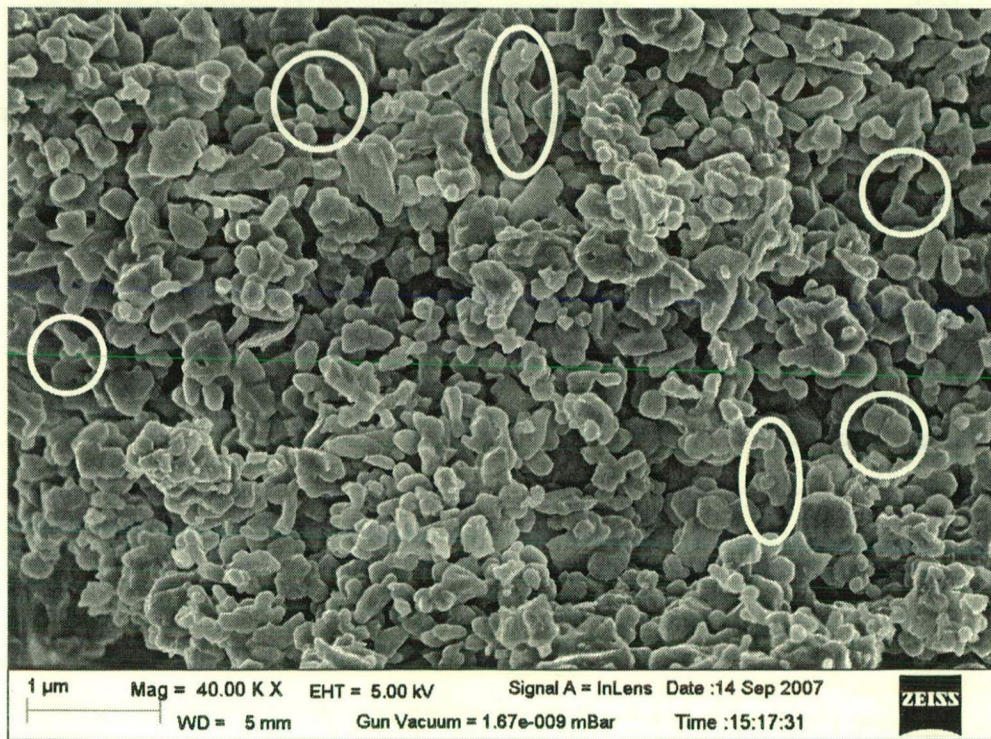
Fig. 4.1.4: Micrograph showing the growth of the various particles (Circles and ellipsoid marked in order to show the required mechanism)

99

Micrographs of the particles at higher magnification are shown in Fig. 4.1.3 (c) to demonstrate the average particle size and morphology. The average particle size of the sample is about 250 nm. However the particle size lies in a wide range of 100 - 350 nm and can be seen from Fig. 4.1.3 (b) and (c). The particle morphology is truncated octahedron. Step growth of the primary particles can be seen in the micrograph shown in Fig. 4.1.3 (c). Surface diffusion of the particles initially leads to the filling of the necked region formed by two adjacent particles. The neck growth is prominent until the neck attains a size that is comparable to that of the smaller particle. The densification in powder compact occurs finally when the larger elongated grains develop as shown in Fig. 4.1.4.

4.1.3 Thermal study

Differential thermal analysis and thermogravimetry (DTA/TG) analyses have been carried out to investigate the thermal stability of the spinel $LiMn_2O_4$. The thermal stability of the lithium manganese spinel has been reported by Thackeray et al., 1996. TG traces given in Fig. 2.9 shows three distinct processes that occur at 780, 915 and 1060 ^{o}C. In the temperature range between 780 and 915 ^{o}C, oxygen loss occurs from the cubic $LiMn_2O_4$. This oxygen loss from the structure is accompanied by the lithium diffusion to the particle surface where a disproportionation reaction occurs, leading to the formation of Li_2MnO_3 and a tetragonal spinel in which manganese oxidation state is < 3.5. The extent of tetragonal distortion depends upon the oxygen loss from the structure. In the temperature range from 915 to 1060 ^{o}C, the oxygen loss occurs rapidly from the sample and the Li_2MnO_3 phase is consumed by manganese rich spinel phase to produce $LiMnO_2$. $LiMnO_2$ phase is stable upto the temperature of ~1100 ^{o}C, beyond which it is reincorporated into the spinel phase to yield a single phase spinel product.
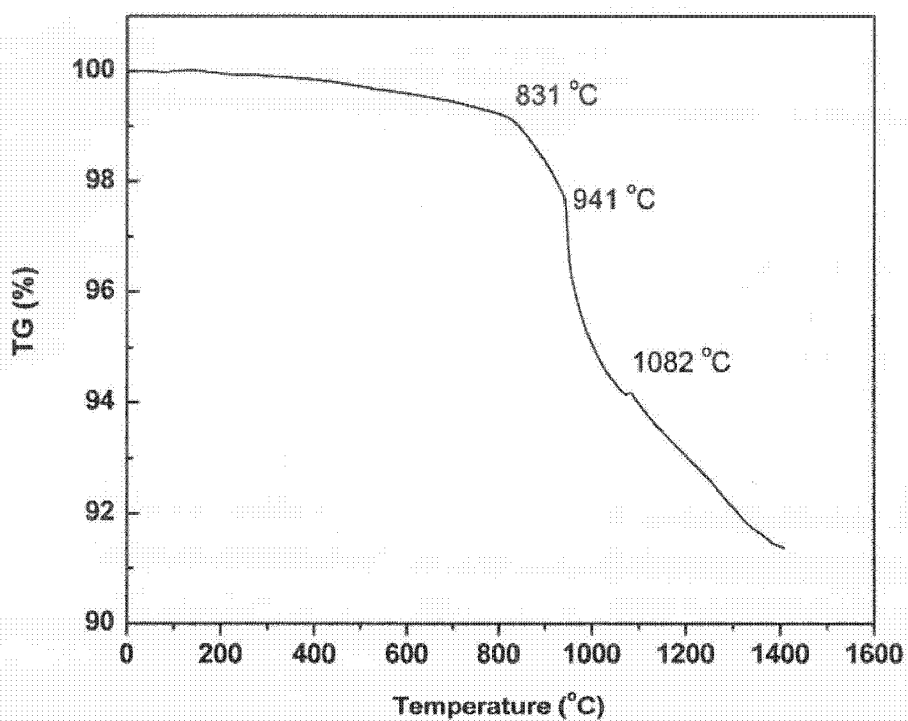
Fig. 4.1.5: TG plot of $LiMn_2O_4$ powdered sample heated up to $1400\ ^oC$ in the presence of air

Fig. 4.1.6: DTG plot of $LiMn_2O_4$ powdered sample heated up to $1400\ ^oC$ in the presence of

air

101

In the TG trace, which is shown in Fig. 4.1.5, three transitions taking place at temperatures 831, 941 and 1082 $^{\circ}$C are observed. The major weight loss begins at ~ 831 $^{\circ}$C and the loss becomes appreciable at 941 $^{\circ}$C onwards, during which the oxygen loss occurs rapidly. A weight gain can be observed from the graph when the temperature reaches close to 1082 $^{\circ}$C and the Li_2MnO_3 phase is consumed by manganese rich spinel phase leading to the formation of $LiMnO_2$. From DTG curve, which is shown in Fig. 4.1.6, the transformations are clear. The weight loss begins at 831 $^{\circ}$C and becomes prominent at temperature of ~ 940 $^{\circ}$C, at which a long spike appears, as can be seen from the Fig. 4.1.6. The maximum appears exactly at 948 $^{\circ}$C. The weight gain though nominal observed at ~ 1080 $^{\circ}$C gives a clear indication of Li_2MnO_3 absorption by manganese rich spinel for the formation of $LiMnO_2$. Therefore, the thermal analysis shows that the structure of the cubic spinel phase is stable upto a temperature of ~831 $^{\circ}$C, above which an appreciable oxygen loss takes place.
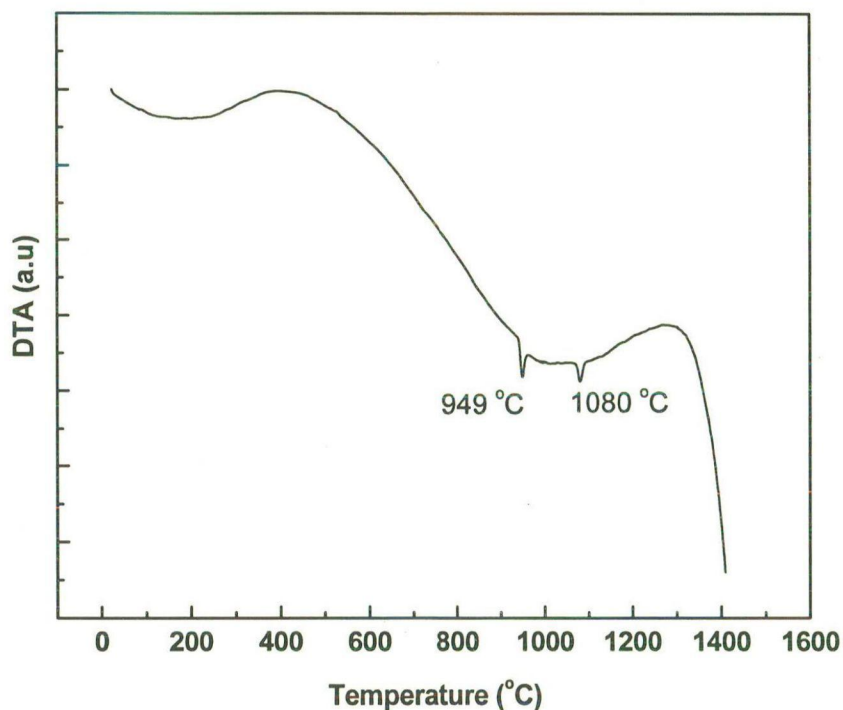
Fig. 4.1.7: DTA plot of $LiMn_2O_4$ powdered sample heated up to 1400 $^{\circ}$C in the presence of air

The DTA curve of the sample in Fig. 4.17 shows two endothermic peaks at 949 and 1080 $^{\circ}$C and the result is in agreement with the TG/DTG analysis results. The transition at ~949 $^{\circ}$C is

102

attributed to the formation of single phase tetragonal spinel $LiMn_2O_4$. The second transition at ~1080 °C corresponds to the reversible transition of a tetragonal to cubic spinel.

4.1.4 Spectroscopic studies

FTIR spectrum of the $LiMn_2O_4$ powder is shown in Fig. 4.1.8, which shows two strong bands at 502 and 613 cm^{-1}. The two strong bands correspond to the asymmetric stretching modes of MnO_6 octahedra, whereas the weak band at around 421 cm^{-1} is attributed to the asymmetric stretching in the vibration of LiO_4 tetrahedra in $LiMn_2O_4$. Cubic $LiMn_2O_4$ spinel has a space group Fd3m $[O_h^7]$, with eight formula units per unit cell. The smallest Bravais cell is rhombohedral with 2 formula units per unit cell and contains almost the entire information regarding the crystal structure.
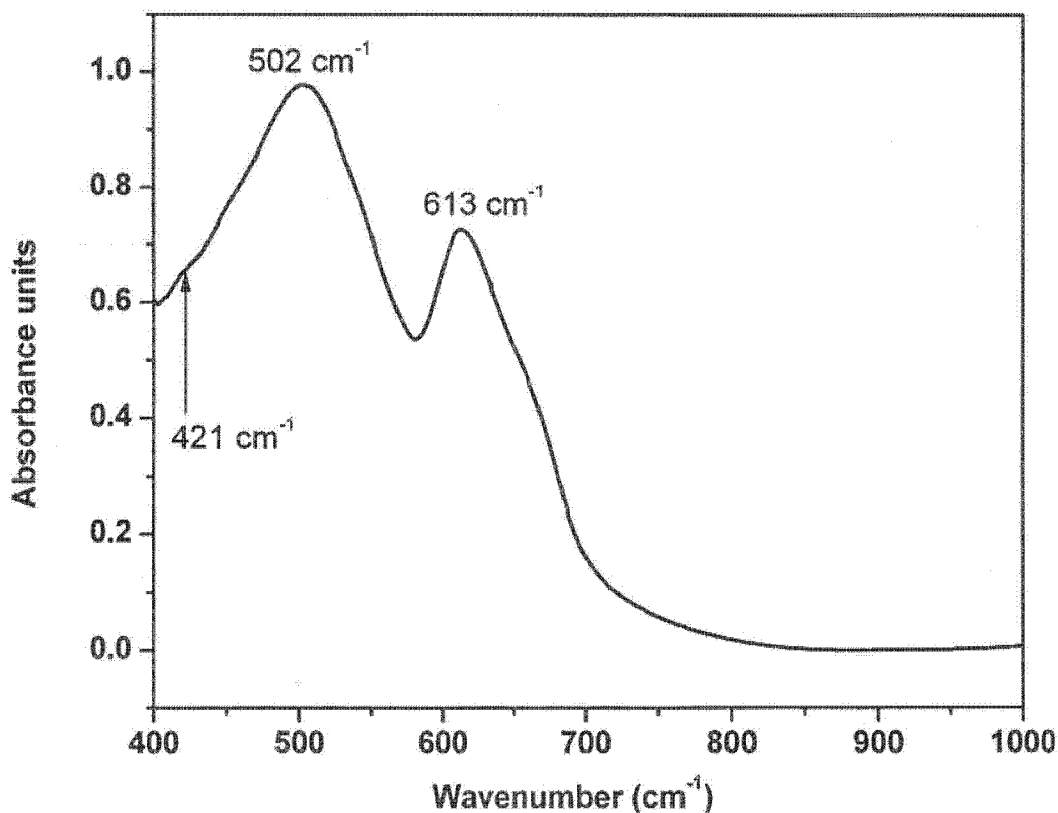
Fig. 4.1.8: FTIR spectrum of the $LiMn_2O_4$ powder at room temperature

103

Lithium ions of a normal spinel occupy 8a tetrahedral sites and have point group symmetry of T_d. The Mn ions occupy 16d sites and have point group symmetry of D_{3d}. The oxygen ions occupy 32e sites with site symmetry of C_{3v}. The cubic closed packed array of oxide ions incorporates MnO_6 octahedron sharing two opposite corners with LiO_4 tetrahedra. MnO_6 octahedra are connected to one another in three dimensions by edge sharing. The LiO_4 tetrahedra share four corners with a different MnO_6 unit, however, the tetrahedral remain essentially isolated from each other. The number of active bands in the vibrational spectra of lithium manganese oxide depends on the symmetry and increases significantly for tetragonal or ordered spinel structure. There are four infrared active bands of the cubic spinel structure of $LiMn_2O_4$.

4.1.5 Impedance Spectroscopy

A known amount of calcined powder was compacted in the form of cylindrical pellet. Impedance measurements of the pellet were made in a frequency range of 40 to 110 MHz at room temperature. Fig. 4.1.9 shows the variation of real part (Z') of the impedance with its imaginary part (Z") in a complex impedance plane. Bulk resistance of the sample was calculated from the extrapolated semicircular plot in the low frequency region on the x-axis. The electrical conductivity (σ) for the sample was calculated using the following relation

$$\sigma = (1/R) \times (l/A)$$

where R is the bulk resistance of the sample, l the thickness and A the area of the cylindrical sample.
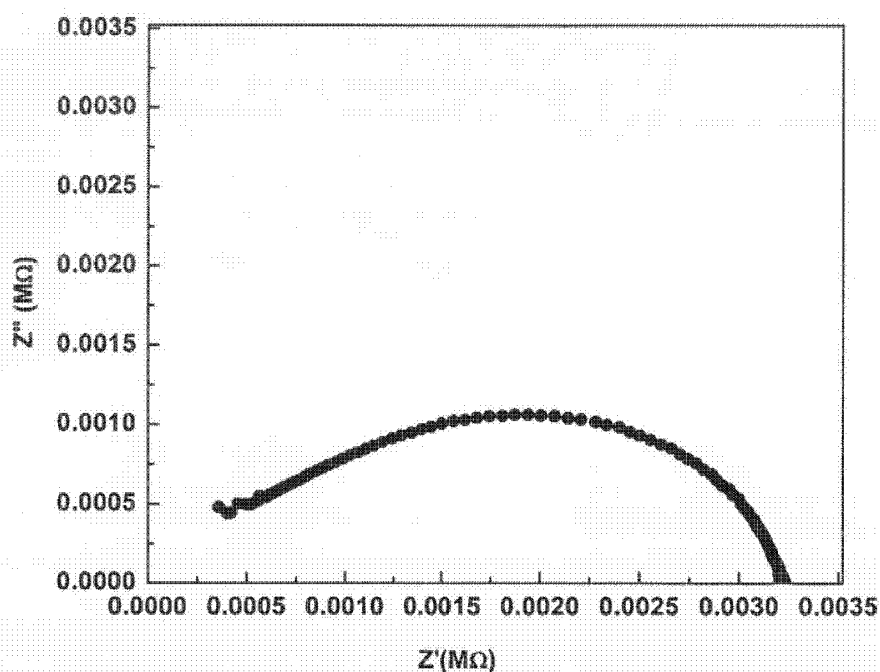
Fig. 4.1.9: Variation of the real part (Z') with the imaginary part of impedance (Z")

The variation of the real part of the impedance with the frequency is shown in Fig. 4.1.10 which shows that the impedance is higher at lower frequency showing the molecules are in the state of polarization at lower frequencies. The relaxation state of the molecules in the compound develops with the increase in frequency.
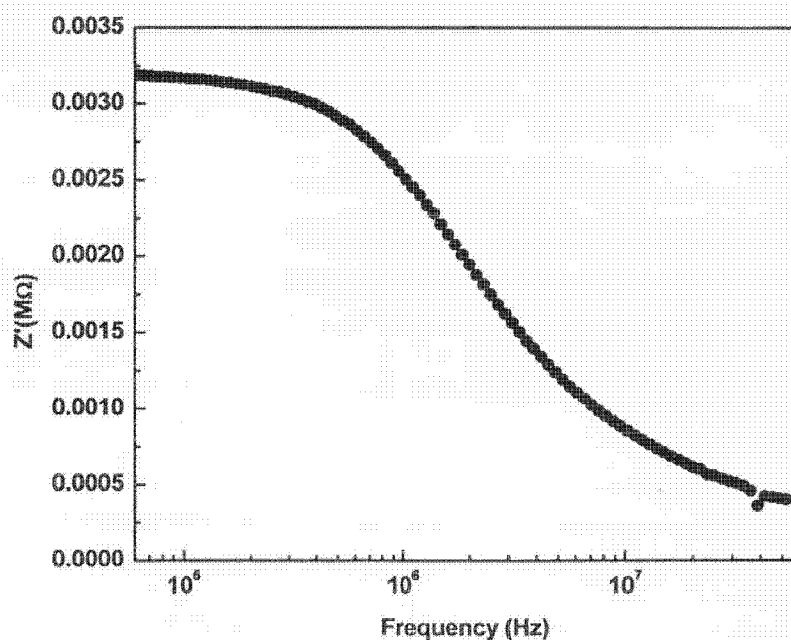
Fig. 4.1.10: Variation of the real part of impedance (Z') with the frequency

A minor decrease in the impedance over the frequency range of 40 Hz to 10^5 Hz shows that the material can remain in the polarized state over this frequency range. The electrical conductivity of the material at room temperature is of the order of 10^{-5} S/cm.

4.1.6 Electrochemical Study

Electrochemical measurements on the calcined powder have been carried out to determine the cathode performance in battery operation. Lithium metal in the form of thin strip was used as counter electrode (anode). Charge and discharge curves of the sample are shown in Fig. 4.1.11, which shows that lithium can be extracted from $LiMn_2O_4$ at a voltage of about 4 V. The extraction occurs in two steps with a voltage step of approximately 120 mV. This two step process as reported by Thackeray et al., 1997 is due to the ordering of the lithium ions on one half of the tetrahedral sites. Similar trend has been observed during the lithium insertion in the host structure. Ohzuku et al., 1990, have shown that this voltage step is associated with the cubic-cubic transition occurring during the discharge stage of the material. A tail at the end of discharge (capacity at around 3.2 V) is seen in the Fig. 4.1.11.
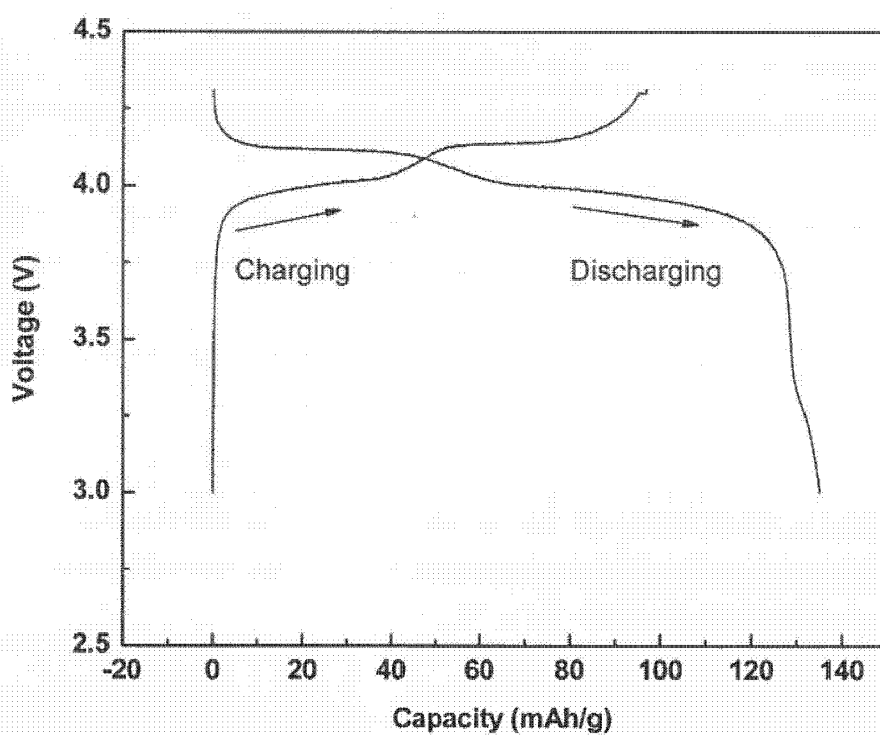
Fig. 4.1.11: First cycle of charging and discharging of $LiMn_2O_4$

Such a tail in the characteristic curve is due to the oxygen nonstoichiometry of the compound. Cyclic stability of the material has also been estimated for the first 10 cycles. Discharge capacity values for the first and 10th cycle are ~135 mAh/g and ~124 mAh/g respectively.

4.2.1 Phase Analysis

Chromium (Cr) doped LiMn$_2$O$_4$ samples have been prepared by sol-gel technique using citric acid as a chelating agent. X-ray diffraction data for the powdered samples of different compositions have been collected over 2θ ranging from 10 to 120° with a step size of 0.0190° and dwell time of 0.2 second per step. The patterns are presented in Fig. 4.2.1.
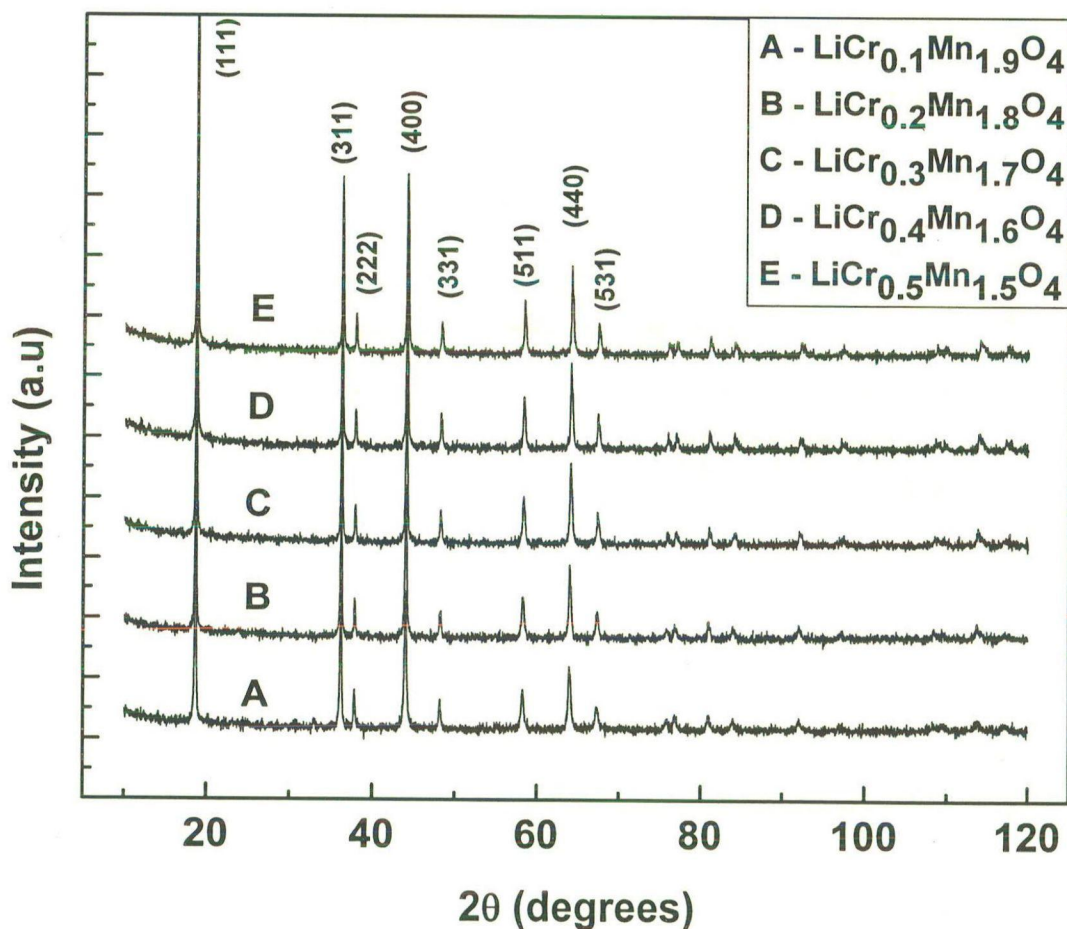
Fig. 4.2.1: X-ray diffraction patterns of powdered samples in the system LiCr$_x$Mn$_{2-x}$O$_4$

(0.1≤x≤0.5)

The phase analysis of the XRD pattern shows that all the samples have single phase spinel structure with a space group of Fd3m. Rietveld refinement of the XRD patterns was done to determine the atomic positions in the structure and lattice parameter of the unit cell.
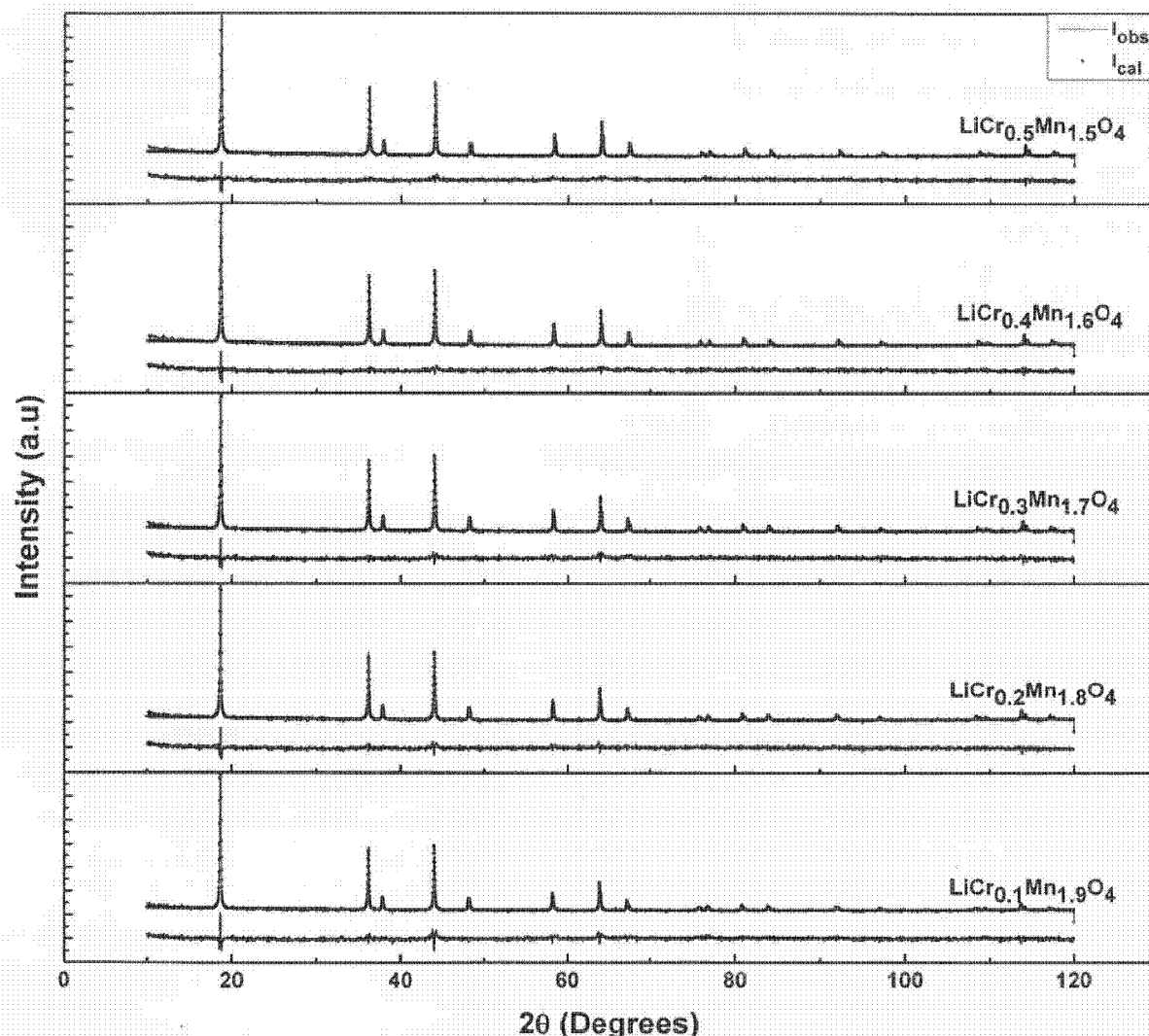
Fig. 4.2.2: Rietveld refined XRD patterns of $LiCr_xMn_{2-x}O_4$ ($0.1 \leq x \leq 0.5$)

The model used for the refinement considered Li ions in 8a tetrahedral sites, Mn and Cr ions both occupy 16d octahedral sites and O ions are present in the 32e sites. The occupancies of Mn and Cr at 8a and 16c sites are negligibly small. The profile fitting of the XRD pattern yields good results by taking the occupancies of Mn and Cr ions at 16d positions. The refined patterns along with the difference plots for different compositions are shown in Fig. 4.2.2.

109

The Rietveld refinement results for the various compositions are summarized in Table 4.2.1. The O ion position parameter is almost same for all the compositions. Lattice parameters have also been calculated, which decreases linearly with the increase in Cr content. Such decrease can be explained on the basis of the difference in ionic radii of the Cr and Mn in different oxidation states with coordination number six. Mn in the compound $LiMn_2O_4$ exists in two possible oxidation states such as Mn^{3+} and Mn^{4+}. Mn^{3+} can further be classified into high spin and low spin. Mn^{3+} high spin is a Jahn-Teller active ion which gives a local distortion in the structure, however Mn^{3+} low spin is Jahn-Teller inactive ion. The radii of these ions having coordination number of 6 are given in the Table 4.2.2.

Table 4.2.1: Rietveld refinement results of the various compositions under study

Systems Studied	Lattice parameter (Å)	R_p(%)	R_{wp}(%)	R_{exp}(%)	GOF (Goodness of Fit)
$LiMn_2O_4$	8.2369	10.12	12.61	8.83	2.03
$LiCr_{0.1}Mn_{1.9}O_4$	8.2287	5.81	7.44	5.80	1.64
$LiCr_{0.2}Mn_{1.8}O_4$	8.2236	5.51	6.98	5.96	1.37
$LiCr_{0.3}Mn_{1.7}O_4$	8.2169	5.50	6.93	5.82	1.41
$LiCr_{0.4}Mn_{1.6}O_4$	8.2135	5.58	6.99	5.73	1.48
$LiCr_{0.5}Mn_{1.5}O_5$	8.2064	5.84	7.38	6.02	1.50

Table 4.2.2: Ionic Radii of various ions with coordination number 6

Mn^{3+}		Mn^{4+}	Cr^{3+}
Low Spin	High Spin	0.67	0.755
0.72	0.785		

Cr also exists in different oxidation states. However, the probability of existence of Cr in +3 oxidation state is more, because ionic radii of Cr^{3+} compared to Cr^{6+} is close to Mn^{3+} or

Mn^{4+}. The decrease in the lattice parameters signifies that the Cr^{3+} ions substitute Mn^{3+} that is in the high spin state. This intern increases the Mn^{4+} ions content in the structure, giving rise to a decrease in the lattice parameter. If Cr^{3+} substitutes Mn^{3+} (low spin) or Mn^{4+}, the lattice parameter then should increase because Cr^{3+} has higher ionic radius than that of Mn^{3+} (low spin) or Mn^{4+}. However, this is not the case, therefore it is evident that the presence of Cr in the structure reduces the Jahn-Teller distortion.

The variation of the lattice parameter with the increase in Cr content is shown in Fig. 4.2.3. A shift in the peak positions towards higher angle in the XRD pattern gives a clear indication of the decrease in the lattice parameter value. Shift in the peak position towards higher angles is shown in Fig. 4.2.4.
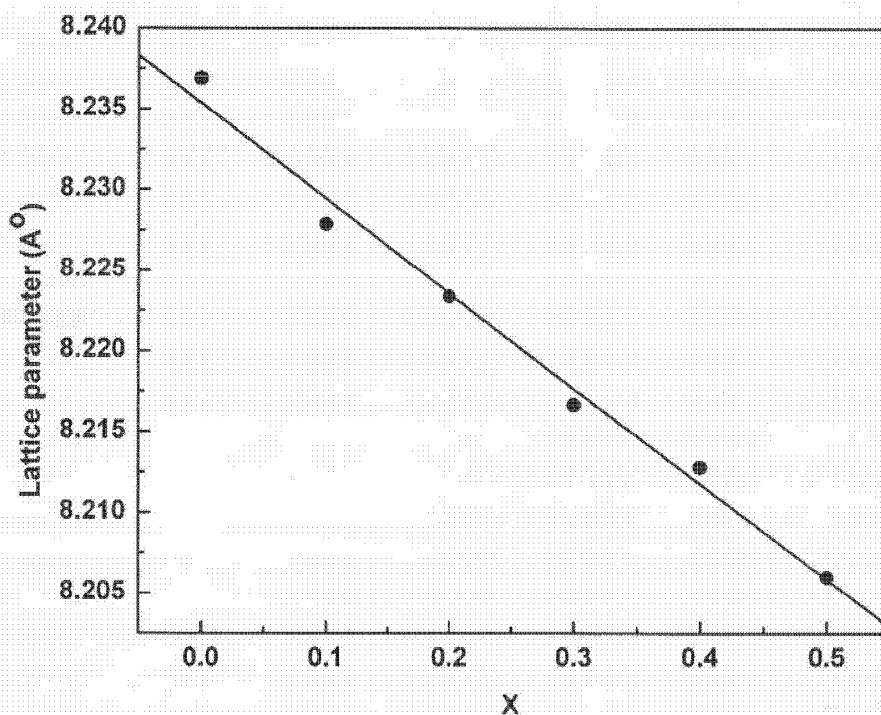
Fig. 4.2.3: Variation of the lattice parameter with the increase in Cr content

111
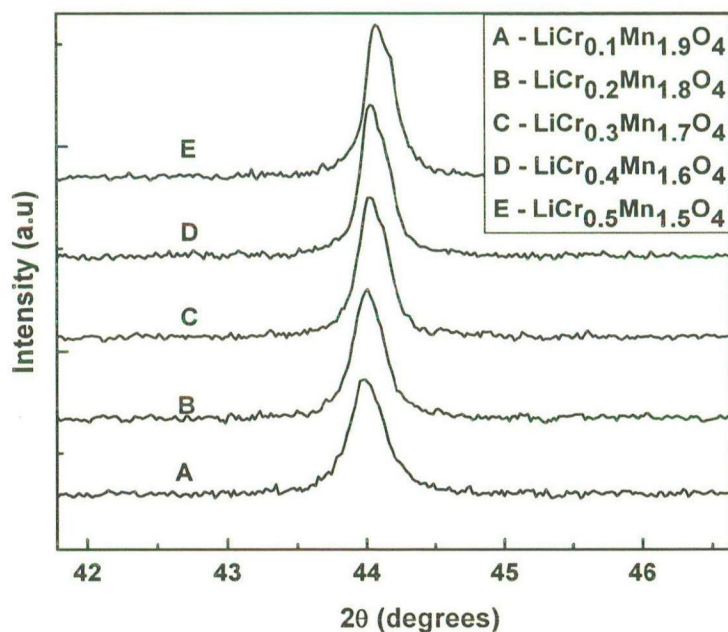
Fig. 4.2.4: Shifting of angular position of the peak (400) with the increase in Cr content

4.2.2 Morphological Studies

Morphology of the various powdered samples has been studied using field emission scanning electron microscopy (FESEM) and the micrographs captured at low magnification are shown in Fig. 4.2.5, which shows that the particles are in highly agglomerated state for all the compositions.
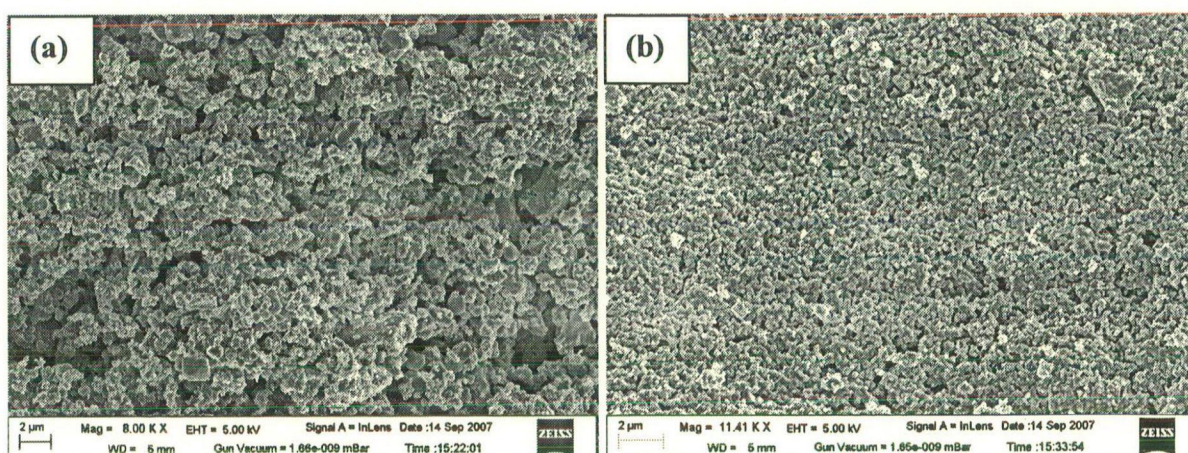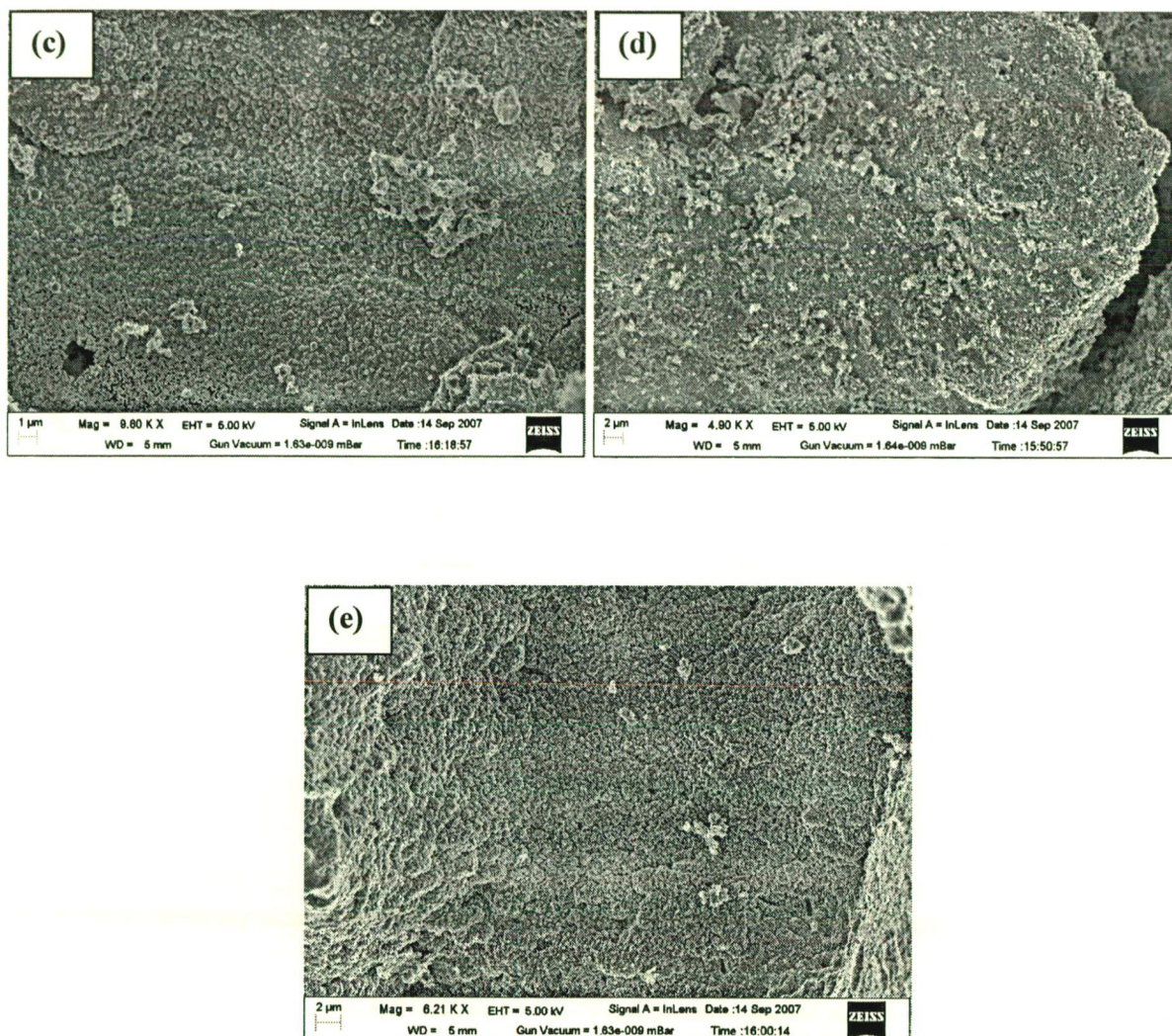
Fig. 4.2.5: Micrographs of the powder samples of $LiCr_xMn_{2-x}O_4$ ($0.1 \leq x \leq 0.5$); [(a) x = 0.1; (b) x = 0.2; (c) x = 0.3; (d) x = 0.4; (e) x = 0.5]

A good particle-particle contact in all the samples is observed. Average particle size for all the compositions decreases with the increase in Cr content, indicating the nucleation rate becomes higher than the growth rate as the Cr content increases in the compound. To show the decrease in particle size, images at the same magnification have been shown in Fig. 4.2.6.

(a)

| 200 nm | Mag = 154.34 K X | EHT = 5.00 kV | Signal A = InLens | Date :14 Sep 2007 |
| | WD = 5 mm | Gun Vacuum = 1.65e-009 mBar | | Time :15:29:10 |

(b)

| 200 nm | Mag = 154.34 K X | EHT = 5.00 kV | Signal A = InLens | Date :26 Oct 2007 |
| | WD = 5 mm | Gun Vacuum = 1.23e-009 mBar | | Time :15:44:01 |

114

(c)

200 nm | Mag = 154.34 K X | EHT = 5.00 kV | Signal A = InLens | Date :26 Oct 2007
WD = 5 mm | Gun Vacuum = 1.24e-009 mBar | Time :15:40:36

(d)

200 nm | Mag = 154.34 K X | EHT = 5.00 kV | Signal A = InLens | Date :26 Oct 2007
WD = 5 mm | Gun Vacuum = 1.23e-009 mBar | Time :15:38:18

Fig. 4.2.6: Micrographs of powders at same magnification having composition $LiCr_xMn_{2-x}O_4$
[(a): x = 0.1; (b): x = 0.2; (c): x = 0.3; (d): x = 0.4; (e): x = 0.5]

The particle distribution in $LiCr_xMn_{2-x}O_4$ is not uniform. The particle size range is wide. The size ranges are shown in Table 4.2.3.

Table 4.2.3: Average particle size and particle size range in $LiCr_xMn_{2-x}O_4$ ($0.1 \leq x \leq 0.5$)

Compound	Average particle size	Particle size range
$LiCr_{0.1}Mn_{1.9}O_4$	~ 155 nm	200 -100 nm
$LiCr_{0.2}Mn_{1.8}O_4$	~ 150 nm	180 - 120 nm
$LiCr_{0.3}Mn_{1.7}O_4$	~ 130 nm	150 – 80 nm
$LiCr_{0.4}Mn_{1.6}O_4$	~ 116 nm	160 -70 nm
$LiCr_{0.5}Mn_{1.5}O_5$	~ 80 nm	100 -60 nm

116

The particle morphology has been depicted from the images at higher magnification and Fig. 4.2.7 shows such micrographs. The particle morphology as highlighted by circles changes from truncated octahedron for x = 0.1 to perfect octahedron for x = 0.5. In some particles the truncation of the square faces from the corners can be seen (Fig. 4.2.7 (a) and (b)), which gives rise to truncated hexaoctahedron. However, majority of the particles have truncated octahedron geometry. A truncated octahedron has 8 regular hexagonal faces, 6 square faces, 24 vertices and 36 edges. The square faces in the truncated octahedron shrinks with the increase in Cr content, which leads to the formation of triangular faces in place of hexagonal faces and resulting in a change in symmetry from truncated octahedron to octahedron which consists of eight equilateral triangles. The change in the morphology of the particles has been explained through schematic geometry in Fig. 4.2.8.

200 nm   Mag = 151.45 K X   EHT = 5.00 kV   Signal A = InLens   Date :14 Sep 2007
WD = 5 mm   Gun Vacuum = 1.65e-009 mBar   Time :15:42:58

200 nm   Mag = 123.87 K X   EHT = 5.00 kV   Signal A = InLens   Date :14 Sep 2007

WD = 5 mm   Gun Vacuum = 1.65e-009 mBar   Time :15:54:52
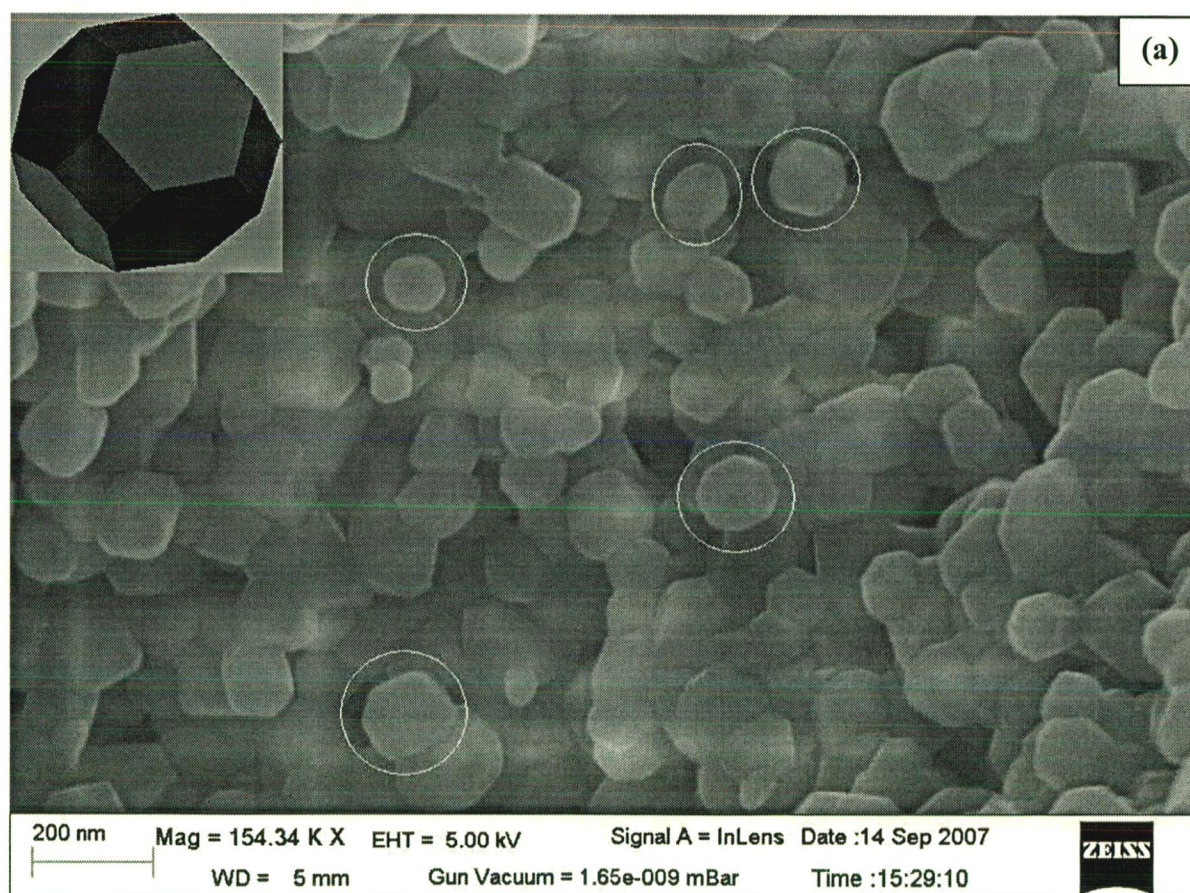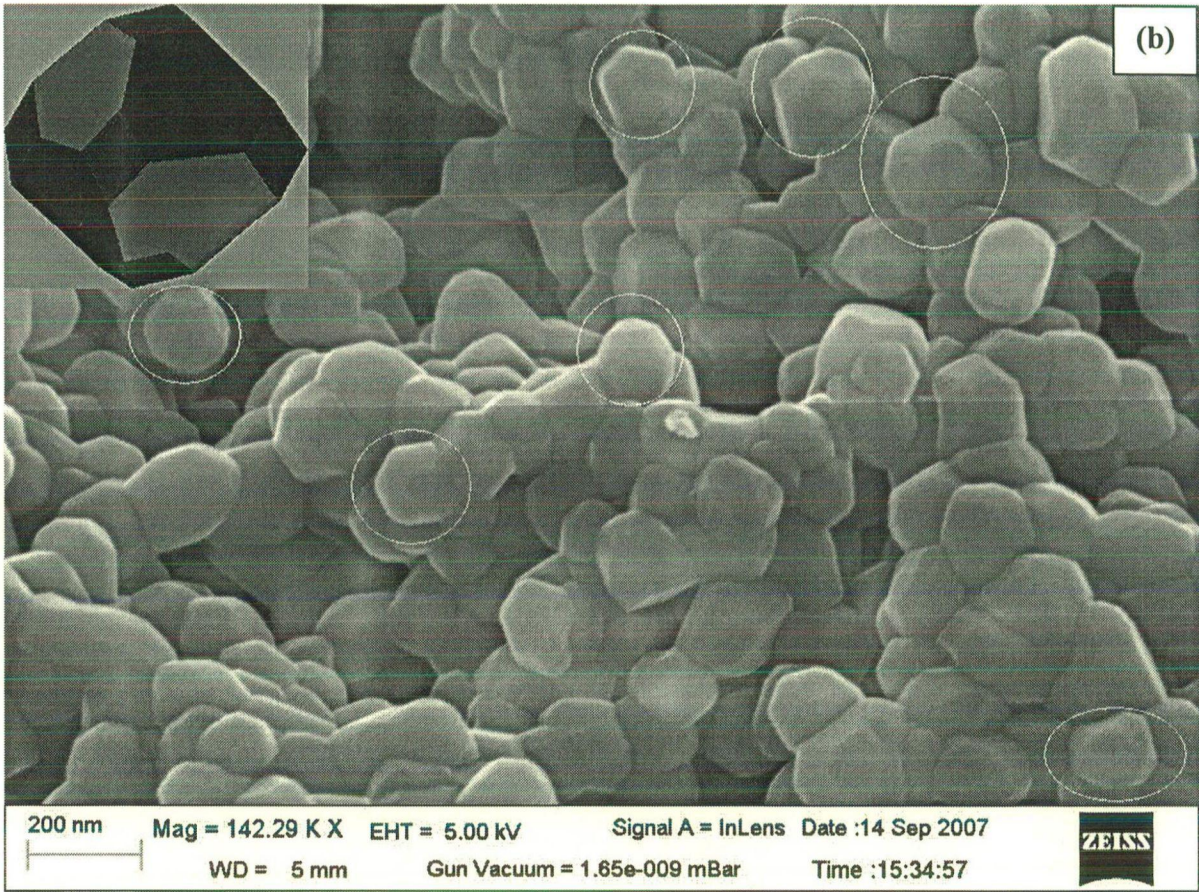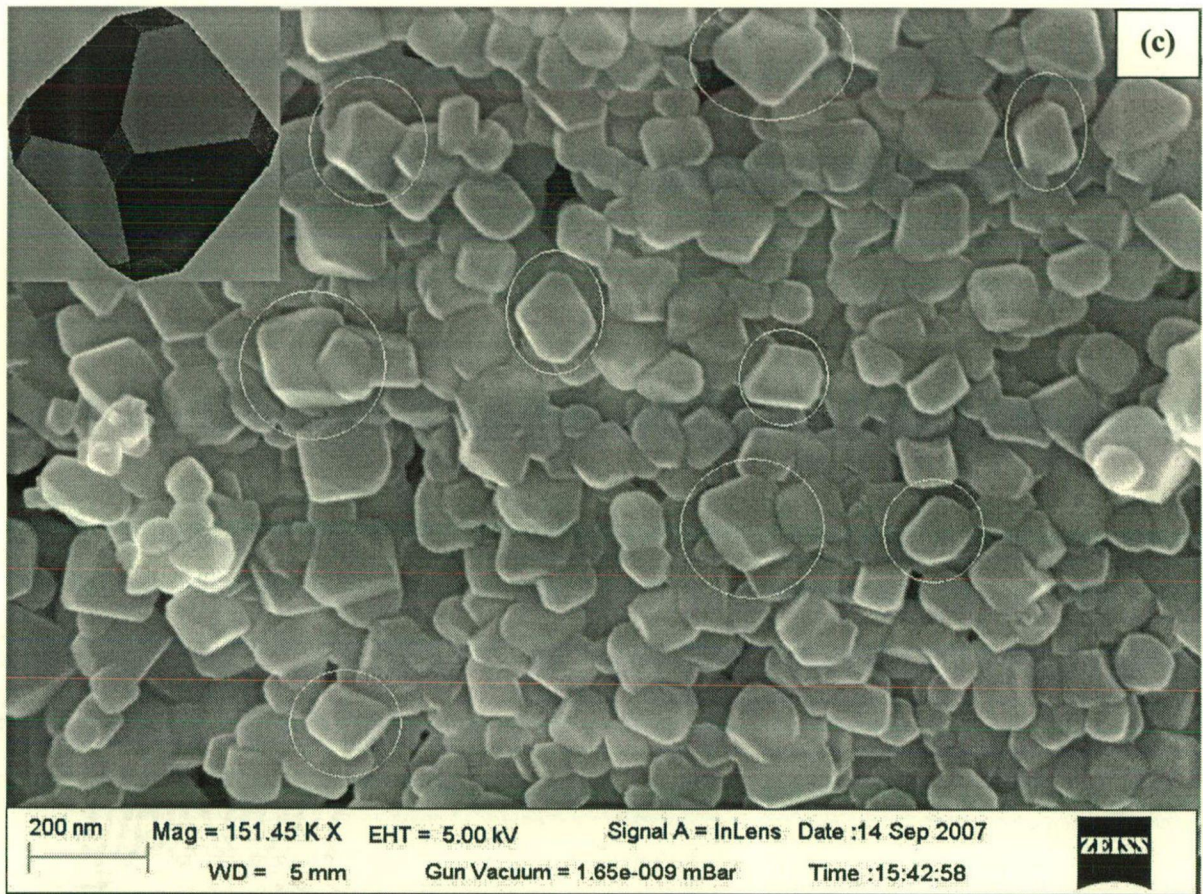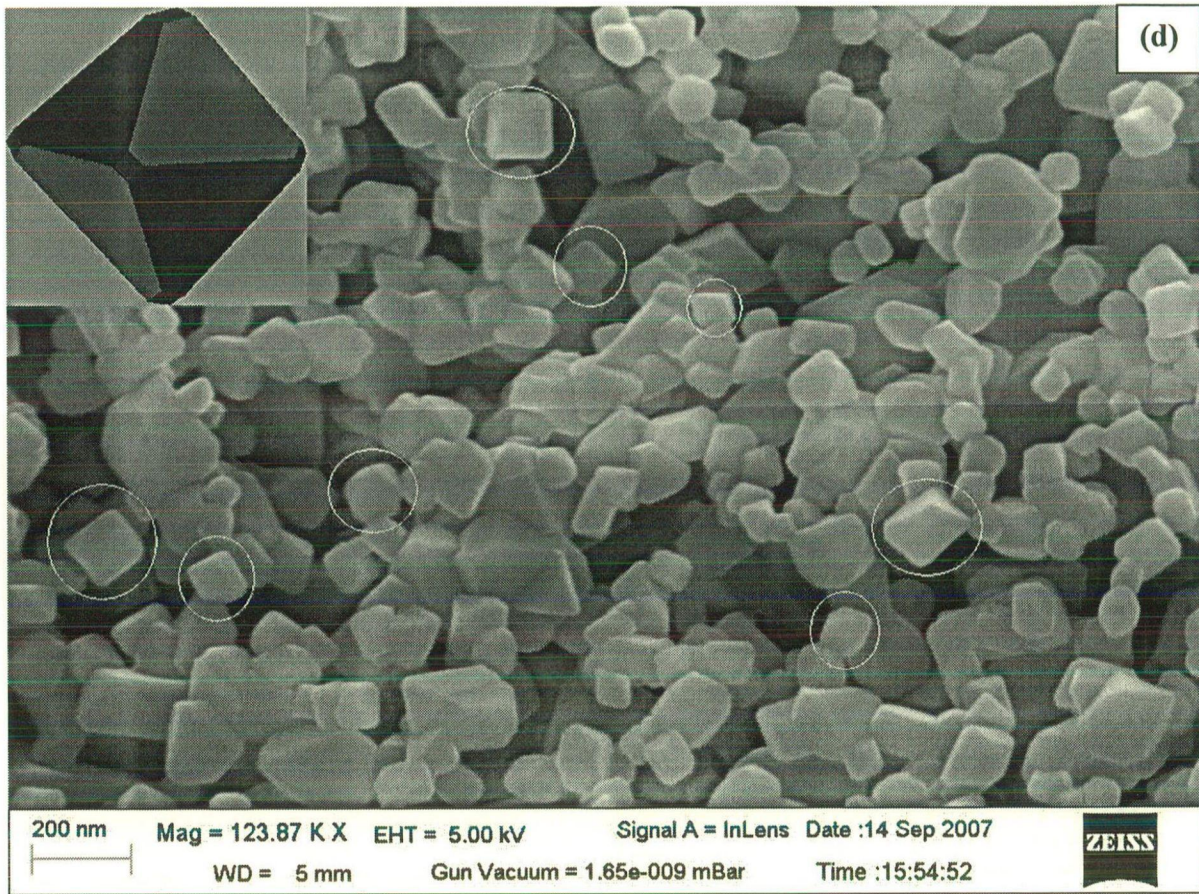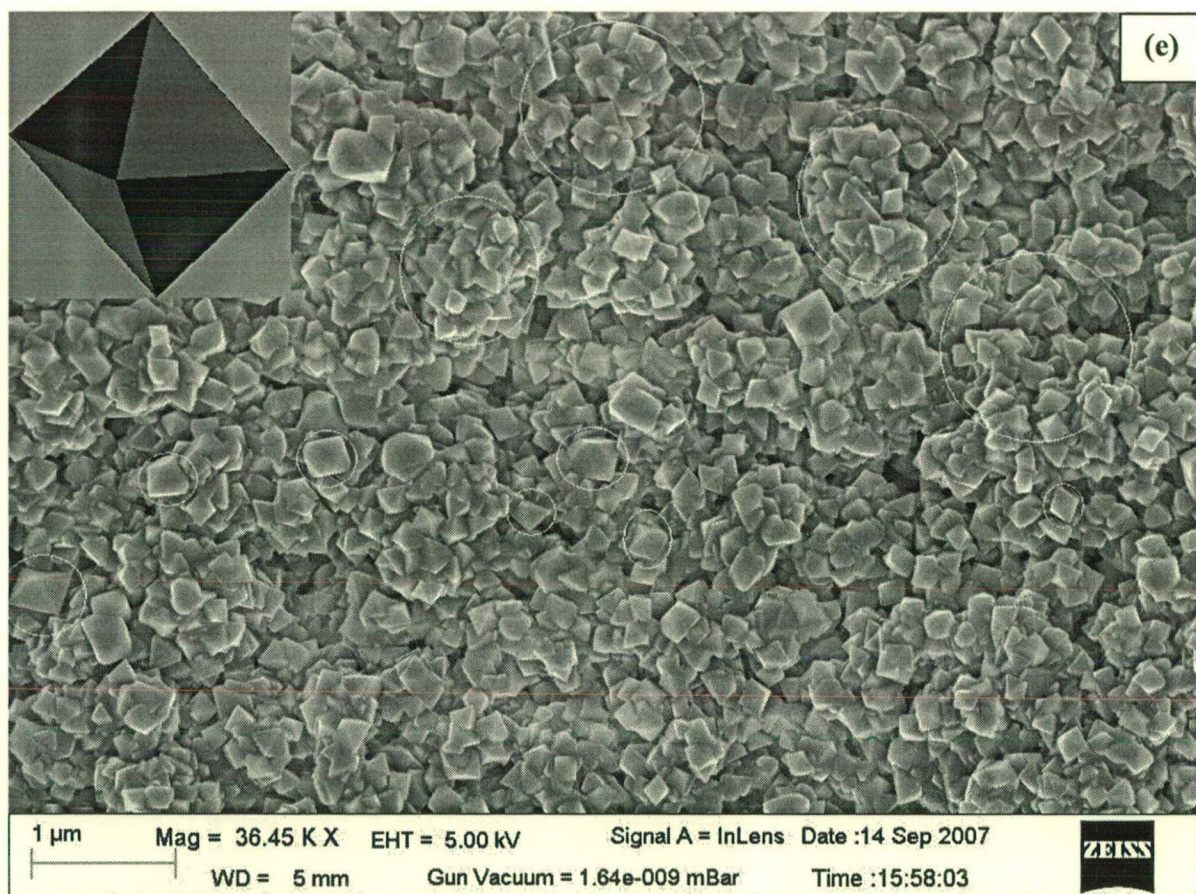
Fig. 4.2.7: Micrographs of $LiCr_xMn_{2-x}O_4$ showing the change in particle morphology [(a) x = 0.1; (b) x = 0.2; (c) x = 0.3; (d) x = 0.4; (e) x = 0.5]
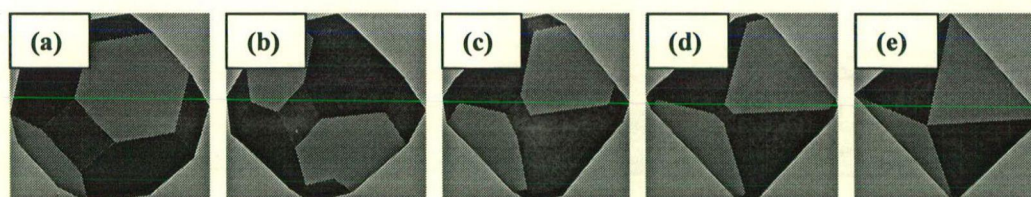
Fig. 4.2.8: Schematic change in morphology from truncated octahedron to perfect octahedron $LiCr_xMn_{2-x}O_4$ [(a) x = 0.1; (b) x = 0.2; (c) x = 0.3; (d) x = 0.4; (e) x = 0.5]

Such a change in the morphology and decrease in average particle size can be explained on the basis of surface area to volume ratio of the particles. If one considers an face centered cubic (FCC) structure (metal) and ensures that only the most stable faces (111) type are exposed, then one ends up with a crystal which is an octahedron. A compromise between

121

exposing only the lowest energy surface planes and minimizing the surface area can be obtained by truncating the vertices of the octahedron, which generates a truncated octahedron with 8 number of (111) type surface and 6 smaller (100) type surface giving rise to a lower ratio of surface area/volume. This satisfactorily explains the decrease in particle size with the increase in Cr content. High surface area to volume ratio minimizes the free energy and hence gives rise to more stable structure.

4.2.3 Spectroscopic studies

FTIR spectra of the calcined powders in different compositions have been obtained in the range of 400 to 4000 cm^{-1} with a step size of 2 cm^{-1} and are shown in Fig. 4.2.9. The Spectra for all the compositions are similar to that of $LiMn_2O_4$, which shows two strong bands at 501 cm^{-1} and 613 cm^{-1}. These bands correspond to the asymmetric stretching vibration of MnO_6 octahedra.
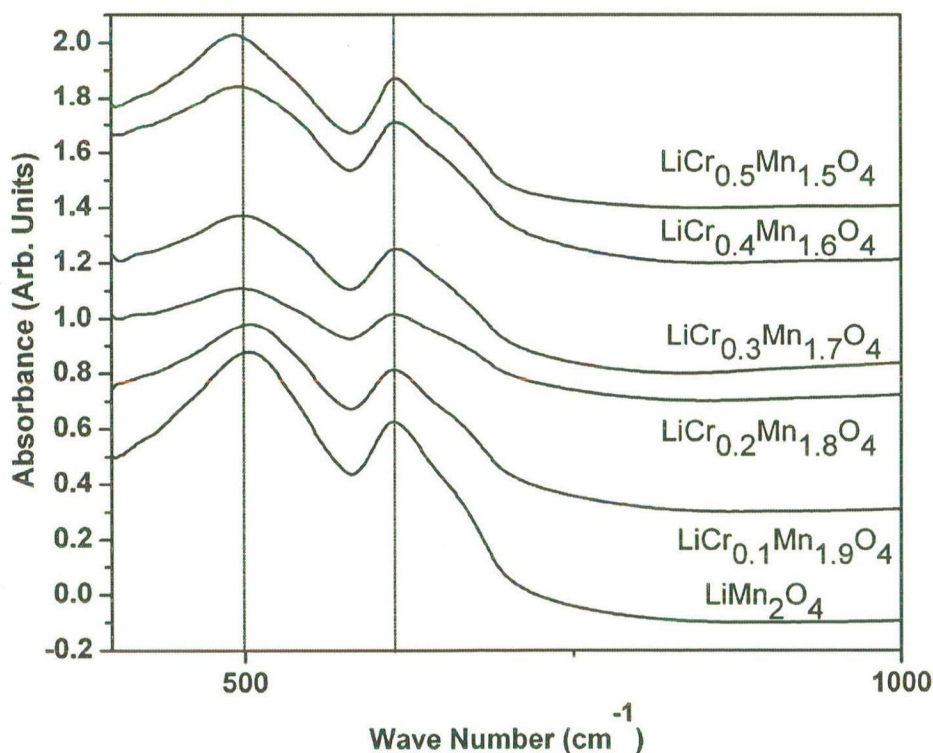
Fig. 4.2.9: FTIR spectra of $LiCr_xMn_{2-x}O_4$ ($0.1 \leq x \leq 0.5$)

With the increase in Cr doping concentration, no feasible change in the peak position occurs in different spectra. This shows that the symmetry of the basic $LiMn_2O_4$ cubic spinel

structure O_h^7 is maintained even after the compound is doped with higher Cr content. The reason for peak position remained almost unchanged is attributed to the masses and ionic radii of Mn^{3+} and Cr^{3+} are not very different. The results are in agreement with the study reported by Wu et al., 2001, who have shown that a small change in the peak positions can be observed only for $x \geq 0.6$. This is because Cr oxidizes to +6 state at $x \geq 0.6$. The conversion of Cr^{3+} to Cr^{6+} state breaks down the charge balance criterion in the spinel structure. To maintain the electroneutrality condition, the Mn^{3+} content increases. The diversity of the cations may disturb the interaction between the cation-oxygen bonds, and leads to an obvious shift on the vibration bands.

4.2.4 Impedance Spectroscopy

Impedance measurements of the samples in the form of cylindrical pellets over the frequency range from 40 Hz to 10 MHz have been made at room temperature. Real and imaginary parts of the impedances plotted in a complex plane are shown in Fig. 4.2.10. The plots in the semicircular nature have been extrapolated towards low frequency side on the resistance axis to obtain the bulk resistances of the samples.
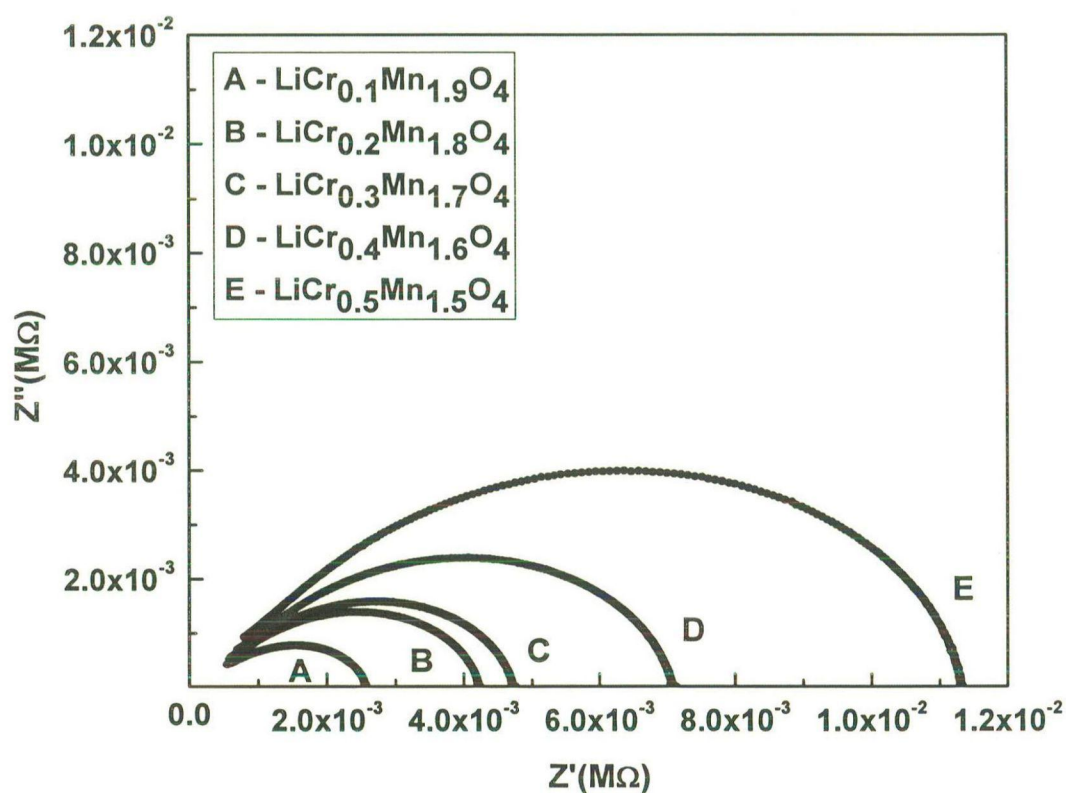
Fig. 4.2.10: Variation of the real part (Z') with the imaginary part (Z'') of the impedance

The electrical conductivities (σ) of the samples have been calculated using the following relation

$$\sigma = (1/R) \times (l/A)$$

where l is thickness, R is the bulk impedance and A, the area of the cylindrical samples. The conductivity values for various compositions are given in Table 4.2.4.

Table 4.2.4: Electrical conductivities values for various compositions

Compound	Electrical conductivity value (S/cm)
$LiCr_{0.1}Mn_{1.9}O_4$	6.61×10^{-5}
$LiCr_{0.2}Mn_{1.8}O_4$	3.93×10^{-5}
$LiCr_{0.3}Mn_{1.7}O_4$	3.67×10^{-5}
$LiCr_{0.4}Mn_{1.6}O_4$	2.53×10^{-5}
$LiCr_{0.5}Mn_{1.5}O_4$	1.57×10^{-5}
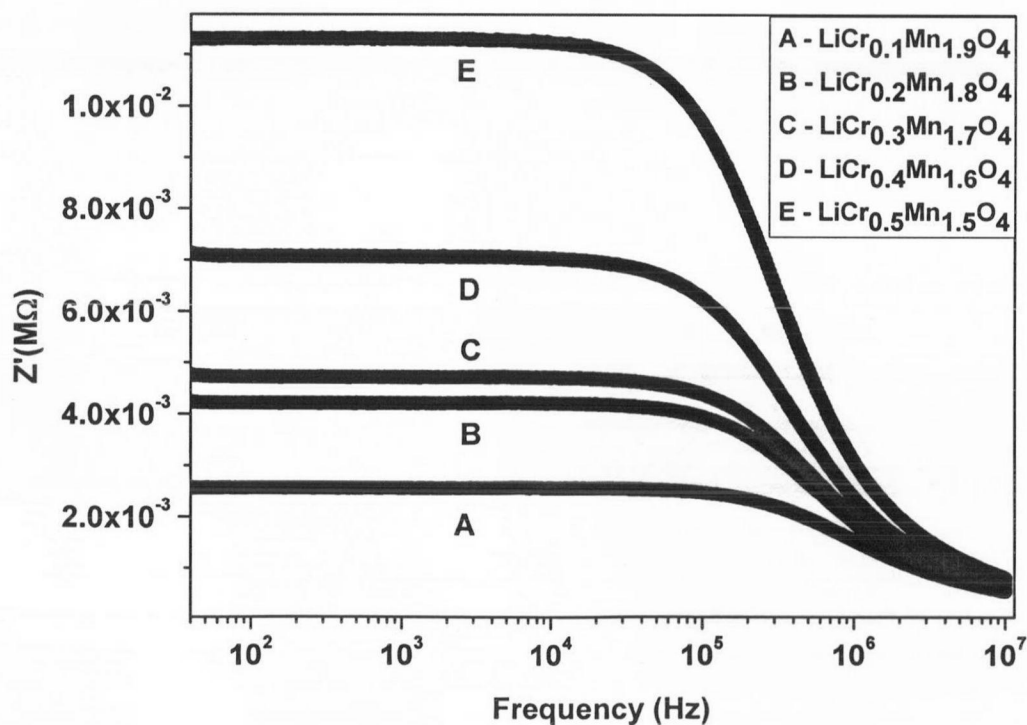
Fig. 4.2.11: Variation of real part (Z') of impedance with frequency

An increase in the impedance at low frequency occurs with the increase in Cr content. However, impedances for all the compositions are same at higher frequencies ($\sim 1 \times 10^{-3} M\Omega$ at $10^7 Hz$), as shown in Fig. 4.2.11. This shows that polarization in lightly doped spinel structure is small at low frequencies and increases with the increase in Cr concentration giving rise to high resistances. Fig. 4.2.12 shows a loss spectrum which is the variation of imaginary part (Z'') of impedance with frequency. Peaks with higher intensity are observed for the spinel having higher Cr content compared to that of the compositions with low Cr content. The broadening of the peaks suggests the presence of relaxation phenomenon in the material. The peak width which is related to relaxation time decreases with the increase in Cr content. Since relaxation process occurs due to delay in molecular polarization with respect to changing electric field, therefore the process in the present case is composition dependent phenomenon. Further the magnitude of Z'' increases with the increase in Cr content and the frequencies at which the maxima occur, shifts towards the lower frequency. Such spectrum probably generates due to the presence of space charge in the material.
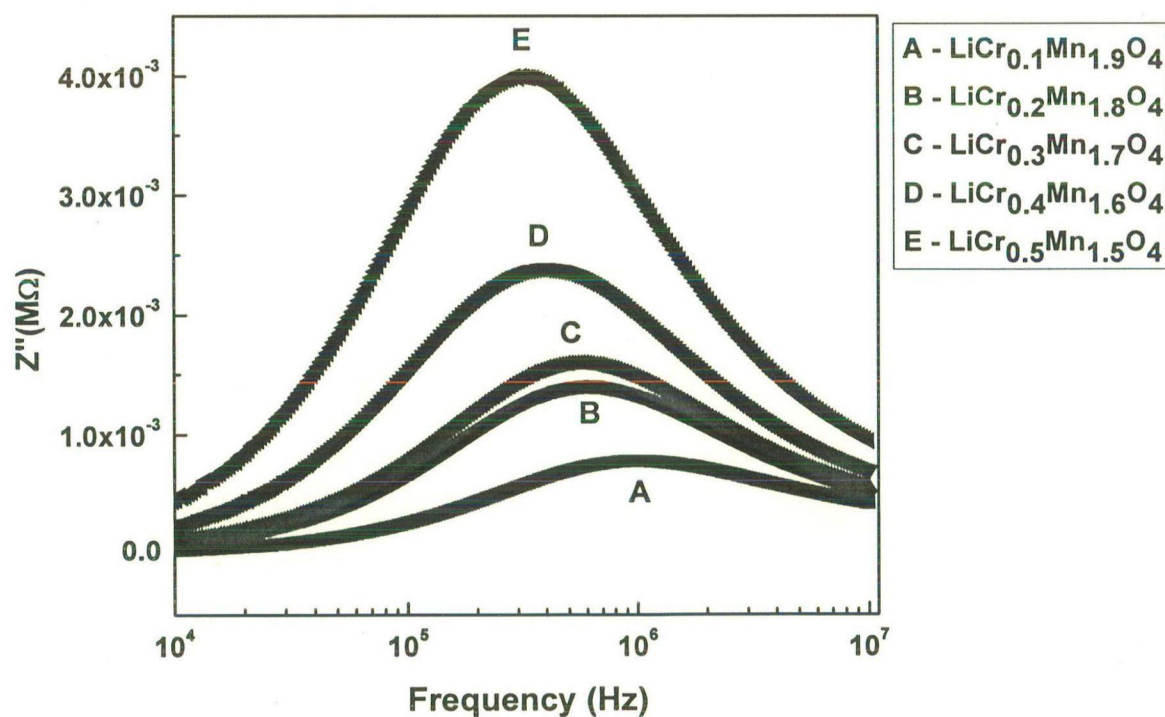
Fig. 4.2.12: Variation of the imaginary part of impedance (Z'') with the increase in frequency

4.2.5 Electrochemical Studies

Electrochemical studies on the Cr doped samples have been performed at room temperature in the voltage range of 3.0 to 4.3 V. Discharge profiles of the compounds with various compositions are shown in Fig. 4.2.13, which shows that the discharge capacities decrease with the increase in Cr content. This can be explained on the basis of the fact that as the Cr content increases the number of Mn^{3+} ions decreases while Mn^{4+} increases. Mn^{3+} can easily be oxidized, however the oxidation of Mn^{4+} is not possible in this voltage range. The ideal composition ($Li_4Mn_5O_{12}$) in which the Mn oxidation state is +4, does not show up any capacity in the voltage range considered. Therefore the capacity corresponding to the 4 V region decreases with the increase in Cr content.

The Fig. 4.2.13 also shows that the voltage profile corresponding to the reduction of the Mn^{4+} exists at higher voltage for highly doped compositions. This means that the lithium insertion in the host structure takes place at higher voltages. In case of λ-Mn_2O_4 and at 4.3 V almost all of the lithium sites are available in the host structure to accommodate lithium. Therefore lithium ions can be easily inserted into the structure and hence a voltage plateau at higher voltage ~ 4.15 V results in the discharge profile. On partial occupation of the lithium sites in $Li_xMn_2O_4$ for nearly x = 0.5, the repulsive interaction between Li-Li increases and gives rise to a voltage plateau at ~ 4 V with a voltage step. As the Cr doping increases, the available sites for the lithium insertion also reduces. This is because during charging whole of the lithium can not be extracted from the cathode in the voltage range of 4.3 to 3.0 V and a part of the lithium content is left behind in the structure. Therefore lithium ions during insertion experience repulsive interaction even at 4.3 V from the other lithium ions that are already present in the structure.
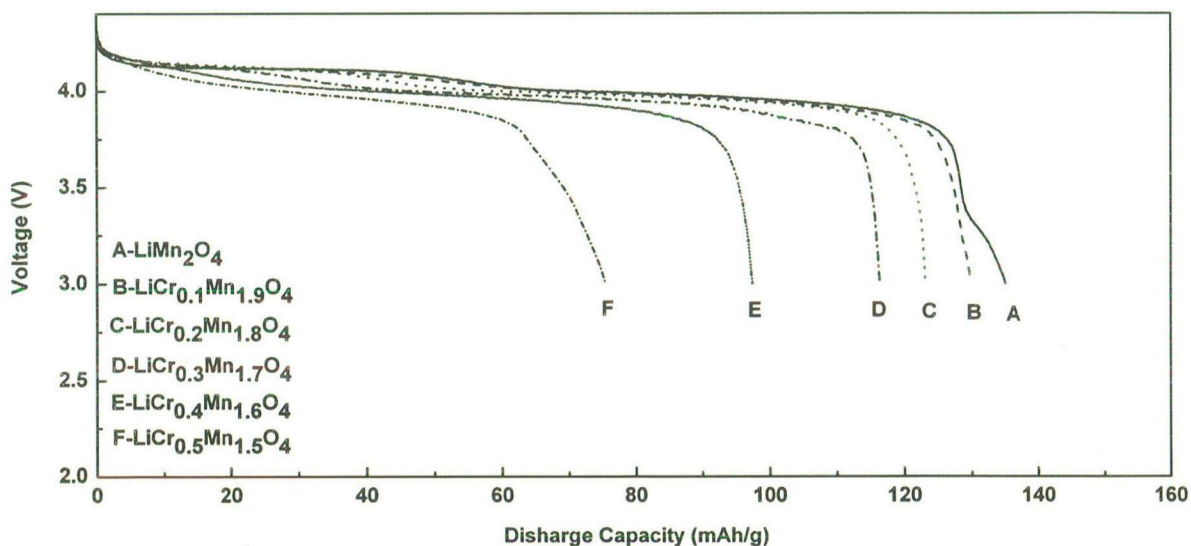
Fig. 4.2.13: Discharge curves of $LiCr_xMn_{2-x}O_4$ ($0.0 \leq x \leq 0.5$) obtained after first cycle

The fall in the capacity with the increase in Cr content has been observed for the first ten cycles of charging and discharging. Variation of discharge capacity with cycle is shown in Fig. 4.2.14. The fall in the discharge capacity is less for the heavily doped compounds even though the initial capacity is less for these compositions. Therefore the Cr doping is beneficial for the stability of the structure. To compensate the capacity loss, the material with higher Cr content should be charged in the higher voltage range so that the oxidation of Cr^{3+} becomes possible.
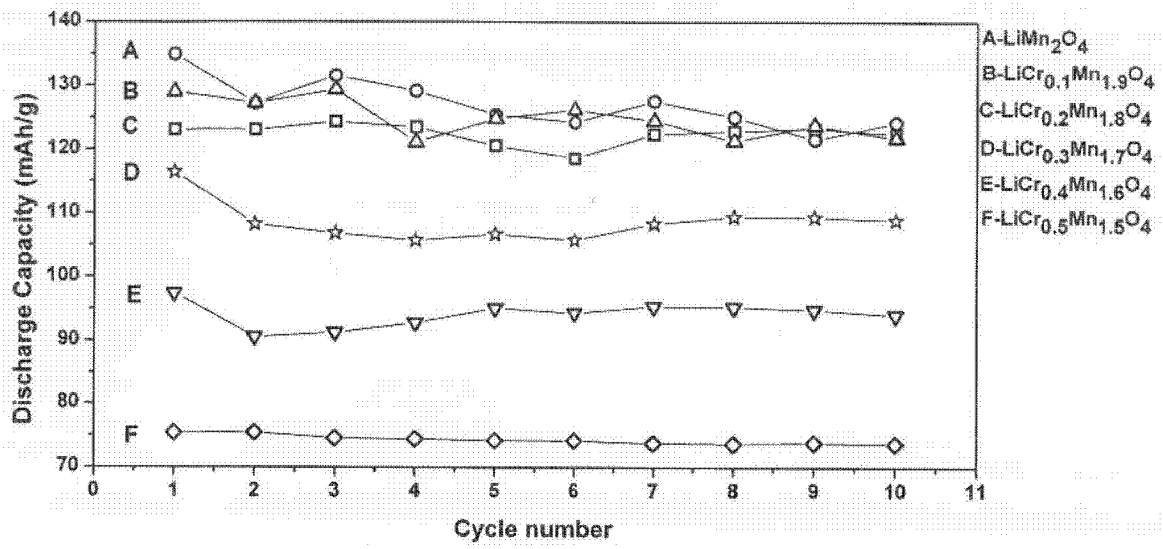
Fig. 4.2.14: Variation of the discharge capacity of $LiCr_xMn_{2-x}O_4$ with the number of cycles

4.3 *Magnesium Doped LiMn$_2$O$_4$*

4.3.1 Phase Analysis

Mg doped LiMn$_2$O$_4$ samples have been made by sol-gel synthesis route using citric acid as a chelating agent. X-ray diffraction analysis of the various samples has been performed for the phase determinations. X-ray diffraction patterns of all the samples in the system LiMg$_x$Mn$_{2-x}$O$_4$ (0.05≤x≤0.5) were collected for 2θ over the range of 10 to 120°. The patterns have been analyzed using X'pert High score plus software. Rietveld refinement of the patterns has been carried out. Fig. 4.3.1 shows XRD patterns along with difference plots for all the compositions after refinement. Refinement results of the various compositions are given in Table 4.3.1. Two models have been used for the refinement. In the first model atomic arrangement is in accordance with Fd3m (O$_h^7$) space group symmetry while the second model involves ordered spinel structure with space group symmetry P4$_3$32 (O^7). The refined atomic positions for the two phase groups are given in Tables 4.3.2 (a) and 4.3.2 (b).
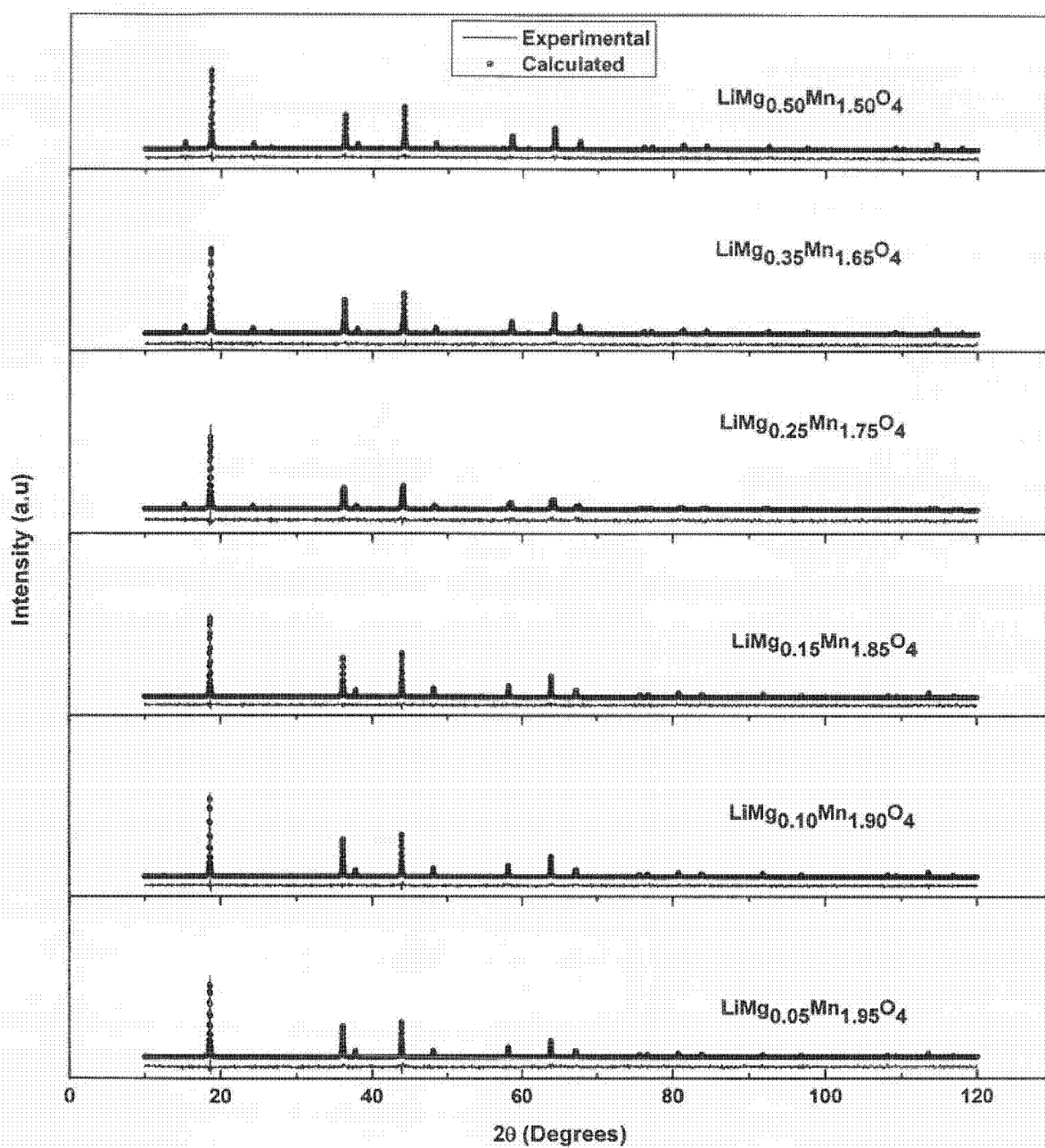
Fig. 4.3.1: XRD patterns along with difference plots for all the compositions after refinement

Table 4.3.1: Refinement results of $LiMg_xMn_{2-x}O_4$; $0.05 \leq x \leq 0.5$

Systems studied		Lattice parameter ($\overset{\circ}{A}$)	R_p(%)	R_{wp}(%)	R_{exp}(%)	GOF (Goodness of Fit)
$LiMg_{0.05}Mn_{1.95}O_4$		a=8.2345	6.04	7.68	7.60	1.01
$LiMg_{0.10}Mn_{1.90}O_4$		a=8.2325	5.69	7.24	7.35	0.97
$LiMg_{0.15}Mn_{1.85}O_4$		a=8.2282	6.14	7.78	7.46	1.08
$LiMg_{0.25}Mn_{1.75}O_4$	Fd3m	a=8.2237	5.76	7.25	6.78	1.14
	$P4_332$	a=8.1882				
$LiMg_{0.35}Mn_{1.65}O_4$		a=8.1852	5.91	7.41	6.97	1.13
$LiMg_{0.50}Mn_{1.50}O_4$		a=8.1856	7.83	6.23	7.82	1.00

Table 4.3.2 (a) Atomic positions in $P4_332$ symmetry for $LiMg_{0.25}Mn_{1.75}O_4$

Atom	Wyckoff positions	Site occupancy factor (s.o.f.)	x	y	z
Li1	8c	1.000000	0.759000	0.759000	0.759000
Mg1	4a	0.925000	0.375000	0.375000	0.375000
Mn2	4a	0.075000	0.375000	0.375000	0.375000
Mn1	12d	0.975000	0.125000	0.120000	0.370000
Mg2	12d	0.025000	0.125000	0.120000	0.370000
O1	8c	1.000000	0.134500	0.134500	0.134500
O2	24e	1.000000	0.125900	0.353000	0.358000

Table 4.3.2 (b): Atomic positions in Fd3m symmetry for $LiMg_{0.25}Mn_{1.75}O_4$

Atom	Wyckoff positions	Site occupancy factor (s.o.f.)	x	y	z
Li	8a	1.000000	0.125000	0.125000	0.125000
Mn	16d	0.875000	0.500000	0.500000	0.500000
O	32e	1.000000	0.260000	0.260000	0.260000
Mg	16d	0.125000	0.500000	0.500000	0.500000

As the characteristic peaks lie in the range of 56 to 70°, therefore, XRD data were collected for this range with slow scanning in order to enhance the signal to noise ratio. From the Fig. 4.3.2 (a) it can be seen that a peak associated to (440) of the cubic spinel phase appears at a composition x = 0.25. An abrupt change in the XRD pattern of the composition x = 0.35 as compared to that of x = 0.25, has been noticed. The (440) peak of Fd3m phase has been found to suppress and a new (440) peak of $P4_332$ phase appears. On further increasing the concentration of Mg two more peaks can be seen, which correspond to the two space groups mentioned. The phase equilibrium has been ensured by grinding and recalcining the powders of various compositions for 12 hours. Fig. 4.3.2(b) shows the slow scan data obtained after two-time calcination process. A clear change in the patterns is observed compared to the patterns which were obtained after one-time calcination. It can be seen from the Fig. 4.3.2(b) that for $LiMg_{0.5}Mn_{1.5}O_4$, peak corresponding to Fd3m got completely suppressed and the pattern can be indexed as single phase ordered cubic spinel with space group $P4_332$. However in case of $LiMg_{0.35}Mn_{1.65}O_4$, (440) peak shoulder can be observed. The two peaks corresponding to (440) for both the Fd3m and $P4_332$ phases which were found to exist for the compositions x = 0.25, 0.35 and 0.50 of the one-time calcined powder, are observed at the composition x = 0.25 after two-time calcined powder, indicating the onset of phase equilibrium. This observation has further been verified by conducting Rietveld refinement of the patterns, which shows an increased phase content of the $P4_332$ in the compositions x≥0.25. In order to confirm the phase equilibrium whether reached, further regrinding and calcinations (three and four time) of the powder have been done. The XRD patterns with slow scanning have been shown in Fig. 4.3.2(c) and 4.3.2(d). A clear evidence of peaks splitting in the pattern of the three time calcined powder of composition x = 0.25, can be seen

from the Fig. 4.3.2(c). The pattern after four time calcination is almost similar to that observed after three times calcined an d this shows that the phase equilibrium has been attained after three time of calcination.
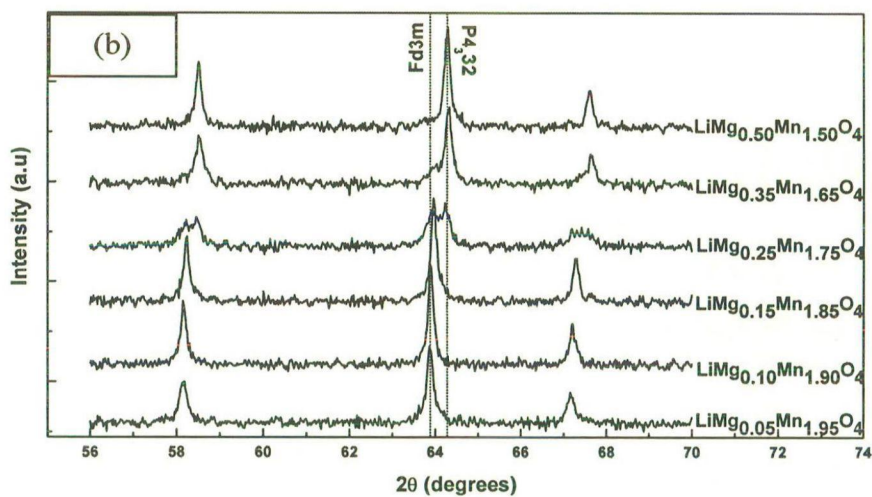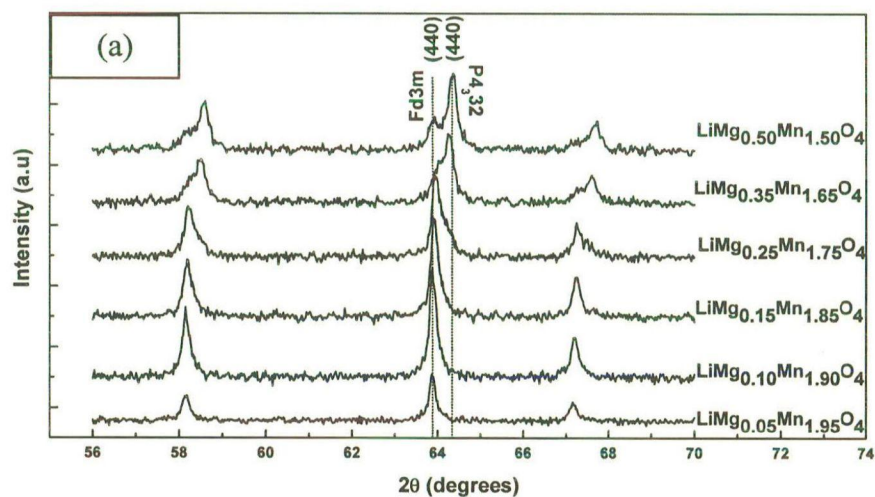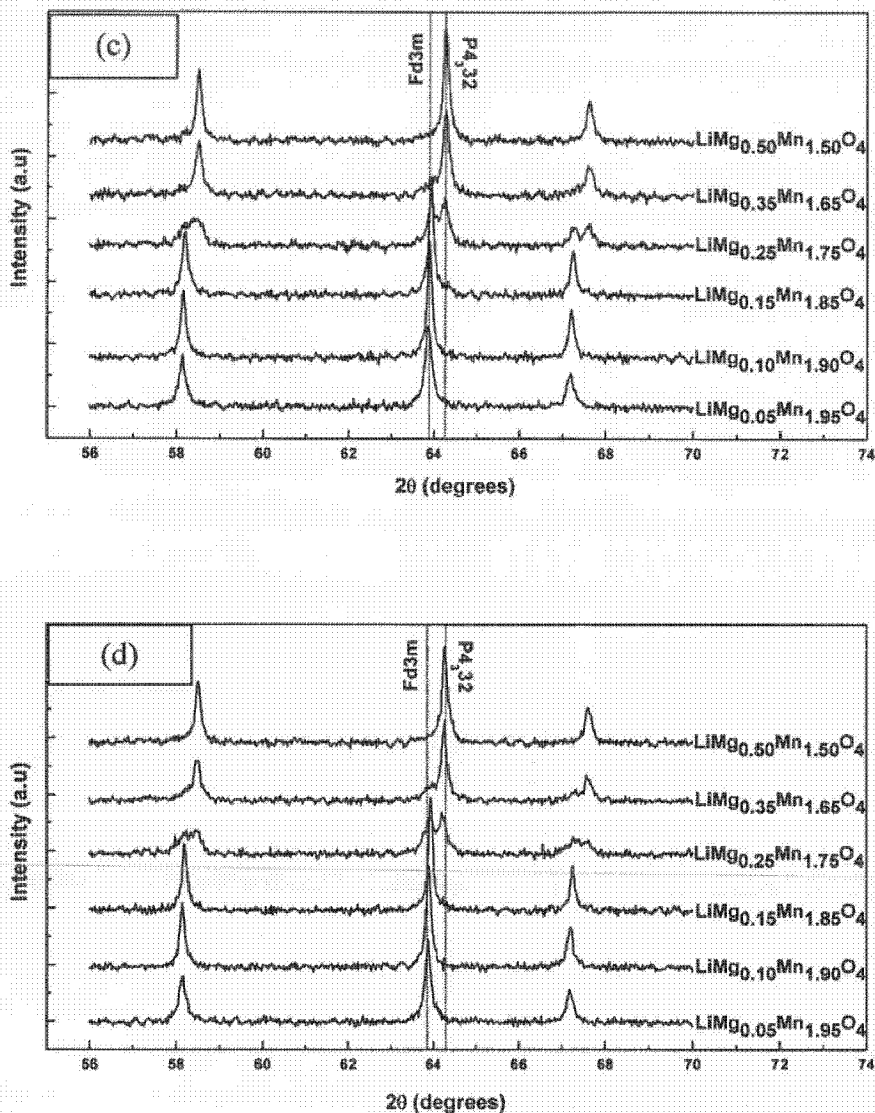
Fig. 4.3.2: Slow scanned XRD data after (a) one-time calcination (b) Two time calcination (c) three times calcination and (d) four times calcination

The relative proportions of different phases with space group Fd3m and P4₃32 have been estimated from the results of Rietveld refinement. The variations of different phase groups with composition have been shown by plotting graphs in Fig. 4.3.3 using sigmoidal function. It has been observed that the compound $LiMg_xMn_{2-x}O_4$ with $x \leq 0.15$ has spinel structure having space group Fd3m. As the concentration of Mg increases, the proportion of spinel phase having space group P4₃32 increases. Hence it can be concluded that in $LiMg_xMn_{2-x}O_4$

for x≤0.15, the structure is a single phase disordered cubic spinel with space group of Fd3m and for x>0.25, the structure is an ordered cubic spinel having space group of $P4_332$. However, a striking feature is observed in the case of $LiMg_{0.25}Mn_{1.75}O_4$ which contains both the space groups of Fd3m and $P4_332$. This implies that the transition from Fd3m to $P4_332$ is gradual over a composition range rather than abrupt at a composition of $LiMg_{0.3}Mn_{1.7}O_4$ as reported in the literature Nakamura et al., 2008.

The coexistence of two space groups has been reported for $CuNi_{0.5}Mn_{1.5}O_4$ system, in which better Rietveld refinement results were obtained when multiphase refinement using both the ordered $P4_332$ and disordered Fd3m structures were considered Branford et al., 2002.
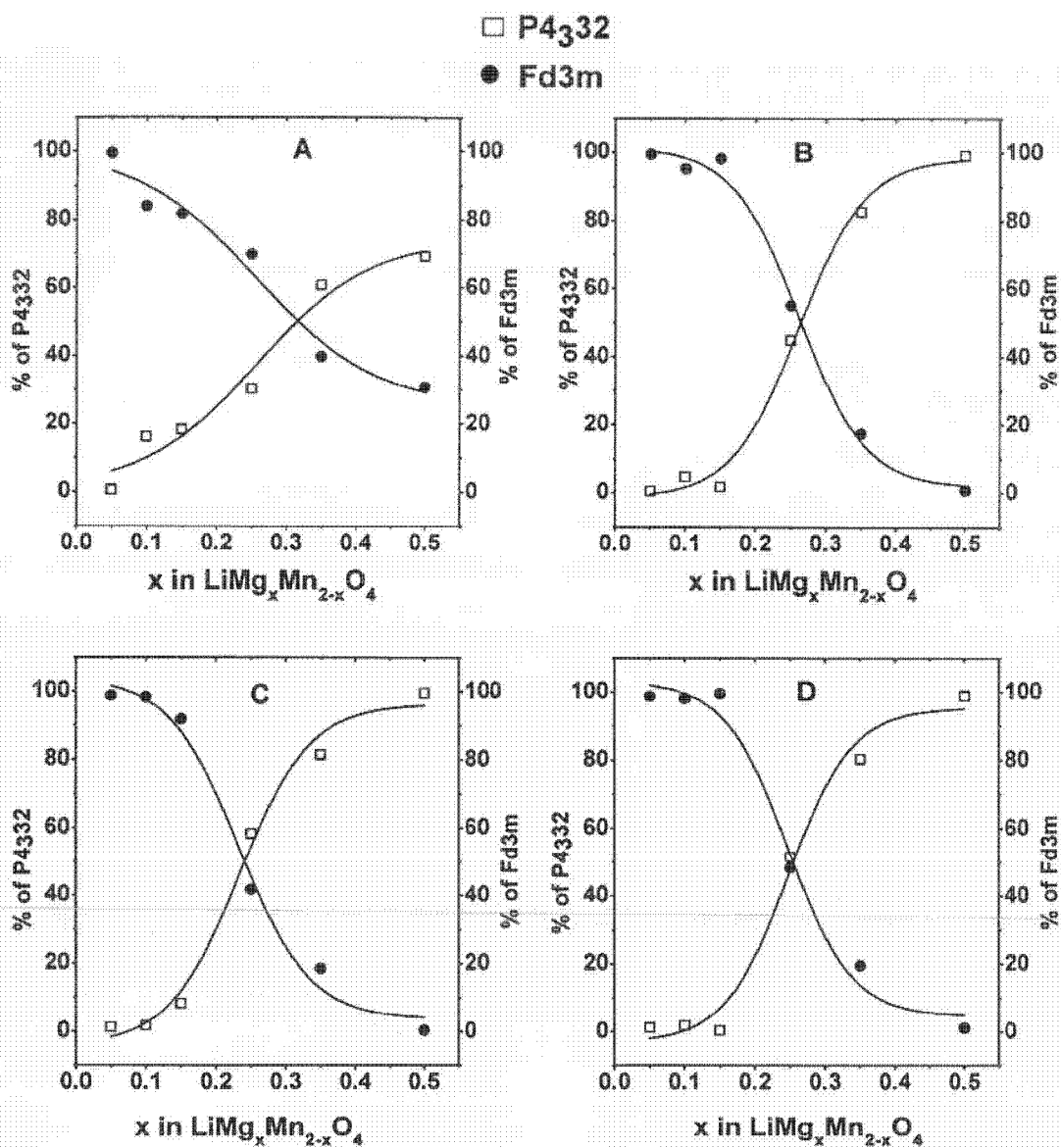
Fig. 4.3.3: Percentage variation of various space groups with the increase in Mg content in LiMg$_x$Mn$_{2-x}$O$_4$ (0.05≤x≤0.50) after (a) one time calcination (b) two time calcination (c) three time calcination and (d) four time calcination.

The colour of the synthesized powder in $LiMg_xMn_{2-x}O_4$ changes from grey for x = 0.25 to dark brown for x = 0.35 and then to light brown for x = 0.50. The colour change is also an indication of the phase transformation, as colour of transition metal oxides is highly sensitive to the structural transformation and valence change. The following model has been suggested for maintaining the charge neutrality condition in the octahedral doped $LiMn_2O_4$ having Fd3m as space group:

$$Li^+[Mg_x^{2+}Mn_{1-2x}^{3+}Mn_{1+x}^{4+}]O_4^{2-}$$
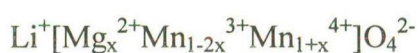
The ratio $Y = Mn^{3+}/Mn^{4+}$ has been calculated for the various compositions. Y decreases with the increase in Mg^{2+} content and this in turn shows that the Mn^{4+} increases in the compound. Y has been calculated to be 0.4 and 0.22 for x = 0.25 and 0.35 respectively. Therefore the present XRD results show that phase transformation from Fd3m to $P4_332$ space group takes place when the Y becomes nearly 0.4.

4.3.2 Morphology Studies

FESEM micrographs of the powders obtained after first and fourth calcination are shown in Fig. 4.3.4 and 4.3.5 respectively. Micrographs show that the particles are in a state of higher agglomeration. Agglomeration is still more in case of the four-time calcined samples.
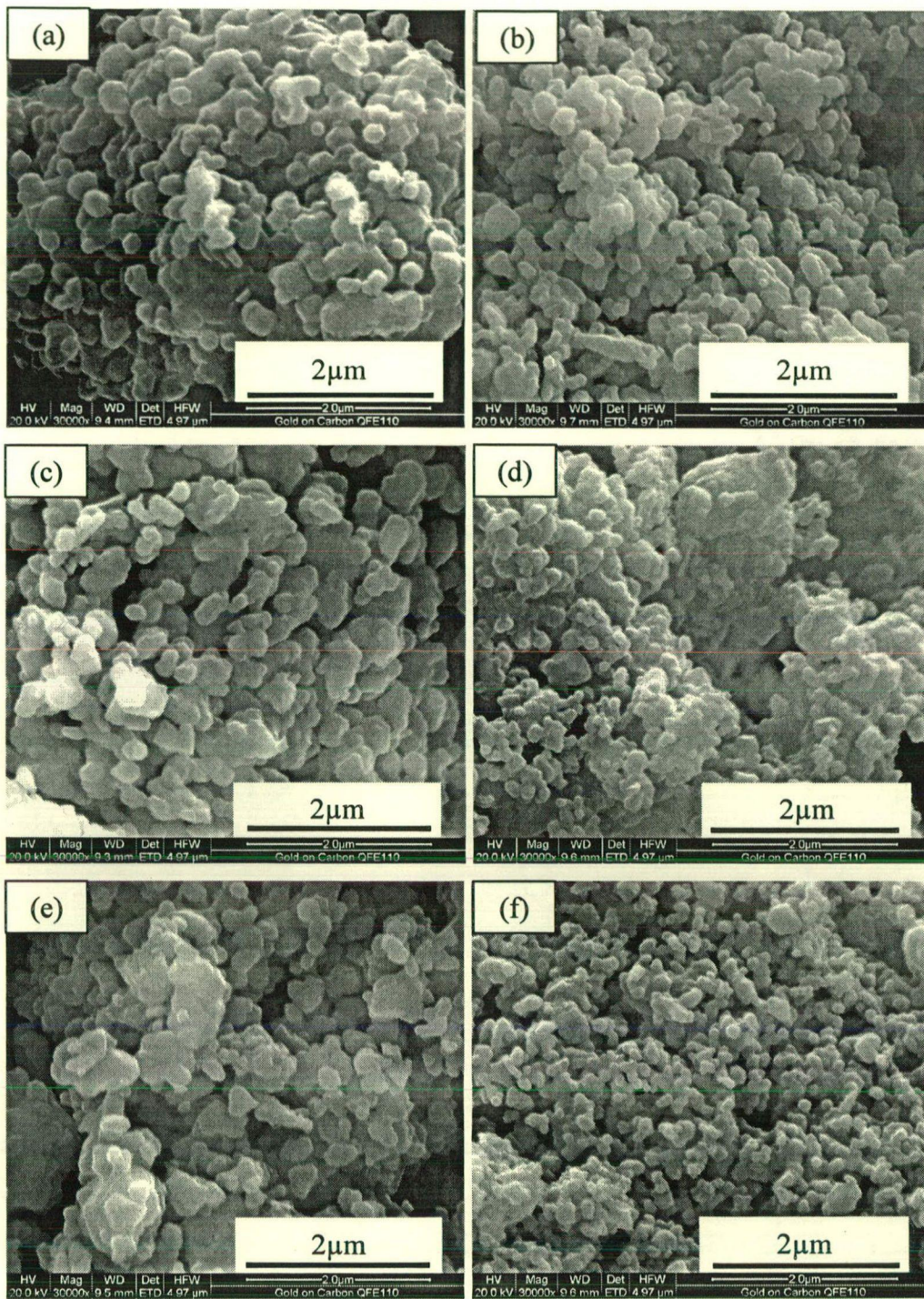
Fig. 4.3.4: Micrographs of the powder $LiMg_xMn_{2-x}O_4$ obtained after one-time calcination
[(a): x = 0.05; (b): x = 0.10; (c): x = 0.15; (d): x = 0.25; (e): x = 0.35; (f): x = 0.50]
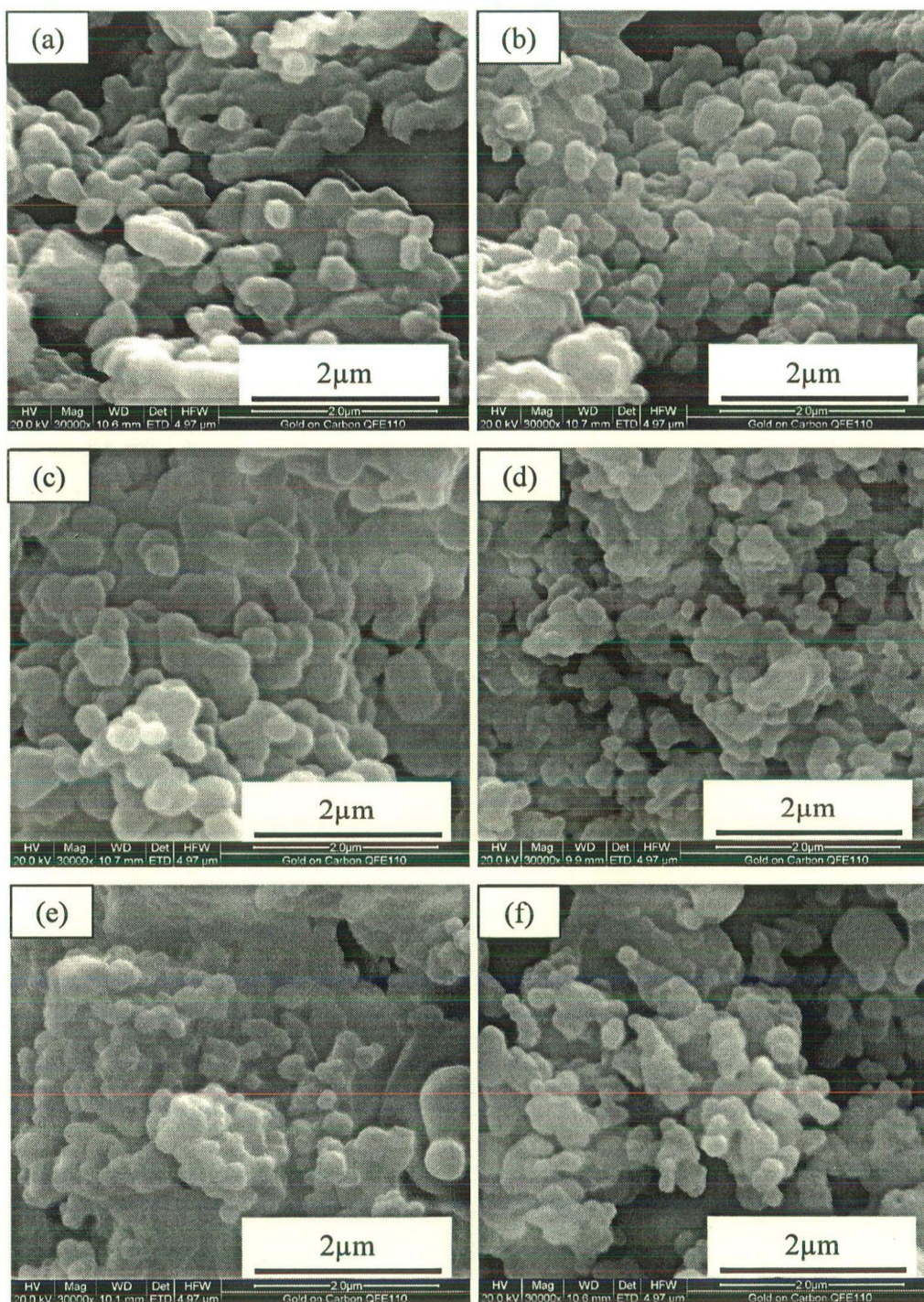
Fig. 4.3.5: Micrographs of the powder $LiMg_xMn_{2-x}O_4$ obtained after four-time calcination [(a): x = 0.05; (b): x = 0.10; (c): x = 0.15; (d): x = 0.25; (e): x = 0.35; (f): x = 0.50]

Agglomeration can be explained on the basis of the fact that primary particles tend to join each other in order to minimize their surface energy. Micrographs show truncated octahedron

morphology in all the compositions studied. No noticeable change in the morphology of the particles has been observed with the increase in Mg content.

For the powders having higher Mg content ($x \geq 0.25$), the average particle size is lower than that containing lower Mg content. This shows that with the increase in Mg content the surface area to volume ratio increases, which leads to a decrease in particle size. The decrease in the particle size can also be explained on the basis of the fact that with the increase in Mg content the nucleation rate becomes higher than the growth rate of the particles. The average particle size of the various samples after one time calcination lies in a range of 250 to 100 nm. After the calcination for four times the particle size increases and the average particle size falls in the range of 350 to 200 nm.

4.3.3 Thermal Analysis

Thermal stability of the materials has been evaluated in a wide temperature range from room temperature to 1400 °C. Fig. 4.3.6 illustrates the TG traces of various samples calcined in air. The figure shows that there exist two temperatures T_{c1} and T_{c2}, at which the weight losses are significant. Thackeray et al., 1996 have shown that T_{c1} corresponds to the oxygen loss from the structure, leading to the oxygen nonstoichiometry in the structure. This results in the formation of Li_2MnO_3 and tetragonal spinel depending on the amount of oxygen loss from the structure. Above T_{c2} the oxygen loss is very high, which leads to the consumption of the Li_2MnO_3 phase by the Mn rich spinel phase to produce $LiMnO_2$. TG plot shows that the transition T_{c1} shifts towards lower temperature and the weight loss corresponding to this temperature decreases with the increase in Mg content from 0.15 to 0.5. This shows that the oxygen loss from the structure starts at lower temperature with the increase in Mg content. The weight loss corresponding to a fixed temperature (~ 852 °C) is found to be less for the composition x = 0.15 compared to x = 0.05 and 0.1. This shows that the oxygen loss in the structure, with x = 0.15, is less compared to x = 0.05 and 0.1, even though this loss starts at lower temperature.
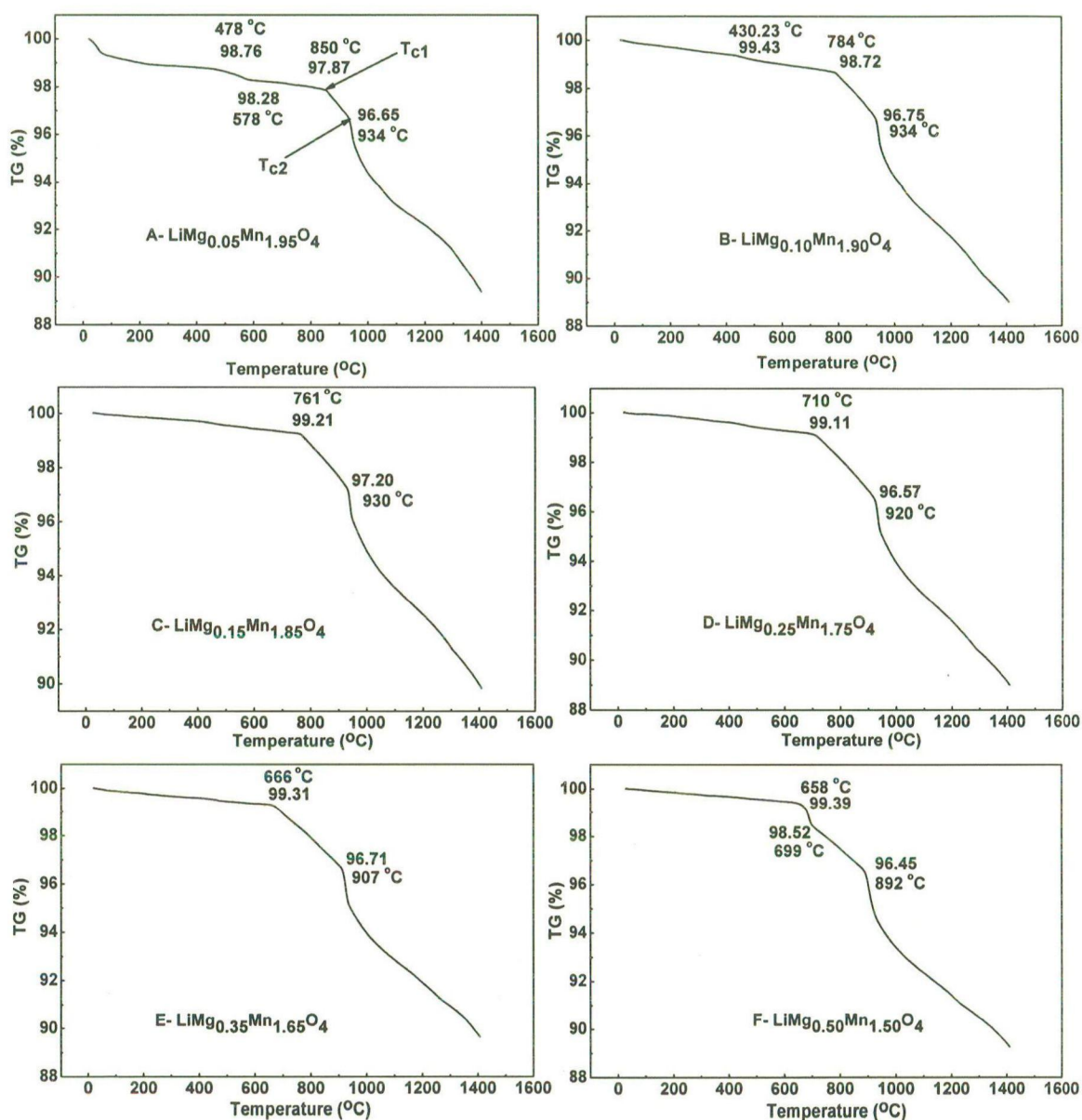
Fig. 4.3.6: TG plots of various calcined powders heated up to the temperature of 1400 ^{o}C in air

There is also a slight decrease in the net weight loss up to a transition temperature T_{c2} as the Mg content increases from 0.05 to 0.15. Upon further increasing the Mg content upto x = 0.25, a sudden increase in the weight loss is observed up to a fixed temperature i.e. 852 ^{o}C. The weight loss increases corresponding to a fixed temperature i.e. 852 ^{o}C for x ≥ 0.25,

however the transition temperature T_{c2} decreases sharply. The sudden initial weight loss in the composition $LiMg_{0.05}Mn_{1.95}O_4$ is considered as an experimental artifact. The critical observation on the TG plots show that as the Mg content increases the weight loss increases over the temperatures between T_{c1} and T_{c2}. Since weight loss between T_{c1} and T_{c2} correspond to the formation of monoclinic Li_2MnO_3 and tetragonal $LiMn_2O_4$, depending upon the oxygen loss from the structure, therefore it can be inferred that the formation of Li_2MnO_3 and tetragonal $LiMn_2O_4$ increases with the increase in Mg content. Variation of T_{c1} with the increase in Mg content is exponential and is shown in Fig. 4.3.7.
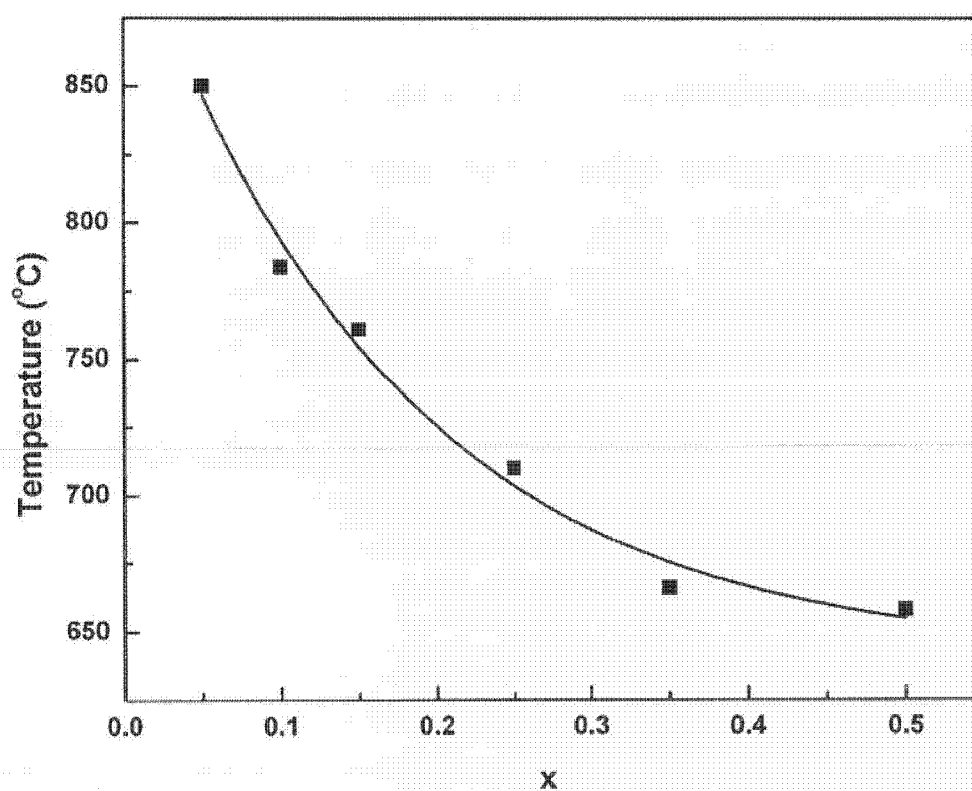
Fig. 4.3.7: Relationship between the Mg doping content and the decomposition temperature to form nonstoichiometry ($LiMg_xMn_{2-x}O_{4-\delta}$) in the air

DTA plots for all the samples are shown in Fig. 4.3.8. The transition corresponding to the formation of $LiMnO_2$ shifts to the lower temperatures as the Mg content increases. In case of $x \geq 0.25$, a few additional peaks can be observed at lower temperatures. These peaks are

perhaps due to the formation of tetragonal spinel $LiMn_2O_4$, because the oxygen and lithium loss from the structure above x = 0.25 is high. Such observations in the DTA trace can further be confirmed if temperature dependent XRD studies on the samples are carried out.
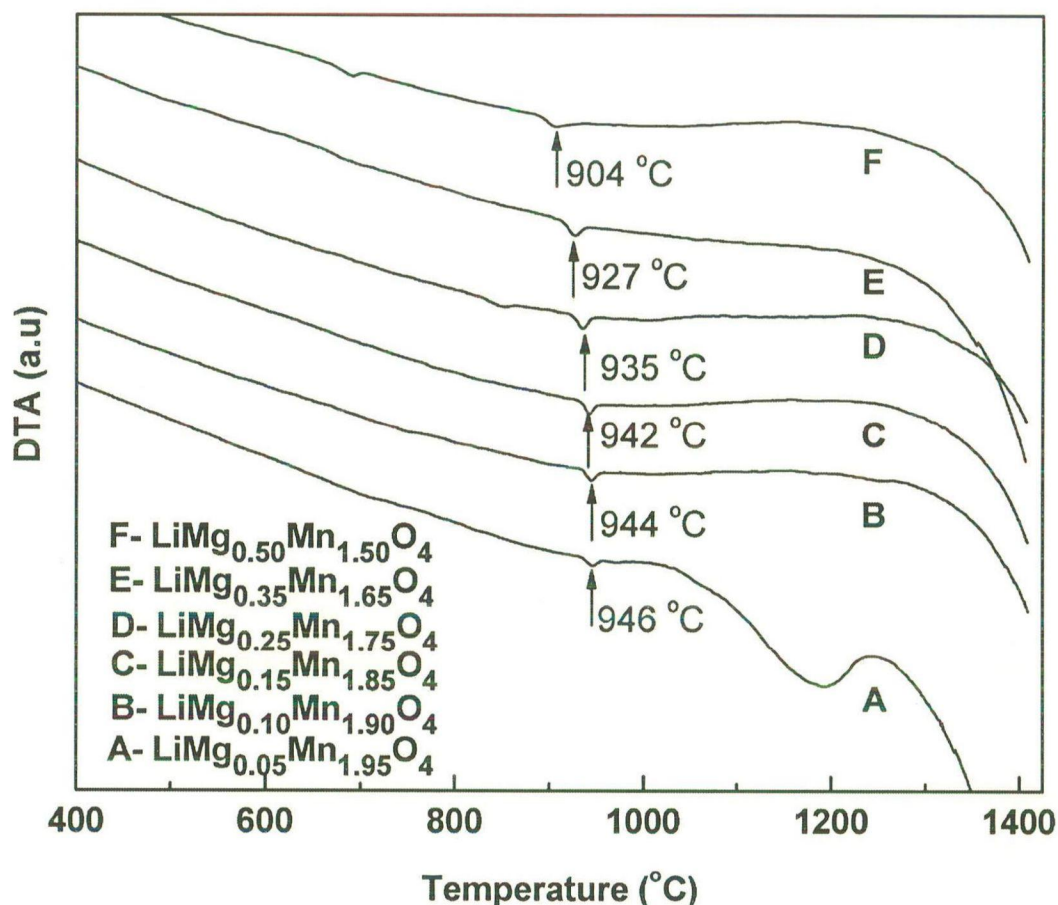
Fig. 4.3.8: DTA curves for the various compositions of $LiMg_xMn_{2-x}O_4$ ($0.05{\leq}x{\leq}0.5$)

4.3.4 Spectroscopic Studies

The disordered normal cubic spinel structure consists of a cubic close packed array of O ions with the transition metal ions occupying octahedral and Li ions occupying tetrahedral interstices. In the structure having space group O_h^7, Li ions occupy 8a sites with a point group symmetry of T_d, transition metal ions occupy 16d sites which has point group symmetry of D_{3d} and O ions occupy 32e sites with site symmetry of C_{3v}. The ordering of the ions in case

144

of ordered spinel reduces the space group symmetry from O_h^7 to O^7. The symmetry reduction leads to the increase in cell volume which results in increase in the number of allowed modes. Therefore, the higher number of IR active modes present in the highly doped compositions compared to the case with lesser number of modes present in the lightly doped compositions, is a reliable indication of existence of ordered spinel structure. It has been shown by White and deAngelis, 1967 using group theory that in case of disordered cubic spinel with space group symmetry Fd3m, only four fundamental modes exist. However, the number of modes increases to 21 for the ordered spinel structure. The bands become sharper as the structure transforms to an ordered cubic spinel.
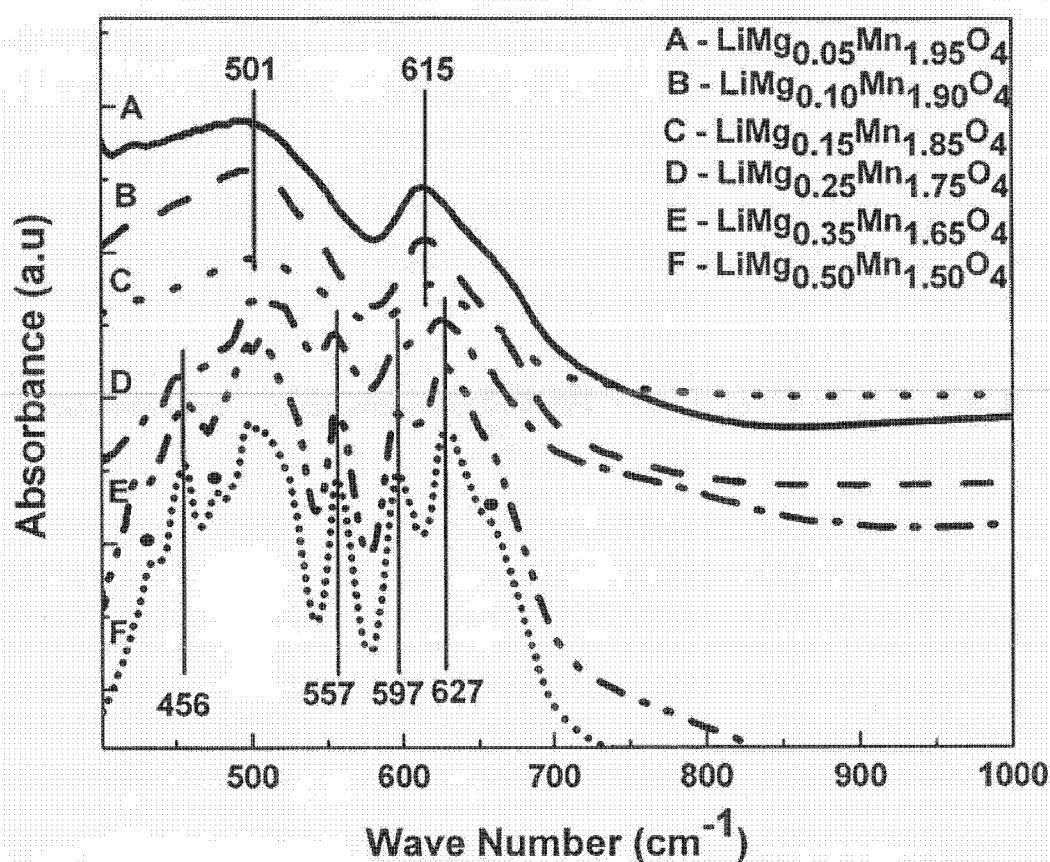
Fig. 4.3.9: Absorbance FTIR spectrum of $LiMn_2O_4$ doped with various Mg content

The FTIR spectra of $LiMg_xMn_{2-x}O_4$ consist of two bands located at approximately 615 and 501 cm^{-1} as shown in Fig. 4.3.9 and these bands correspond to the asymmetric stretching modes of MnO_6 group. Julien et al., 2003 in their spectroscopic studies of $LiMn_2O_4$ have

shown that the vibrations present at the higher wave numbers correspond to the octahedral symmetry of the ions and these bands occur in the 500-900 cm^{-1} range. However Li-O bands appearing at lower frequency, corresponding to LiO_4, occurs mainly in the absence of the important vibrational interaction between LiO_4 and other coordination groups. As the Mg content increases to x = 0.25 in $LiMg_xMn_{2-x}O_4$, the bands present at higher frequency of 615 cm^{-1} starts splitting with the evolution of two new bands at 627 and 597 cm^{-1}. However, these bands are not very sharp for x=0.25, which shows the partial ordering of the ions present with this composition in the structure. Similarly the evolutions of other bands present at ~ 557 and 456 cm^{-1} have taken place. The new bands became sharper (noticeably at x = 0.35 and x = 0.50) as the content of Mg increased. Few very low intensity bands can also be seen in the figure for the highly doped compositions. This shows that structure gets more ordered with the increase in Mg content and this is in full agreement with the XRD results which has shown that the space group of $LiMg_xMn_{2-x}O_4$ changes from Fd3m (disordered cubic spinel) to P4$_3$32 (ordered cubic spinel) with the increase in Mg content.

4.3.5 Impedance Spectroscopy

The room temperature impedance measurements on the samples were made in a frequency range of 40Hz to 10MHz. The real and imaginary parts of the impedances for different frequencies have been plotted in a complex plane as shown in Fig. 4.3.10. The data lies on a depressed semicircular arc, extrapolation of which towards lower frequency region intercepts the x-axis giving the bulk resistance of the sample. The electrical conductivities (σ) of the samples have been calculated using the following relation

$$\sigma = (1/R) \times (l/A)$$

where R is the bulk resistance, l is thickness and A the area of the flat face of cylindrical samples (this of course you are writing in every sections). The σ values of undoped $LiMn_2O_4$ and doped samples in the systems $LiMg_xMn_{2-x}O_4$, (0.05 $\geq$ x $\geq$ 0.15) are given in Table 4.3.3. Variations of the real (Z') and imaginary (Z") parts of impedance as a function

of frequency are shown together in Fig. 4.3.11 and 4.3.12 respectively. Fig. 4.3.11 shows that at higher frequencies particularly from 5 MHz and above, Z′ becomes almost same for all the three compositions in the system $LiMg_xMn_{2-x}O_4$ studied. However, at lower frequencies the Z′ increases with increase in Mg content.

Table 4.3.3: Conductivity values for $LiMg_xMn_{2-x}O_4$; $0.0 \leq x \leq 0.15$

$LiMn_2O_4$	$LiMg_{0.05}Mn_{1.95}O_4$	$LiMg_{0.1}Mn_{1.9}O_4$	$LiMg_{0.15}Mn_{1.85}O_4$
6.71×10^{-5} S/cm	3.05×10^{-5} S/cm	2.46×10^{-5} S/cm	1.67×10^{-5} S/cm
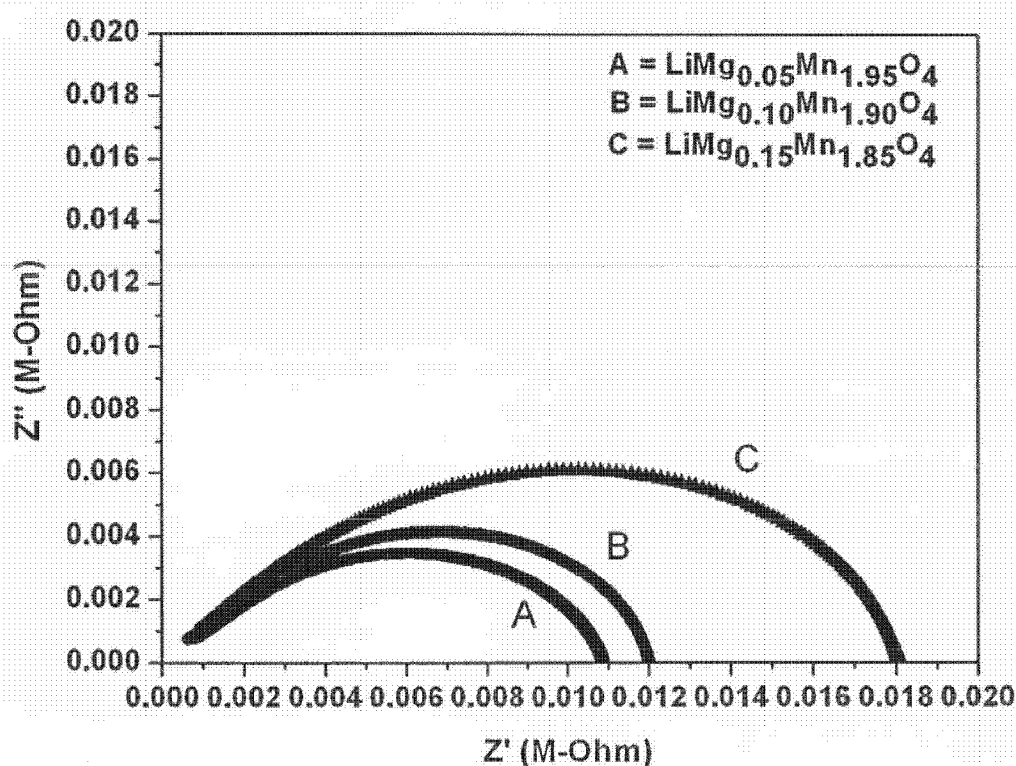
Fig. 4.3.10: Variation of the real part (Z′) with the imaginary part (Z″) of impedance

This shows that the degree of electric polarization in the material is low at lower frequencies for doping with lower Mg content. Polarization increases as the Mg content increases.

147
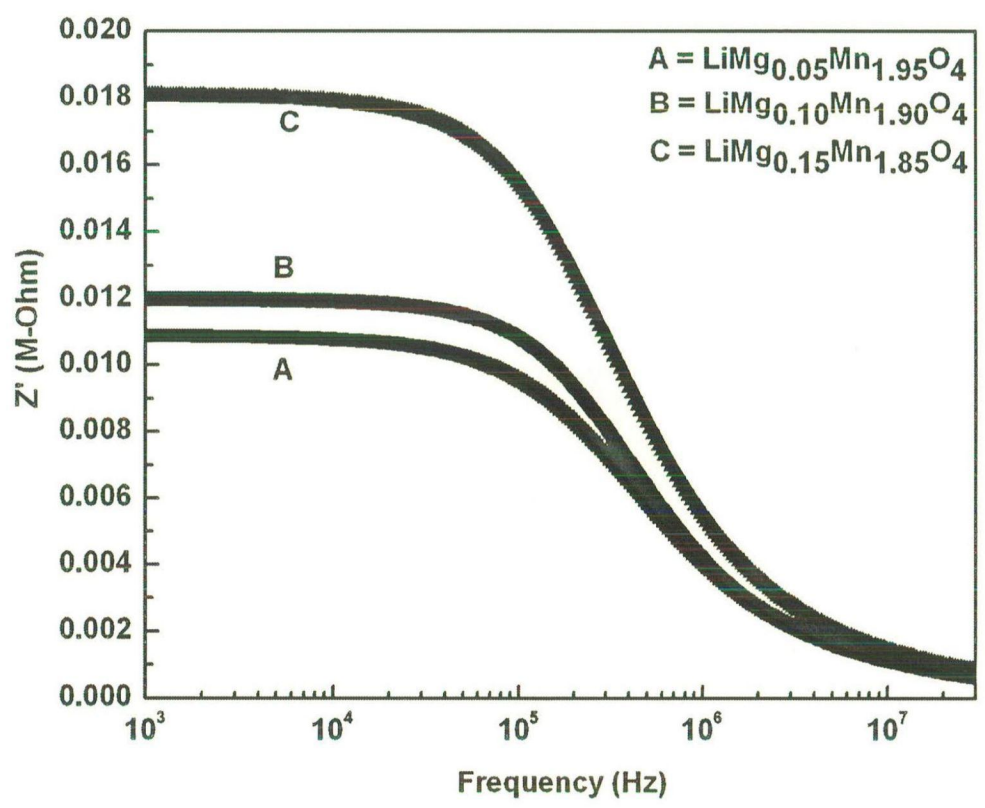
Fig. 4.3.11: Variation of the real part (Z') of impedance with the increase in frequency
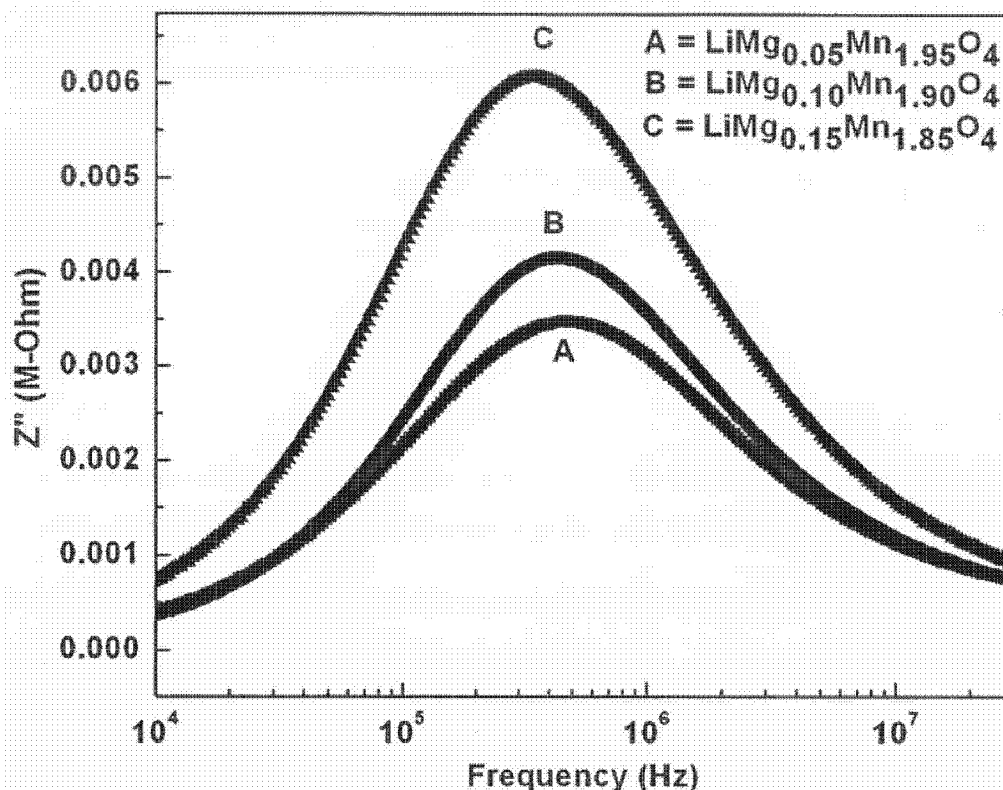
Fig. 4.3.12: Variation of the imaginary part (Z″) of impedance with the increase in frequency

Fig. 4.3.12 shows the loss spectrum i.e. variation of Z″ with frequency. Peak width (full width at half maximum) reduces and the peak intensity increases with the increase in Mg content. Broadening of the peak suggests the relaxation effect present in the material. The broadening of course decreases with the increase in Mg content in $LiMn_2O_4$. Hence the molecules are in more relaxed state in the case of lower doping level. Since relaxation is generally caused by the delay in molecular polarization with respect to changing electric field, therefore relaxation process is a composition dependent phenomenon.

4.3.6 Electrochemical Studies

Performance of Mg doped $LiMn_2O_4$ material as a cathode of the Li ion battery has been checked in a voltage range of 4.3 V to 3.0 V at room temperature. Performance of the

$LiMn_2O_4$ doped with Mg is checked only for the lightly doped compositions, because the fall in capacity is tolerable only up to a limited extent. Since it has been observed that the capacity falls with the increase in Mg content, therefore the measurements have been made only for the compositions $LiMg_xMn_{2-x}O_4$ ($0.0 \leq x \leq 0.15$). Discharging curves of the various samples in the voltage range 4.3 to 3.0 V are shown in Fig. 4.3.13. The discharging capacity decreases with the increase of Mg content in $LiMn_2O_4$. Such a decrease in the discharge capacity value is due to the decrease in the content of Mn^{3+} with the increase of Mg doping concentration. With the increase of Mg content the amount of Mn^{4+} increases and hence a decrease in the capacity value can be observed. Mn^{3+} can be oxidized easily, however the oxidation of Mn^{4+} is not possible in this voltage range.
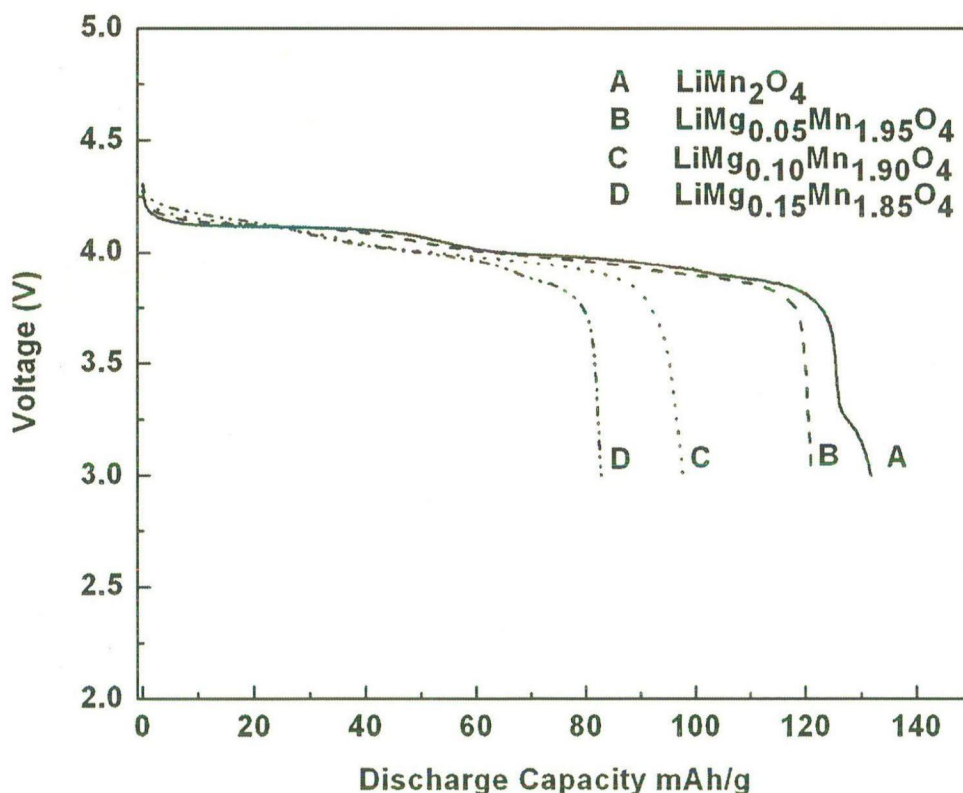
Fig. 4.3.13: First cycle discharge curves for the various compositions in the voltage range of 4.3 V to 3.0 V

150

The ideal composition in which the Mn oxidation state is +4 ($Li_4Mn_5O_{12}$) does not show any capacity in this voltage range. Therefore with the increase in chromium content the capacity corresponding to the 4 V region decreases. Fig. 4.3.13 shows that the voltage profile which corresponds to the reduction of the Mn^{4+} occurs at the higher voltage in case of highly doped compositions. Therefore the material shows small capacity in the higher voltage region. This shows that the some of the Li insertion in the host structure takes place at higher voltages. In case of λ-Mn_2O_4, at 4.3 V almost all of the Li sites are available in the host structure to accommodate Li therefore Li ions can be easily inserted in the structure and hence a voltage plateau at higher voltage ~ 4.15 V can be seen in the discharge profile. After partial occupation of the Li sites at approx x=0.5 in $Li_xMn_2O_4$, the repulsive interaction between Li-Li increases and give rise to a voltage plateau at ~ 4 V. With the increase in Mg content the available sites for the Li insertion are less, because during charging whole of the Li can not be extracted from the cathode in this voltage range (4.3 - 3.0 V) and some Li left behind in the structure. Therefore Li ions face repulsive interaction from the other Li ions which are already present in the structure even at 4.3 V, and hence find difficulty in the insertion process. Ohzuku et al., 1990, have shown that the voltage step at ~ 4.15 V, in case of $LiMn_2O_4$, corresponds to the cubic–cubic structural transition. Hence from the present study it can be concluded that disappearance of the voltage step with the increase in Mg content shows the suppression of the structural transition.

Charging-discharging behavior of the compounds has also been studied for the 10 cycles. Slight Mg doping reduces the fading of discharge capacity significantly. The decrease in the fall of the discharge capacity with the number of cycles show the stability of the Mg doped $LiMn_2O_4$. The discharge capacity values after second and 10th cycle is given in the table 4.3.4.

Table 4.3.4: Discharge capacity values for $LiMg_xMn_{2-x}O_4$; $0.0 \leq x \leq 0.15$

Various Compositions	$LiMn_2O_4$	$LiMg_{0.05}Mn_{1.95}O_4$	$LiMg_{0.1}Mn_{1.9}O_4$	$LiMg_{0.15}Mn_{1.85}O_4$
2nd discharge capacity	131 mAh/g	121 mAh/g	97 mAh/g	82 mAh/g
Discharge capacity after 10 cycles	124 mAh/g	119 mAh/g	96 mAh/g	80 mAh/g

4.4.1 Phase Analysis

LiCo$_{1/3}$Mn$_{1/3}$Ni$_{1/3}$O$_2$ with R′ (citric acid to metal ion ratio) = 1, 2, 3 have been synthesized. XRD patterns of all the three powdered samples having R′ = 1, 2, and 3 are shown in Fig. 4.4.1, which shows that the XRD patterns of LiNi$_{1/3}$Mn$_{1/3}$Co$_{1/3}$O$_2$ are quite similar to that of single phase LiCoO$_2$ and LiNiO$_2$ as reported in the literature (Mizushima et al. 1980, Thongtem et al. 2005).
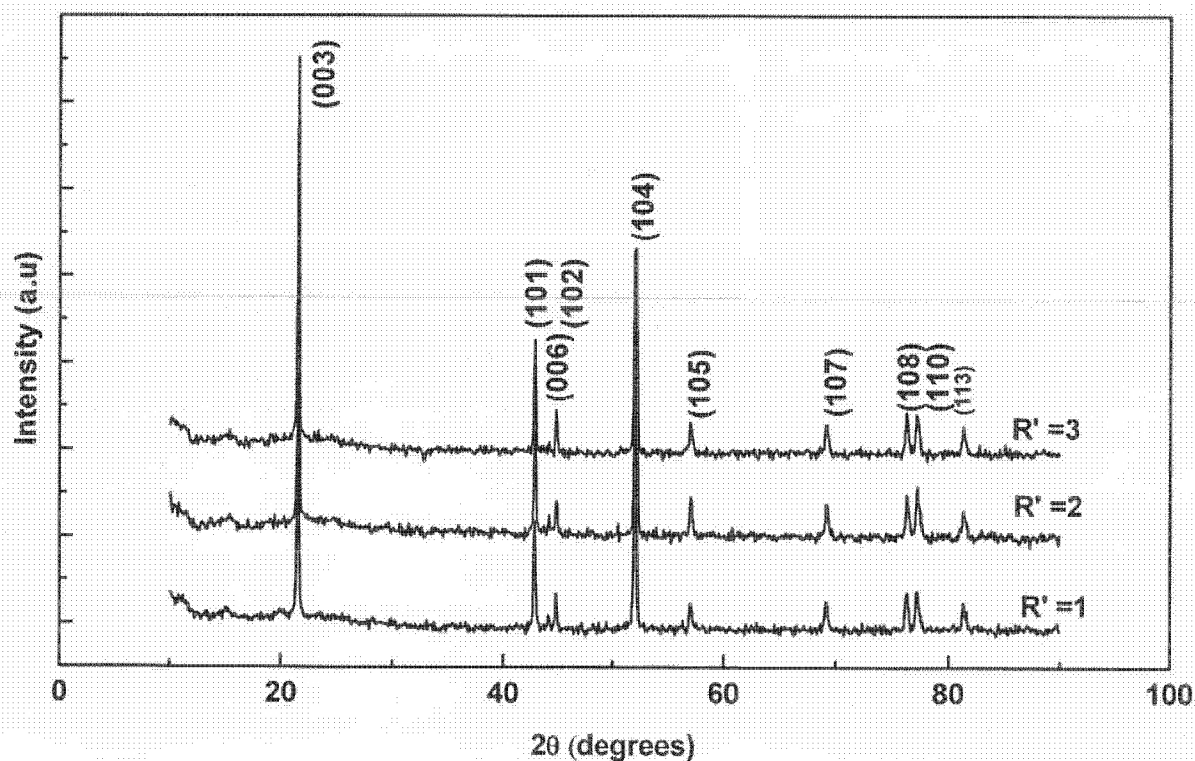
Fig. 4.4.1: XRD patterns of LiCo$_{1/3}$Mn$_{1/3}$Ni$_{1/3}$O$_2$ obtained for different concentrations of citric acid

The materials have single phase layered rhombohedral structure with space group of R3m. This indicates that single phase in the compound can be obtained for all the concentrations of

153

citric acid used. Rietveld refinement of the XRD patterns has been performed and the various parameters have been refined in order to get the good fitting of the experimental profile. Refined XRD patterns along with the difference plots for the different R′ are given in Fig. 4.4.2. Atomic coordinates and other refined parameters are given in Table 4.4.1 (a) and (b). For the higher citric acid content i.e. R′ = 3, the lattice parameter values are found to be higher compared to R′ =1, 2.
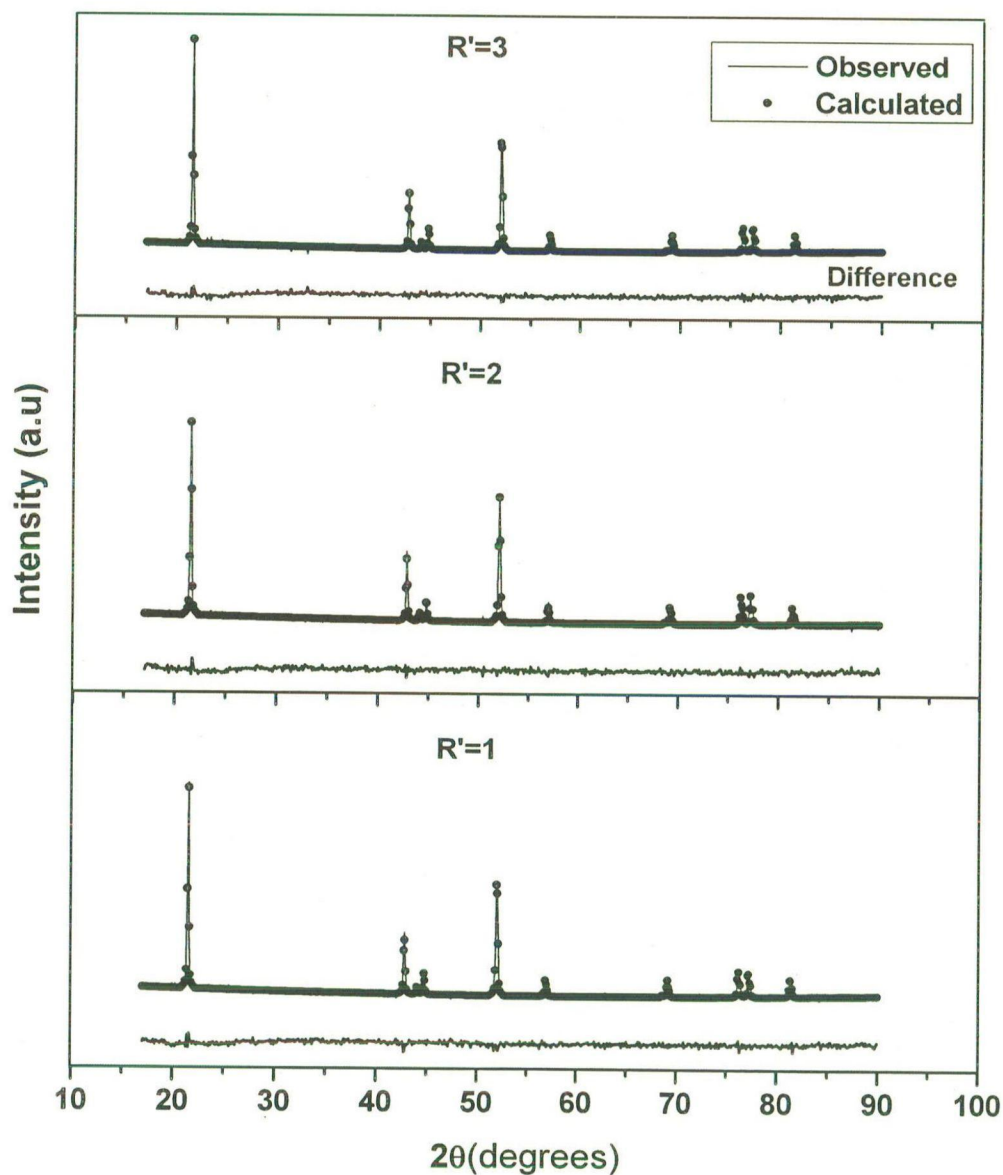
Fig. 4.4.2: Refined XRD patterns along with the difference plots of $LiCo_{1/3}Mn_{1/3}Ni_{1/3}O_2$ obtained for different concentration of citric acid.

Table 4.4.1 (a): Lattice parameters and agreement indices for $LiNi_{1/3}Mn_{1/3}Co_{1/3}O_2$

R'	Latice paramerters		c/a	Agreement indices %			
	a (Å)	c (Å)		Rex	Rp	Rwp	GOF
1	2.8617(1)	14.251(2)	4.9799	3.14	2.87	3.66	1.35
2	2.8617(2)	14.242(2)	4.9767	3.02	2.83	3.62	1.44
3	2.8620(3)	14.254(2)	4.9804	3.10	2.94	3.71	1.43

Table 4.4.1 (b): Occupancy and atomic coordinates for $LiNi_{1/3}Mn_{1/3}Co_{1/3}O_2$ for R' =3

Atom	Wyckoff Position	S.O.F	x	y	z
Li1	3a	0.966300	0.000000	0.000000	0.000000
Ni1	3a	0.033700	0.000000	0.000000	0.000000
Li2	3b	0.033700	0.000000	0.000000	0.500000
Ni2	3b	0.299600	0.000000	0.000000	0.500000
Mn	3b	0.333300	0.000000	0.000000	0.500000
Co	3b	0.333300	0.000000	0.000000	0.500000
O	6c	1.000000	0.000000	0.000000	0.241300

4.4.2 Morphological Studies

FESEM micrographs of all three samples with R'=1, 2 and 3 are shown in Fig. 4.4.3, which shows that the average particle size increases from 200 nm to 350 nm as R' changes from 1 to 2.
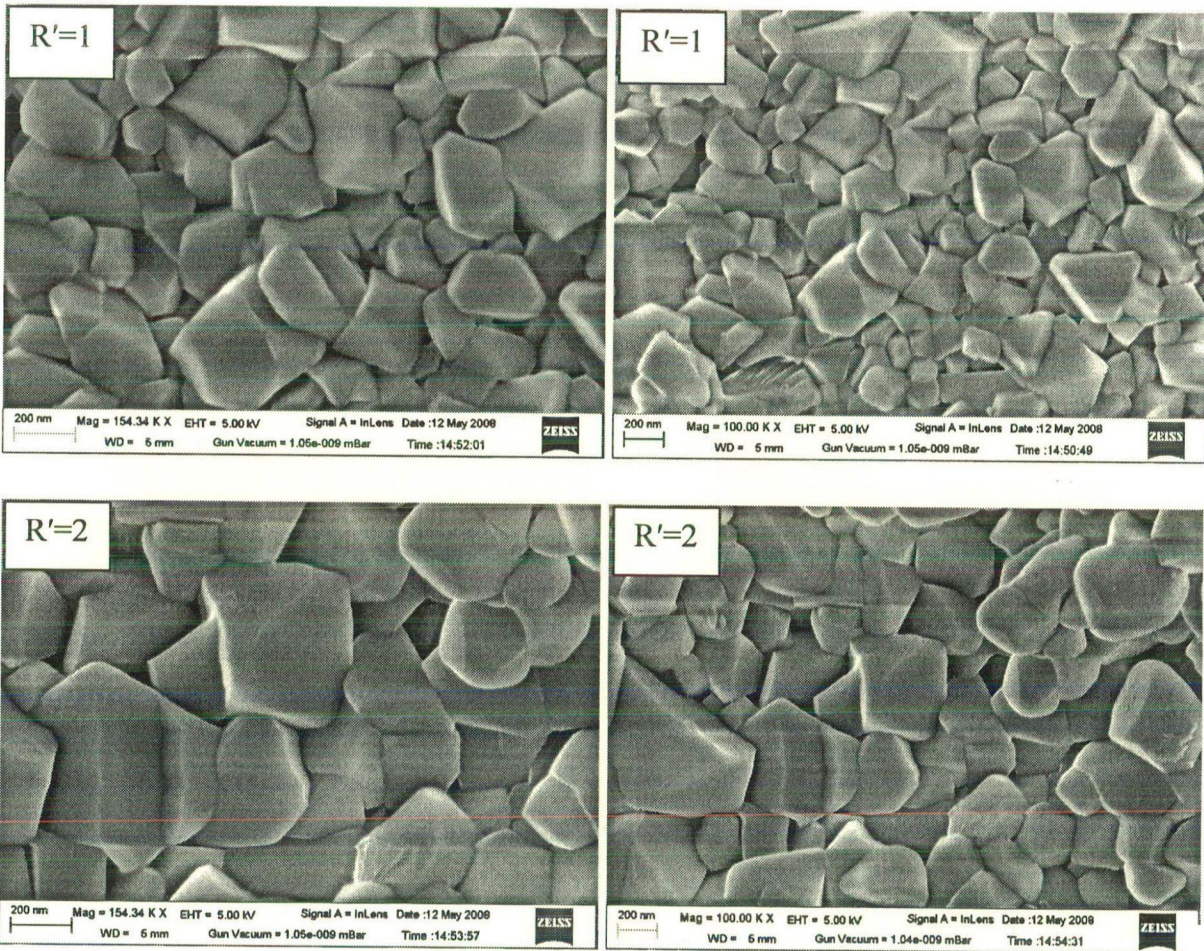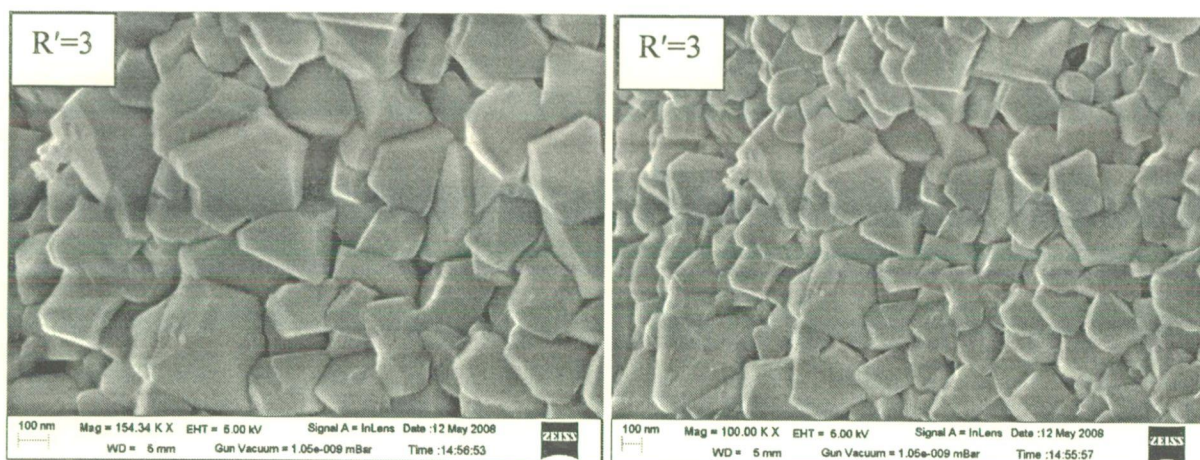
Fig. 4.4.3 Micrographs of $LiCo_{1/3}Mn_{1/3}Ni_{1/3}O_2$ powders obtained for different concentration of citric acid (R'=1, 2 and 3)

On further increasing the citric acid content the average particle size becomes 200 nm for R' =3. This is presumably due to the fact that at R' = 3 nucleation rate dominates growth rate leading to the formation of smaller particles. The decrease in particle size also shows the increase in surface area to volume ratio in the case of R' = 3, since the surface area to volume ratio decreases with the increase in particle size. The overall size range considering all the three cases of R' is 100 nm to 500 nm. In case of R' = 2, some of the particles are even larger in size. The compound $LiNi_{1/3}Mn_{1/3}Co_{1/3}O_2$ synthesized by sol-gel route has already been reported in the literature and particle size is of 1-3 μm (Hong et al. 2007), which is large, in comparison to that obtained in the present study. The morphology of the particles is found to be elongated truncated octahedron in all the samples studied, however it is found to be non uniform in all the samples. Fig. 4.4.4 shows the results of EDX analysis of the various samples conducted in the area scan mode. The compositions in atomic percent of Ni, Co and Mn in the samples are given in Tables 4.4.2 (a), (b) and (c). It is clear from the table that the composition is quite uniform across the volume of the materials.

157
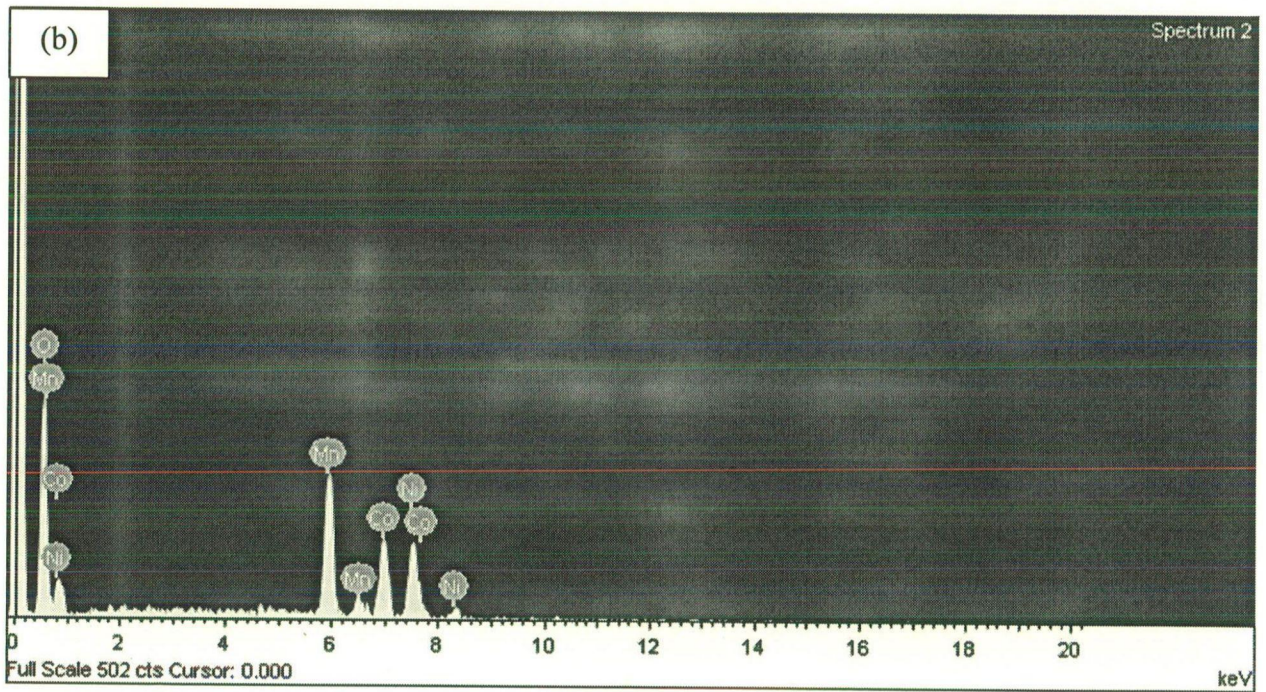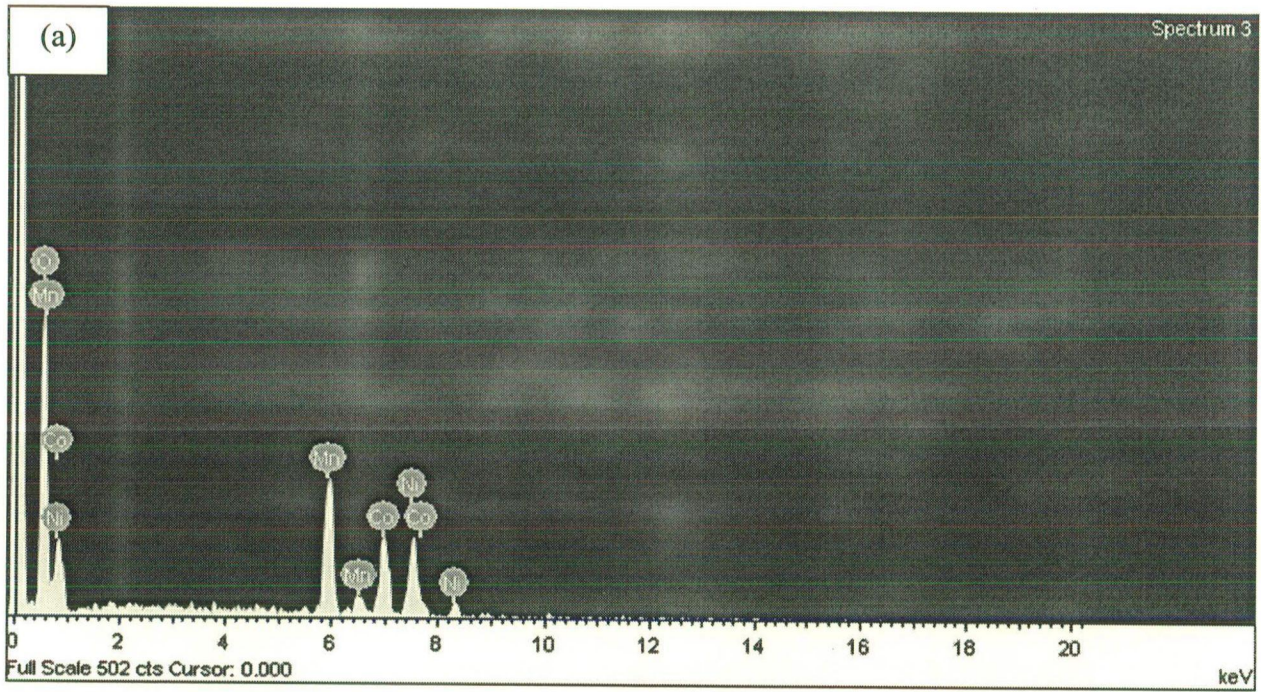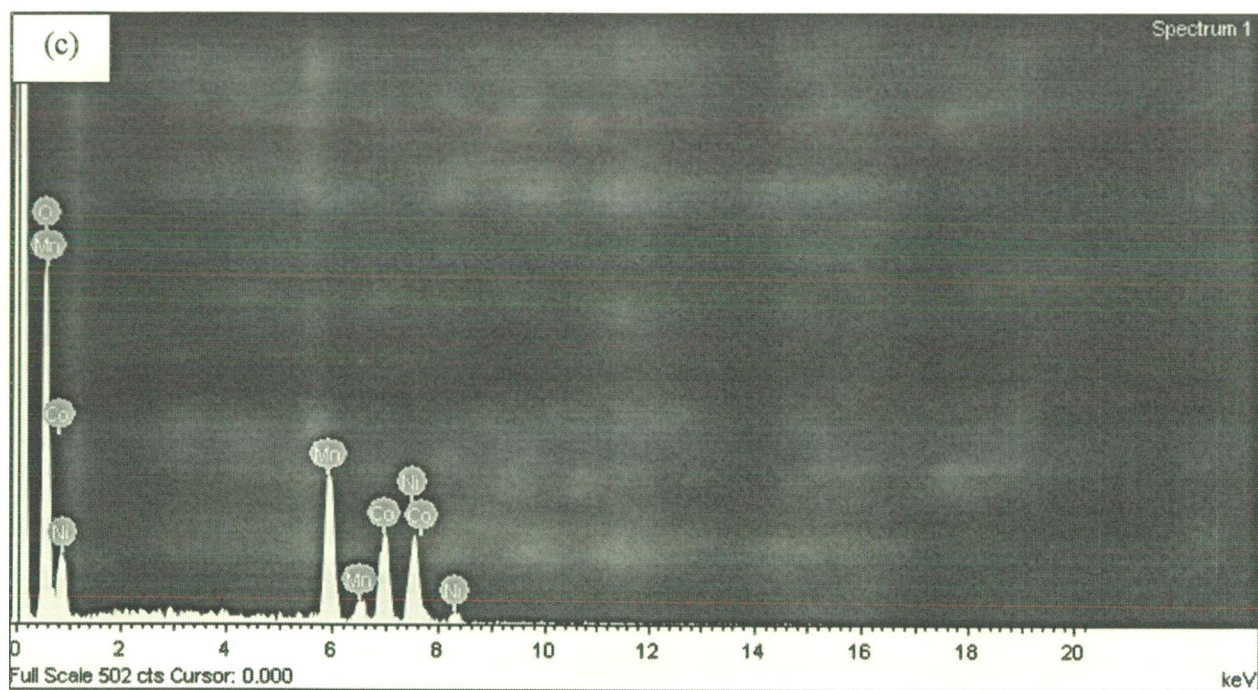
Fig. 4.4.4: EDX analysis of the various powdered sample of $LiCo_{1/3}Mn_{1/3}Ni_{1/3}O_2$ [(a): R′=1; (b): R′=2; (c): R′=3]

Table 4.4.2: Weight % and Atomic % of various elements present in three different samples as shown by EDX analysis

(a) R′=1

Element	Weight%	Atomic%
O	35.61	66.49
Mn	22.86	12.43
Co	19.69	9.98
Ni	21.83	11.11
Totals	100.00	100.00

(b) R′=2

Element	Weight%	Atomic%
O	29.75	60.32
Mn	24.23	14.30
Co	22.61	12.44
Ni	23.41	12.93
Totals	100.00	100.00

(c) R′=3

Element	Weight%	Atomic%
O	37.00	67.85
Mn	20.60	11.00
Co	20.01	9.96
Ni	22.39	11.19
Totals	100.00	100.00

This is due to the fact that in case of sol-gel synthesis of the material the reaction takes place at the molecular level, which allows the uniform mixing of the various metal salts. Therefore,

it may be inferred that the sol-gel synthesis yields homogeneous composition throughout the bulk. The results show that citric acid content for the powder synthesis has no effect on the synthesized powder composition, though a slightly better atomic distribution can be obtained in the case of R'=3.

4.4.3 Impedance Spectroscopy

Impedance measurements of various samples were made to determine their bulk impedances. Bulk impedance has been obtained by plotting real and imaginary parts of the impedance data in a complex plane as shown in Fig. 4.4.5. Electrical conductivity of the samples has been calculated from the resistance values obtained by extrapolating the impedance data on the x-axis. The impedance spectra were generated for different temperatures ranging from room temperature to 150 °C at an interval of 25 °C. The intercept of the semicircular arc in the lower frequency on the x-axis gives the bulk resistance. The electrical conductivity (σ) of the samples is calculated from the following relation

$$\sigma = (1/R) \times (l/A)$$

where R is the bulk resistance, l the thickness and A the area of the flat surface of the cylindrical sample.
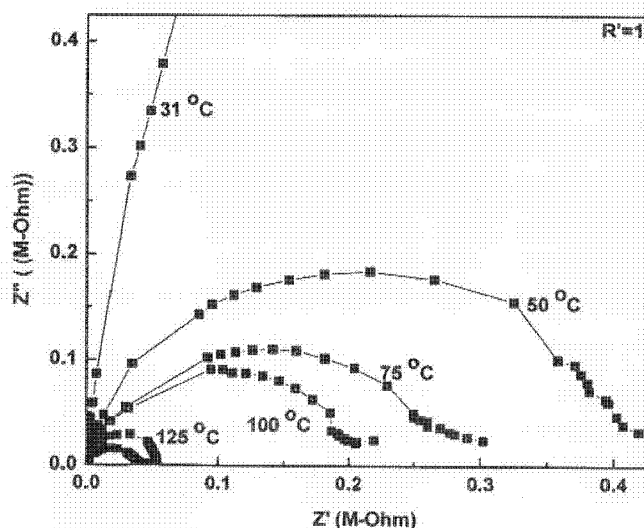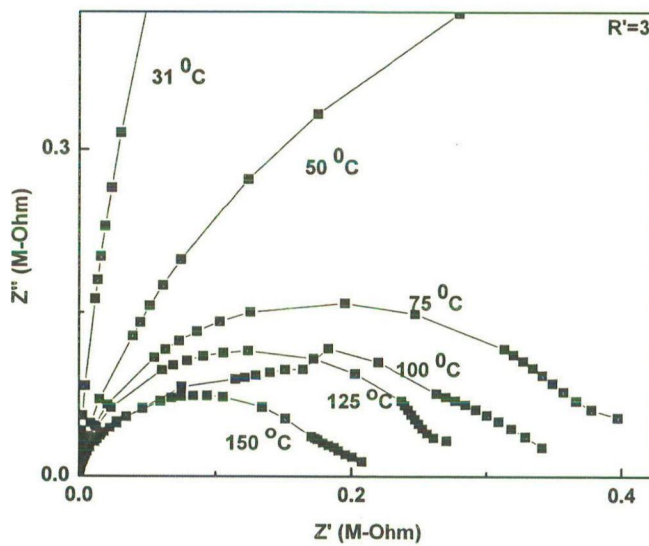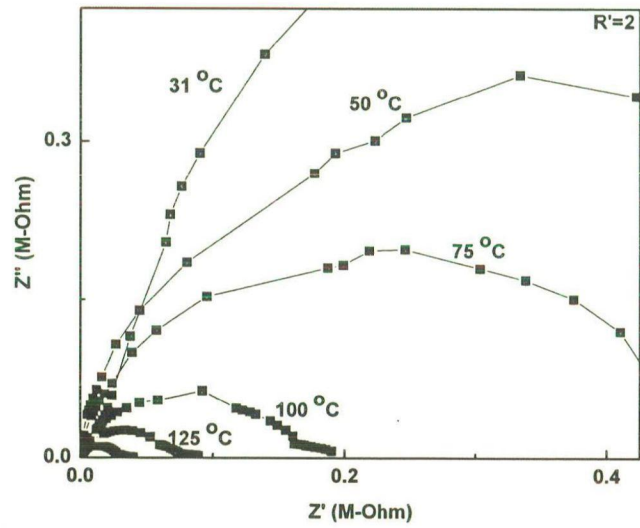
Fig. 4.4.5: Complex impedance plots for $LiCo_{1/3}Ni_{1/3}Mn_{1/3}O_2$ synthesized with $R'=1$, 2 and 3.

The variation of the electrical conductivity with temperature is shown in Fig. 4.4.6. The electrical conductivity of the materials as a function of temperature T can be described by using following relation

$$\sigma = \sigma_0 \, exp \, (-E_a/KT)$$

162

where σ_0, E_a and K are the pre exponential factor, activation energy of mobile charge carrier and Boltzmann constant respectively. E_a was calculated from the slope of the graph between *log (σ)* and *1000/T*.
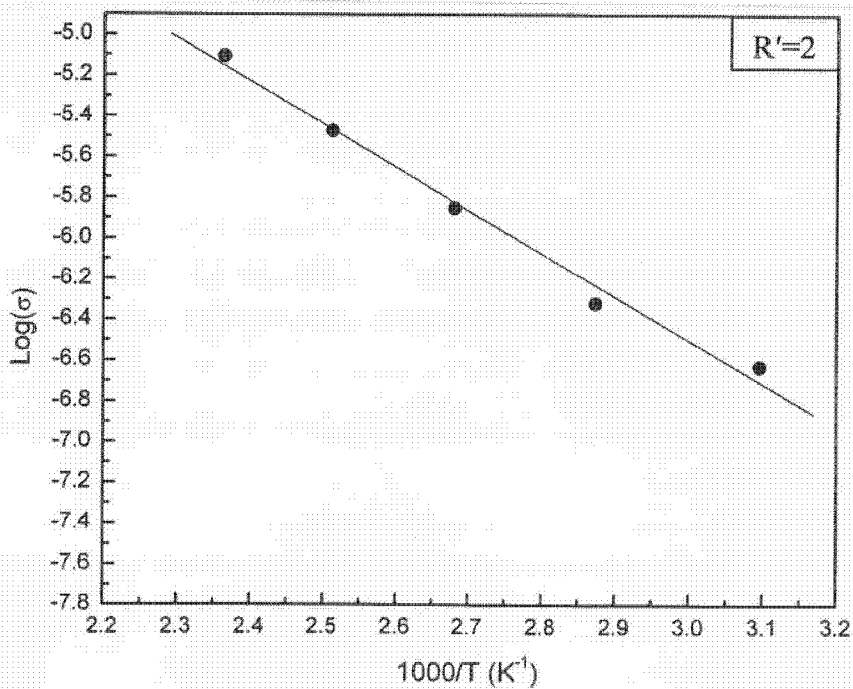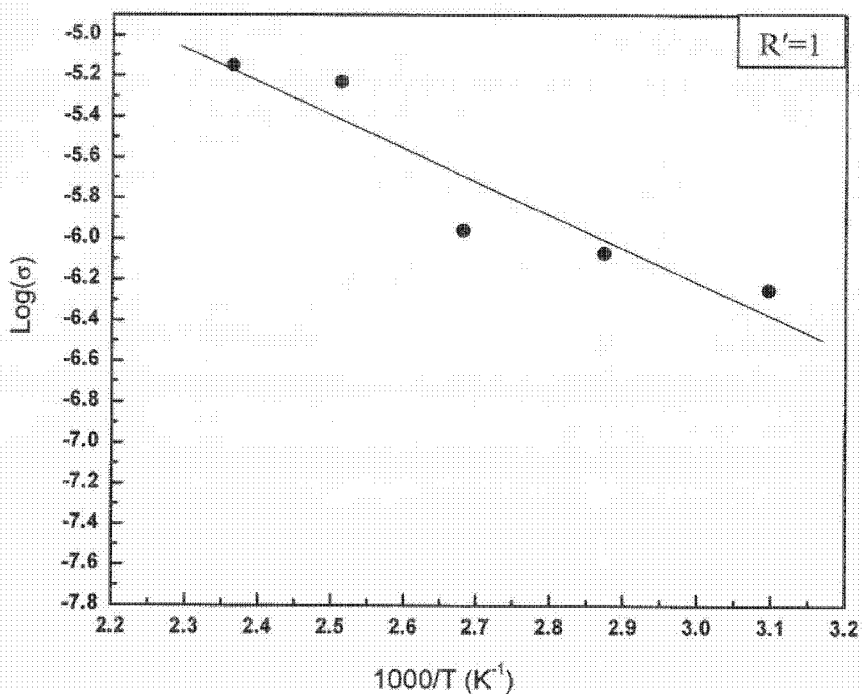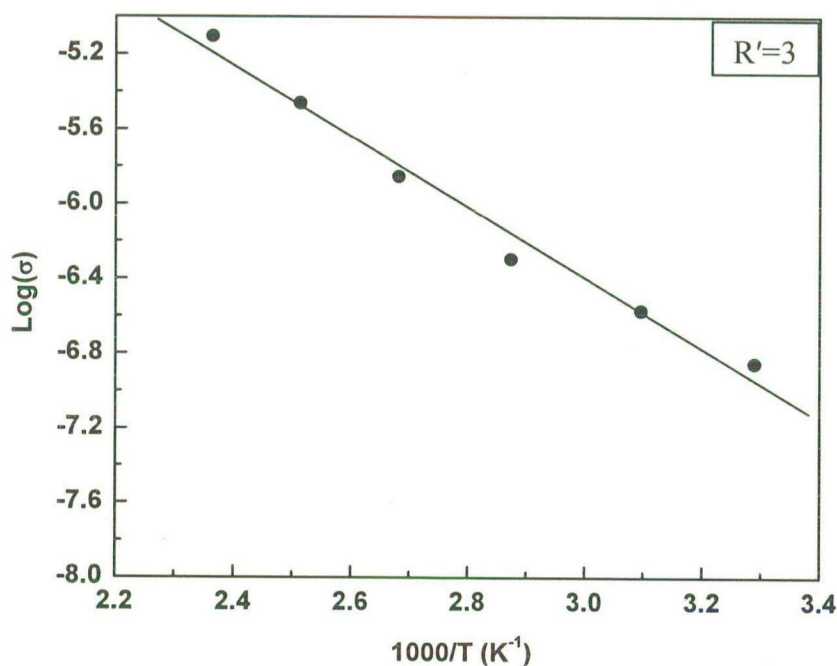
Fig. 4.4.6: Plot of log(σ) vs. 1000/T for $LiCo_{1/3}Ni_{1/3}Mn_{1/3}O_2$ synthesized with R'= 1, 2 and 3

E_a is approximately same for all the samples and the values are 0.38, 0.37 and 0.39 eV for R' = 1, 2 and 3 respectively. The electrical conductivity at room temperature for the various samples is in the range of 10^{-7} to 10^{-8} S/cm. In $LiNi_{1/3}Mn_{1/3}Co_{1/3}O_2$, the electronic configurations of Mn^{4+}, Co^{3+} (Low Spin) and Ni^{2+} are $(t_{2g}^3 e_g^0)$, $(t_{2g}^6 e_g^0)$, and $(t_{2g}^6 e_g^2)$ respectively. Due to the absence of free charge carriers, no effective transport can take place. Hence low electrical conductivities and high activation energies are resulted. These results are in agreement with the earlier studies reported (Gozu et al. 2008).

4.4.4 Electrochemical Studies

Electrochemical measurements were made at room temperature on various samples for R'=1, 2 and 3 in a voltage range of 4.3 - 3.0 V. Cells were charged and discharged at a constant current density of 100 μA/cm². First discharge curves of the various samples are shown in Fig. 4.4.7, which shows that the materials of all compositions have almost same discharge

capacities which are 146.15 mAh/g, 153.76 mAh/g and 151.76 mAh/g for R'=1, 2 and 3, respectively. From all three discharge curves it was found that the behavior of discharge is same as reported earlier (Hwang et al., 2003). The electrochemical performance of the material with R'=3 was studied for 8 cycles over a wide voltage range of 4.6 – 2.5 V and the result is shown in Fig. 4.4.8. The discharge capacity for the first cycle to next cycle decreases from 200.67 mAh/g to 189.42 mAh/g, which indicates that during first charge of sample a proportion of Li inserted to anode may not be reinserted into the cathode during the subsequent discharge stage because of irreversible internal chemical reactions (Song et al., 2008).
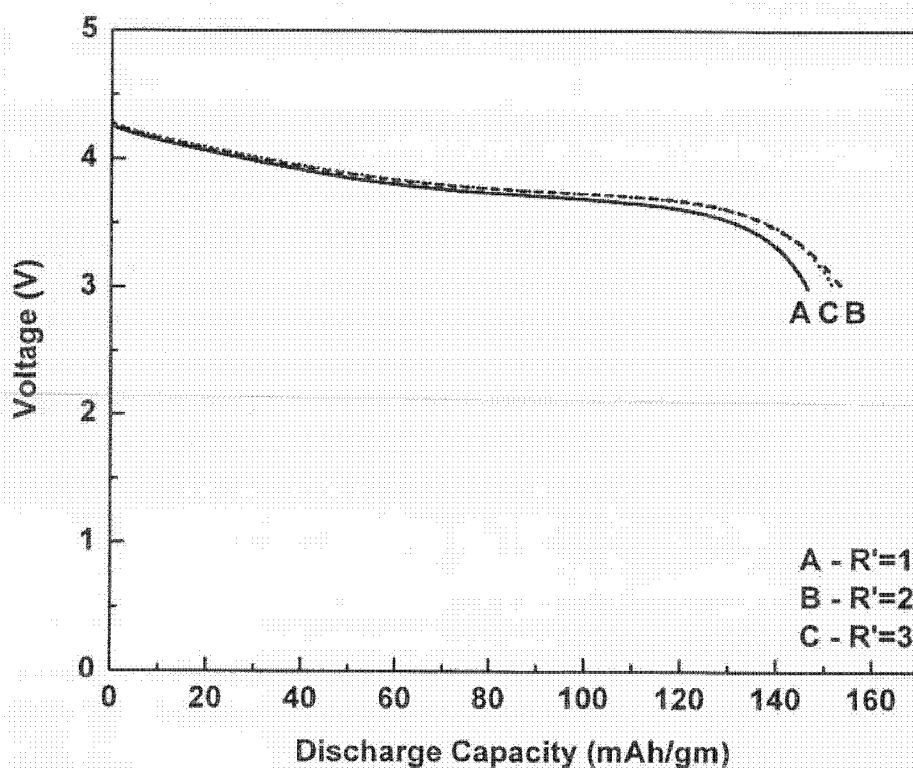
Fig. 4.4.7: First discharge curves of $LiCo_{1/3}Ni_{1/3}Mn_{1/3}O_2$ for R' = 1, 2 and 3 in a voltage range of 4.3 - 3.0 V.

It has been reported (Hwang et al., 2003) that irreversible capacity of $Li_xNi_{1/3}Mn_{1/3}Co_{1/3}O_2$ is required to be reduced for a full scale commercial exploitation of such cathode material. The

irreversible capacities of the $LiNi_{1/3}Mn_{1/3}Co_{1/3}O_2$ material synthesized at 800 and 900 °C by sol-gel route are 36 and 24 mAh/g, respectively (Hwang et al., 2003).

Some other studies on the sol-gel synthesis of $LiNi_{1/3}Mn_{1/3}Co_{1/3}O_2$ have shown the coulombic efficiency of 87.3% when cell was cycled at 100 $\mu A\text{-}cm^{-2}$ in the potential range of 2.8 - 4.5 V (Meng et al., 2007).
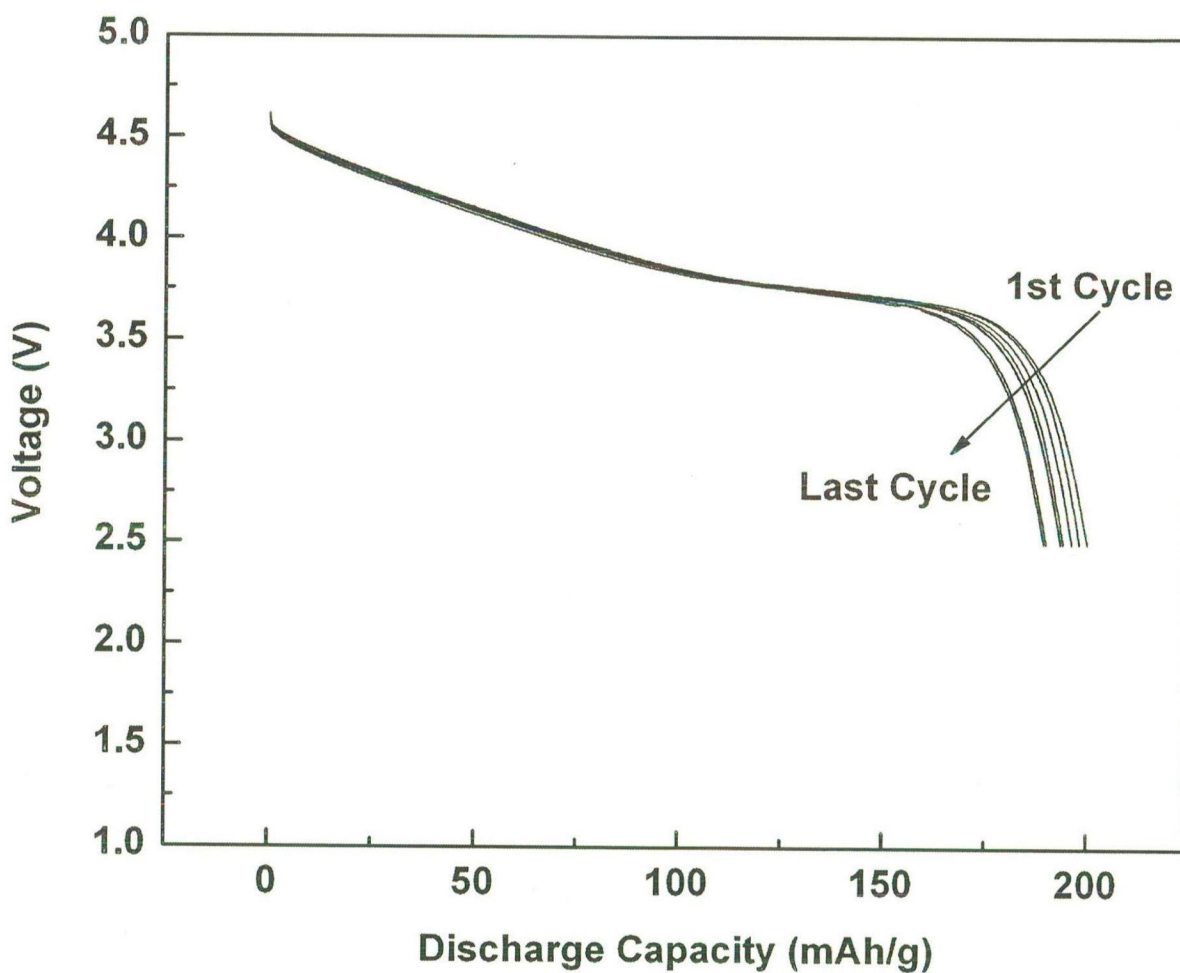
Fig. 4.4.8: Discharge curves for the first 8 cycles of $LiCo_{1/3}Ni_{1/3}Mn_{1/3}O_2$ for R'= 3 in a voltage range of 4.6 - 2.5 V
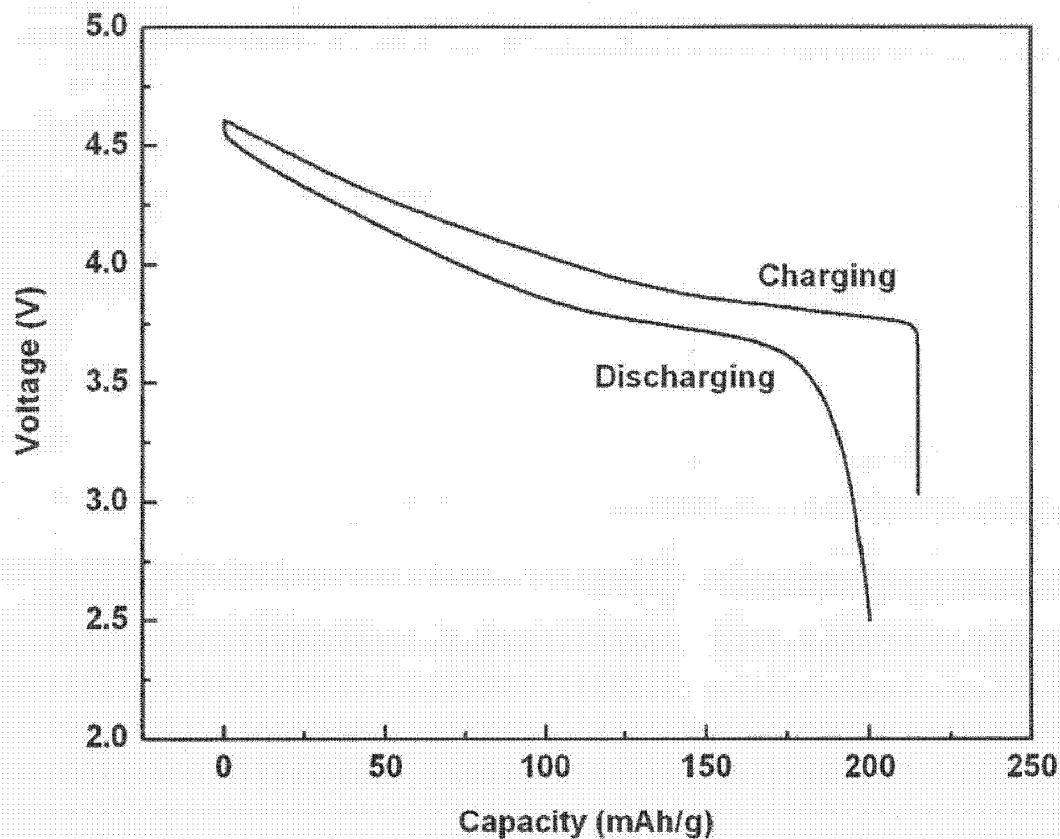
Fig. 4.4.9: First charge-discharge cycle of $LiCo_{1/3}Ni_{1/3}Mn_{1/3}O_2$ for R′=3 in the voltage range

of 4.6 -2.5 V

The present study shows higher coulombic efficiency of 93%, as shown in Fig. 4.4.9, for R′=3 when cell cycles at a rate of 100 μA-cm^{-2} in the potential range of 2.5 - 4.6 V. Hence it can be concluded that the sol-gel synthesis of the material with high citric acid content is beneficial for the electrochemical performance.

Results and Discussion: Computational

5.1.1 Structural Information

The primitive unit cell of the pristine $LiMn_2O_4$ system has been considered, which contains 14 atoms as shown in Fig. 5.1.1.
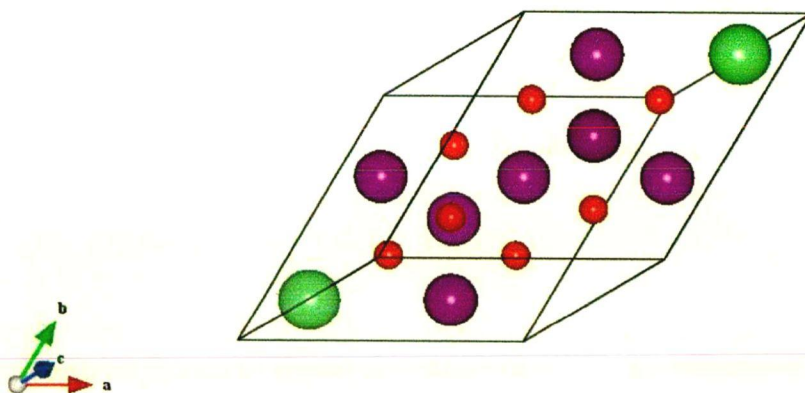
Fig. 5.1.1 Primitive cell of $LiMn_2O_4$ (Li: Green, Mn: Purple, O: Red)

Optimization of the structure has been performed using the procedure discussed in the section 3.2, keeping the shape unchanged. This procedure gives rise to lattice constant of 8.218 Å and 8.376 Å using GGA and GGA+U respectively. The GGA calculations on orthorhombic phase and GGA+U calculations on orthorhombic and tetragonal phases have been performed. The structural information given in reference (Akimoto et al., 2001) for the orthorhombic phase has been used as the initial unrelaxed structure in order to reduce the computational time. The results are found in agreement with the earlier studies reported by Grechnev et al., 2002 using both LSDA (Local spin density approximation) and GGA and that by Ouyang et al., 2008 using GGA+U.

The final optimized structures obtained after relaxing the shape for GGA and GGA+U are different. The final optimized structure for GGA is body centered tetragonal ($I4_1/amd$) with a = 5.851 Å and c = 8.123 Å and for GGA+U it is face centered orthorhombic with a = 8.088 Å, b = 8.528 Å and c = 8.530 Å. Although the lattice constants of body centered tetragonal and orthorhombic primitive unit cell seem to be different, their volumes are nearly same. Lattice parameter values in the latter case (i.e. GGA+U) show that the b/a and c/a ratios are close to 1. The optimized structural parameters for all the systems studied are given in Table 5.1.1. These results are found to be consistent with the earlier ab-initio studies conducted on the system (Mishra and Ceder, 1999) using GGA.

Table 5.1.1: Lattice parameters of the various systems studied

Various systems studied	$LiMn_2O_4$	
	GGA	GGA+U
a(Å)	5.851	8.332
b(Å)	5.851	8.382
c(Å)	8.123	8.416
$Cos(\beta)$	0.000	0.000

The Mn-O bond length in spinel $LiMn_2O_4$ (un-relaxed structure) was found to be same for all Mn-O bonds in the octahedron (1.945 Å). In case of GGA after relaxing the structures two different kinds of bond lengths were obtained in $LiMn_2O_4$. One with d_1^{Mn-O} =1.965 Å and other with d_2^{Mn-O} =1.921 Å. These results are consistent with the earlier experiments which also observed two different bond lengths (Paolone et al., 2003). Similarly in the case of GGA+U calculations after relaxing the structure two different kinds of bond lengths were obtained in $LiMn_2O_4$. One with d_1^{Mn-O} = 1.932 Å and other with d_2^{Mn-O} = 2.021 Å. These

results are in consistence with the study carried by Carvajal et al., 1998. This shows that there exists two different kinds of Mn ions with different oxidation states.

An effort was made to determine the oxidation state of the metal ion by comparing the average bond lengths of M-O (M = Mn) obtained from first principles study using VASP with predictions based on tabulated ionic radii. The bond length of the M-O was calculated by assuming the oxygen ionic radii to be 1.40 Å and various possible hypothetical oxidation states of each metal ion. Manganese exists in two possible states, Mn^{3+} and Mn^{4+}. Mn^{3+} can be further subdivided into two possibilities of low spin and high spin. In low spin configuration all the four electrons will be present in the t_{2g} states, but in the high spin configuration one of the electrons among the four jumps into e_g state. This causes the Jahn-Teller distortion in the structure. Two different bond lengths predicted by GGA are close to the values of theoretical bond lengths of Mn^{3+}-O^{2-} low spin (LS) and Mn^{4+}-O^{2-} respectively. However, the two different bond lengths predicted by GGA+U are close to the values of theoretical bond lengths of Mn^{3+}-O^{2-} high spin (HS) and Mn^{4+}-O^{2-}. Since Mn^{3+} (HS) is a Jahn-Teller active ion, which causes the distortion of the spinel structure, therefore it can be concluded that calculations using GGA+U is giving a clearer picture of the Jahn-Teller distortion in the cubic spinel structure compared to calculation using GGA. Plots showing the difference between calculated bond lengths using hypothetical oxidation state of transition metal ion and bond lengths obtained from the first principles study using GGA and GGA+U are given in Fig. 5.3.2 of the section 5.3. Solid line shows the limit of exact match between the two values.

5.1.2 Density of States (DOS) and Band Structure

The total DOS calculated using GGA and GGA+U for pristine $LiMn_2O_4$ in cubic, orthorhombic and tetragonal structure are shown in Fig. 5.1.2 and 5.1.3 respectively. The GGA based calculation predicts the metallic ground state as there DOS at Fermi level is finite, where as the GGA+U based computation predicts the insulating ground state with zero DOS at the Fermi level. In both GGA and GGA+U based results, the DOS is dominated by the manganese atoms in all the three phases. GGA+U based predictions are well in agreement with the experimentally observed behavior. In case of GGA it has been observed

172

that for orthorhombic structure the spin up and spin down DOS are overlapping, which shows the equal contribution from spin up and spin down states to the total density of states. Therefore it can be concluded from the Fig 5.1.3 that GGA+U drives the system away from the metallic behavior.
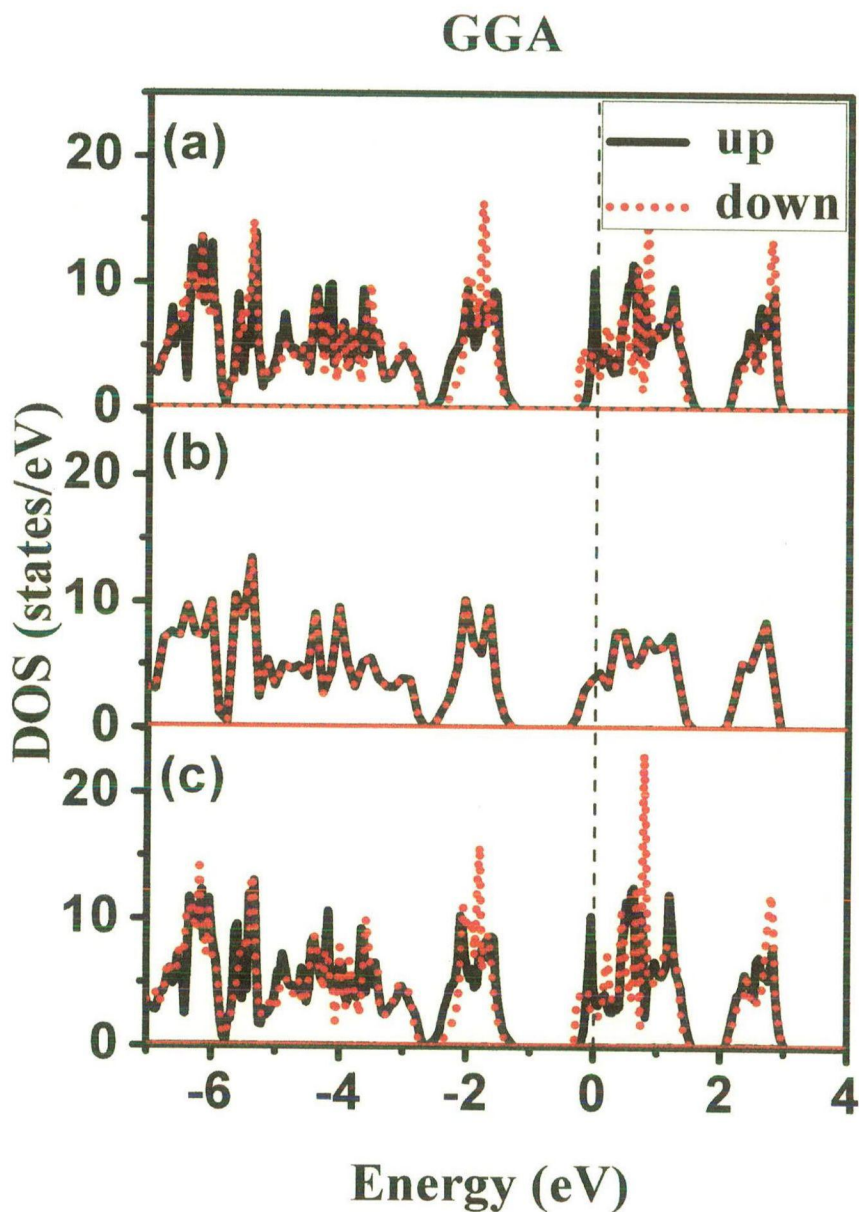
Fig. 5.1.2: DOS of LiMn$_2$O$_4$ in optimized (a) Cubic, (b) Orthorhombic and (c) Tetragonal phases for GGA where black solid line shows spin up and dotted red shows spin down DOS
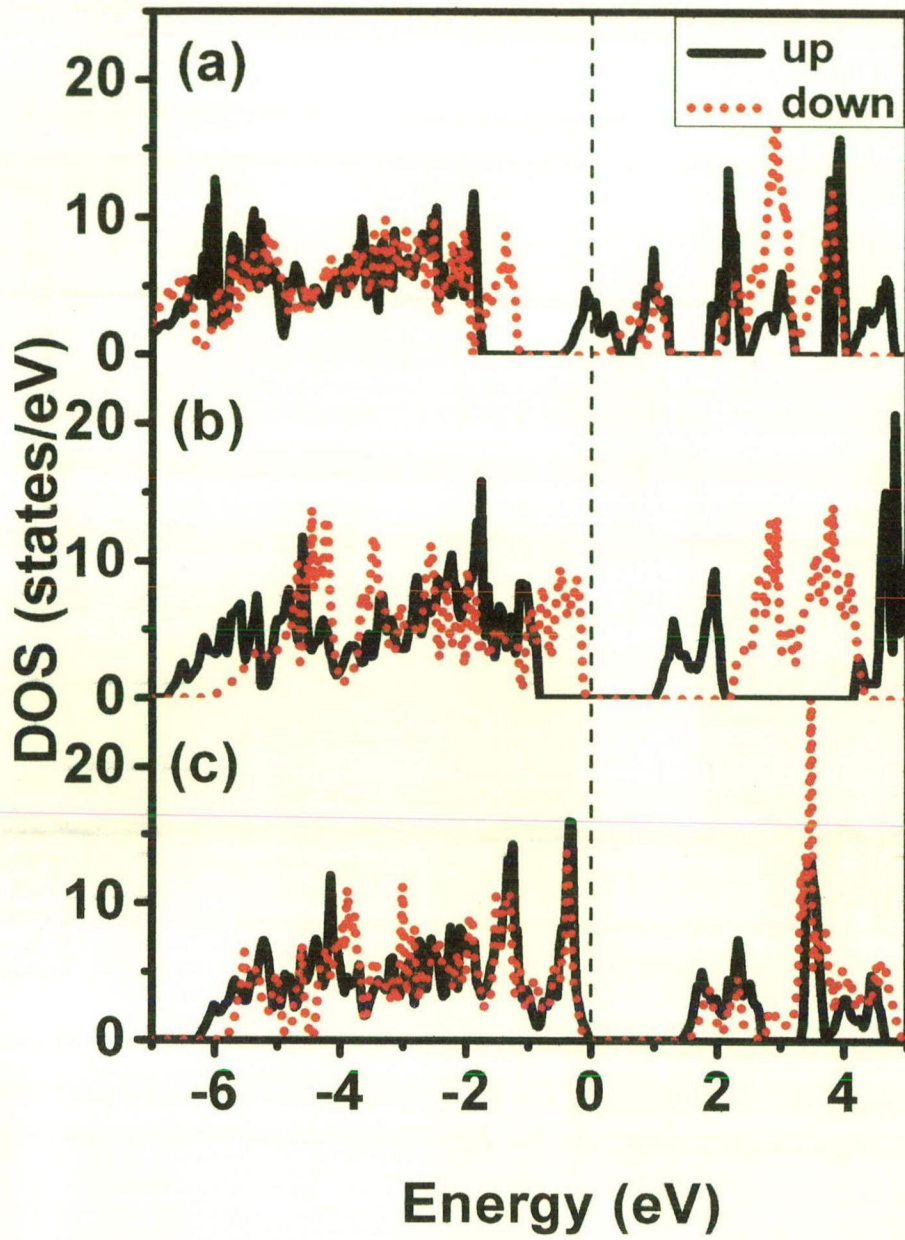
Fig. 5.1.3: DOS of $LiMn_2O_4$ in optimized (a) Cubic, (b) Orthorhombic and (c) Tetragonal phases for GGA+U where black solid line shows spin up and dotted red shows spin down DOS

The t_{2g} (d_{xy}, d_{yz} and d_{xz}) and e_g (d_{z^2} and $d_{x^2-y^2}$) components of the partial DOS for optimized pristine $LiMn_2O_4$ under GGA and GGA+U respectively have been plotted in Fig. 5.1.4 and 5.1.5. DOS behaviors of Mn(I) and Mn(III) are similar to those of Mn(II) and Mn(IV) respectively, therefore the DOS for only Mn(I) and Mn(III) have been shown in both cases. It is seen from the partial DOS (Fig. 5.1.4) that in case of GGA, there is a clear splitting of the e_g states. It was found that the four ligands in the xy plane move towards the metal ion and two along the z-axis simultaneously move away. This results in a splitting of the e_g states. From the Fig. 5.1.5 for GGA+U, the splitting of the e_g states can be observed for all the manganese atoms, however the splitting is more pronounced in the case of Mn(III) (and Mn(IV)). In case of GGA a finite density of states can be observed at Fermi level, however a finite energy gap can be observed in case of GGA+U. This is in agreement with the total DOS plots in which GGA+U predicts the insulating behavior.
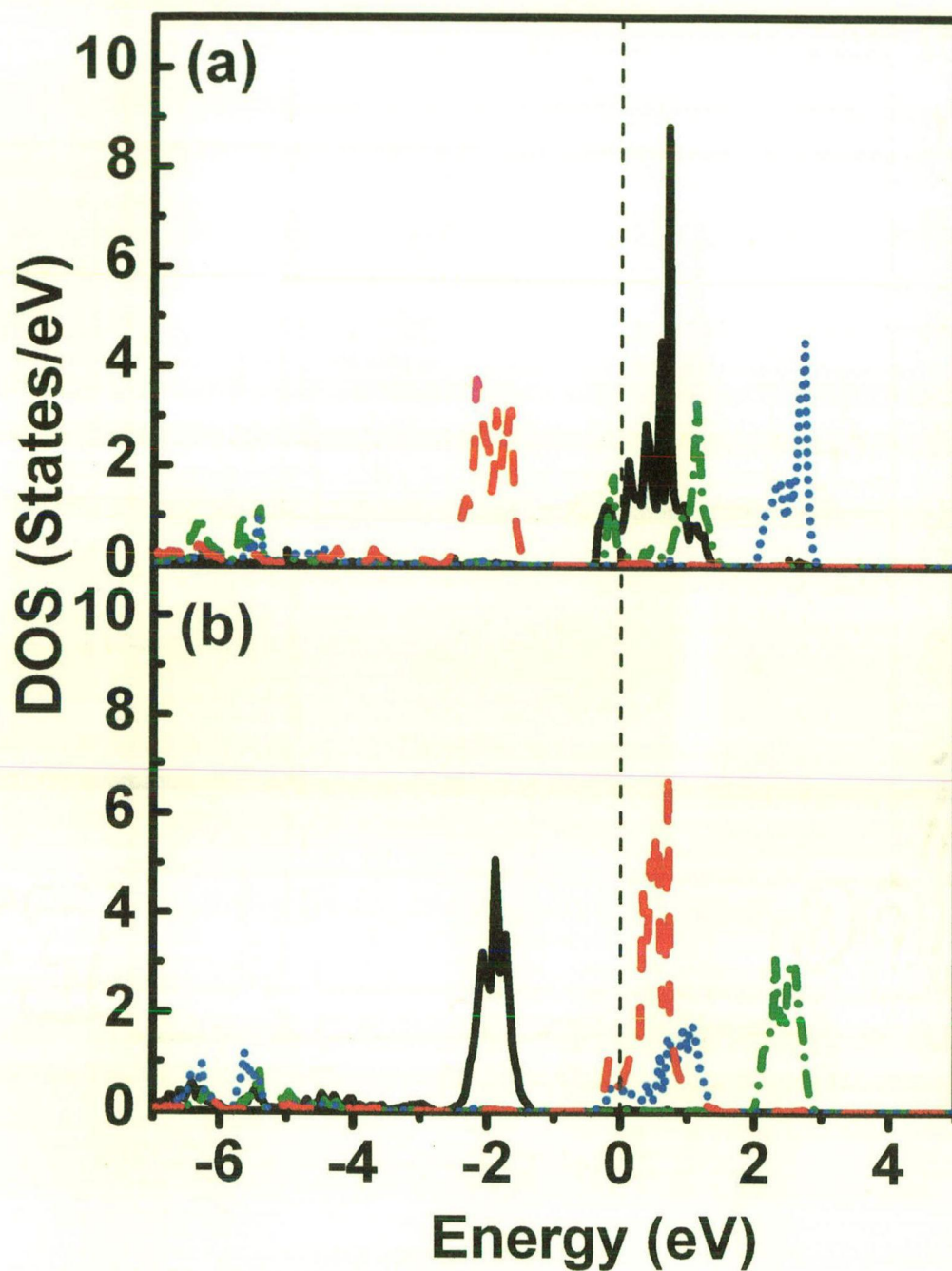
Fig. 5.1.4: Partial DOS of the manganese atoms in relaxed $LiMn_2O_4$. (a) Mn(I) – (0.5, 0.5, 0.5) (b) Mn(III) – (0.0, 0.5, 0.5) for GGA where black line is for t_{2g} (up), red line for t_{2g} (down), blue for e_g (up) and green for e_g (down)
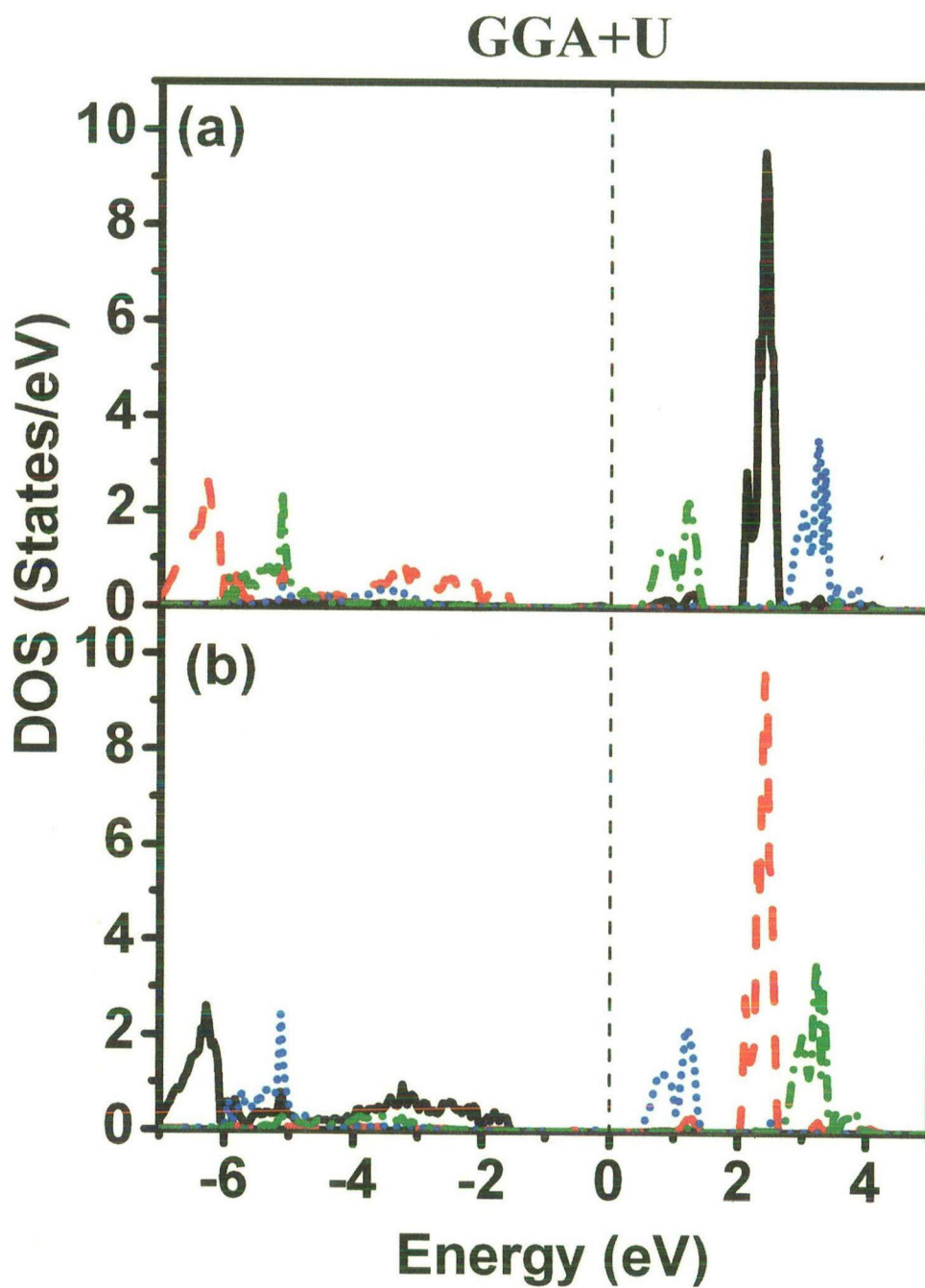
Fig. 5.1.5: Partial DOS of the manganese atoms in relaxed $LiMn_2O_4$. (a) Mn(I) − (0.5, 0.5, 0.5) (b) Mn(III) − (0.0, 0.5, 0.5) for GGA+U where black line is for t_{2g} (up), red line for t_{2g} (down), blue for e_g (up) and green for e_g (down)

Fig. 5.1.6 (a) and (b) show the band structure plots for both spin up and spin down states of pristine $LiMn_2O_4$ calculated using GGA. There exists finite numbers of bands around the Fermi level for both spin up and spin down cases, which show the metallic nature of $LiMn_2O_4$. The stable structures mentioned earlier differ very slightly from the FCC structure. In fact the length of the lattice vectors differs by less than 0.1 % from the ideal FCC lattice vectors. Therefore the band structure has been plotted for FCC structure.
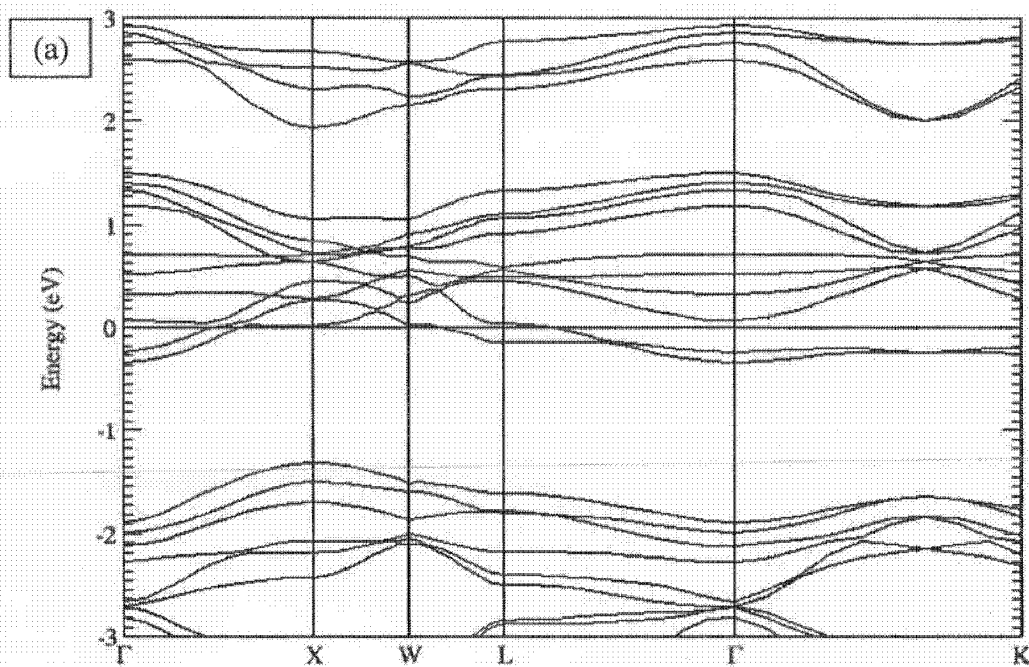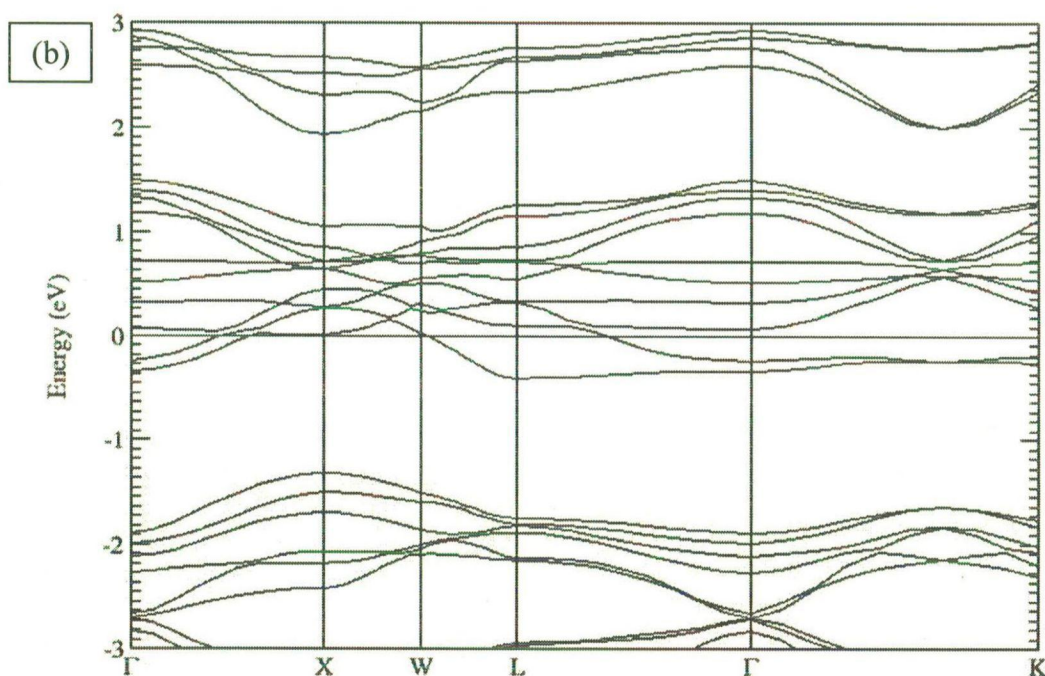
Fig. 5.1.6: Band structure plot for LiMn$_2$O$_4$ in case of GGA (a) for spin up state (b) for spin down states

5.1.3 Charge Density

Charge density plots in the (110) plane for the pristine LiMn$_2$O$_4$ is shown in Fig 5.1.7 (a) and (b) for the case of GGA and GGA+U respectively. (110) plane has been chosen to show the charge density plots because of the fact that (110) gives a clear picture of charge density contribution from all kind of ions present in the structure. It has been observed that the charge on the transition metal ions decreases while on the oxygen ions it increases. This shows that there is a charge transfer from manganese ions to the neighboring oxygen ions in the (110) plane.
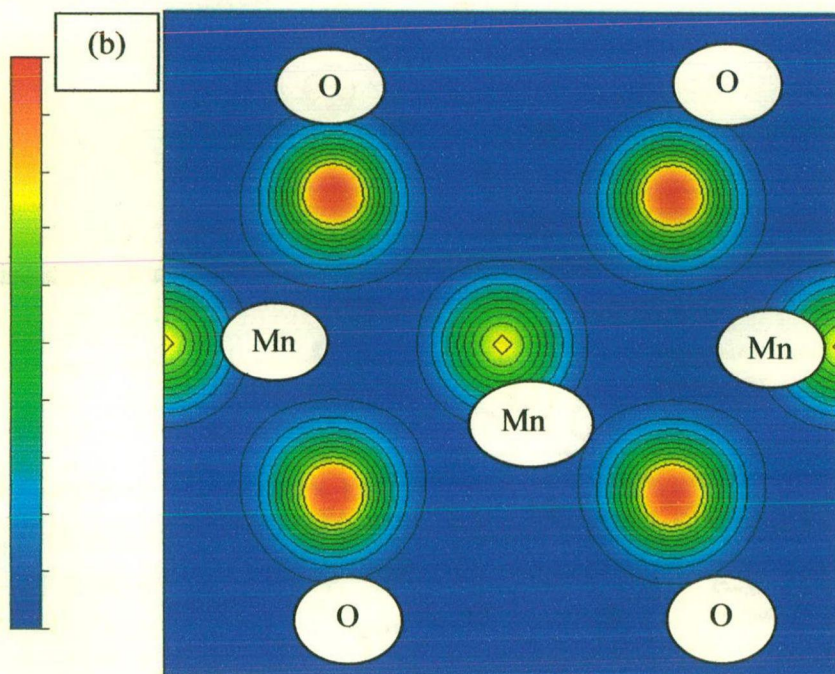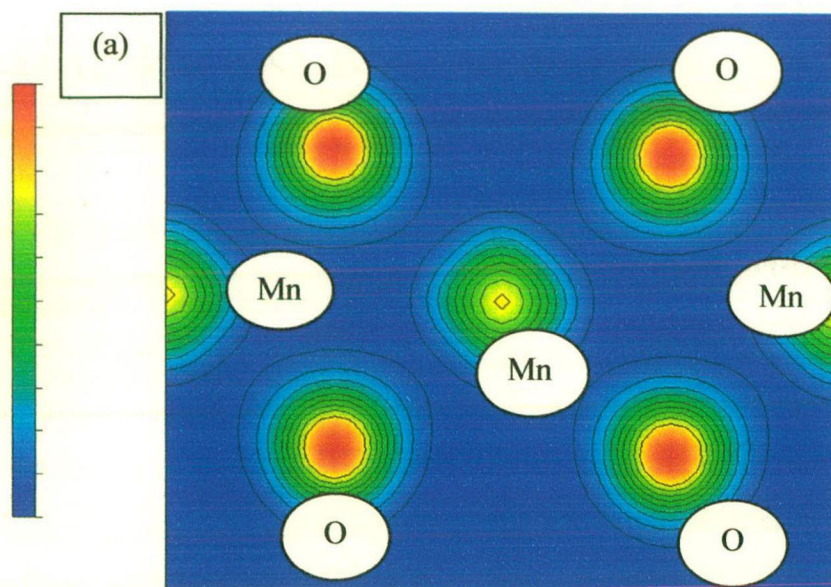
Fig. 5.1.7 Charge density plots in the (110) plane for $LiMn_2O_4$ under GGA and (b) GGA+U.
Contour lines are separated by linear increment of $0.1/Å^3$. Red region corresponds to high
charge density and the blue region corresponds to low charge density

5.2.1 Structural Information

In the pristine structure the Mn atoms were replaced by Cr one by one so as to obtain LiCr$_x$Mn$_{2-x}$O$_4$ for x = 0.5, 1.0. All the structures were optimized after doping. Calculations have been performed on the primitive unit cell consisting of 14 atoms as shown in Fig. 5.2.1 (a) and 5.2.1 (b) for x = 0.5 and 1.0 respectively.
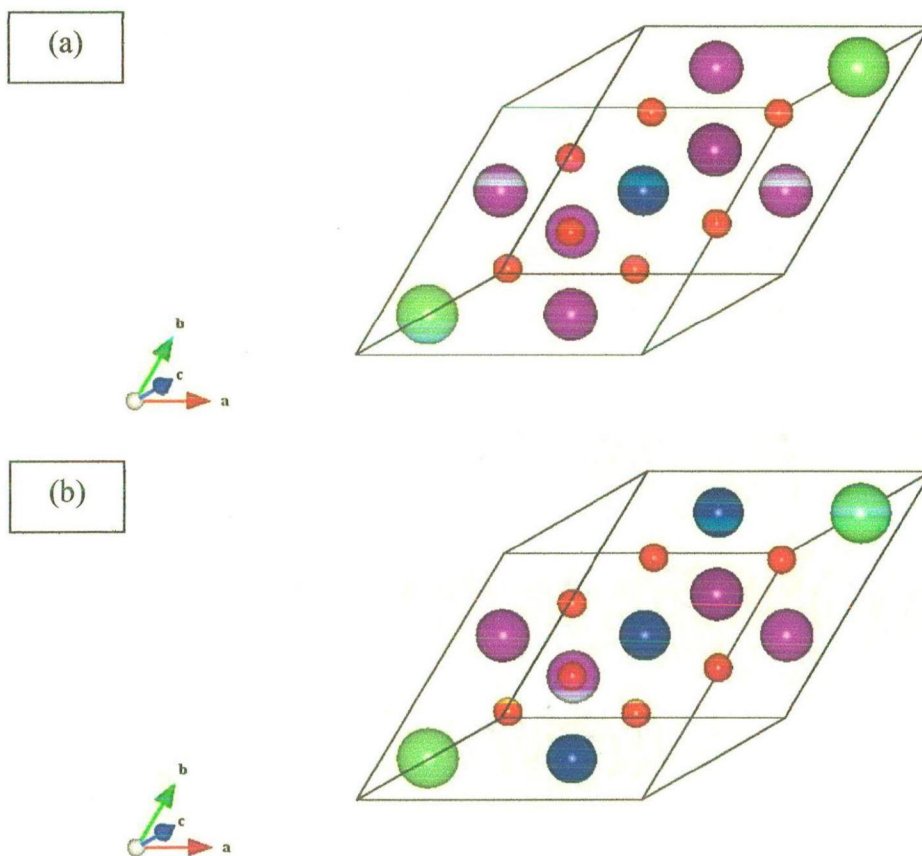
Fig. 5.2.1: Primitive cells of LiCr$_x$Mn$_{2-x}$O$_4$: (a) x=0.5, (b) x=1.0

For the cases of both GGA and GGA+U, the final optimized structure for LiCr$_{0.5}$Mn$_{1.5}$O$_4$ was found to be base centered monoclinic and for LiCrMnO$_4$ was found to be body centered

orthorhombic. The lattice parameters are given in Table 5.2.1. In case of GGA+U the lattice parameters for all the compositions are slightly larger than those calculated using GGA.

Table 5.2.1: Lattice parameters of various systems studied

Various systems studied	$LiCr_{0.5}Mn_{1.5}O_4$		$LiCrMnO_4$	
	GGA	GGA+U	GGA	GGA+U
a(Å)	10.007	10.162	5.775	5.831
b(Å)	5.778	5.991	5.915	5.971
c(Å)	17.274	17.517	8.156	8.320
$Cos(\beta)$	-0.831	-0.829	0.000	0.000

Two different bond lengths predicted by GGA are close to the values of theoretical bond lengths of $Mn^{3+}_{low\ spin\ (LS)}$-$O^{2-}$ and Mn^{4+}-O^{2-} respectively. On doping Cr (x=0.5) four kinds of Mn-O bond lengths were obtained viz. 1.92, 1.94, 1.95 and 1.97 Å. It has been observed that the number of Mn-O bonds with bond length 1.97 Å decreased. This shows that Mn is moving away from +3 oxidation state. On increasing Cr content it has been observed that there exists only two kinds of Mn-O bond lengths viz. 1.94 Å and 1.92 Å. The theoretical bond length of Mn^{4+}-O^{2-} is 1.93 Å. This shows that chromium has shifted the oxidation state of Mn from +3 to +4. Two different bond lengths predicted by GGA+U are close to the values of theoretical bond lengths of Mn^{3+} high spin (HS) and Mn^{4+}. Mn^{3+} (HS) is a Jahn-Teller active ion, which causes the distortion of the spinel structure. Therefore it can be concluded that GGA+U is giving a clearer picture of the Jahn-Teller distortion in the cubic spinel structure. On doping Cr it has been observed that there exist five kinds of Mn-O bond lengths viz. 1.93, 1.95, 1.96, 1.97 and 2.05 Å. On further increasing the Cr content, it has been found that only two kinds of bond lengths remain in the structure viz. 1.93 Å and 1.95 Å. This shows that the Cr is driving the Mn oxidation states towards Mn^{+3} (LS) and Mn^{4+},

and hence suppressing the Jahn-Teller distortion because Mn^{3+} (LS) is a Jahn-Teller inactive ion.

Oxidation state of doped metal ion was determined by comparing the average bond lengths of M-O (M = Cr, Mn) obtained from first principles study using VASP with predictions based on tabulated ionic radii. The bond length of the M-O was calculated by assuming the oxygen ionic radii to be 1.40 Å and various possible hypothetical oxidation states of each metal ion. Manganese exists in two possible states, Mn^{3+} and Mn^{4+}. Mn^{3+} can be further sub-divided into two possibilities of low spin and high spin. In low spin configuration all the four electrons will be present in the t_{2g} states, but in the high spin configuration one of the electrons among the four jumps into e_g state. This causes the Jahn-Teller distortion in the structure. Chromium can also have two possible valence states 3+ and 4+ but it is not a Jahn-Teller active ion. Plot between the average M-O bond lengths obtained from VASP and calculated using GGA and GGA+U for different oxidation states are shown in the Fig. 5.3.2 of the Section 5.3. The solid line represents the exact match between the $[R(M^{z+}) + R(O^{2-})]$, where $R(M^{z+})$ and $R(O^{2-})$ are the ionic radii of the transition metal ion and oxygen ion respectively, and those obtained from the first principle calculations. It is clear from the Fig. 5.3.2 of section 5.3 that Mn and Cr are possibly present in 3+ and 4+ oxidation states as the points corresponding to these are close to the solid line.

5.2.2 Density of States (DOS) and Band Structure

Fig. 5.2.2 and 5.2.3 show the total DOS of the doped systems which were obtained using GGA and GGA+U respectively. Total DOS obtained by using GGA and GGA+U for the system $LiCr_{0.5}Mn_{1.5}O_4$ are shown in Fig. 5.2.2 (a) and 5.2.3 (a) respectively. For the system with higher doping content of Cr i.e. $LiCrMnO_4$ the total DOS plots are shown in Fig. 5.2.2 (b) and 5.2.3 (b) for the cases of GGA and GGA+U respectively. GGA based computation predicts that the Cr doping brings the system towards the insulator via a half metallic state (Fig. 5.2.2). This is because for x = 0.5, there is non-zero spin up DOS and for spin down it is zero DOS and for x = 1, it becomes insulator. On the other hand GGA+U based

computations gives the metallic state for x=0.5 and an insulator for x=1.0 for Cr (Fig. 5.2.3). It is interesting that GGA+U based computation predicts an insulator-metal-insulator transition as a function of Cr doping. This can be understood qualitatively as follows. The parent $LiMn_2O_4$ has equal number of Mn^{3+} and Mn^{4+} ions which are antiferromagnetically aligned. As a result of crystal field the d-levels at these sites are split into t_{2g} and e_g levels. The e_g level of Mn^{3+} has one electron and Mn^{4+} has no electron in the e_g level. Thus the parent $LiMn_2O_4$ is insulating because the e_g electron can not go to the neighboring Mn^{4+} sites. This is because it would involve flipping of a spin which is unlikely due to the strong Hund's coupling. When the system is doped with Cr, which is in 3+ state, it replaces the isovalent Mn^{3+} site. At x=0.5 doping, half the Mn^{3+} sites are replaced by Cr^{3+}. Since Cr^{3+} has no electron in the e_g level, the e_g electron on the Mn^{3+} site can get delocalized and thus the system becomes metallic. But at x=1, all the Mn^{3+} sites are replaced by Cr^{3+}. As a result, there is no electron in any e_g level and the system becomes insulating.

GGA
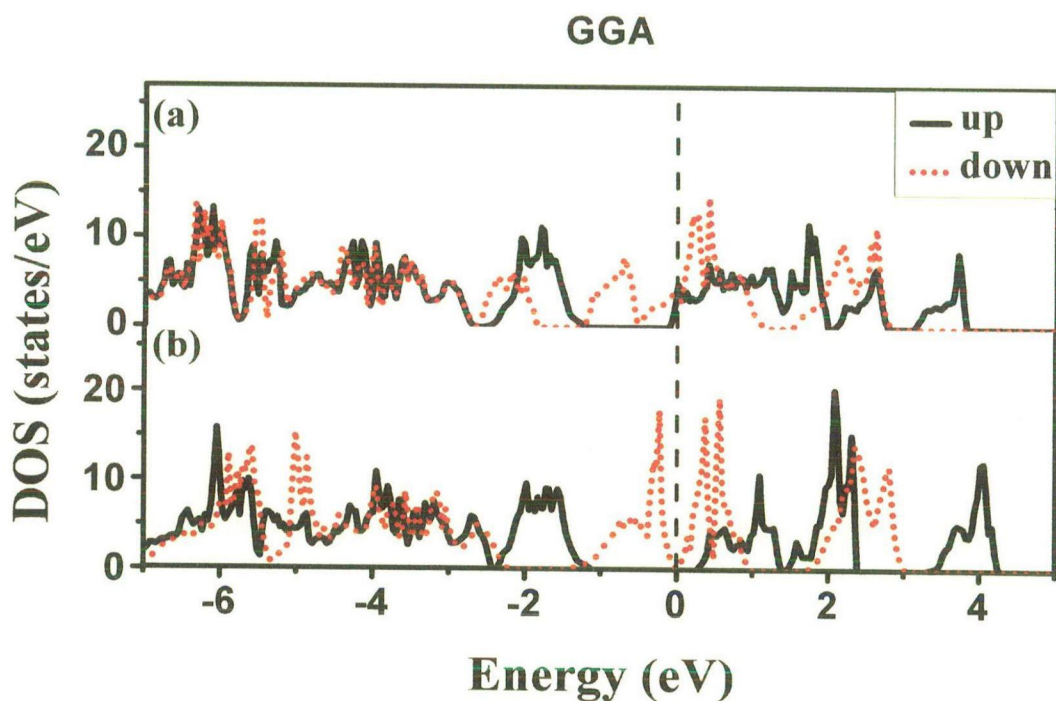
Fig. 5.2.2: Total DOS plot for $LiCr_xMn_{2-x}O_4$ computed using GGA [(a) x=0.5; (b) x=1.0], where solid black line is for spin up and dotted red line is for spin down states
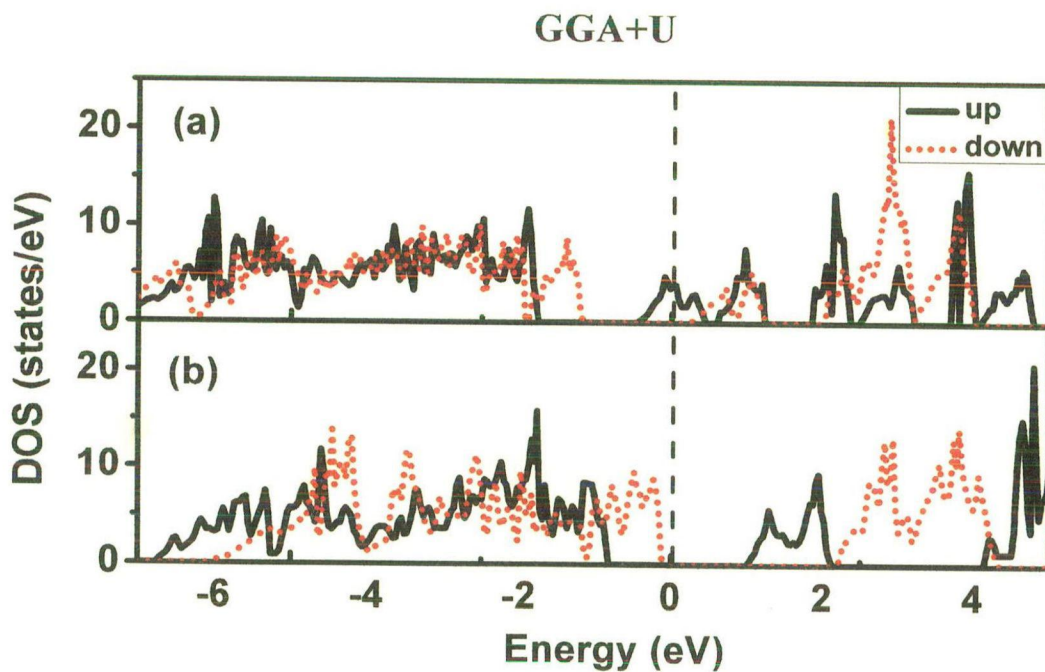
GGA+U

Fig. 5.2.3: Total DOS plot for $LiCr_xMn_{2-x}O_4$ computed using GGA+U [(a) x=0.5; (b) x=1.0], where solid black line is for spin up and dotted red line is for spin down states

185

The partial DOS with t_{2g} (d_{xy}, d_{yz} and d_{xz}) and e_g (d_{z^2} and $d_{x^2-y^2}$) components for the Mn atoms computed using GGA and GGA+U in $LiCr_xMn_{2-x}O_4$ (x=0.5, 1.0) are shown in Figs. (5.2.4, 5.2.5) and Figs. (5.2.6, 5.2.7) respectively. The splitting of t_{2g} orbitals is clearly observed in both cases. On increasing the Cr concentration a finite energy gap is observed for both the spin-up as well as spin-down energy states. It can also be seen that the energy gap is larger in case of GGA+U compared to GGA. This shows that GGA+U based computation predicts insulating character while GGA based computation predicts semi metallic character for x = 1.0. Splitting of e_g states of Mn(I) and Mn(III) can be seen from the partial DOS plots of pristine $LiMn_2O_4$ in case of GGA (Fig. 5.1.4 of section 5.1). In case of GGA+U based computation, the splitting of the e_g states is more pronounced for the Mn(III) and Mn(IV) compared to Mn(I) and Mn(II). Splitting of the e_g states is more clear in case of results obtained by using GGA+U compared to GGA. Both the computation using on GGA and GGA+U predict that in case of chromium doped $LiMn_2O_4$ (for x=0.5), the number of electrons in the e_g state of Mn(III) are less compared to the pristine $LiMn_2O_4$ and the number of electrons in the t_{2g} state of Mn(III) are more compared to the pristine system using GGA. In computational results obtained by using GGA+U, t_{2g} (down) density of states is found to be absent around the Fermi level, however the t_{2g} (up) density of states at lower energy levels is more compared to the pristine $LiMn_2O_4$. As the Cr content is increased (x=1.0), GGA based calculation shows that the number of electrons present in the lower energy states of Mn(III) is higher than for x=0.5. In the case of x=1.0 the e_g orbital of Mn (III) was found to be totally empty, while for x=0.5 some electrons were present in the e_g state. These results are in agreement with the charge density distribution obtained from the VASP output, which shows the total charge to be larger by 0.016 electronic charge for Mn (III) in $LiCrMnO_4$ than $LiCr_{0.5}Mn_{1.5}O_4$. However in case of GGA+U, spin up density of states is found to be absent around the Fermi level as the Cr content increases from x= 0.5 to 1.0. This shows the half metallic behavior for $LiCrMnO_4$.
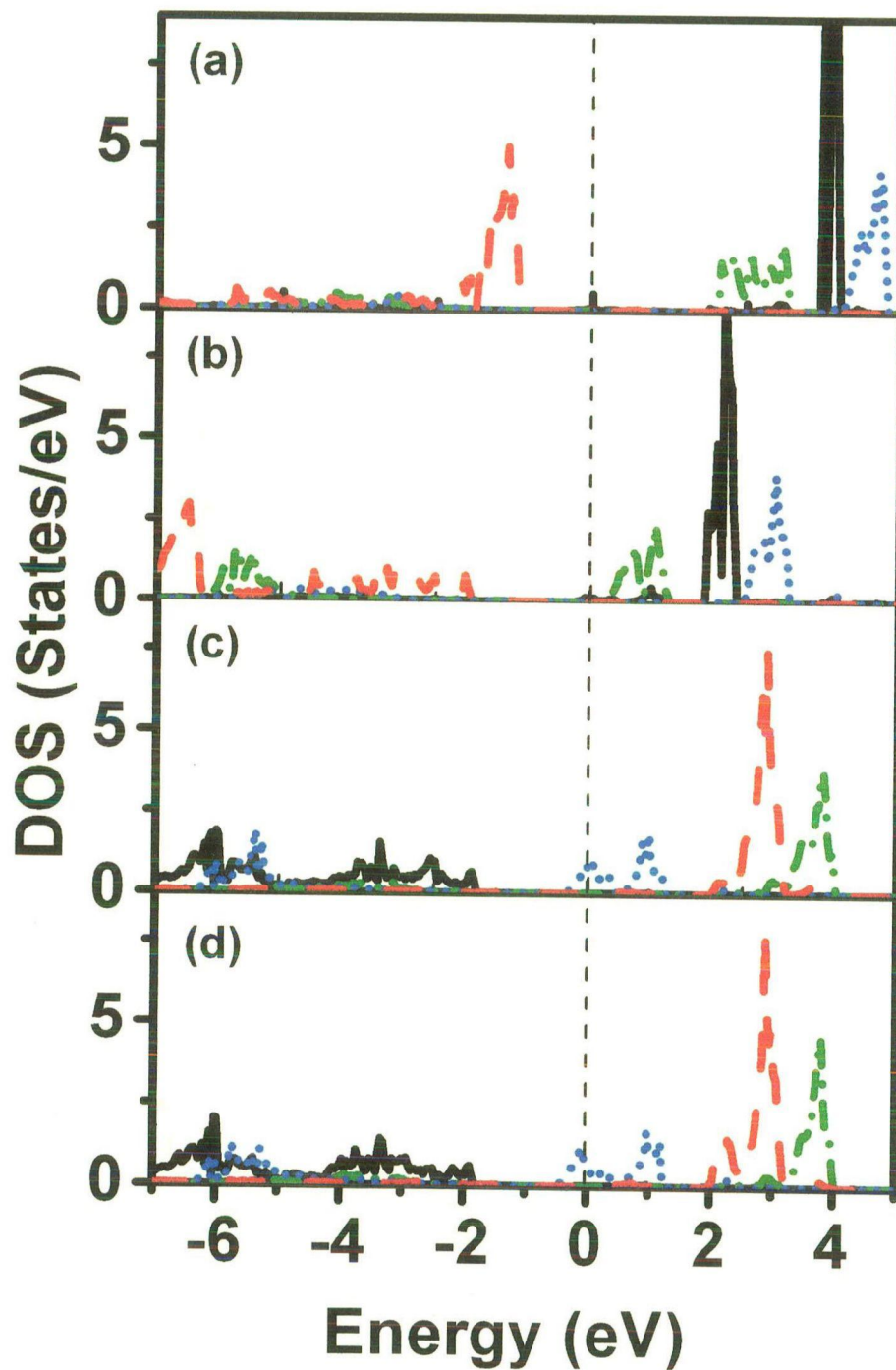
Fig. 5.2.6: Partial DOS plot for $LiCr_{0.5}Mn_{1.5}O_4$ computed using GGA+U [(a) Cr(I) − (0.5, 0.5, 0.5), (b) Mn(II) − (0.5, 0.0, 0.5), (c) Mn(III) − (0.0, 0.5, 0.5), (d) Mn(IV) − (0.5, 0.5, 0.0)]
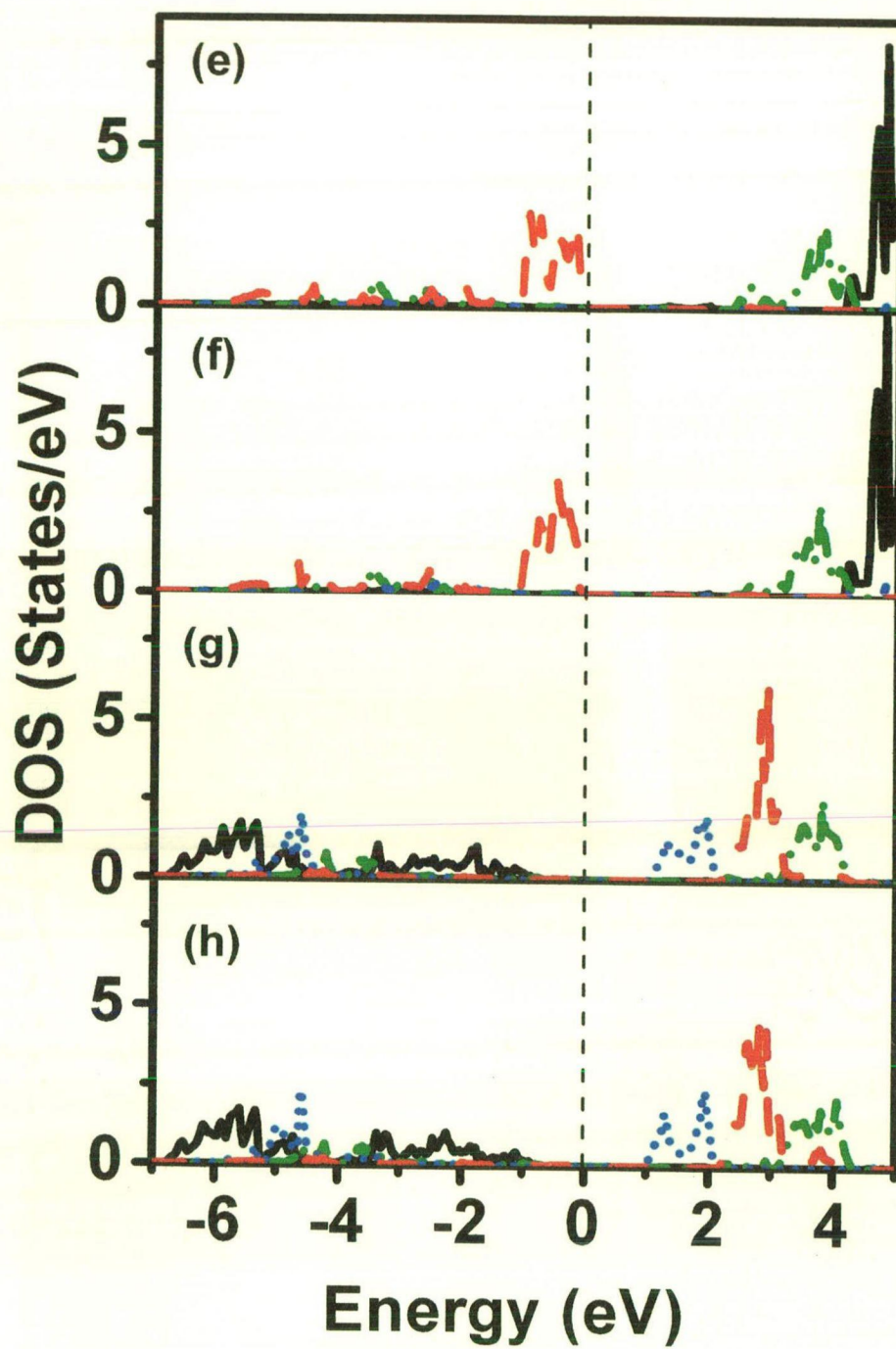
Fig. 5.2.7: Partial DOS plot for LiCrMnO$_4$ computed using GGA+U [(e) Cr(I) – (0.5, 0.5, 0.5), (f) Cr(II) – (0.5, 0.0, 0.5), (g) Mn(III) – (0.0, 0.5, 0.5), (h) Mn(IV) – (0.5, 0.5, 0.0)]

Fig. 5.2.8 and 5.2.9 show the band structure plots of Cr doped $LiMn_2O_4$ computation using GGA for $LiCr_{0.5}Mn_{1.5}O_4$ and $LiCrMnO_4$ respectively. In case of pristine $LiMn_2O_4$ it has been observed that there exists finite number of bands in both spin up as well as spin down states. Band structure plots of Cr doped $LiMn_2O_4$ show that with Cr doping (x=0.5) the Fermi level shifts towards the lower energy. It was observed that for the spin-up state some of the t_{2g} levels lie just below the Fermi energy value. For the spin-down states continuous energy bands were found around the Fermi level. But as the chromium content increases (x=1.0) the Fermi level shifts even more towards the lower energy. In this case the Fermi level just touches the top of valence and there is very small energy gap between the valence and conduction bands. For spin-up states it lies well inside the energy gap of valence and conduction bands. This shows that the Cr is driving the system away from the metallic nature.
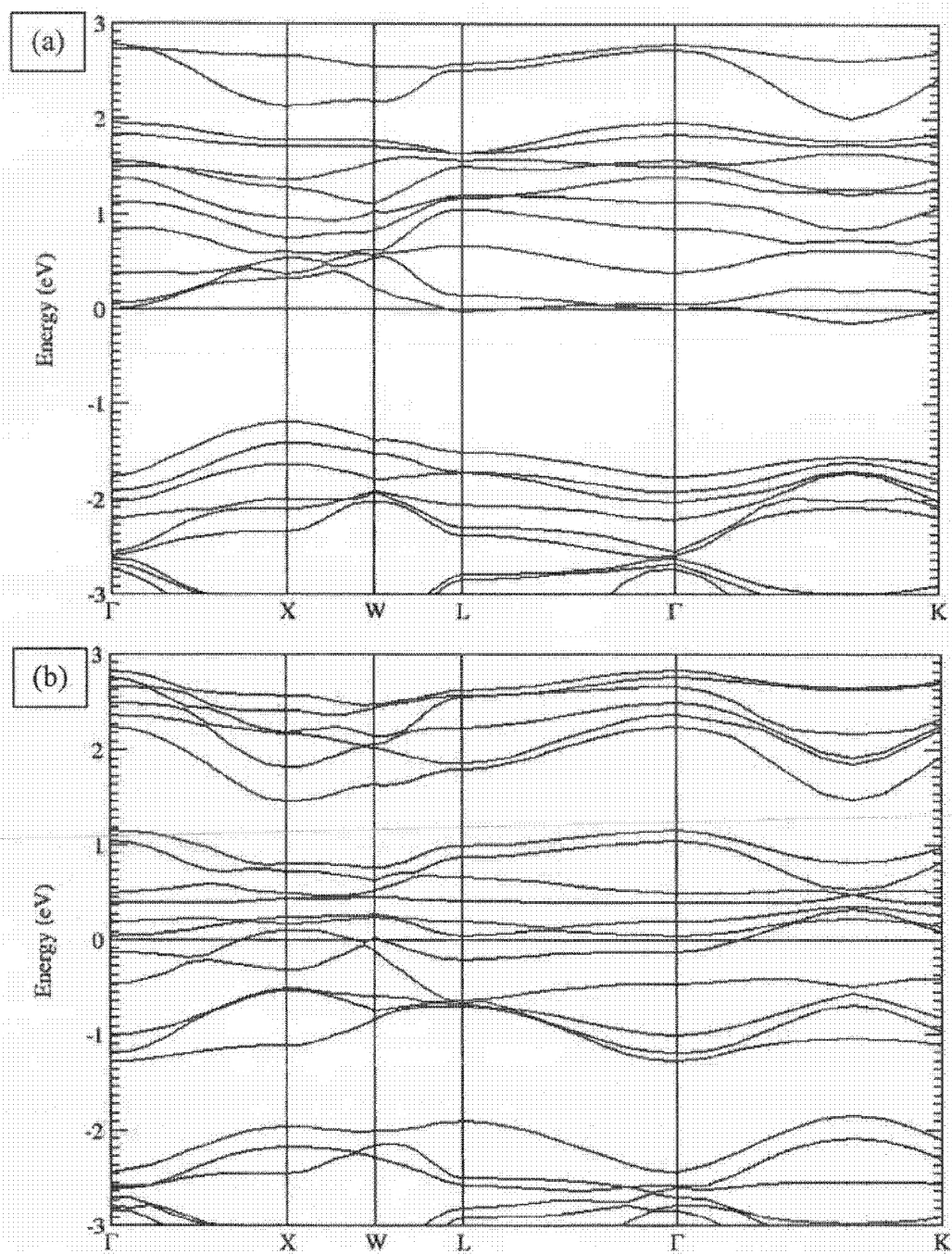
Fig. 5.2.8: Band structure plots for (a) spin up and (b) spin down states of $LiCr_{0.5}Mn_{1.5}O_4$ computed using GGA
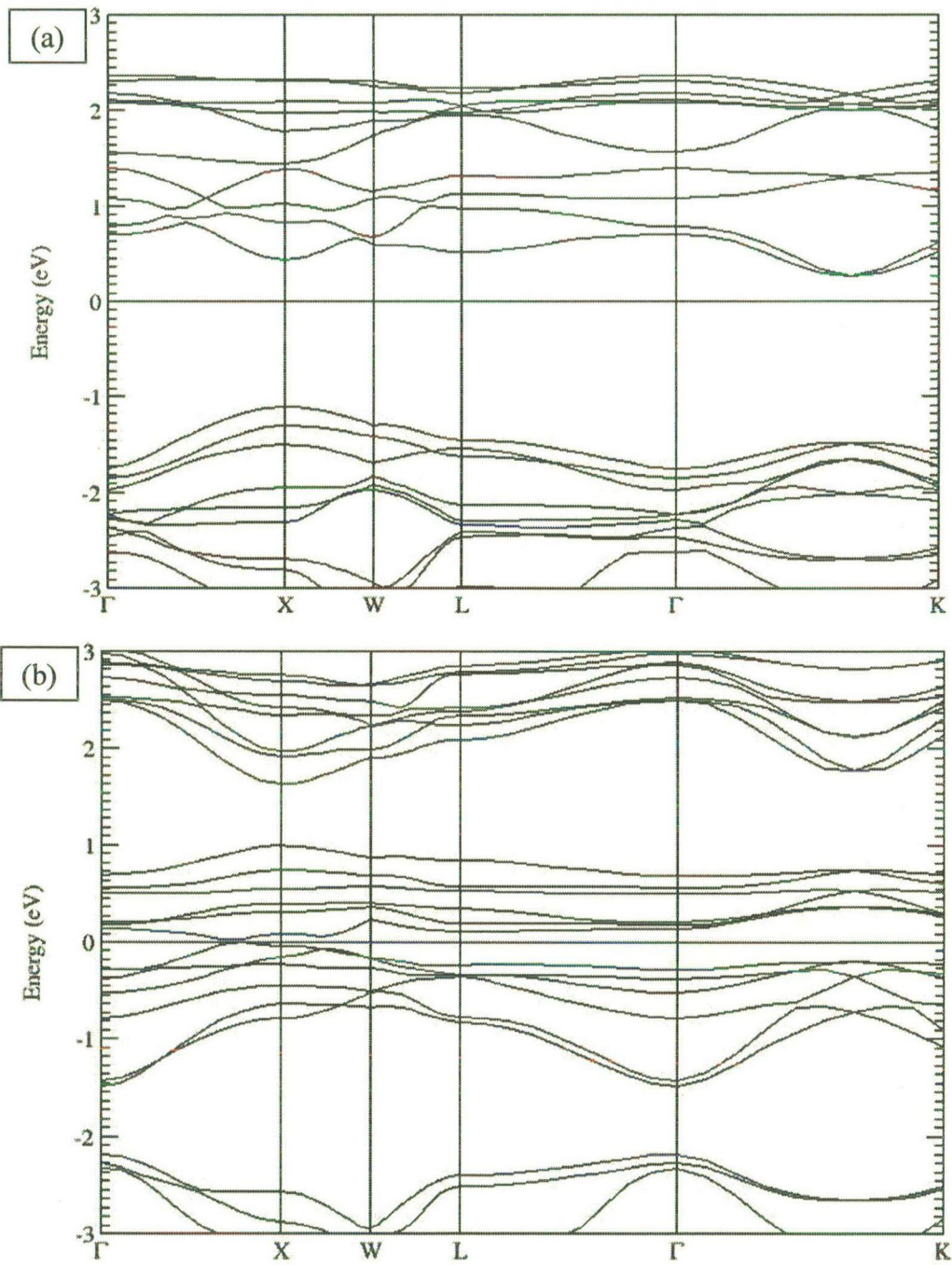
Fig. 5.2.9: Band structure plots for (a) spin up and (b) spin down states of LiCrMnO$_4$ computed using GGA

Charge Density

Charge density plot for Cr doped $LiMn_2O_4$ in the (110) plane has been shown in Fig 5.2.10 and 5.2.11 for GGA and GGA+U respectively. GGA and GGA+U predict the charge transfer from the transition metal ions to neighboring oxygen ions.
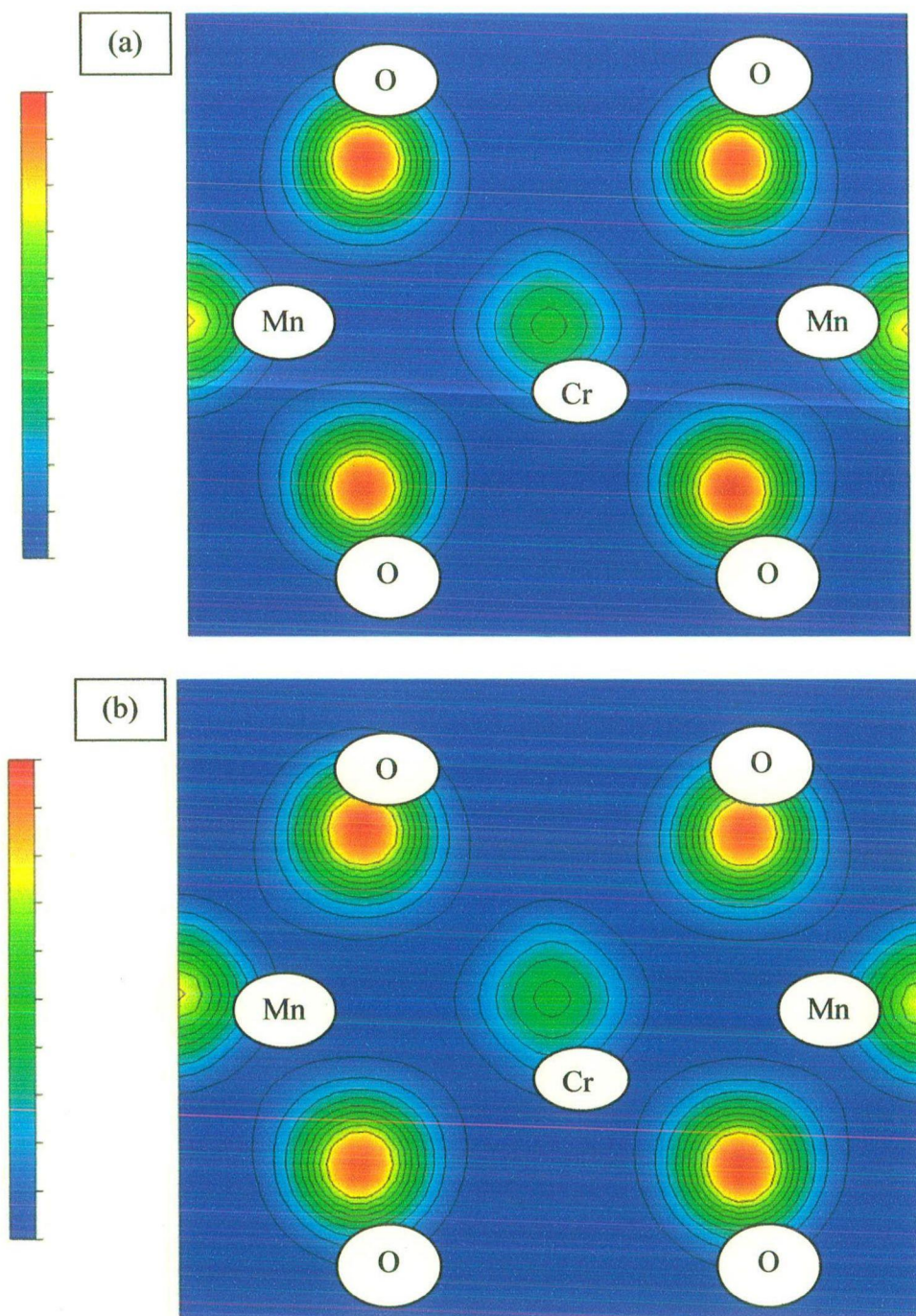
Fig. 5.2.10: Charge density plot for $LiCr_xMn_{2-x}O_4$ [(a) x=0.5, (b) x=1.0] in the (110) plane under GGA, Contour lines are separated by linear increment of $0.1/Å^3$. Red region corresponds to high charge density and the blue region corresponds to low charge density
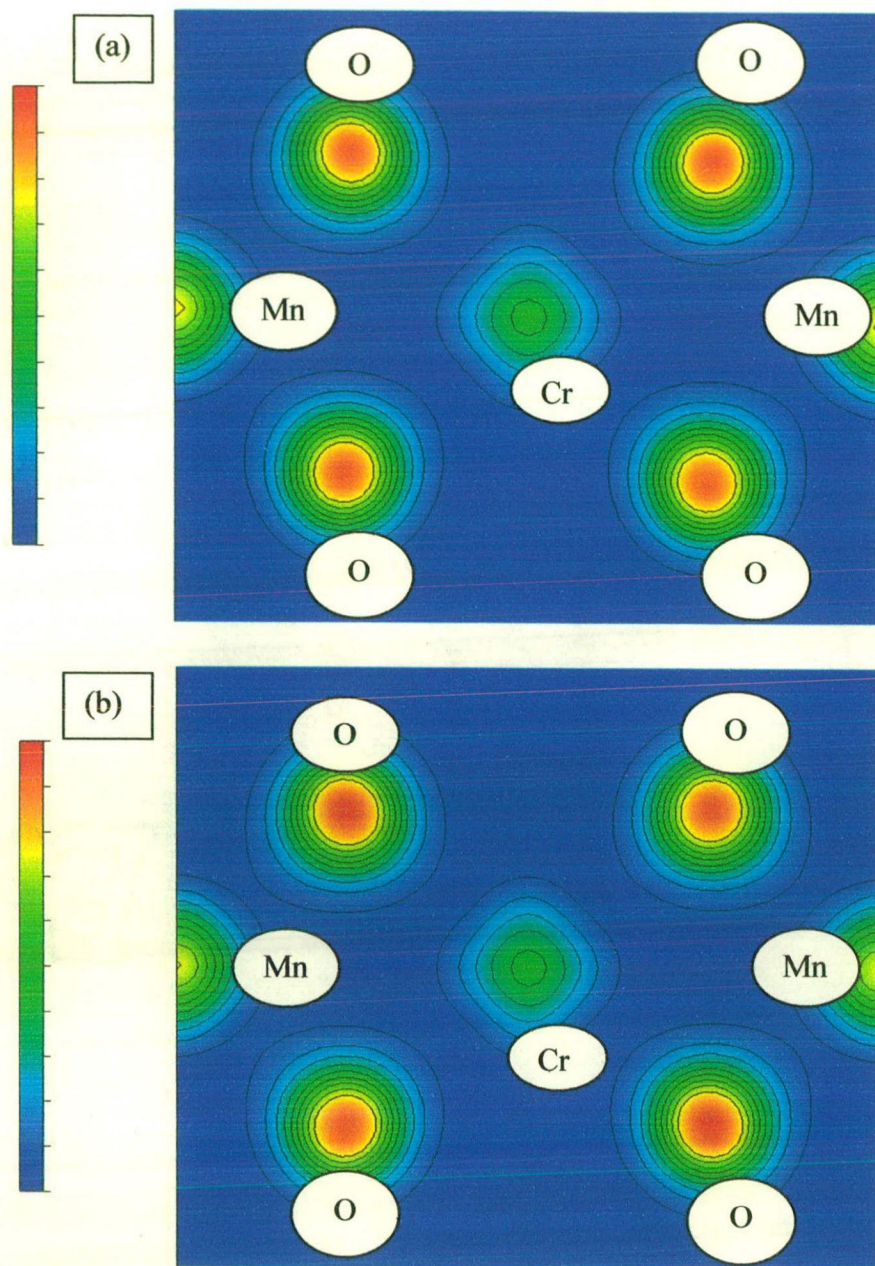
Fig. 5.2.11: Charge density plot for $LiCr_xMn_{2-x}O_4$ [(a) x=0.5, (b) x=1.0] in the (110) plane under GGA+U, Contour lines are separated by linear increment of $0.1/Å^3$. Red region corresponds to high charge density and the blue region corresponds to low charge density

5.3.1 Structural Information

In the pristine structure the Mn atoms were replaced by Mg one by one so as to obtain LiMg$_x$Mn$_{2-x}$O$_4$ for x=0.5, 1.0. Calculations have been performed on the primitive cell consisting of 14 atoms as shown in Fig. 5.3.1 (a) and (b) for x=0.5 and 1.0 respectively.
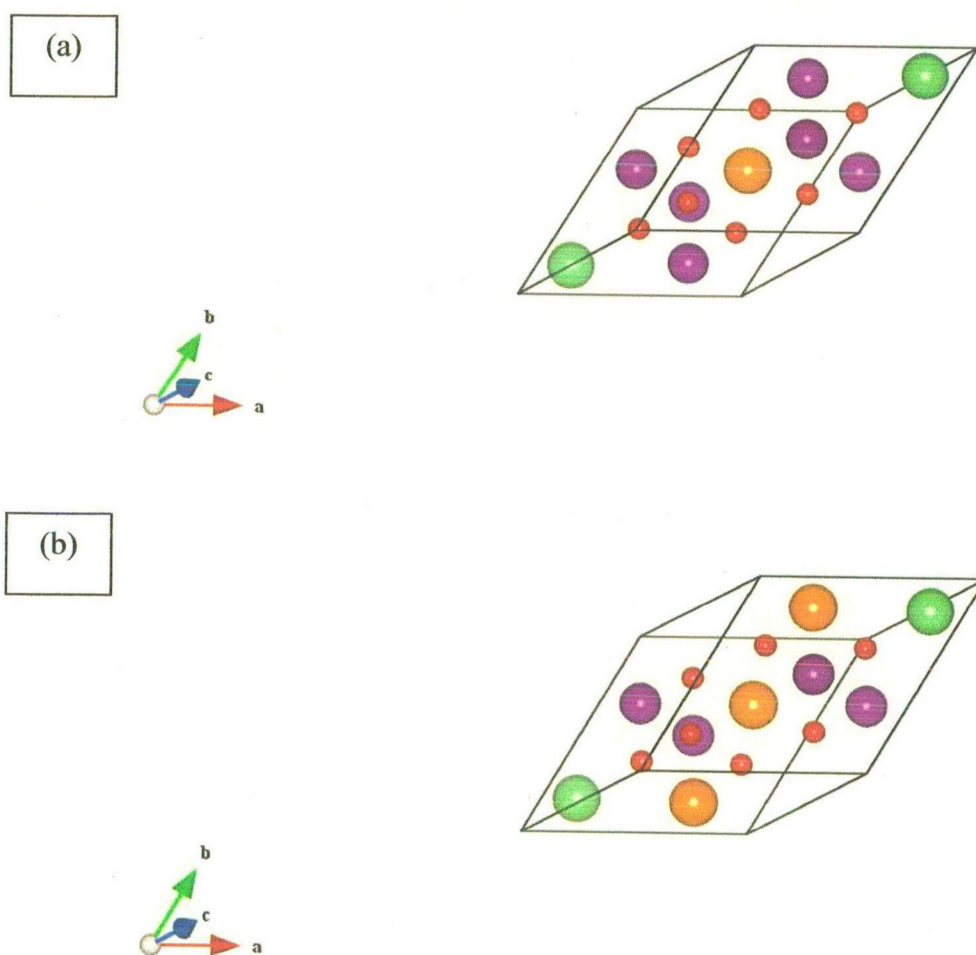
Fig. 5.3.1: Primitive cell of LiMg$_x$Mn$_{2-x}$O$_4$ [(a) x=0.5, (b) x=1.0], Li: Green, Mn: Purple, O: Orange

All the structures were optimized after doping. For the case of both GGA and GGA+U, the final optimized structure for $LiMg_{0.5}Mn_{1.5}O_4$ it was found to be base centered monoclinic and for $LiMgMnO_4$ was found to be body centered orthorhombic. The various lattice parameter values are given in table 5.3.1. In case of GGA+U the lattice parameters for all the compositions are slightly higher than that of GGA.

Table 5.3.1: Lattice parameters of various systems studied

Various systems studied	$LiMg_{0.5}Mn_{1.5}O_4$		$LiMgMnO_4$	
	GGA	GGA+U	GGA	GGA+U
a(Å)	9.965	10.064	5.723	5.697
b(Å)	5.782	5.825	6.015	6.291
c(Å)	23.761	23.987	8.369	8.368
$Cos(\beta)$	-0.846	-0.847	0.000	0.000

Two different bond lengths predicted by GGA are close to the values of theoretical bond lengths of Mn^{3+} low spin (LS) and Mn^{4+} respectively. In case of Mg doping (x=0.5) there exists two kinds of Mn-O bond lengths viz. 1.91 Å and 1.96 Å. On increasing the Mg content the Mn-O bond lengths are observed to be 1.82 and 1.93 Å. Two different bond lengths predicted by GGA+U are close to the values of theoretical bond lengths of Mn^{3+} high spin (HS) and Mn^{4+}. Mn^{3+} (HS) is a Jahn-Teller active ion, which causes the distortion of the spinel structure. Therefore it can be concluded that computation based on GGA+U is giving a clearer picture of the Jahn-Teller distortion in the cubic spinel structure. On doping Mg in $LiMn_2O_4$, it has been observed that there exist two kinds of Mn-O bond lengths viz. 1.93 and 1.97 Å. This shows that manganese is present in Mn^{+4} and Mn^{+3} (LS). As the content of Mg increases the Mn-O bond lengths are found to be 1.91 and 1.94 Å.

Oxidation state of doped metal ion was calculated by comparing the average bond lengths of M-O (M = Mg, Cr, Mn) obtained from first principles study using VASP with predictions based on tabulated ionic radii. The bond length of the M-O was calculated by assuming the oxygen ionic radii to be 1.40 Å and various possible hypothetical oxidation states of each metal ion. Manganese exists in two possible states, Mn^{3+} and Mn^{4+}. Mn^{3+} can be further subdivided into two possibilities of low spin and high spin. In low spin configuration all the four electrons will be present in the t_{2g} states, but in the high spin configuration one of the electrons among the four jumps into e_g state. This causes the Jahn-Teller distortion in the structure. Mg can exist in 2+ state only. A graph between the average M-O bond lengths obtained from VASP and calculated for different oxidation states is shown in Fig. 5.3.2 for the cases of GGA and GGA+U. The solid line represents the exact match between the calculated values and those obtained from the first principles calculations.
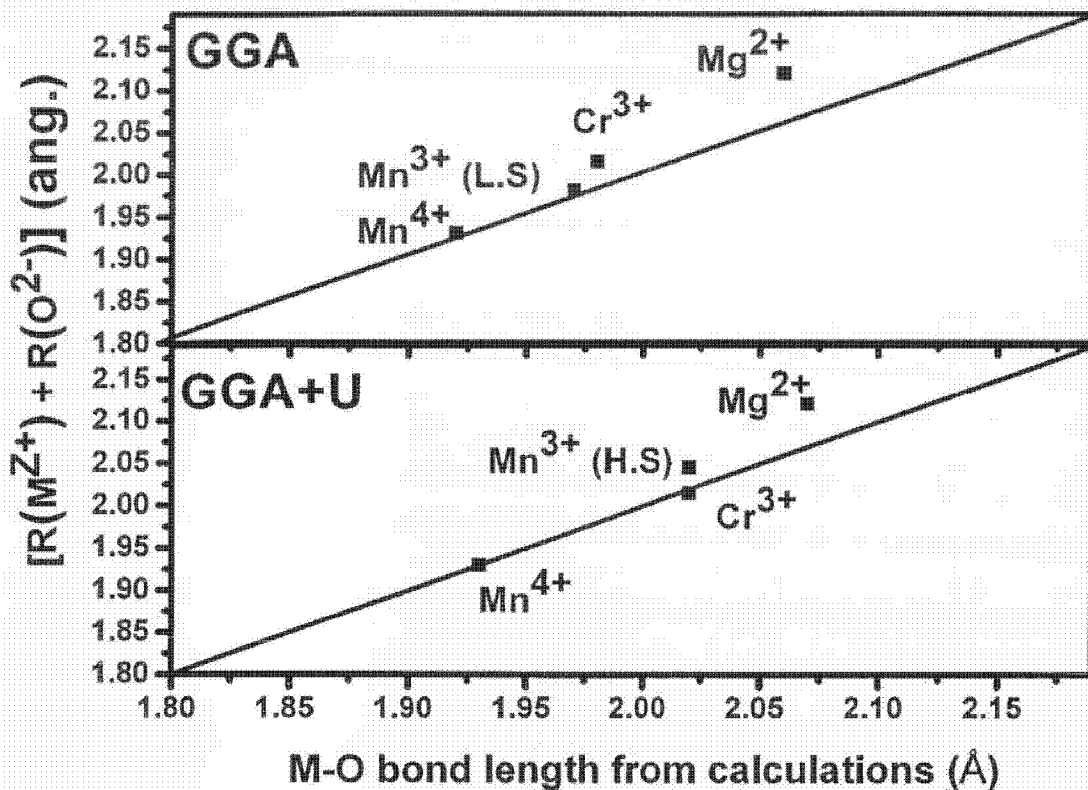
Fig. 5.3.2: Plots showing the difference between calculated bond lengths using hypothetical oxidation state of transition metal ion and bond lengths obtained from the first principles study for GGA and GGA+U. Solid line shows the limit of exact match between the two values. L.S. and H.S. correspond to low spin and high spin configuration respectively.

5.3.2 Suppression of Jahn-Teller Distortion: Comparison between Cr and Mg as Dopants

The suppression of Jahn-Teller distortion by Cr and Mg doping has been discussed in this section. In $LiMn_2O_4$ the Jahn-Teller effect occurs because manganese exists in Mn^{3+} and Mn^{4+} states. Mn^{3+} is a Jahn-Teller active ion; therefore there will be a distortion of the octahedron in this case. Since Cr and Mg are not Jahn-Teller active ions, therefore doping with these elements into the structure of $LiMn_2O_4$ is expected to suppress Jahn-Teller distortion. This suppression is further enhanced because some Mn^{3+} ions get promoted to Mn^{4+} ions which are not Jahn-Teller ions. One can analyze the Jahn-Teller distortion in terms of Jahn-Teller amplitudes.

Van Vleck, 1939, in his study on Jahn-Teller effect showed that there exists three symmetrical modes of vibration of an octahedral complex XY_6 viz. v_1 (Q_1), v_2 (Q_2,Q_3) and v_3 (Q_4,Q_5,Q_6) (Fig. 5.3.3). The magnitude of elongation is proportional to the amplitude Q_3 of e_g (Jahn-Teller active) frozen mode. Values of Q_1, Q_2 and Q_3 are given as follows

Q_1= $[u_x(1)-u_x(4)+u_y(2)-u_y(5)+u_z(3)-u_z(6)]/\sqrt{6}$

Q_2= $[u_x(1)-u_x(4)-u_y(2)+u_y(5)]/2$

Q_3= $[2u_z(6)-2u_z(3)-u_x(1)+u_x(4)-u_y(2)+u_y(5)]/\sqrt{12}$
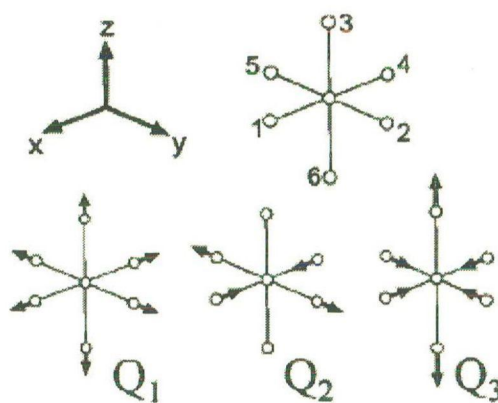
Fig. 5.3.3: Selected symmetrized octahedral modes (Vleck, 1939)

where the value of $u_i(j)$ refers to atomic displacement (bond length changes) with respect to the perfect undistorted octahedron. Values of Q_3 (Jahn-Teller active) frozen mode were plotted against breathing mode Q_1 for each manganese atom in each composition. It can be seen from the Fig. 5.3.4 that Q_1 and Q_3 values, in case of GGA, for manganese atoms in Cr doped $LiMn_2O_4$ are smaller compared to the Mg doped $LiMn_2O_4$. Hence, it can be concluded that doping with Cr suppresses the Jahn-Teller distortion more effectively compared to Mg. The GGA+U based calculations show that the Q_1 values for the manganese atoms in Mg doped $LiMn_2O_4$ are less compared to GGA calculation. Therefore it can be concluded that GGA+U based computation is showing less distortion in case of Mg doped $LiMn_2O_4$ compared to GGA. For the Cr doped $LiMn_2O_4$ ($x=0.5$), the Q_1 values for two of the manganese atoms are found to be closer to zero in case of GGA+U compared to GGA, however the Q_3 values for these atoms are found to be more. In case of $x=1.0$, the Q_1 values are found to be more compared to GGA but the Q_3 values are close to zero. This shows higher magnitude of elongation for two of the manganese atoms of $LiCr_{0.5}Mn_{1.5}O_4$.
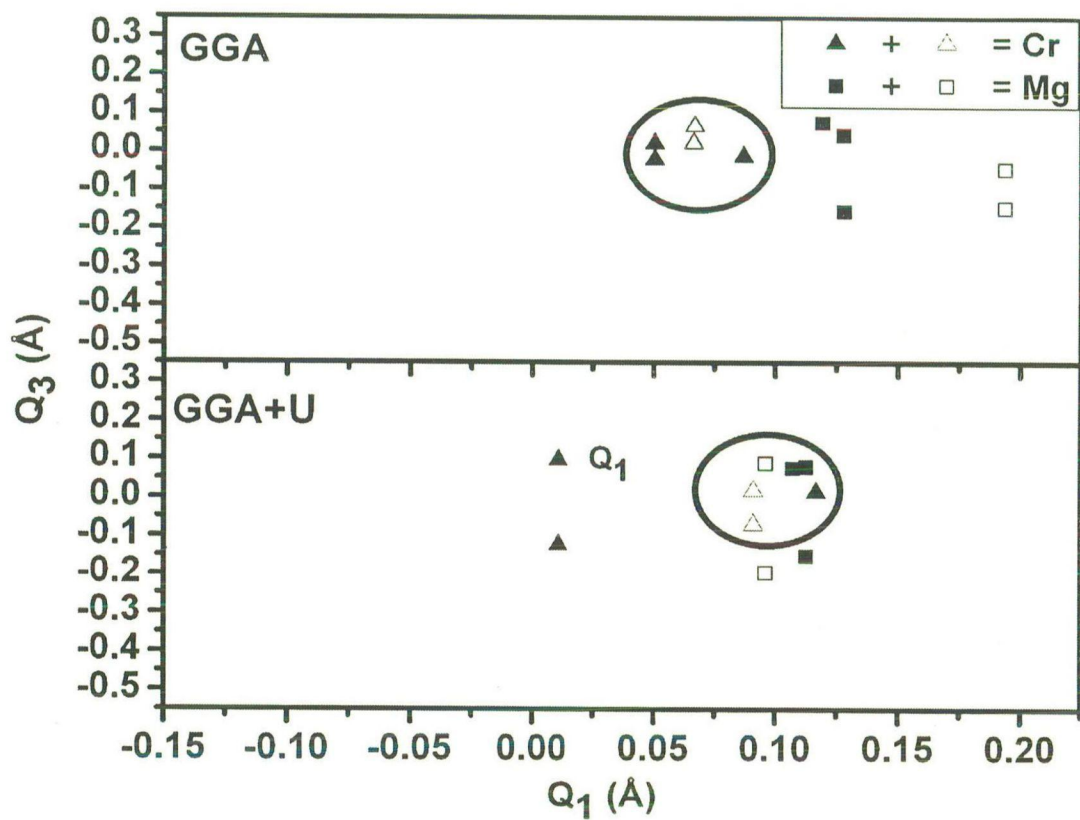
Fig. 5.3.4: Plots showing the Jahn-Teller active frozen phonon mode Q_3 as a function of the breathing mode coordinate Q_1 in $LiM_xMn_{2-x}O_4$ for GGA and GGA+U. Triangles are for Cr and squares are for Mg. The circle is a guide to the eye showing suppression of Jahn-Teller mode for Cr doping (filled correspond to x = 1.0 and empty correspond to x = 0.5).

5.3.3 Density of States and Band Structure

Both GGA and GGA+U based computations predict that Mg doping leads the system towards the half metallic state. Total DOS plots of $LiMg_xMn_{2-x}O_4$ observed using GGA and GGA+U are given in Fig. 5.3.5 and 5.3.6 respectively. On doping with Mg (x=0.5) the density of states around the Fermi level is found to be less compared to $LiMn_2O_4$ in case of GGA based calculations. In case of GGA+U the energy gap between the valence and the conduction band is found to be more compared to that obtained GGA. Finite spin-up density

of states at the Fermi level is present, but the Fermi level lies well in the gap for the spin-down states for x=1.0.
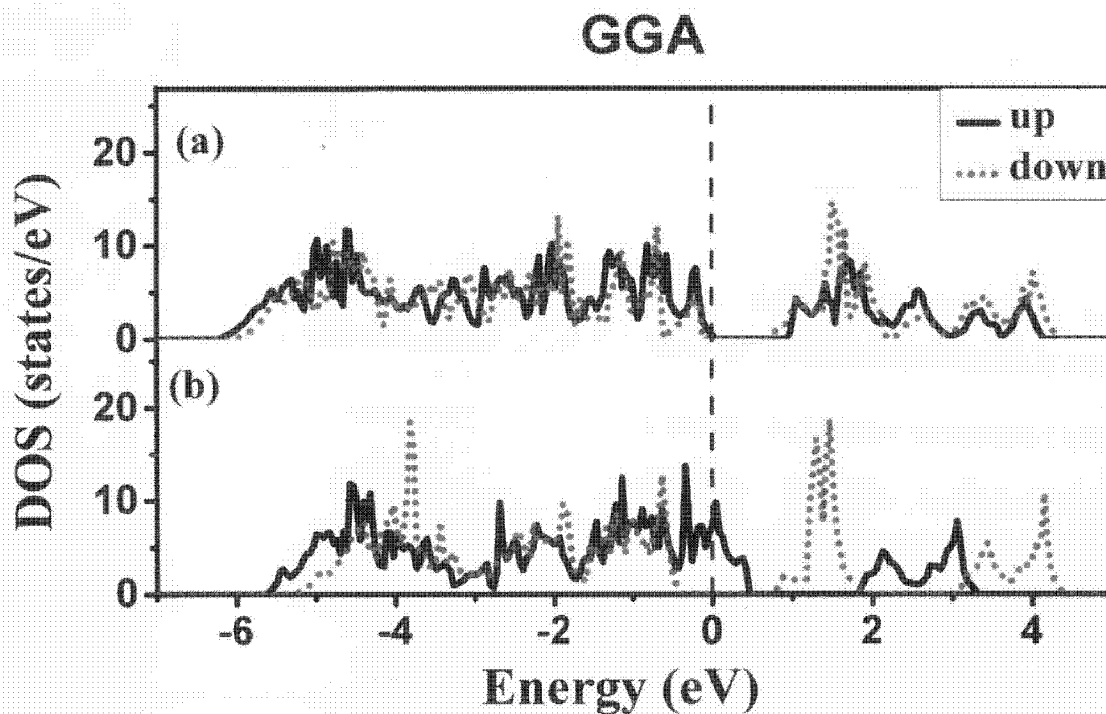
Fig. 5.3.5: Total DOS plot for $LiMg_xMn_{2-x}O_4$ under GGA [(a) x=0.5; (b) x=1.0], where solid black line is for spin up and dotted red line is for spin down states
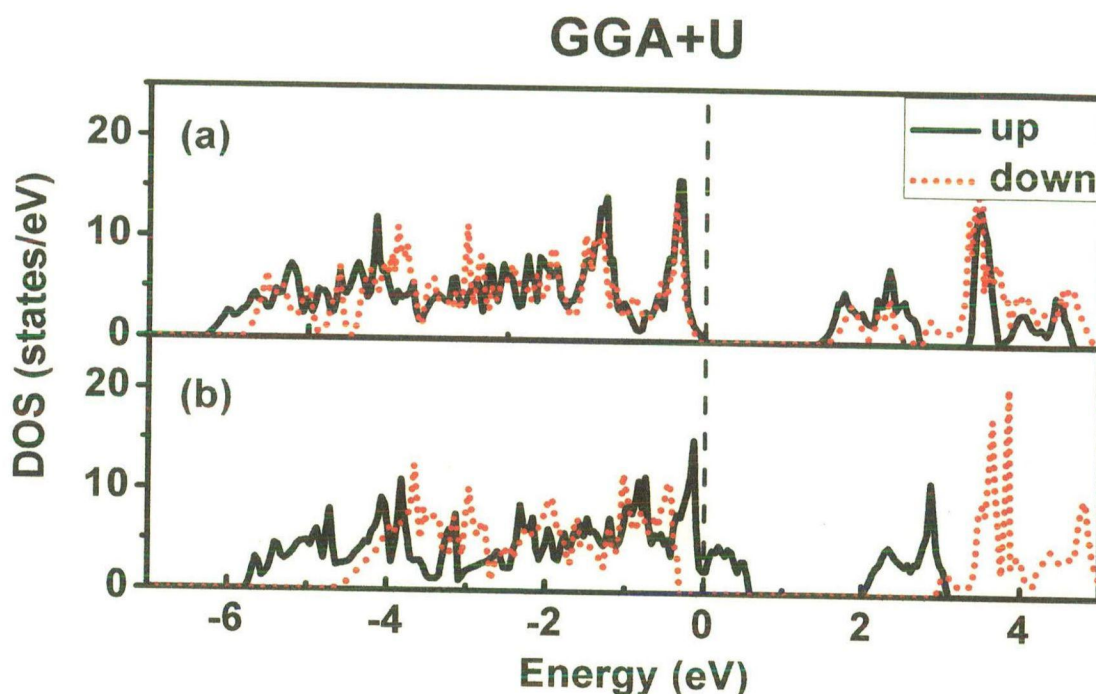
Fig. 5.3.6: Total DOS plot for LiCr$_x$Mn$_{2-x}$O$_4$ computed using GGA+U [(a) x=0.5; (b) x=1.0], where solid black line is for spin up and dotted red line is for spin down states

The GGA results for the partial DOS plots of Mg doped LiMn$_2$O$_4$ for x=0.5 (Fig. 5.3.7), show a clear splitting of the t$_{2g}$ states into triplet for the case of Mn(II) atom. The t$_{2g}$ (down) states of Mn(II) were found to be totally filled. Even though a clear splitting of e$_g$ can be seen from the plots, these states were found to be empty. A similar trend was also found in other manganese atoms. As the content of Mg is increased to x = 1.0, the splitting of the t$_{2g}$ states almost disappears and the number of electrons in the lower energy states decreases. The energy gap between the t$_{2g}$ (up) and t$_{2g}$ (down) states also decreases (Fig. 5.3.8). The GGA+U based results for the partial DOS plots of LiMg$_x$Mn$_{2-x}$O$_4$ (for x=0.5 and 1.0) are shown in Fig. 5.3.9 and 5.3.10. From the GGA+U based calculations it can be seen that in case of x=0.5, the Fermi level shifts towards the lower energy value and it touches the top of the valence band. In case of x=1.0, this shifts even more towards the lower energy and it lies well within the t$_{2g}$ energy states. The energy gap between the t$_{2g}$ (up) and t$_{2g}$ (down) states is found to increase with the increase in Mg content.
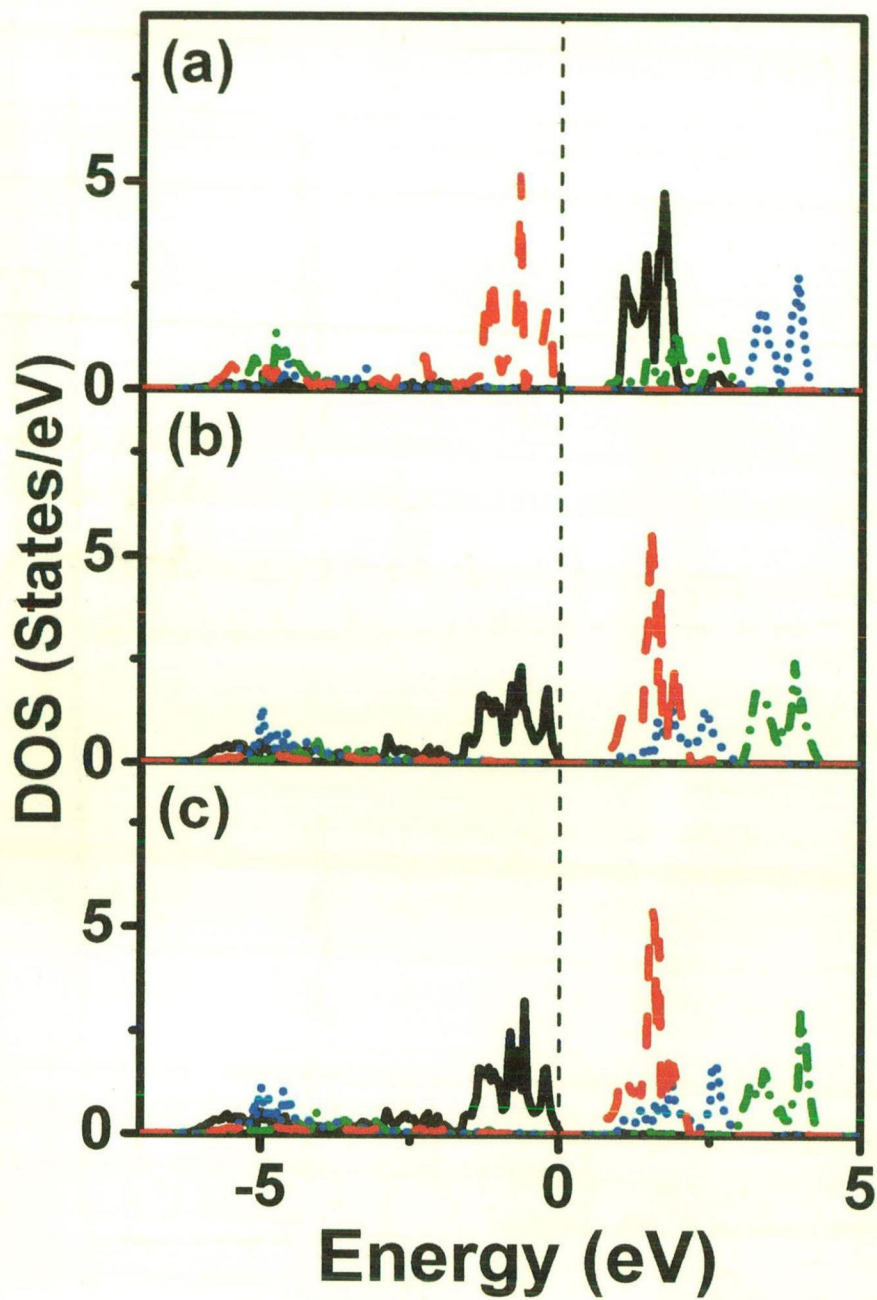
Fig. 5.3.7: Partial DOS plot for $LiMg_{0.5}Mn_{1.5}O_4$ using GGA [(a) Mn(II) – (0.5, 0.0, 0.5), (b) Mn(III) – (0.0, 0.5, 0.5), (c) Mn(IV) – (0.5, 0.5, 0.0)]
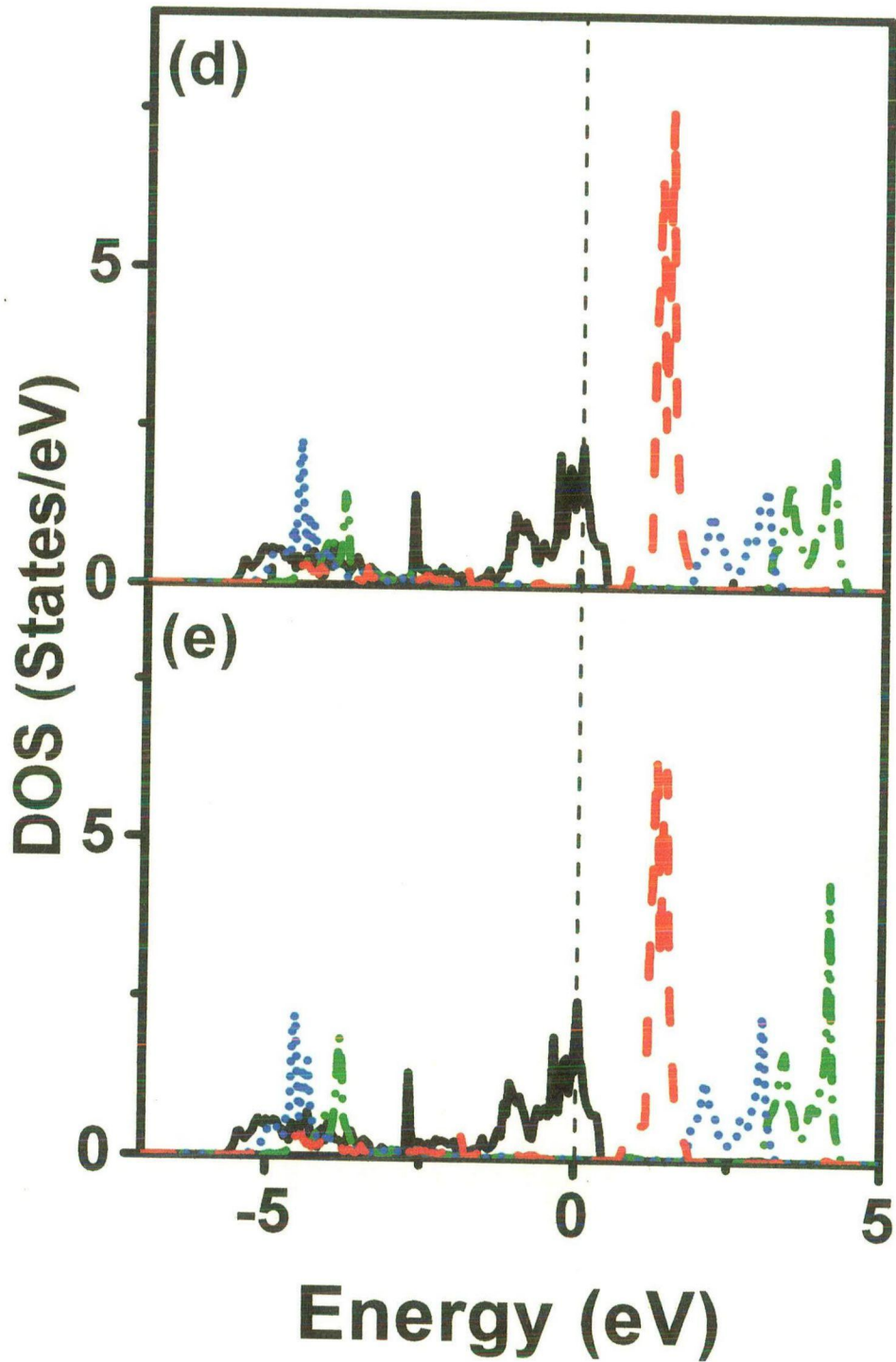
Mg=1.0

Fig. 5.3.8: Partial DOS plot for LiMgMnO$_4$ using GGA [(d) Mn(III) – (0.0, 0.5, 0.5), (e) Mn(IV) – (0.5, 0.5, 0.0)]
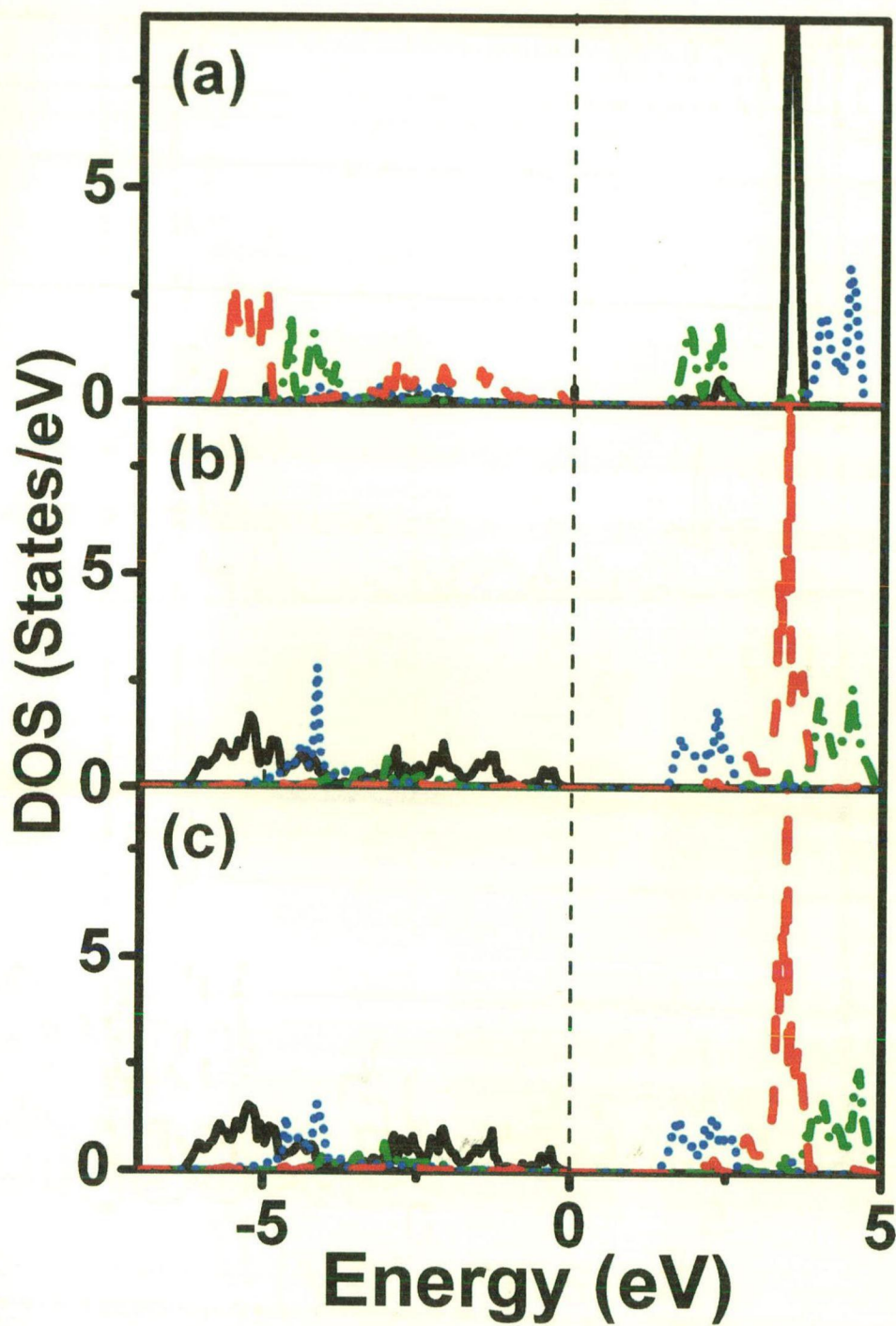
Fig. 5.3.9: Partial DOS plot for $LiMg_{0.5}Mn_{1.5}O_4$ using GGA+U [(a) Mn(II) – (0.5, 0.0, 0.5),
(b) Mn(III) – (0.0, 0.5, 0.5), (c) Mn(IV) – (0.5, 0.5, 0.0)]

Mg=1.0
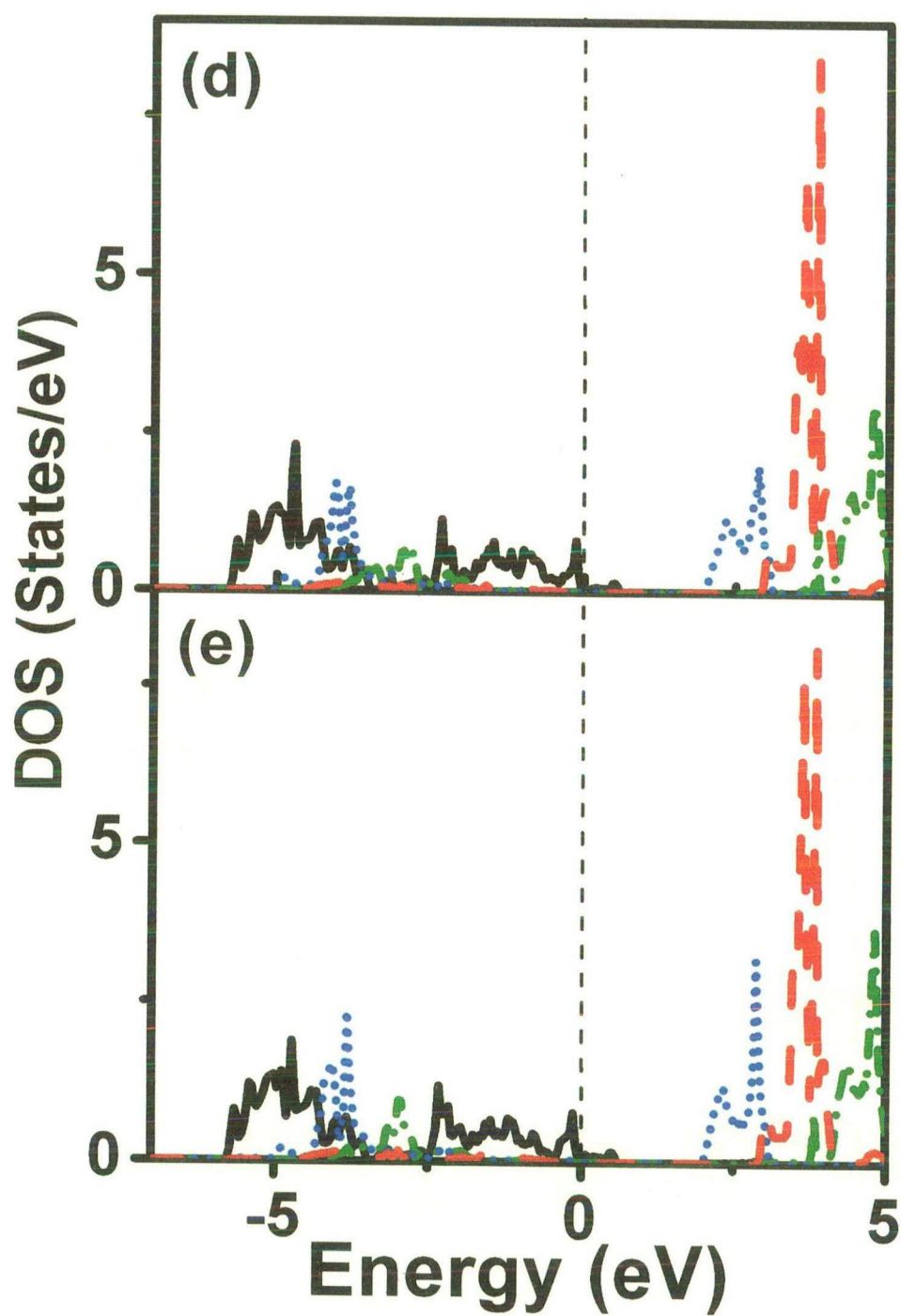
Fig. 5.3.10: Partial DOS plot for LiMgMnO$_4$ using GGA+U [(d) Mn(III) – (0.0, 0.5, 0.5), (e) Mn(IV) – (0.5, 0.5, 0.0)]

Fig. 5.3.11 and 5.3.12 show the band structure plots for both spin up and spin down states in case of GGA, for $LiMg_{0.5}Mn_{1.5}O_4$ and $LiMgMnO_4$ respectively. In case of pristine $LiMn_2O_4$ it has been observed that there exists finite numbers of bands in both spin up as well as spin down cases. However for the Mg doped $LiMn_2O_4$ (x=0.5) the Fermi level just touches the top of valence band for the spin up state, but in case of spin down it lies well inside the energy gap between valence and conduction bands. But as Mg doping increases (x=1.0) in $LiMn_2O_4$, the Fermi level shifts drastically downward to the lower energy for the spin up states and lies inside the valence band. But in case of spin down state it was found to lie within the band gap.
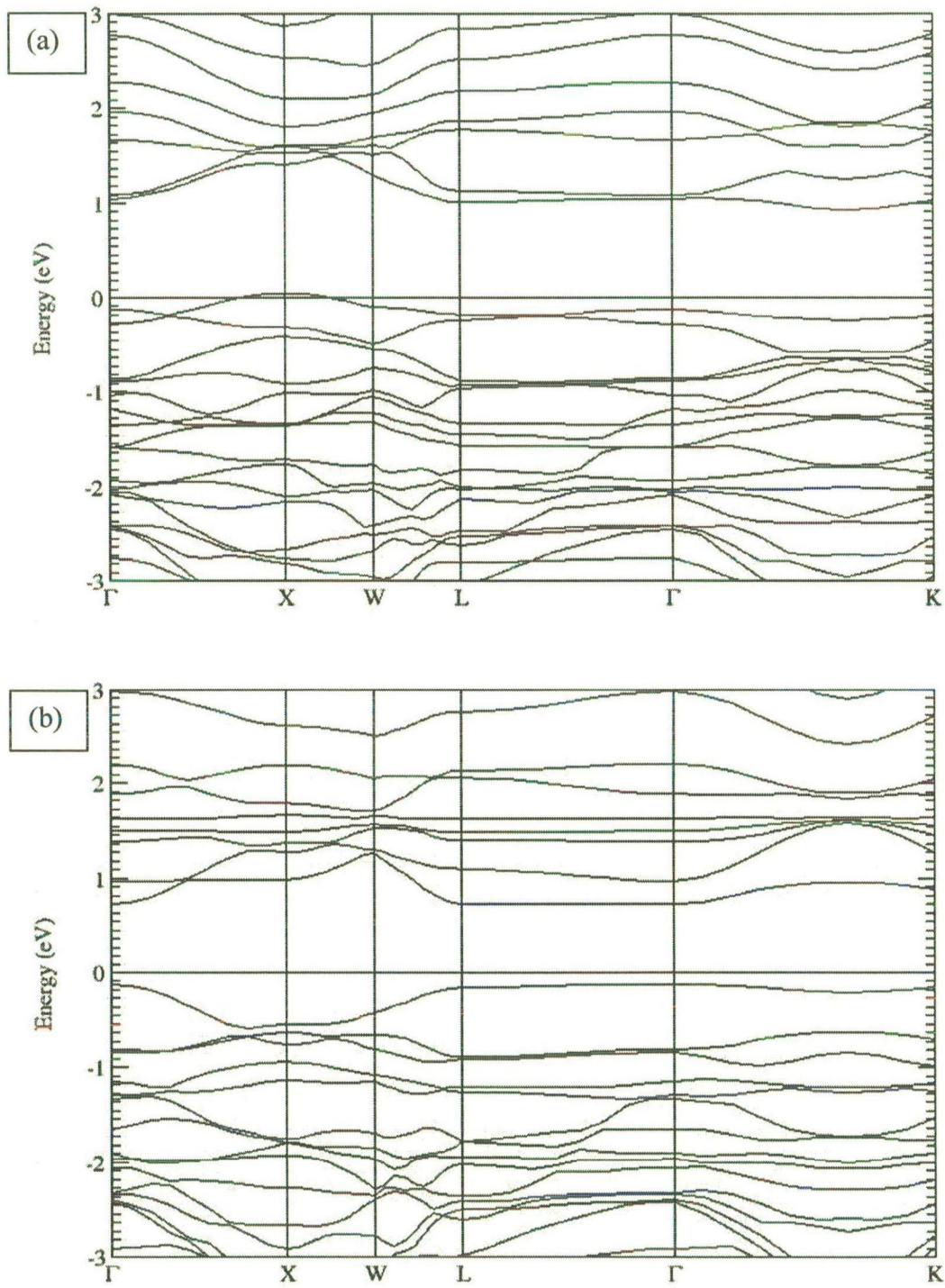
Fig. 5.3.11: Band structure plots for (a) spin up and (b) spin down states of $LiMg_{0.5}Mn_{1.5}O_4$ using GGA
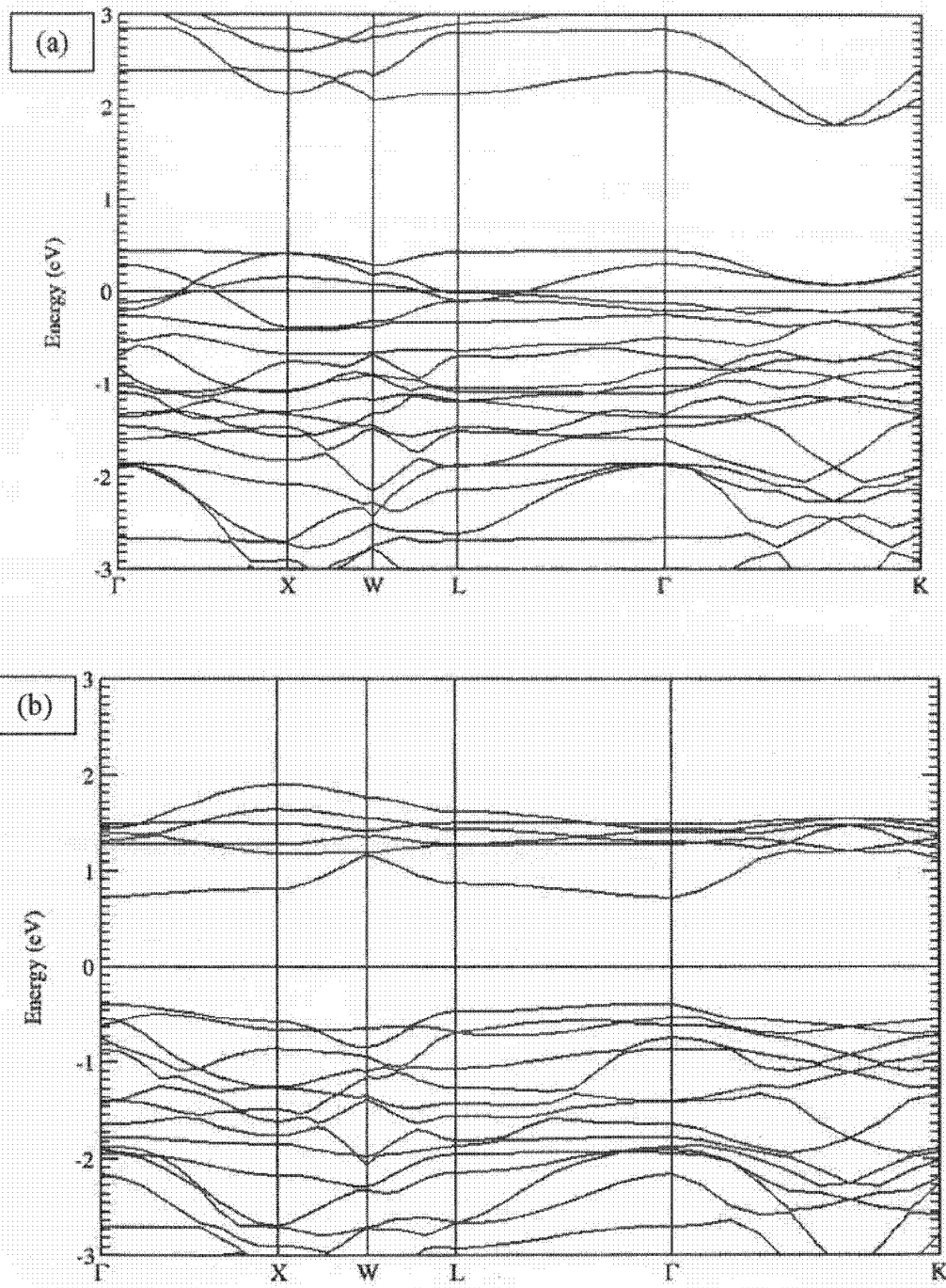
Fig. 5.3.12: Band structure plots for (a) spin up and (b) spin down states of LiMgMnO$_4$ using GGA

5.3.4 Charge Density

Charge density plot for Mg doped $LiMn_2O_4$ in the (110) plane has been shown in Fig 5.3.13 and 5.3.14 for the case of GGA and GGA+U respectively. GGA and GGA+U based computation predict the charge transfer from the transition metal ions to neighboring oxygen ions.
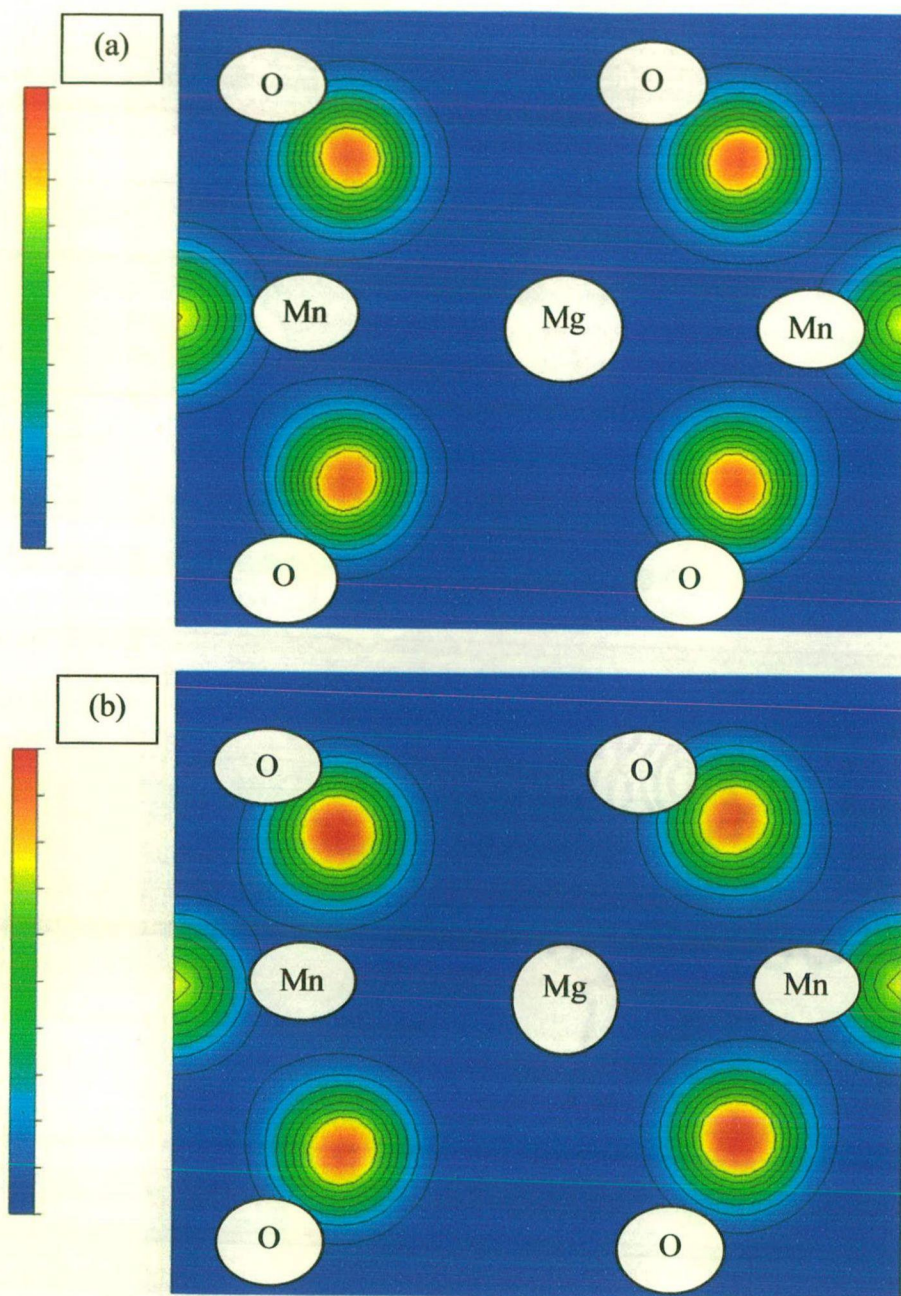
Fig. 5.3.13: Charge density plot for $LiMg_xMn_{2-x}O_4$ [(a) x=0.5, (b) x=1.0] in the (110) plane under GGA, Contour lines are separated by linear increment of $0.1/Å^3$. Red region corresponds to high charge density and the blue region corresponds to low charge density
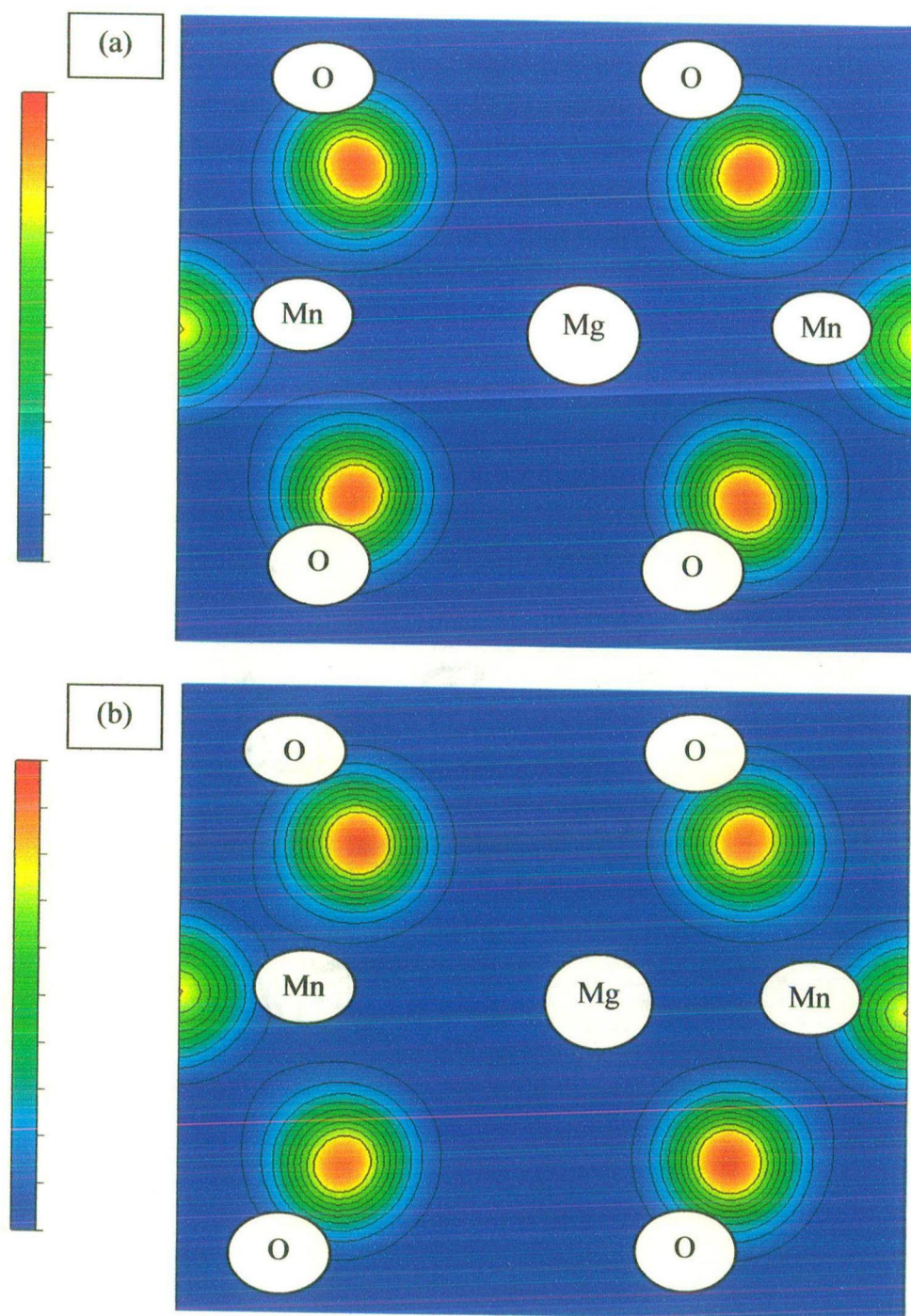
Fig. 5.3.14: Charge density plot for $LiMg_xMn_{2-x}O_4$ [(a) x=0.5, (b) x=1.0] in the (110) plane under GGA+U, Contour lines are separated by linear increment of $0.1/Å^3$. Red region corresponds to high charge density and the blue region corresponds to low charge density

Chapter 6

Conclusions and Future Work

217

The aim of the present work was to study the various aspects of the cathode materials for lithium ion battery and to gain the better understanding of the various mechanisms occurring in the systems. Among the various cathode materials available to us, materials based on the spinel manganese oxides have been chosen as the materials to work upon because of the presence of less toxic and cheaper manganese compared to highly toxic and expensive cobalt or nickel present in other compounds such as $LiCoO_2$, $LiNiO_2$ etc. Some studies have been carried out on the $LiCo_{1/3}Mn_{1/3}Ni_{1/3}O_2$, which contains all of Co, Ni and Mn in equal amount. The effect of citric acid content used as a chelating agent, has been studied on the various properties of the material. One of the major problems with $LiMn_2O_4$ is that the manganese exists in the +3 and +4 oxidation states. Jahn-Teller distortion is highly active in Mn^{+3} ions. Due to the presence of Mn^{+3} (high spin), the structure undergoes phase transformation leading to the unstable host for lithium ions. This in turn reduces the capacity after few cycles of charging and discharging. In order to avoid such structural transformation and loss in capacity after a few cycles of charging and discharging, the dopants such as Cr and Mg were chosen. Cr in its +3 oxidation state is Jahn-Teller inactive ion and is nontoxic in nature. Similarly Mg^{+2} is also a Jahn-Teller inactive ion. It has been shown in the earlier studies that divalent dopants are much effective in avoiding the Jahn-Teller distortion to occur in the layered systems such as $LiMnO_2$. Some contradictions were observed in the literature regarding the doping of Mg in $LiMn_2O_4$. It has been shown by Suryakala et al., 2006 that the structure remains cubic spinel with space group Fd3m up to a doping content of x=0.5 in $LiMg_xMn_{2-x}O_4$, however study carried by Nakamura et al., 2008 shows that the structure changes its space group symmetry from Fd3m to $P4_332$ when the dopant concentration exceeds 0.3. Therefore an in-depth structural analysis has been made in the $LiMg_xMn_{2-x}O_4$ compounds. In case of $LiCo_{1/3}Mn_{1/3}Ni_{1/3}O_2$, Mn is present in its +4 oxidation state which is a Jahn-Teller inactive ion.

Other properties such as microstructural, thermal, impedance spectroscopy and Fourier transform infrared spectroscopy have been studied for both the Cr and Mg doped compounds. Electrochemical performance of the resultant materials has been carried out.

First principles studies have also been carried out in order to study the electronic properties of the Cr and Mg doped materials. Suppression of the Jahn-Teller distortion with these dopants has been studied using the Generalized Gradient Approximation (GGA) and GGA+U (U = Hubbard parameter) approximations. An effort has been made to determine the oxidation states and bond lengths of the various ions present in the structure.

The conclusions drawn from the present study have been summarized as follows

1. Sol-gel is a promising technique for synthesis of the cathode materials of lithium ion battery. Materials such as $LiMn_2O_4$, $LiCr_xMn_{2-x}O_4$, $LiMg_xMn_{2-x}O_4$, and $LiCo_{1/3}Mn_{1/3}Ni_{1/3}O_2$ have been synthesized in the present study by sol-gel technique.

2. X-ray studies of the Cr doped materials ($LiCr_xMn_{2-x}O_4$ where $0.1 \leq x \leq 0.5$) have shown that the structure remains cubic spinel with Fd3m space group symmetry. This shows that Cr can be doped in $LiMn_2O_4$ without changing its crystal symmetry and replace the Mn ions present in the structure. A decrease in lattice constant with the increase in Cr content has been observed because ionic radius of Cr^{+3} is smaller than that of Mn^{+3}.

3. Change in particle morphology from truncated octahedron to perfect octahedron has been observed in $LiCr_xMn_{2-x}O_4$ ($0.1 \leq x \leq 0.5$) with the increase in Cr content. Such change in morphology with the increase in Cr content can be attributed to the decrease in free energy of the system and hence stabilization of the cubic spinel structure. Particle size has been observed to decrease with the increase in Cr content showing that the rate of nucleation becomes more than the growth rate for larger Cr content.

4. Electrochemical studies show that the capacity loss in the Cr doped $LiCr_xMn_{2-x}O_4$ is less compared to undoped $LiMn_2O_4$. However, the first cycle capacity decreases with the increase in Cr content, which is because of the fact that Mn^{+3} content decreases in

219

the structure and Cr^{+3} can not be oxidized or reduced in the 4 V regions. The voltage step observed in the 4 V regions in case of $LiMn_2O_4$ has been suppressed with doped materials.

5. Impedance spectroscopy shows that the bulk impedance of the doped materials increases with the increase in Cr content. The electrical conductivity of the various doped materials is of the order of 10^{-5} S/cm.

6. In the FTIR spectra of the doped compounds no major shift in the positions of the bands at 501 and 613 cm^{-1} has been observed. These bands correspond to the asymmetric stretching of the MnO_6 octahedra. It shows that Cr^{+3} ions have effectively replaced the Mn^{+3} ions.

7. XRD studies on the Mg doped $LiMn_2O_4$ shows that the structure remains cubic spinel for the entire doping range of $0.05 \leq x \leq 0.5$ in $LiMg_xMn_{2-x}O_4$. However, the space group symmetry changes from Fd3m to $P4_332$ for x>0.25, above which the material is single phase cubic spinel with space group $P4_332$. At x=0.25 both the phase groups are found to be present.

8. Particle size decreases with increase in Mg content. The average particle size in the powders ranges from 100 to 350 nm. No significant change in the powder morphology has been observed with Mg as dopant.

9. FTIR spectra show that the number of bands increases with increase in Mg doping content. This is because of the fact that the structure becomes more ordered with increasing the doping content. The space group symmetry changes from O_h^7 to O_7 as the structure becomes ordered and hence the number of bands increases.

10. From the thermal study it has been observed in $LiMg_xMn_{2-x}O_4$ that the decomposition temperature falls exponentially with the increase in Mg doping content and hence nonstoichiometry in the structure of $LiMg_xMn_{2-x}O_{4-\delta}$ increases in the air atmosphere. It can be inferred from the TG plots that the formation of Li_2MnO_3 and tetragonal $LiMn_2O_4$ increases with the increase in Mg content at higher temperatures.

11. The electrical conductivity is of the order of 10^{-5} S/cm and it decreases with the increase in Mg content. At lower frequencies the degree of electric polarization in the material is low when doped with low Mg content and the polarization increases with the increase in Mg content.

12. Electrochemical studies show that the capacity decreases sharply with the increase in Mg content. However the capacity fall with the number of cycles reduces with the increase in Mg content. This shows that Mg stabilizes the host structure. The fall in capacity is attributed to the fact that each dopant removes two Mn^{+3} ions from the transition metal sublattice in order to maintain charge balance. Since the Mg^{+2} or Mn^{+4} can not be oxidized or reduced in the 4 V range and hence give rise to fall in capacity.

13. Average particle size obtained in case of $LiNi_{1/3}Mn_{1/3}Co_{1/3}O_2$ is ~ 200 nm for R′=3 (R′=citric acid to metal ion ratio), which is less than that of the earlier reported particle size in the same system Meng et al., 2007.

14. The first cycle coulombic efficiency for R′=3 in the voltage range of 4.6 - 2.5 V is 93%, whereas, the highest efficiency Meng et al., 2007 in the voltage range of 4.6 - 2.8 V reported so far by others is 87.3% using sol-gel technique. The first cycle discharge capacities for R′=1, 2 and 3 are 146.15 mAh/g, 153.76 mAh/g and 151.76 mAh/g respectively in the voltage range of 4.3 - 3.0 V. Discharge capacity of 200 mAh/g has been observed for R′=3 in the voltage range of 4.6 - 2.5 V.

15. The activation energies (E_a) for conduction are almost same for all the samples synthesized with various citric acid contents. E_a for R′ = 1, 2 and 3 are 0.38, 0.37 and 0.39 eV respectively. The electrical conductivity at room temperature for the various samples is in the range of 10^{-7} to 10^{-8} S/cm. In $LiNi_{1/3}Mn_{1/3}Co_{1/3}O_2$, the electronic configurations of Mn^{4+}, Co^{3+} and Ni^{2+} are ($t_{2g}^3 e_g^0$), ($t_{2g}^6 e_g^0$), and ($t_{2g}^6 e_g^2$) respectively. Due to the absence of free charge carriers, no effective transport can take place. Hence the material has low electrical conductivity.

16. Using First principles studies results in different ground states for pristine $LiMn_2O_4$ were generated using approximations of GGA and GGA+U. For $LiMn_2O_4$ GGA based computation shows body centered tetragonal phase is the ground state whereas face centered orthorhombic is the ground state under GGA+U. GGA based calculation predicts that the pristine $LiMn_2O_4$ is metallic whereas GGA+U finds it insulating.

17. GGA and GGA+U based calculations show that for the doped systems $LiM_{0.5}Mn_{1.5}O_4$ (M= Cr or Mg) the ground state is base centered monoclinic and for $LiMMnO_4$ (M= Cr or Mg) it is body centered orthorhombic.

18. For doped spinels, GGA based computation predicts the ground state to be half metallic while GGA+U based computation predicts it to be insulating or metallic depending on the doping concentration. GGA+U based computational studies predicts insulator-metal-insulator transition as a function of doping in case of Cr and in case of Mg the ground state is found to go from insulating to a half metallic state with the increase in dopant.

19. Suppression of splitting of the e_g states for doped systems shows the suppression of JT distortion. GGA+U based calculation shows the effectiveness of the magnesium doping in suppressing the JT distortion while GGA shows chromium to be more effective for suppression of JT distortion. Both GGA and GGA+U based calculations predict a significant charge transfer between the manganese atoms and the dopant atoms.

20. An attempt was made to calculate the average oxidation state of manganese, chromium and magnesium present in the various structures. Two types of Mn-O bond lengths were found in the relaxed structure of pristine $LiMn_2O_4$ generated using GGA (d_1^{Mn-O} = 1.92 Å and d_2^{Mn-O} = 1.96 Å) and that generated using GGA+U (d_1^{Mn-O} = 1.93 Å and d_2^{Mn-O} = 2.02 Å). The values predicted by GGA+U are in better agreement with the experimental results. This shows the presence of two kinds of manganese ions with different ionic radii. Chromium was found to be present in oxidation state

of +3 while magnesium is present in +2 oxidation state in the doped systems. Thus the content of Mn^{+3} in doped systems is less compared to the pristine compound which implies less Jahn-Teller distortion in doped system. Thus, the doping of $LiMn_2O_4$ with chromium and magnesium increases the structural stability.

6.2.   Future Work

The research work which can be further carried out is summarized as follows

1. $LiMn_2O_4$ undergoes structural changes from cubic spinel to orthorhombic spinel below room temperature. It also shows phase transformations at higher temperatures. The in-situ XRD study can lead to some interesting results. Structural stability above and below room temperature using Cr and Mg as dopant in $LiMn_2O_4$ can also be checked by using in-situ XRD.

2. The presence of two different space groups in $LiMg_xMn_{2-x}O_4$ can be studied at non-ambient temperatures.

3. Different ground states in Cr and Mg doped $LiMn_2O_4$ (base centered monoclinic and body centered orthorhombic) predicted by First principles can be crosschecked experimentally.

4. Relation between different morphologies of the powder particles and their electrochemical behavior can be studied. Mechanism behind the change in morphology in Cr doped $LiMn_2O_4$ can be clearly understood using TEM (transmission electron microscopy) studies.

5. Since Co is highly toxic and costly, therefore dopants which can maintain the layered structure of $LiCo_{1/3}Mn_{1/3}Ni_{1/3}O_2$ and effectively replace Co can be tried. Dopants which can reduce the activation energy of the compound and increase its electrical conductivity can be studied.

6. Experimental studies on insulator-metal-insulator transition (in Cr doped $LiMn_2O_4$) and insulator-half metallic transition (in Mg doped $LiMn_2O_4$) observed by using First principles can be carried out.

References

1. Akimoto, J., Takahashi, Y., Gotoh, Y., and Mizuta, S., J., "Single crystal growth of the spinel-type $LiMn_2O_4$", Crystal Growth, 229 (2001) 405.

2. Amatucci, G. G., Tarascon, J. M., and Klein, C., "CoO_2, The end member of the $LiCoO_2$ solid solution", J. Electrochem. Soc., 143 (1996) 1114.

3. Amemiya, C., Iriyama, J., Yonezawa, M., NEC R&D, 42 (2001) 241.

4. Anis, A., Banthia, A. K., and Bandyopadhyay S., "Synthesis & Characterization of PVA/STA Composite Polymer Electrolyte Membranes for Fuel Cell Application", Journal of Materials Engineering and Performance, 17 (2008) 772.

5. Armstrong, A.R. and Bruce, P.G., "Synthesis of layered $LiMnO_2$ as an electrode for rechargeable Lithium batteries", Nature, 381 (1996) 499.

6. Aurbach, D., Eli, Y. E., Markovsky, B., and Zaban, A., "The study of electrolyte solutions based on ethylene and diethyl carbonates for rechargeable Li batteries II. Graphite electrodes", J. Electrochem. Soc., 142 (1995) 2882.

7. Basu, US Patent 4304825, Dec. 8, 1981.

8. Basu, R. and Seshadri, R., "Suppressing the charge-ordering transition in $LiMn_2O_4$ through substitution of Li by Mg", J. Mater. Chem., 10 (2000) 507.

9. Bhattacharya, D., Pandya D. K.,Kashyap, S. C., Pathak, L.C., Mishra, S.,Sen, D.,and Chpra, K. L., "Lattice and electronic structure of $YBa_2Cu_2PbO_x$ superconductors", Physica C, 170 (1990)245.

10. Blochl, P. E., "Projector augmented-wave method", Phys. Rev. B, 50 (1994) 17953.

11. Blugel, Ph.D Thesis, RWTH Aachen (1998)

12. Boucher, B., Buhl, R., and Perrin, M., "Magnetic structure of Mn_3O_4 by neutron diffraction", J. Appl. Phys., 42 (1971) 1615.

13. Bragg, W.H., "The structure of the spinel group of crystals", Philos. Mag., 10 (1915) 199.

14. Brahma, P., Banerjee, S., Das, D., Mukhopadhyay, P.K., Chatterjee, S., Nigam, A. K., Chakravorty, D., "Properties of nanocomposites of a-Fe and Fe_3O_4", Journal of Magnetism and Magnetic Materials, 246 (2002) 162.

15. Branford, W., Green, M. A., and Neumann, D. A., "Structure and ferromagnetism in Mn^{4+} spinels: $AM_{0.5}Mn_{1.5}O_4$ (A = Li, Cu; M = Ni, Mg)", Chem. Mater., 14 (2002) 1649.

16. Capsoni, D., Bini, M., Chiodelli, G., Massarotti, V., Mozzati, M. C., and Azzoni, C. B., "Structural transition in Mg-doped $LiMn_2O_4$: A comparison with other M-Doped Li–Mn spinels", Solid State Comm., 125 (2003) 179.

17. Carvajal, J. Rodrı́guez, Rousse, G., Masquelier, C., and Hervieu, M., "Electronic crystallization in a Lithium battery material: Columnar ordering of electrons and holes in the spinel $LiMn_2O_4$", Phys. Rev. Lett., 81(1998) 4660.

18. Chadi and Cohen, "Special Points in Brillouin zone", Phys. Rev. B, 8 (1973) 5747.

19. Choi, S. and Manthiram, A., "Chemical synthesis and properties of spinel $Li_{1-x}Co_2O_{4-\delta}$", J. Solid State Chem., 164 (2002) 332.

20. Crabtree, G. W. and Dresselhaus, M. S., "The hydrogen fuel alternative", Mater. Res. Soc. Bull. 33 (2008) 421.

21. Cullity, B.D., "Elements of X-Ray Diffraction", Addition–Wesley publishing company, Inc.1977.

22. Dahn, J. R., Sleigh, A. K., Shi, H., Reimers, J. N., Zhong, Q., and Way B. M., "Dependence of the electrochemical intercalation of lithium in carbons on the crystal structure of the carbon", Electrochimica Acta, 38 (1993) 1179.

23. Dahn, J.R., Fuller, E.W., Obrovac, M., Sacken, U. yon, "Thermal stability of Li_xCoO_2, Li_xNiO_2 and $\lambda-MnO_2$ and consequences for the safety of Li-ion cells", Solid State Ionics, 69 (1994) 265.

24. Daniel, C., "Materials and processing for lithium ion battery", Journal of Materials, 60 (2008) 43.

25. Davidson, E. R., "Methods in Computational molecular physics" Plenum, New York, 1983, p. 95.

26. Deng, B., Nakamura, H., Zhang, Q., Yoshio, M., and Xia, Y., "Greatly improved elevated-temperature cycling behavior of $Li_{1+x}Mg_yMn_{2-x-y}O_{4+\Delta}$ spinels with controlled oxygen stoichiometry", Electrochimica Acta, 49 (2004) 1823.

27. Dreizler, R. and Gross, E., "Density Functional Theory", Plenum Press, New York (1990).

28. Dunitz, J. D. and Orgel, L. E., "Electronic properties of transition-metal Oxides-I Distortions from cubic symmetry", J. Phys. Chem. Solids, 3 (1957) 20.

29. Dunitz, J. D. and Orgel, L. E., "Electronic properties of oxides-II Transition-metal cation distribution amongst octahedral and tetrahedral sites", J. Phys. Chem. Solids, 3 (1957) 318.

30. Dutta, G., Manthiram, A., Goodenough, J. B., Grenier, J.-C., "Chemical synthesis and properties of $Li_{1-\delta}Ni_{1+\delta}O_2$ and $Li[Ni_2]O_4$", J. Solid State Chem., 96 (1992) 123.

31. Dutta, A. and Ghosh, A., "Effect of alkaline earth ions on the dynamics of lithium ions in bismuthate glasses", Phys. Rev. B, 72 (2005) 224203.

32. Eisenberg M., "Performance of Ambient Temperature Sulfospinel and TiS_2-Lithium Secondary Cells", Electrochimica Acta, 26 (1981) 955.

33. Endo, M., Kim, C., Nishimura, K., Fujino, T., and Miyashita, K., "Recent development of carbon materials for Li-ion batteries", Carbon, 38 (2000) 183.

34. Farrell, A. E., Gopal, A. R., "Bioenergy research needs for heat, electricity, and liquid fuels", Mater. Res. Soc. Bull., 33 (2008) 373.

35. Feng, G. F., Katiyar, M., Abelson, J. R., and Maley, N., "Dielectric functions and electronic band states of a-Si and a-Si:H", Phys. Rev. B, 45 (1992) 9103.

36. Flandrois, S. and Simon, B., "Carbon materials for Lithium ion rechargeable batteries", Carbon, 37 (1999) 165.

37. Fong, R., Sacken, U. Y., and Dahn, J. R., "Studies of Lithium intercalation into carbons using nonaqueous electrochemical cells", J. Electrochem. Soc., 137 (1990) 2009.

38. Furthmuller, J., Hafner, J., and Kresse, G., "Ab initio calculation of the structural and electronic properties of carbon and boron nitride using ultrasoft pseudopotentials", Phys. Rev. B, 50 (1994) 15606.

39. George J. Methlie II, Ambler, Pa, US patent 3415687, Dec. 10, 1968

40. Ginley, D., Green, M. A., and Collins, R., "Solar energy conversion toward 1 Terawatt", Mater. Res. Soc. Bull., 33 (2008) 355.

41. Goodenough, J. B., "Jahn-Teller Phenomena in Solids", Annu. Rev. Mater. Sci., 28 (1998) 1.

42. Haas, C., "Phase transitives in crystals with the spinel structure", .J. Phys. Chem. Sol., 26 (1955) 1225.

43. Goodenough, J. B., "Magnetism and the Chemical Bond", Wiley, New York (1963).

44. Goodenough, J. B., Manthiram, A. and Wnetrzewski, B., "Electrodes for Lithium batteries", J. Power Sources, 43-44 (1993) 269.

45. Goodenough John B., "Cathode materials: A personal perspective", J. Power Sources 174 (2007) 996.

46. Gozdz, A. S., Scmutz, C. N., and Tarascon, J. M., US Patent 5296318, (1994).

47. Goztz, A. S., Schmutz, C., Tarascon, J. M., and Waren P. A., US Patent no. 5,418,091, (1995).

48. Gozu, M., Swierczek, K., and Molenda, J., "Structural and transport properties of layered $Li_{1+x}(Mn_{1/3}Co_{1/3}Ni_{1/3})_{1-x}O_2$ oxides prepared by a soft chemistry method", J. Power Sources. in press, doi: 10.1016/j.jpowsour.2008.11.088

49. Grechnev, G.E., Ahuja, R., Johansson, B., and Eriksson, O., "Electronic structure, magnetic, and cohesive properties of $Li_xMn_2O_4$: Theory", Phys. Rev. B, 65, (2002) 174408.

50. Gummow, R. J., de Kock, A., Thackeray, M.M., "Improved capacity retention in rechargeable 4 V Lithium/Lithium Manganese Oxide (spinel) cells", Solid State Ionics, 69 (1994) 59.

51. Hamon, Y., Brousse, T., Jousse, F., Topart, P., Buvat, P., and Schleich, D.M., "Aluminum negative electrode in Lithium ion batteries", J. Power Sources, 97-98 (2001)185.

52. Hayashi, N., Ikuta, H., and Wakihara, M., "Cathode of $LiMg_yMn_{2-y}O_4$ and $LiMg_yMn_{2-y}O_{4-\delta}$ spinel phases for Lithium secondary batteries", J. Electrochem. Soc., 146 (1999) 1351.

53. Hayman, B., Heinen, J. W., and Brondsted, P., "Materials Challenges in present and future wind energy", Mater. Res. Soc. Bull., 33 (2008) 343.

54. Hohenberg, P. C. and Kohn, W., "Inhomogeneous electron gas", Phys. Rev., 136, (1964) B864.

55. Hong, J., Fang, B., and Wang, C., "The electrochemical performance of $LiNi_{1/3}Mn_{1/3}Co_{1/3}O_2$ prepared by sol-gel method", 211th ECS Meeting, 89 (2007)

56. Hwang, B. J., Tsai, Y. W., Carlier, D., and Ceder, G., "A Combined Computational/Experimental study on $LiNi_{1/3}Co_{1/3}Mn_{1/3}O_2$", Chem. Mater., 15 (2003) 3676.

57. Ikuta Hiromasa, Takanaka Kouichi, Wakihara Masataka, "The effect of Chromium substitution on the phase transition of Lithium Manganese spinel Oxides", Thermochimica Acta 414 (2004) 227.

58. Jeong, I. S., Kim, J. U., and Gu, H. B., "Electrochemical properties of $LiMg_yMn_{2-y}O_4$ spinel phases for rechargeable Lithium batteries", J. Power Sources, 102 (2001) 55.

59. Johnson D. D., "Modified Broyden's method for accelerating convergence in self-consistent calculations", Phys. Rev. B, 38 (1988) 12807.

60. Julien, C.M. and Massot, M., "Lattice vibrations of materials for Lithium rechargeable batteries I. Lithium Manganese Oxide spinel", Materials Science and Engineering B, 97 (2003) 217.

61. Julien, C.M. and Massot M., "Spectroscopic studies of the structural transitions in positive electrodes for Lithium batteries", J. Power Sources, 119–121 (2003) 743.

62. Julien, C.M. and Camacho-Lopez, M. A., "Lattice vibrations of materials for Lithium rechargeable batteries II. Lithium extraction–insertion in spinel structures", Materials Science and Engineering B, 108 (2004) 179.

63. Julien C.M. and Massot M., "Lattice vibrations of materials for Lithium rechargeable batteries III. Lithium Manganese Oxides", Materials Science and Engineering B, 100 (2003) 69.

64. Kasuh, T., Mabuchi, A., Tokumitsu, K., and Fujimoto, H., "Recent trends in carbon negative electrode materials", J. Power Sources 68 (1997) 99.

65. Kern, G., Kresse, G., and Hafner, J., "Ab inito calculation of the lattice dynamics and phase diagram of boron nitride", Phys. Rev. B, 59 (1999) 8551.

66. Kim, H. S., Kong, M., Kim, K., Kim, I. J., and Gu, H. B., "Effect of Carbon coating on $LiNi_{1/3}Mn_{1/3}Co_{1/3}O_2$ cathode material for Lithium secondary batteries", J. Power Sources, 171 (2007) 917.

229

67. Kobayashi, H., Arachi, Y., Emura, S., Kageyama, H., Tatsumi, K., and Kamiyama, T., "Investigation on Lithium de-intercalation mechanism for $Li_{1-y}Ni_{1/3}Mn_{1/3}Co_{1/3}O_2$", J. Power Sources, 146 (2005) 640.

68. Kohn, W. and Sham, L. J., "Self-consistant equations including exchange and correlation effects", Phys. Rev., 140 (1965) A1133.

69. Kono, M., Hayashi, E., and Watanabe, M., "Preparation, Mechanical properties, and electrochemical characterization of polymer gel electrolytes prepared from Poly(alkylene oxide) macromonomers", J. Electrochem. Soc., 146 (1999) 1626.

70. Kresse, G. and Hafner, J., "Ab-initio molecular dynamics for liquid metals", Phys. Rev. B, 47 (1993) 558.

71. Kresse, G. and Hafner, J., "Ab-initio molecular dynamics for open shell transition metal", Phys. Rev. B, 48 (1993) 13115.

72. Kresse, G. and Furthmuller, J., "Efficiency of ab-initio total energy calculations for metals and semiconductors using a plane wave basis set", Comp. Mat. Sci., 6 (1996) 15.

73. Kresse, G. and Furthmuller J., "Efficient iterative schemes for ab initio total-energy calculations using a plane-wave basis set", Phys. Rev. B, 54 (1996) 11169.

74. Kresse, G. and Joubert, J., "From ultrasoft pseudopotentials to the projector augmented-wave method", Phys. Rev. B, 59 (1999) 1758.

75. Kubo, K., Fujiwara, M., Yamada, S., Arai, S., Kanda, M., "Synthesis and electrochemical properties for $LiNiO_2$ substituted by other elements", J. Power Sources, 68 (1997) 553.

76. Kulova, T. L., Skundin, A. M., Pleskov, Yu. V., Konkov, O. I., Terukov, E. I., and Trapeznikova, I. N., "Lithium intercalation into amorphous silicon thin films", Semiconductors, 40 (2006) 468.

77. Lauer, M., R., Valenti, Kandpal, H. C., and Sheshadri, R., "First-principles electronic structure of spinel $LiCr_2O_4$: A possible half-metal", Phys. Rev. B, 69 (2004) 075117.

78. Leroux Fabrice and Nazar Linda F., "3-volt manganese dioxide: the amorphous alternative", Solid State Ionics, 100 (1997) 103

79. Li, W. and Currie, J. C., "Morphology effects on the electrochemical performance of $LiNi_{1-x}Co_xO_2$", J. Electrochem. Soc., 144 (1997) 2773

80. Li, D., Kato, Y., Kobayakawa, K., and Noguchi, H., "Preparation and electrochemical characteristics of $LiNi_{1/3}Mn_{1/3}Co_{1/3}O_2$ coated with metal Oxides coating", J. Power Sources, 160 (2006) 1342.

81. Lin, J. S, Qteish, A, Payne, M. C., and Heine, V., "Optimized and transferable non local separable ab-inito psedopotentials", Phys. Rev. B, 47 (1993) 4174

82. Liu, B., in report on workshop "Numerical Algorithms in chemistry: Algebraic Methods" edited by C. Moler and I. Shavitt (Lawrence Barkley Lab. Univ. of California, 1978), p. 49.

83. Liu, D., Wang, Z., and Chen, L., "Comparison of structure and electrochemistry of Al- and Fe-doped $LiNi_{1/3}Co_{1/3}Mn_{1/3}O_2$", Electrochimica Acta, 51 (2006) 4199.

84. Manev, V., Momchilov, A. and Nassalevska, A., "Rechargeable Lithium battery with spinel-related $\lambda-MnO_2$ I. Synthesis of $\lambda-MnO_2$ for battery applications", J. Power Sources, 43-44 (1993) 551.

85. Martin, R. M., "Electronic structure: Basic theory and practical Methods", Cambridge University Press, 2004.

86. Meng, W., Feng, W., and Yue-feng, S., "Synthesis and characterization of $LiCo_{1/3}Ni_{1/3}Mn_{1/3}O_2$ by an improved sol-gel method", Journal of Beijing Institute of Technology. 27 (Suppl. 2) (2007) 95.

87. Mishra, S. K. and Ceder, G., "Structural stability of Lithium Manganese Oxides", Phys. Rev. B, 59 (1999) 6120.

88. Mizushima, K., Jones, P. C., Wiseman, P. J., and Goodenough, J. B., "Li_xCoO_2 (0 < x < 1): A new cathode material for batteries of high energy density", Mater. Res. Bull., 15 (1980) 783.

89. Molenda, M., Dziembaj, R., Majda, D., Dudek, M., "Synthesis and Characterization of Sulphided Lithium Manganese Spinels $LiMn_2O_{4-y}S_y$ Prepared By Sol–Gel Method", Solid State Ionics, 176 (2005) 1705.

90. Monkhorst, H. J. and Pack, J. D., "Special points for Brillouin-zone integration", Phys. Rev. B, 13 (1976) 5188.

91. Murphy, D. W., Trumbore, F. A. US Patent 4035555, July 12, 1977

92. Murphy, D. W., Cava, R. J., Zahurak, S. M. and Santoro, A., "Ternary Li_xTiO_2 Phases From Insertion Reactions", Solid State Ionics, 9 & 10 (1983) 413.

93. Nakai Izumi, Takahashi Kouta, Shiraishi Youhei, Nakagome Tatsuji, and Nishikawa Fumishige, "Study of the Jahn–Teller distortion in $LiNiO_2$, a cathode material in a rechargeable Lithium battery, by in situ X-ray absorption fine structure analysis", J. Solid State Chem., 140 (1998) 145.

94. Nakamura, T., Demidzu, H., and Yamada, Y., "Synthesis and magnetic study On Mg^{2+}-substituted Li–Mn spinel oxides", J. Phys. Chem. Solids, 69 (2008) 2349.

95. Narayan, J. and Bhosle, V. M., "Phase transition and critical issues in structure-property correlations of vanadium oxide", J. Appl. Phys., 100 (2006) 103524.

96. Narukawa, S., Nakane, I., Imachi, N., Fukuoka, S., Yamasaki, M., 11th IMLB, Monterey, CA, USA, June 2002, Abs 2.

97. Nishi, Y., Azuma, H., and Omaru, A., US Patent 4959281, Sep. 25, 1990.

98. Nishikawa, "Structure of Some Crystal of the Spinel Group", Proc. Math. Phys. Soc. Tokyo, 8 (1915) 199.

99. Noel, M. and Suryanarayanan, V., "Role of carbon host lattices in Li-ion intercalation/de-intercalation processes", J. Power Sources, 111 (2002) 193.

100. Numata, T., Amemiya, C., Iriyama, J., Miura, T., Shirakata, M., NEC R&D 41 (2000) 8.

101. Ohzuku, T. and Makimura, Y., "Layered Lithium insertion material of $LiCo_{1/3}Ni_{1/3}Mn_{1/3}O_2$ for Lithium-ion batteries", Chem. letters, 30 (2001) 642.

102. Ohzuku Tsutomu, Kitagawa Masaki, and Hirai Taketsugu, "Electrochemistry of manganese dioxide in Lithium nonaqueous cell III. X-Ray diffractional study on the reduction of spinel-related manganese dioxide", J. Electrochem. Soc., 137 (1990) 769.

103. Ohzuku Tsutomu, Ueda Atsushi, Nagayama Masatoshi, Iwakoshi Yasunobu and Komori Hidekhi, "Comparative study of $LiCoO_2$, $LiNi_{1/2}Co_{1/2}O_2$ and $LiNiO_2$ for 4 volt secondary Lithium cells", Electrochimica Acta, 38 (1993) 1159.

104. Oikawa, K. Kamiyama, T., Izumi, F., Nakazato, D., Ikuta, H., and Wakihara, M., "Neutron and X-Ray powder diffraction studies of $LiMn_{2-y}Cr_yO_4$", J. of Solid State Chem., 146 (1999) 322.

105. Oikawa Kenichi, Kamiyama Takashi, Izumi Fujio, Chakoumakos Bryan C., Ikut Hiromasa, Wakihar Masataka, Li Jianqi, Matsu Yoshio, "Structural phase transition of the spinel-type oxide $LiMn_2O_4$", Solid State Ionics, 109 (1998) 35.

106. Ooms, F.G.B., Kelder, E.M., Schoonman, J., Wagemaker, M., Mulder, F.M., "High-voltage $LiMg_\delta Ni_{0.5-\delta}Mn_{1.5}O_4$ spinels for Li-ion batteries", Solid State Ionics, 152–153 (2002) 143.

107. Orman, H.J. and Wiseman, P.J., "Cobalt (III) Lithium Oxide, $CoLiO_2$: Structure refinement by powder neutron diffraction", Acta Crystallogr., 40 (1980) 12.

108. Ouyang, C. Y., Shi, S. Q., and Lei, M. S., "Jahn–Teller distortion and electronic structure of $LiMn_2O_4$", J. Alloys Compd., 474 (2009) 370.

109. Padhi, A.K., Nanjundaswamy, K. S., and Goodenough, J. B., "Phospho-olivines as positive- electrode Materials for Rechargeable Lithium batteries", J. Electrochem. Soc., 144 (1997) 1188.

110. Paolone, A., Castellano, C., Cantellli, R., Rousse, G., and Masquelier, C., "Evidence of a splitting of the Mn-O distance and of a large lattice disorder in the charge-ordered phase of $LiMn_2O_4$ obtained by EXAFS", Phys. Rev. B, 68 (2003) 014108.

111. Park, S. H., Park, K. S., Sik, S. M., Sun, Y. K., and Nahm, K. S., "Synthesis and electrochemical characterization of $Li_{1.02}Mg_{0.1}Mn_{1.9}O_{3.99}S_{0.01}$ using sol-gel method", J. Power Sources, 92 (2001) 244.

112. Payne, M. C., Teter, M. P., Allan, D. C., Arias, T. A. and Joannopoulos, J. D., "Iterative minimization techniques for ab-initio total-energy calculations: molecular dynamics and conjugate gradient", Rev. of Modern Phys., 64 (1992) 1045.

113. Peled, E., Golodnitsky, D., Menachem, C., and BarTow, D., "An advanced tool for the selection of electrolyte components for rechargeable Lithium batteries", J. Electrochem. Soc., 145 (1998) 3482.

114. Perdew, J. P. and Wang Y., "Accurate and simple analytic representation of the electron-gas correlation energy", Phys. Rev. B 45, (1992) 13244.

115. Picciotto, L A de, Thackeray, M. M., David, W I F, Bruce, P G and Goodenough, J B, "Structural Characterization of Delithiated $LiVO_2$", Mat. Res. Bull.,19 (1984) 1497

233

116. Picciotto, L A de and Thackeray M. M., *"Insertion/Extraction Reactions of Lithium with LiV_2O_4"*, Mat. Res. Bull., 20 (1985) 1409.

117. Pistoia, G., Rossi, M. D., and Scrosati, B., *"Study of the behavior of ethylene carbonate as a nonaqueous battery solvent"*, J. Electrochem. Soc., 117 (1970) 500.

118. Prasad, R., Benedek, R., and Thackeray, M. M., *"Dopant-Induced Stabilization of Rhombohedral $LiMnO_2$ against Jahn-Teller Distortion"*, Phys. Rev. B, 71 (2005) 134111.

119. Press, W. H., Flannery, B. P., Teukolsky, S. A., and Vetterling, W. T., *"Numerical Recipes"*, Cambridge University Press, New York (1986).

120. Preudhomme, J., Ann. Chim. (Paris), 9 (1974) 31.

121. Pulay, P., *"Convergence acceleration in iterative sequences, The case of SCF iteration"*, Chem. Phys. Lett., 73 (1980) 393.

122. Robertson, A. D., Lu, S. H., Averill, W. F., and Howard, W. F., Jr., *"M^{3+} Modified $LiMn_2O_4$ Spinel Intercalation Cathodes I. Admetal effects on morphology and electrochemical performance"*, J. Electrochem. Soc., 144 (1997) 3500

123. Robertson, A. D., Lu, S. H., and Howard, W. F., Jr., *"M^{3+} modified $LiMn_2O_4$ spinel intercalation cathodes II. Electrochemical stabilization by Cr^{3+}"*, J. Electrochem. Soc., 144 (1997) 3505.

124. Rojas Rosa Maria, Petrov, K., Avdeev, G., Amarilla, J. M., Pascual, L. and Rojo, J. M., *"High-temperature thermal behavior of Cr-Doped $LiMn_2O_4$ spinels synthesized by the Sucrose-aided combustion method"*, Journal of Thermal Analysis and Calorimetry, 90 (2007) 67.

125. Sanyal, M. K., Datta, A., and Hazra, S., *"Morphology of nanostructured materials"*, Pure Appl. Chem., 74 (2002) 1553.

126. Shi, S., Wang, D. S., Meng, S., Chen, L., and Huang, X., *"First-Principles studies of cation-doped spinel $LiMn_2O_4$ for Lithium Ion batteries"*, Phys. Rev. B, 67 (2003) 115130.

127. Sigala, C., Verbaere, A., Mansot, J. L., Guyomard, D., Piffard, Y., and Tournoux, M., *"The Cr-substituted spinel Mn oxides $LiCr_yMn_{2-y}O_4$ ($0 \leq y \leq 1$): Rietveld analysis of the structure modifications induced by the electrochemical Lithium deintercalation"*, J. Solid State Chem., 132 (1997) 372.

128. Sigala, C., Salle, A. Le Gal La, Piffard, Y., and Guyomard, D., "Influence of the Cr content on the Li deinsertion behavior of the $LiCr_yMn_{2-y}O_4$, $0 < y < 1$. Compounds I. separation of bulk and superficial processes at high voltage", J. Electrochem. Soc., 148 (2001) A812.

129. Sigala, C., Salle, A. Le Gal La, Piffard, Y., and Guyomard, D., "Influence of the Cr content on the electrochemical behavior of the $LiCr_yMn_{2-y}O_4$ $0<y<1$. Compounds II. Cyclovoltammetric study of bulk and superficial processes", J. Electrochem. Soc., 148 (2001) A819.

130. Sigala, C., Salle, A. Le Gal La, Piffard, Y., and Guyomard, D., "Influence of the Cr content on the electrochemical behavior of the $LiCr_yMn_{2-y}O_4$.$0 < y < 1$. Compounds III. Galvanostatic study of bulk and superficial processes", J. Electrochem. Soc., 148 (2001) A826.

131. Silva, S. R. P. and Carey, J. D., "Enhancing the electrical conduction in amorphous carbon and prospects for device applications", Diamond and Related Materials, 1 2 (2003) 151.

132. Simon, P. and Gogotsi, Y., "Materials for electrochemical capacitors", Nature Materials, 7 (2008) 846.

133. Sims, R. E. H., "Hydropower, Geothermal, and Ocean energy", Mater. Res. Soc. Bull., 33 (2008) 389.

134. Sinha, S. and Murphy, D.W., "Lithium Intercalation in Cubic TiS_2", Solid State Ionics, 20 (1986) 81.

135. Son, J.T., Kim, H.G., "New investigation of Fluorine-Substituted spinel $LiMn_2O_{4-x}F_x$ by using sol–gel process", J. Power Sources, 147 (2005) 220

136. Song, M. Y., Song, J., Bang, E., and Mumm, D. R., "Electrochemical properties of $LiNi_{1-y}Co_yO_2$ cathode materials synthesized from different starting materials by the solid-state reaction method", Ceramics Inter. in press, doi:10.1016/j.ceramint.2008.09.003.

137. Subbarao, S., Shen, D. H., Deligiannis, F., Huang, C. K., and Halpert, G., "Advances in ambient temperature secondary Lithium cells", J. Power Sources, 29 (1990) 579.

138. Sun Yang-Kook and Oh In-Hwan, "Cycling Behavior of oxysulfide spinel $LiCr_{0.19}Mn_{1.81}O_{3.98}S_{0.02}$ cathode material which shows no capacity loss in the 3-V region", J. Power Sources, 94 (2001) 132

139. Surampudi, S., Shen, D. H., Huang, C. K., Narayanan, S. R., Attia, A., Halpert, G., and Peled, E., "Effect of cycling on the Lithium/electrolyte interface in organic electrolytes", J. Power Sources, 43 (1993) 21.

140. Suryakala, K., Kalaignan, G. P., and Vasudevan, T., "Synthesis and electrochemical improvement of nanocrystalline $LiMn_{2-x}Mg_xO_4$ powder using sol-gel method", Int. J. Electrochem. Sci., 1 (2006) 372.

141. Tarascon, J. M., Gozdz, A. S., Schmutz, C., Shokoohi, F., and Warren, P. C., "Performance of Bellcore's plastic rechargeable Li-ion batteries", Solid State Ionics, 86-88 (1996) 49.

142. Tarascon, J. M. and Armand, M., "Issues and challenges facing rechargeable Lithium batteries", Nature, 414 (2001) 359.

143. Tarte, P. and Peeudhomme, J., "^6Li-^7Li Isotopic Shifts In The Infrared Spectrum Of Inorganic Lithium Compounds-II. Rhombohedral $LiXO_2$ Compounds", Spectrochemica Acta, 26A (1970) 747.

144. Teter, M. P., Payne, M. C., and Allan, D. C., "Solution of Schrodinger's equation for large systems", Phys. Rev. B, 40 (1989) 12255

145. Thackeray, M. M. and Coetzer, J., "A preliminary investigation of the electrochemical performance of α-Fe_2O_3 and Fe_3O_4 cathodes in high temperature cells", Mater. Res. Bull., 16 (1981) 591.

146. Thackeray, M.M., David, W.I.F., Bruce, P.G., and Goodenough, J.B., "Lithium insertion into manganese spinels", Mater. Res. Bull., 18 (1983) 461.

147. Thackeray, M.M., Baker, S.D. and Adendorff, K. T., Goodenough, J.B., "Lithium insertion into Co_3O_4: A preliminary investigation", Solid Stale Ionics 17 (1985) 175

148. Thackeray, M. M., De Picciotto, L. A., Dekock, A., Johnson, P. J., Nicholas, V. A. and Adendorff, K. T., "Spinel Electrodes For Lithium batteries - A Review", J. Power Sources, 21 (1987) 1.

149. Thackeray, M. M., Mansuetto, M. F., Dees, D. W. and Vissers, D. R., "The Thermal Stability of Lithium-Manganese-Oxide Spinel Phases", Mater. Res. Bull., 31 (1996) 133.

150. Thackeray, M. M., "Manganese oxides for lithium batteries", Prog. Solids. Che., 25 (1997) 1.

151. Thackeray, M., "Lithium ion batteries: an unexpected conductor", Nature Materials, 1 (2002) 81.

152. Thirunakaran, R., Kim, Ki-Tae, Kang, Yong-Mook, Seo, Chan-Yeo, Young-Lee Jai, "Adipic acid assisted, sol–gel route for synthesis of $LiCr_xMn_{2-x}O_4$ cathode material", J. Power Sources, 137 (2004) 100.

153. Thirunakaran, R., Sivashanmugam, A., Gopukumar, S., Rajalakshmi, R., "Cerium and zinc: Dual-Doped $LiMn_2O_4$ Spinels as Cathode Material For Use In Lithium Rechargeable batteries", J. of Power Sources, 187 (2009) 565.

154. Thongtem T. and Thongtem, S., "Synthesis of $Li_{1-x}Ni_{1+x}O_2$ using malonic acid as a chelating agent", Ceramics International, 31 (2005) 241.

155. Tian, W., Chisholm, M.F., Khalifah, P.G., Jin, R., Sales, B.C., Nagler, S.E., Mandrus, D., "Single crystal growth and characterization of nearly stoichiometric $LiVO_2$", Mater. Res. Bull., 39 (2004) 1319.

156. Todorov, Y. M. and Numata, K., "Effects of the Li:(Mn + Co + Ni) molar ratio on the electrochemical properties of $LiMn_{1/3}Co_{1/3}Ni_{1/3}O_2$ cathode material", Electrochimica Acta, 50 (2004) 495.

157. Tokumitsu, K., Mabuchi, A., Fujimoto, H., and Kasuh, T., "Electrochemical insertion of Lithium into carbon synthesized from condensed aromatics", J. Electrochem. Soc., 143 (1996) 2235.

158. Tsunoda, M., Oshima, Y., Yoshinaga, M., Shirasu, T., NEC R&D 41 (2000) 13.

159. Tukamoto, H. and West, A. R., "Electronic Conductivity of $LiCoO_2$ and Its Enhancement by Magnesium Doping", J. Electrochem. Soc., 144 (1997) 3164.

160. VASP The Guide, (2009) written by Georg Kresse, Martijn Marsman, and Jurgen Furthmuller Computational Physics, Faculty of Physics, Universit¨at Wien, Sensengasse 8, A-1130 Wien, Austria, (http://cms.mpi.univie.ac.at/VASP/)

161. Venderbilt, D., "Soft self-consistent pseudopotentials in a generalized eigenvalue formalism", Phys. Rev. B, 41 (1990) 7892.

162. Vleck, J. H. V., "The Jahn-Teller Effect and Crystalline Stark Splitting for Clusters of the Form XY_6", J. Chem. Phys., 7 (1939) 72.

163. Wang, Q., Sun, J., Yao, X., and Chen, C., "Thermal stability of $LiPF_6$/EC + DEC electrolyte with charged electrodes for Lithium ion batteries", Thermochimica Acta, 437 (2005) 12.

164. Wang, L., Maxisch, T., and Ceder, G., "Oxidation energies of transition metal oxides within the GGA+U framework", Phys. Rev. B, 73 (2006) 195107.

165. Wang Haifeng, Jang Young-II, Huang Biying, Sadoway Donald R., and Chiang Yet-Ming, "TEM study of electrochemical cycling-induced damage and disorder in $LiCoO_2$ cathodes for rechargeable Lithium batteries", J. Electrochem. Soc., 146 (1999) 473.

166. Wang Hsien-Cheng, Lu Chung-Hsin, "Dissolution Behavior of Chromium-Ion Doped Spinel Lithium Manganate at Elevated Temperatures", J. Power Sources 119–121 (2003) 738.

167. Wen, C. J., Boukamp, B. A., Huggins, R. A., and Weppner, W., "Thermodynamics and mass transport properties of LiAl", J. Electrochem Soc., 126 (1979) 2258.

168. Wen, C. J., and Hugglns, R. A., "Thermodynamic study of the Lithium-Tin system", J. Electrochem. Soc., 128 (1981) 1181.

169. Weydanz, W. J., Mehrens, M. W., and Huggins, R. A., "A room temperature study of the binary Lithium–Silicon and the ternary Lithium–Chromium–Silicon system for use in rechargeable Lithium batteries", J. Power Sources, 81–82 (1999) 237.

170. White, W. B. and Deangelis, B. A., "Interpretation of the vibrational spectra of spinels", Spectrochimica Acta, 25A (1967) 985.

171. Whittingham, M. S. and Zawodzinski, T., "Introduction: Batteries and fuel Cells", Chem. Rev. 104 (2004a) 4243.

172. Whittingham, M. S., "Lithium batteries and cathode materials", Chem. Rev., 104 (2004) 4271.

173. Whittingham, M. S., "Materials challenges facing electrical energy storage", Mater. Res. Soc. Bull., 33 (2008) 411.

174. Robert A. Wiesboeck, Atlanta, Ga., US patent 3654330, Apr. 4, 1972

175. Winter, M., Besenhard, J. O., Spahr, M. E., and Novak, P., "Insertion electrode materials for rechargeable Lithium batteries", Adv. Mater., 10 (1998) 725.

176. Winter, M. and Brodd, R. J., "What are batteries, fuel cells, and supercapacitors?", Chem. Rev., 104 (2004) 4245.

177. Wu, C., Wang, Z., Wu, F., Chen, L., and Huang, X., "Spectroscopic studies on cation-doped spinel $LiMn_2O_4$ for Lithium ion batteries", Solid State Ionics, 144 (2001) 277.

178. Xu, K., Ding, M. S., and Jow, T. R., "Quaternary onium salts as nonaqueous electrolytes for electrochemical capacitors", J. Electrochem. Soc., 148 (2001) A267.

179. Xu, K., "Nonaqueous liquid electrolytes for Lithium-based rechargeable batteries", Chem. Rev., 104 (2004) 4303.

180. Yabuuchi, N. and Ohzuku T., "Novel Lithium insertion material of $LiCo_{1/3}Ni_{1/3}Mn_{1/3}O_2$ for advanced Lithium-ion batteries", J. Power Sources, 119–121 (2003) 171.

181. Yamada, A., D.Eng. Thesis, University of Tsukuba, Tsukuba, Japan.1996

182. Yamada Atsuo and Tanaka Masahlro, "Jahn-Teller Structural Phase Transition Around 280K in $LiMn_2O_4$", Mater. Res. Bull., 30 (1995) 715.

183. Yamaguchi, R., Ikuta, H., and Wakihara, M., "Heat of formation for $LiM_yMn_{2-y}O_4$ (M=Co, Cr, Li, Mg, Ni) spinel solid solution", Journal of Thermal Analysis and Calorimetry, 57 (1999) 797.

184. Yamaura, J., Ozaki, Y., Morita, A., and Ohta, A., "High voltage, rechargeable Lithium batteries using newly developed carbon for negative electrode material", J. Power Sources, 43-44 (1993) 233.

185. Yang, X. Q., Sun, X., Balasubramanian, M., McBreen, J., Xia, Y., Sakai, T., and Yoshio, M., "The population of oxygen vacancies in $Li_{1+y}Mn_{2-y}O_{4-\delta}$ type cathode materials the primary factor of temperature dependent structural changes", Electrochem. and Solid-State Lett., 4 (2001) A117.

186. Yoshio Masaki, Xia Yongyao, Kumada Naoki, Ma Shuhua, "Storage and cyclic performance of Cr-modified spinel at elevated temperatures", J. Power Sources, 101 (2001) 79.

187. Zhang, S. S., Liu, Q. G., and Yang, L. L., *"Polyacene as an anode in Lithium Ion batteries"*, J. Electrochem. Soc., 140 (1993) L107.

188. Zhou, G. T., Palchik, O., Pol, V. G., Sominski, E., Koltypin, Y., and Gedanken A., *"Microwave-assisted solid-state synthesis and characterization of intermetallic compounds of Li_3 Bi and Li_3Sb"*, J. Mater. Chem., 13 (2003) 2607.